Synthesis, Characterization and Electronic Applications of Novel Calamitic Azulenes

Von der Fakultät Chemie der Universität Stuttgart

zur Erlangung der Würde eines Doktors der Naturwissenschaften (Dr. rer. nat.)

genehmigte Abhandlung

Vorgelegt von

Finn Fredrik Schulz

aus Bietigheim-Bissingen

Hauptberichterin:	**Prof. Dr. Sabine Laschat**
Mitberichterin:	**Dr. Johanna Bruckner**
Prüfungsvorsitz:	**Prof. Dr. Anke Krüger**

Tag der mündlichen Prüfung: 27.10.2023

Institut für Organische Chemie der Universität Stuttgart

2023

"There is a whole new world

That you need to explore.

It's the sound of the rail

That you love and adore."

Nico Sallach

Erklärung über die Eigenständigkeit der Dissertation

Ich versichere, dass ich die vorliegende Arbeit mit dem Titel „Synthesis, Characterization and Electronic Applications of Novel Calamitic Azulenes" selbständig verfasst und keine anderen als die angegebenen Quellen und Hilfsmittel benutzt habe. Aus fremden Quellen entnommene Passagen und Gedanken sind als solche kenntlich gemacht. Die elektronische Version stimmt mit der gedruckten überein.

Declaration of Authorship

I hereby certify that the dissertation entitled „Synthesis, Characterization and Electronic Applications of Novel Calamitic Azulenes" is entirely my own work except where otherwise indicated. Passages and ideas from other sources have been clearly indicated. The electronic version matches the printed one.

Stuttgart, den 20. Juni 2023   Finn Fredrik Schulz

Danksagung

Im gleichen Atemzug sollte hier der ganze Ak Giesselmann, insbesondere aber Pierre genannt werden, bei dem ich zwischendurch fast mehr Zeit verbracht habe #Nanostar. Vielen Dank für die Sisyphus-Arbeit einem Org die Künste der PC beizubringen.

Danke auch an Johnny, der so lange auf mich eingeredet hat, bis ich mich zu einer Promotion im AK02 entschieden habe.

Das Studium wurde mir immer versüßt durch die okkulten Machenschaften der Freichemiker, insbesondere auch die schönen Ausflüge nach Bayern, das können wir gerne beibehalten!

Ohne eine gute Basis geht es nicht. Meine Familie hat mich immer unterstützt egal wo ich gerade was. Nur mit dieser Grundlage kam ich dorthin, wo ich gerade bin.

Besonderster Dank geht aber natürlich an Karina, die mit mir jetzt schon seit fast einem Jahrzehnt die top-secret Mission verfolgt die Welt zu erobern. Ohne prahlen zu wollen würde ich sagen, wir haben es schon ganz schön weit geschafft, sollten es aber noch ein wenig länger geheim halten. Vielen Dank für die wunderschöne Zeit, ob beim Yoga, in den Bergen oder zu Hause, ob Quatsch oder Ernst, ich genieße jeden Moment mit Dir und werde damit auch nicht aufhören.

Abstract

Due to its inherent dipole moment and unique electronic properties the azulene moiety is of interest in the development of novel organic semiconductors for optoelectronic applications. Molecular orientation of the applied organic semiconductors is crucial for the performance of organic electronics and can be controlled to some extent e.g., through self-assembly of liquid crystals. We developed a divergent synthetic route starting from 2,6-dibromoazulene to access novel, calamitic mesogens and investigated these azulenes on their mesomorphic behavior and -for selected examples- on their suitability as organic semiconductors.

Azulenes with only one side chain tethered to the 7-membered ring exclusively formed soft-crystalline smectic E-phases (SmE), with 2-(6-(dodecyloxy)azulen-2-yl)benzo[b]thiophene (**12O-Az-BT**) exhibiting the broadest phase width between 51 °C and 270 °C during cooling. Additionally, derivatives with two side chains and a lateral substituent at the 5-membered ring were prepared. Based on 6-dodecyloxy-2-(4-dedecyloxyphenyl)azulene-1-carbonitrile (**12O-AzCN-PhO12**), parameters such as chain length, size, and polarity of the lateral substituent, and (hetero)aromatic moiety in 2-position were systematically varied to understand the complex structure-property-relationship governing mesomorphic properties of our novel azulenes. Mainly SmC phases were observed for derivatives with unhindered interaction of the aromatic azulene cores. Upon disturbance of the stacking due to bulky substituents, less polar side chains or the electronic influence of heteroatoms, less ordered SmA phase were the preferred mesophase.

Some azulene derivatives with a SmA-SmC phase sequence were found to show de Vries-like properties, which are heavily investigated in the context of next generation liquid crystal displays. The best values for important de Vries parameters, namely a maximum layer shrinkage of only 0.16 % resulting in reduction factors of down to 0.14 compete with state of the art deVries materials. Additionally, 6-hexadecyloxy-2-(4-octyloxyphenyl)azulene-1-carbonitrile (**16O-AzCN-PhO8**) exhibited a SmA-SmC-SmA phase sequence. The rarely observed SmA re-entrant phase was explained by a reorientation of the azulene cores which was also identified as a key factor for de Vries-like behavior.

A selected series of azulenes modified with thiophene units was investigated on their suitability as semiconducting layer in organic field effect transistor (OFET) devices. Spin-coating of these azulene derivatives at mesophase temperature resulted in uniform polycrystalline thin films. In the corresponding OFET devices, **12O-Az-BT** achieved the best hole mobility with $\mu^+ = (3.1 \pm 0.5) \cdot 10^{-3} \, \text{cm}^2\text{V}^{-1}\text{s}^{-1}$.

Kurzzusammenfassung

Aufgrund seines inhärenten Dipolmoments und seiner besonderen elektronischen Eigenschaften ist der Azulen Baustein interessant für die Entwicklung neuer organischer Halbleiter für optoelektronische Anwendungen. Die molekulare Orientierung der eingesetzten organischen Halbleiter ist entscheidend für die Leistung der elektronischen Bauteile und kann bis zu einem gewissen Grad kontrolliert werden, z. B. durch die Selbstorganisation von Flüssigkristallen. Mithilfe einer divergenten Synthese ausgehend von 2,6-Dibromazulen wurden neue, kalamitische Mesogene dargestellt, und diese Azulene auf ihr mesomorphes Verhalten und für ausgewählte Beispiele auf ihre Eignung als organische Halbleiter untersucht. Azulene mit nur einer Seitenkette am Siebenring bildeten ausschließlich weichkristalline smektische E-Phasen (SmE), wobei 2-(6-(Dodecyloxy)azulen-2-yl)benzo[b]thiophen (**12O-Az-BT**) beim Abkühlen die größte Phasenbreite zwischen 51 °C und 270 °C aufwies. Außerdem wurden Derivate mit zwei Seitenketten und einem lateralen Substituenten am Fünfring dargestellt. Ausgehend von 6-Dodecyloxy-2-(4-dedecyloxyphenyl)azulen-1-carbonitril (**12O-AzCN-PhO12**) wurden Parameter wie Kettenlänge, Größe und Polarität des lateralen Substituenten und die (hetero)aromatische Einheit in 2-Position systematisch variiert, um die komplexen Struktur-Eigenschafts-Beziehungen zu verstehen, die entscheidend für die mesomorphen Eigenschaften der neuen Azulene sind. Für Derivate mit ungehinderter Wechselwirkung der aromatischen Azulenkerne wurden hauptsächlich die SmC-Phase beobachtet. Wenn die Stapelung durch sperrige Substituenten, weniger polare Seitenketten oder den elektronischen Einfluss von Heteroatomen gestört wurde, war die weniger geordnete SmA-Phase bevorzugt.

Einige Azulenderivate mit einer SmA-SmC-Phasensequenz zeigten de Vries-artige Eigenschaften, die im Zusammenhang mit Flüssigkristallanzeigen der nächsten Generation intensiv untersucht werden. Die besten Werte für wichtige de Vries-Parameter, wie eine maximale Schichtschrumpfung von nur 0.16 %, und ein R-Wert von bis zu 0.14 entsprechen dem Stand der Technik bei de Vries Materialien. Darüber hinaus wies 6-Hexadecyloxy-2-(4-octyloxyphenyl)azulen-1-carbonitril (**16O-AzCN-PhO8**) eine SmA-SmC-SmA-Phasenfolge auf. Die selten beobachtete wiederkehrende SmA-Phase wurde durch eine Umorientierung der Azulenkerne erklärt, die auch als Schlüsselfaktor für das de Vries-artige Verhalten identifiziert wurde.

Eine ausgewählte Reihe von Azulenen, die mit Thiopheneinheiten modifiziert wurden, wurde als Halbleiterelement in organischen Feldeffekttransistoren (OFETs) untersucht. Durch Spin-Coating dieser Azulenderivate bei Mesophasentemperatur wurden einheitliche polykristalline dünne Schichten erhalten. Von den daraus hergestellten OFETs erzielte **12O-Az-BT** die beste Mobilität mit $\mu^+ = (3.1 \pm 0.5) \cdot 10^{-3} \text{cm}^2\text{V}^{-1}\text{s}^{-1}$.

List of Publications

1) **Alkoxy-Bromo-Azulenes Displaying Ambient Temperature Smectic E-Phases.**
   Schulz, F.; Ehni, P.; Wank, B.; Bauer, A.; Frey, W.; Laschat, S.; *Liq. Cryst.* **2021**, *48*
   (6), 832–843. (DOI: 10.1080/02678292.2020.1821919)
   Reproduced from ref [1] with permission from Taylor&Francis.

2) **Phase Behaviour of Alkynyl-Terminated Bicyclo[3.3.0] Octa-1,4-Diene Ligands: A
   Serendipitous Discovery of Novel Calamitic Liquid Crystals.** Schulz, F.; Deimling,
   M.; Laschat, S.; *Liq. Cryst.* **2021**, *48* (11), 1575–1580.
   (DOI: 10.1080/02678292.2021.1891478)
   Reproduced from ref [2] with permission from Taylor&Francis.

3) **Liquid Crystalline Self-Assembly of Azulene–Thiophene Hybrids and Their
   Applications as OFET Materials.** Schulz, F.; Takamaru, S.; Bens, T.; Hanna, J.;
   Sarkar, B.; Laschat, S.; Iino, H.; *Phys. Chem. Chem. Phys.* **2022**, *24* (38), 23481–23489.
   (DOI: 10.1039/D2CP03527H)
   Reproduced from ref [3] with permission from the Royal Society of Chemistry.

4) **First Azulene Liquid Crystal with de Vries behavior and a SmA Re-entrant Phase.**
   Schulz, F.; Wank, B.; Nacke, P.; Frey, W.; Laschat, S.; *Mater. Adv.*, **2023**, *4* (5), 1306–
   1313 (DOI: 10.1039/D2MA01055K)
   Reproduced from ref [4] with permission from the Royal Society of Chemistry, open
   access journal.

5) **Tailoring liquid crystalline self-assembly and de Vries behavior of azulenes *via*
   lateral and core substitution.** Schulz, F.; Lutz, B.; Rück, D.; Batman, D.; Frey, W.;
   Laschat, S.; *Soft Matter* **2023**, *13* (19), 2397–2406. (DOI:10.1039/D3SM00205E)
   Reproduced from [5] with permission from the Royal Society of Chemistry.

6) **Self-Assembly of Aminocyclopropenium Salts: En Route to Deltic Ionic Liquid
   Crystals.** Litterscheidt, J.; Bandar, J. S.; Ebert, M.; Forschner, R.; Bader, K.; Lambert,
   T. H.; Frey, W.; Bühlmeyer, A.; Brändle, M.; Schulz, F.; Laschat, S.; *Angew. Chem. Int.
   Ed.* **2020**, *59* (26), 10557–10565.

7) **Liquid Crystalline Benzoic Acid Ester MIDA Boronates: Synthesis and
   Mesomorphic Properties.** Schilling, C.; Schulz, F.; Köhn, A.; Laschat, S.; *Org. Mater.*
   2020, *02* (4), 288–299.

8) **Liquid Crystalline Hydrazones Revisited: Dipolar Interactions vs Hydrogen Bonding Affecting Mesomorphic Properties.** Knelles, J.; Wanner, C.; Schulz, F.; Freund, M.; Kolmangadi, M. A.; Baro, A.; Huber, P.; Schönhals, A.; Laschat, S.; *Liq. Cryst.* **2021**, *48* (10), 1382–1391.

9) **Hockey-Stick Indoles: Turning a Calamitic Neutral Mesogen into an Ionic Liquid Crystal.** Trübe, K.; Bühlmeyer, A.; Schulz, F.; Grunwald, M. A.; Zens, A.; Baro, A.; Laschat, S.; *Liq. Cryst.* **2021**, *48* (13), 1919–1926.

10) **Tailoring Boron Liquid Crystals: Mesomorphic Properties of Iminodiacetic Acid Boronates.** Schilling, C.; Bauer, A.; Knöller, J. A.; Schulz, F.; Zens, A.; Laschat, S.; *J. Mol. Liq.* **2022**, *367*, 120519.

Contribution Report

1) The compounds described in this publication were synthesized by F.S. and investigated for their mesomorphic properties. He performed the measurement and evaluation, except for the X-ray diffraction measurement of compound **4b**, which was performed by P.E. The UV/VIS measurements and theoretical calculations for this publication were also carried out by F.S. B.W. and A.B. assisted in the synthesis of precursors. W.F. performed and evaluated single crystal measurements. S.L. designed, supervised, and supported the research. F.S. wrote the initial version of the manuscript, which was later edited by F.S. and S.L.

2) The first authorship of this work is shared by Finn Schulz and Max Deimling. F.S. studied the liquid crystalline behavior of the compounds using polarized optical microscopy, differential scanning calorimetry and X-ray diffraction and interpreted the data. M.D. synthesized the compounds described. S.L. supervised and assisted in the research. The initial version was written by S.L. and F.S., with S.L. describing the introduction and synthesis and F.S. writing the liquid crystalline characterization part. All authors contributed to the final version of the manuscript.

3) The materials described in this work were prepared by F.S. and studied for their liquid crystalline properties. F.S. also prepared the thin films of the compounds and characterized them by X-ray diffraction, atomic force microscopy and confocal laser scanning microscopy. He also fabricated the organic field effect transistors and studied their properties. S.T. instructed F.S. in the fabrication and characterization techniques of the films and transistors. He also

assisted in evaluating the measurement of the transistor properties. T.B. performed and evaluated the cyclic voltammetry measurements. J.H. helped with his expertise on liquid crystalline transistors. B.S. supervised the research of cyclovoltammetry measurements. S.L. designed the research and supervised the synthesis and liquid crystalline characterization. H.I. supervised the research of fabrication and characterization of the thin films and transistors. The initial version of the manuscript was written by F.S. All authors contributed to the final version of the manuscript.

4) F.S. prepared most of the compounds and investigated them for their liquid crystalline properties. In particular, he investigated the de Vries properties of the compounds by X-ray diffraction and the measurement of temperature-dependent birefringence. Furthermore, he interpreted the data and supervised B.W.'s work. B.W. synthesized the compound **12O-AzCN-PhO12** and studied the liquid crystalline properties. P.N. contributed his expertise to the measurement and interpretation of temperature-dependent birefringence. W.F. performed and evaluated the single crystal measurements. S.L. supervised and supported the research. F.S. prepared the initial version of the manuscript, which was revised by F.S. and S.L.

5) F.S. synthesized the five compounds **12S-AzCN-PhO12**, **12O-AzCN-PhS12**, **12S-AzCN-PhS12**, **12O-AzF-PhO12**, and **12O-AzNO$_2$-PhO12**. B.L. synthesized the five compounds **12O-AzNO$_2$-MePhO12**, **12O-Az-NO$_2$PhO12**, **12O-Az-Thi12**, **12O-AzCN-Thi12**, and **12O-AzCN-PyriO12** as part of a bachelor's thesis. D.R. prepared the compound **12Yne-AzCN-PhO12** as part of a bachelor's thesis. D.B prepared the four compounds **12O-AzCN-PhYne12**, **12Yne-AzCN-PhYne12**, **12O-Az-PyriO12** and **12Yne-AzNO$_2$-PhO12** as part of a research internship. The investigation of liquid crystalline properties was carried out by F.S. in collaboration with the respective student. F.S. also performed the detailed investigation of the de Vries properties and interpreted the liquid crystalline data in its entirety. In addition, he supervised the laboratory work of the students. W.F. performed and evaluated the single crystal measurements. S.L. supervised and supported the research. F.S. wrote the initial version of the manuscript, which was revised by F.S. and S.L.

x

Contents

1 Abbreviations

A	absorption		eV	Electronvolt
AC	smectic A to Smectic C transition		FET	field effect transistor
AFM	atomic force microscopy		HOMO	highest occupied molecular orbital
a.u.	arbitrary units		I	isotropic liquid phase
Az	azulene		I	detected light beam or current
BP	blue phase		I_0	incoming light beam
BPin	pinacolboranyl		I_{ds}	drain-source current
Γ	retardance		$\hat{k}$	director of the layer normal in smectic phases
c	concentration			
C	capacity		λ	wavelength
CLSM	confocal laser scanning microscopy		L	channel length
			LC	liquid crystal or liquid crystalline
Col_h	columnar hexagonal phase			
Col_r	columnar rectangular phase		lc_{max}	maximum layer contraction
Cr	crystalline phase		LUMO	lowest unoccupied molecular orbital
CV	cyclic voltammetry			
Cp	cyclopentadiene		μ	carrier mobility
d	thickness		Me	methyl
Δn	birefringence		N	nematic Phase
D	Debye		$\hat{n}$	director of the long axis of a mesogen
decomp.	decomposition			
DFT	density functional theory		n	diffraction order
DMF	dimethylformamide		Naph	naphtalene
DMSO	dimethyl sulfoxide		OAc	acetate
dppf	1,1'-bis(diphenylphosphino) ferrocene		OFET	organic field effect transistor
			OLED	organic light emitting diode
DSC	Differential Scanning Calorimetry		opt	optical
			Ox	oxidation
ε	extinction coefficient		p	positively biased
E	potential		p	*para* position
Et	ethyl		Pent	tetrahydropentalene

P_S	spontaneous polarization		SAXS	small angle X-ray scattering
Ph	phenyl		SmA	smectic A phase
POM	polarized optical microscopy		SmB	smectic B phase
Pyri	pyrimidine		SmC	smectic C phase
Θ	tilt angle of the SmC phase or angle of the X-ray during scattering		SmE	crystal-smectic E phase
			T	semperature
R	reduction value		T	2-thienyl
re	re-entrant		TGBA	twist grain boundary A phase
Red	reduction		BT	2-benzo[b]thiophenyl
rt	room temperature		iT	3-thienyl
Σ	translation order parameter		THF	tetrahydrofuran
S_1	first excited state		V_{ds}	drain-source voltage
S_2	orientational order parameter		V_g	gate voltage
SSFLC	surface stabilized ferroelectric liquid crystal		V_{th}	threshold voltage
			W	channel width
SSFLCD	surface stabilized ferroelectric liquid crystal display		WAXS	wide angle X-ray scattering
			XRD	X-ray diffractometry

2 Introduction

2.1 Azulene

Chamomile has long been known for its healing properties for stomach ailments.[6] An essential oil from this plant can be obtained by steam distillation of the flower heads (Figure 1a)[7] or other herbs e.g., wormwood. In 1863, Piesse named this oil azulene after its deep blue color that appeared upon heating (azure, French = blue).[8] However, isolation of the coloring compound by distillation was not possible. In 1914, Sherndal succeeded in isolating an azulene derivative for the first time with the aid of strong acids.[9] The molecular structure of the azulene moiety and thus, the origin of the remarkably blue color stayed unknown until 1936. Plattner and Pfau suggested a bicyclic system consisting of a 5- and a 7-membered ring (Figure 1b).[10] They even proved the structure by synthesizing first artificial azulenes which were equally colorful as the natural derivatives **1** and **2** (Figure 1c).
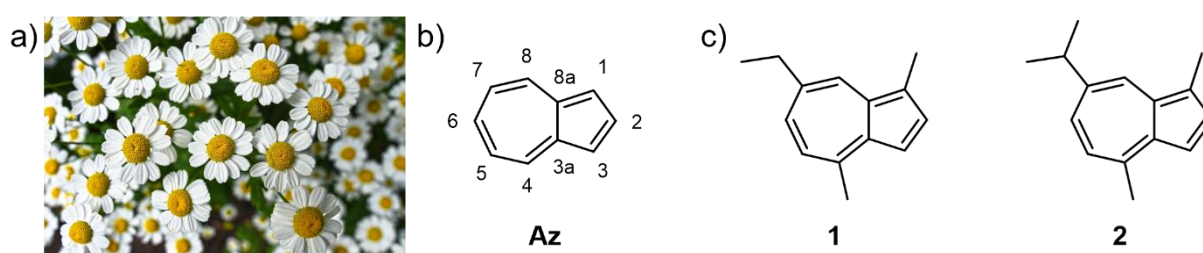

Figure 1: a) Chamomile flower heads. b) Molecular structure of azulene **Az**, the coloring compound in the azulene oil. c) Chamazulene **1** and guaiazulene **2** can be isolated from natural resources. Figure 1a was taken from ref [7].

Despite the successful structure elucidation, the blue appearance of azulene could not be explained at this time. In contrast, the widely known isomer naphthalene **3** and even the tricyclic anthracene are colorless solids. Although the isomeric nature of azulene and naphthalene suggests some similarity at first glance, their electronic structure is inherently different.[11] Azulene is part of the so-called non-alternating polycyclic aromatic hydrocarbons, which means that it has at least one odd-numbered ring. As a result, the frontier orbitals of those compounds are not symmetrical, but localized at different carbon atoms (Figure 3b). Due to the spatial separation, the electronic correlation between electrons in HOMO and LUMO is reduced. Thus, excitation to the S_1 state requires relatively little energy and the transition is in the visible range.[12] In addition to the unusual frontier molecular orbitals, azulene has another special feature: one can formulate a zwitterionic resonance structure **Az-mes** where both rings satisfy Hückel's rule for aromaticity (Figure 3a). The impact of the zwitterionic structure is emphasized by azulene **Az** bearing a permanent dipole moment of 1.08 D.[13]
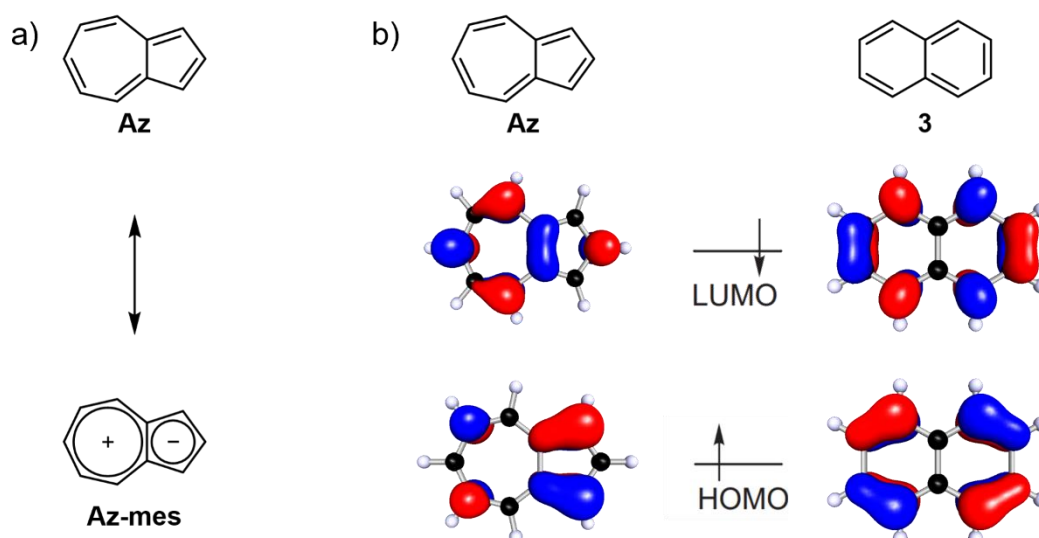
1

Figure 3: a) Azulene in its localized resonance structure **Az** and formulated as a zwitterion **Az-mes**. b) Frontier orbitals of azulene **Az** compared to its isomer naphthalene **3**.

Besides its unique structure, azulenes possess several applications. For example, azulene containing oils were used in medicine for centuries, it is not surprising that numerous azulene derivatives show divers biological applications, e.g. in tumor therapy or as an anti-inflammatory.[14–16] However, the intrinsic dipole moment and non-alternating character also render azulene as an ideal candidate for electronic and optoelectronic applications.[17–30] Yamaguchi described various regioisomers of terazulene, e.g **4** and **5** and azulene thiophene hybrids such as **6** as potent organic field effect transistors (OFETs) (Figure 2a).[31–33] Other derivatives have been shown to be promising candidates for organic solar cells. For example, the acid derivative **7** described by Zhang[34] or the azulene containing polymer **8** by Umeyama[35] have been successfully implemented in solar cells (Figure 2b).
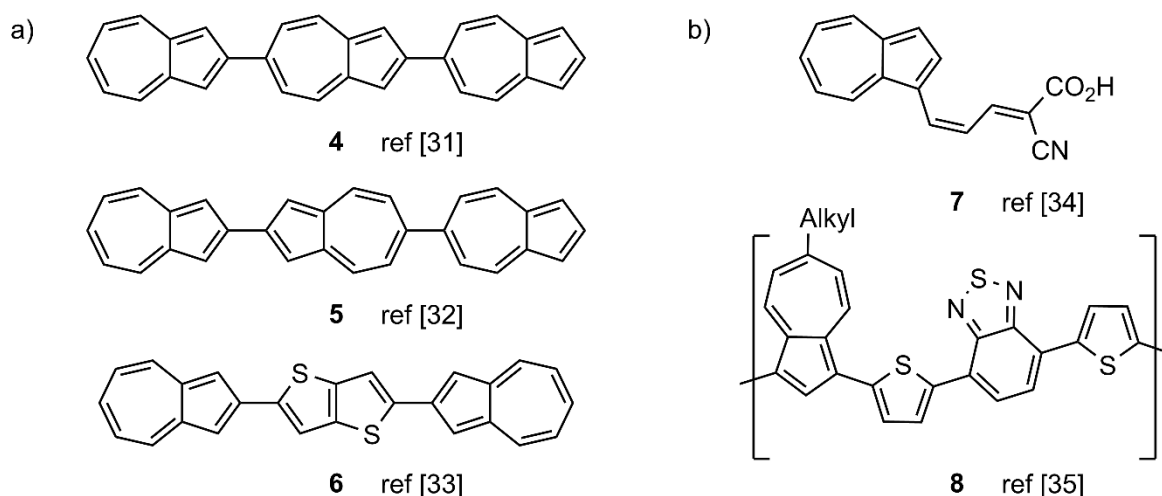

Figure 2: Azulene derivatives proposed for electronic applications in OFETs (a) and organic solar cells (b).

The wide range of applications of azulene derivatives could only be realized by various synthetic routes furnishing the azulene scaffold. For example, early attempts were based on dehydration strategies of the partially hydrated azulene.[36] This was only possible under harsh conditions and resulted in low yields. Soon the focus changed to direct synthetic paths with condensation reactions as the key step. Ziegler proposed cyclopentadiene (**Cp**) as the ideal starting material combined with an adequate partner.[37,38] In the simplest case, a two-fold condensation reaction with glutacondialdehyde should lead to unsubstituted azulene **Az**. Even though, this reaction did not work, it was possible to use the related Zincke-aldehyde **9** for this purpose (Figure 4a). The intermediate fulvene **10** transformed to azulene **Az** in 60 % yield upon heating to 250 °C. The method tolerates alkyl substituents on both starting materials and therefore allows the synthesis of a variety of alkylated azulenes.[11,36]

Pyridine can be considered as a derivative of the Zincke-aldehyde **9** that underwent an intramolecular imine-condensation. Hafner recognized this similarity and reacted *N*-alkyl pyridinium salts **11** with cyclopentadienyl sodium **12** (Figure 4b).[36] The Cp anion added to the pyridine in *ortho* position. Cleavage of the heterocyclic ring **13** to the fulvene **14** led to the reaction pathway already known when Zincke-aldehyde **9** was used. Even better results were obtained by switching the pyridinium salt to a pyrylium perchlorate salt **15** (Figure 4c). In this case, the reaction already takes place at room temperature. Unfortunately, synthesis of the unsubstituted azulene **Az** is not possible, only trisubstituted pyrylium derivatives can be used.[36,39] With the methods described, it is easy to condense a 7-membered ring to the already existing 5-membered ring. However, these routes are limited to alkyl-substituted azulenes and hardly tolerate any other functional groups. Activation of alkyl groups requires harsh conditions and thus limits the scope of accessible azulene derivatives.

A different approach towards the azulene scaffold was explored by Nozoe starting from the 7-membered 2-chlorotropone **17** (Figure 4d).[40] The 5-membered ring was built up by a cascade of condensations with diethyl acetonedicarboxylate **18** in basic medium. 12 equiv. of NaOEt were necessary to yield the 2-hydroxyazulene dicarboxylate **19** in 49 %. This method introduced oxygen based functional groups at the 5-membered ring ready for further functionalization. Besides the azulene dicarboxylate **19**, 2-aminoazulene derivatives proved also accessible when using malononitrile as a condensation partner.[41] Novel developments are usually based on these methods by Ziegler and Hafner or Nozoe.[42,43] Yet, gold catalyzed dimerization reactions of alkynes **20** towards highly substituted azulene derivatives **21** have also been described (Figure 4e).[44,45] The different strategies to build up the azulene core

scaffold, combined with numerous possibilities of post-modification, allow the tailor-made synthesis of almost any azulene derivative ready to be applied in various uses.
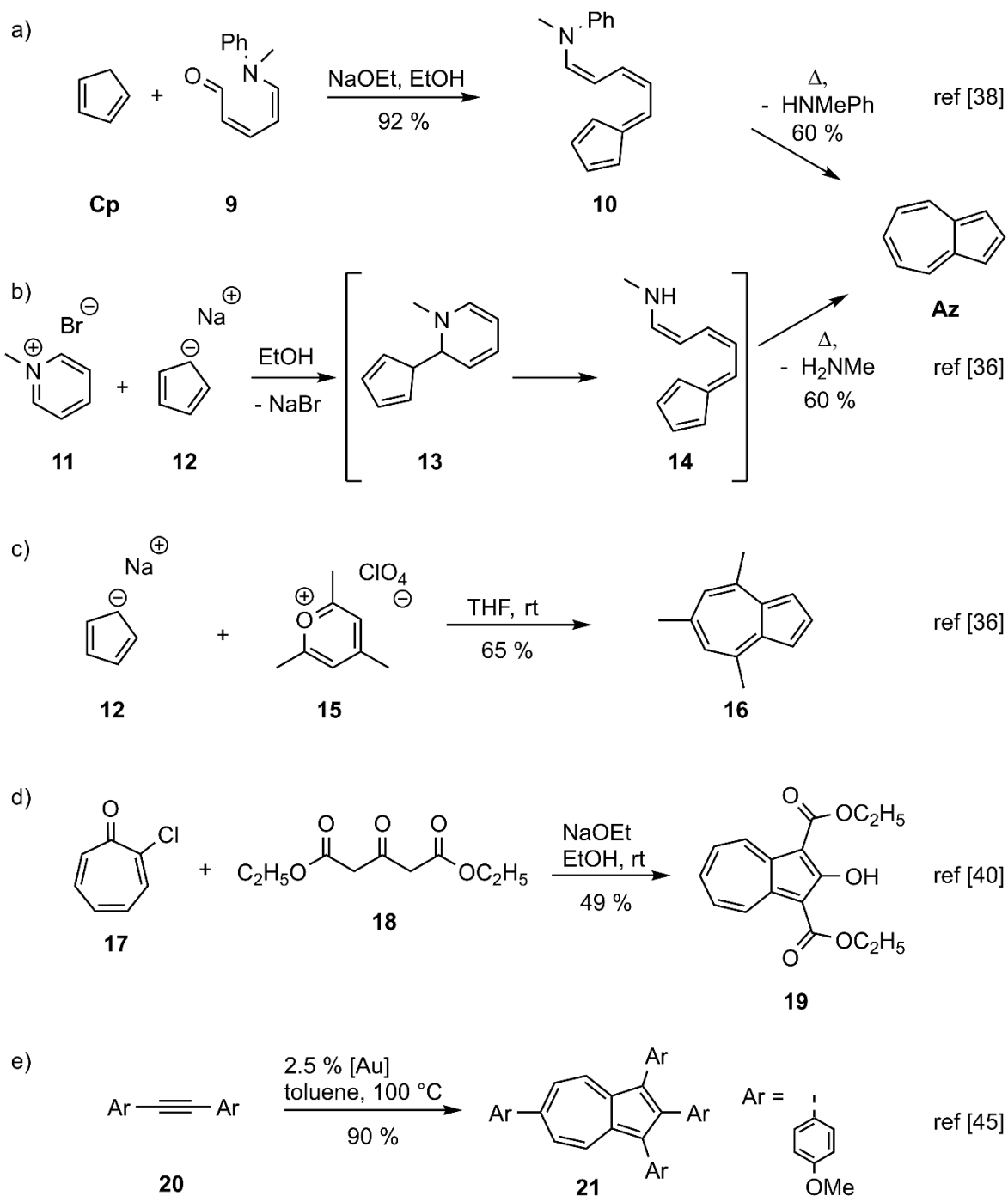

Figure 4: Synthetic routes towards the azulene scaffold: a)-c) methods by Ziegler and Hafner, starting from cyclopentadiene and glutacondialdehyde surrogates.[36,38] d) Route proposed by Nozoe, starting from 2-chlorotropone **17** and diethyl acetone-dicarboxylate **18**.[40] e) Example of a gold catalyzed dimerization of alkyne **20** to azulene **21**.[45]

4

2.2 Liquid Crystals

In 1888, Reinitzer described two melting points under the microscope for a sample of cholesteryl benzoate.[46] Although unknown to him at this point, this was the first observation of a new state of matter. Today, it is widely known that some molecules with anisotropic geometry do not have a direct transition from the crystalline to the liquid phase. They rather pass through a mesophase (meso, Greek = in between), the so-called liquid crystalline state (Figure 5a). Liquid crystals (LCs) combine properties of crystals, e.g. their optical anisotropy, with those of liquids, e.g. their fluidity.[47] Molecules or supramolecular structures that form mesophases are called mesogens. A mesophase that appears upon heating of a compound is called thermotropic. However, self-assembly can also occur when an amphiphile is dissolved in a solvent which then forms a so-called lyotropic liquid crystalline phase. The properties of lyotropic LCs are governed not only on the temperature but by the concentration of the amphiphile. In the following chapter, only thermotropic LCs will be discussed.
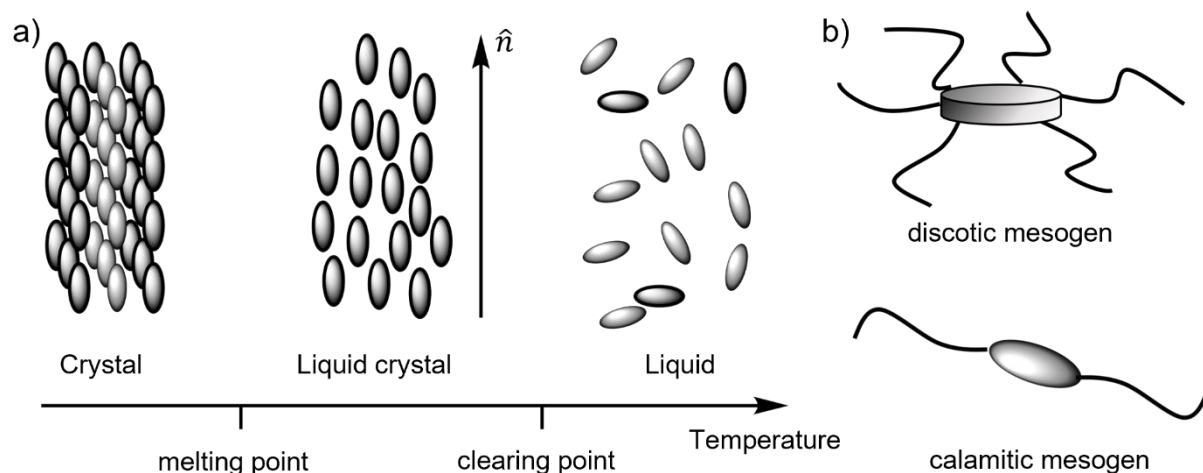
Figure 5: a) The liquid crystalline state positioned between crystals and liquids. b) Discotic and calamitic molecules are the classical building blocks for liquid crystals.

In a mesophase, long-range orientational order of the molecular axes in one or two dimensions is present, while the positional order of the mesogens is liquid-like in at least one dimension.[47] Different mesophases have been classified depending on the degree of order that is found in the respective liquid crystalline phase. The geometry of the mesogen is crucial for the type of the mesophase. Disk-like or discotic mesogens tend to form columnar phases while rod-like or calamitic molecules usually form nematic or smectic phases (Figure 5b). Mesogens often consist of an aromatic core with alkyl chains on both ends.

The nematic phase N, where all molecules align along a director $\hat{n}$ resulting in long-range orientational order, is the simplest mesophase and therefore has the highest symmetry (Figure 6a). When long-range translational order of the mass centers of the mesogens is added, smectic phases form where the mesophase could be viewed as a 1D crystal consisting of layers. The molecules within a single layer behave fluid-like in two dimensions. The direction of these smectic (lamellar) structures is described by the layer normal $\hat{k}$. When $\hat{n}$ and $\hat{k}$ are parallel to each other, a smectic A phase (SmA) is present. However, it is also possible that the directors are tilted to each other by an angle Θ, this phase is defined as a smectic C phase (SmC). The driving force for the formation of smectic layers is based on so-called nanosegregation. For example, the aromatic part of the molecules is rigid and polarizable, while the alkyl side chains are non-polar and flexible. Layer formation allows an optimal interaction between the aromatic cores while the flexible and thus fluid alkyl chains are mixed at the layer ends.[48]
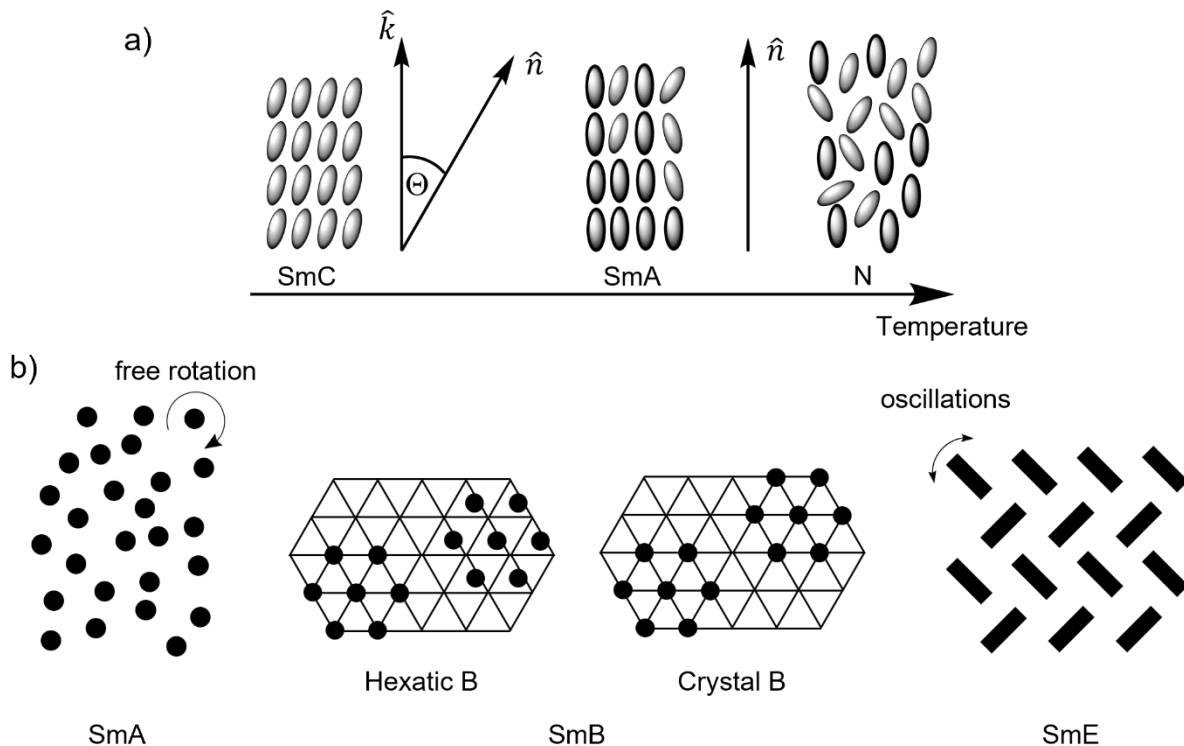
Figure 6: a) Molecular arrangement of the nematic and fluid smectic phases. b) Plan view of the orthogonal smectic phases. The figure was adapted from ref [48].

When cooling a mesophase, the liquid crystal either directly crystallizes, or transforms into a liquid crystalline phase with even higher order. In fact, crystallization can happen in numerous small steps where each step is assigned an individual smectic phase. Therefore, the term smectic polymorphism has been coined. In the following, the higher ordered derivatives of the SmA phase, the so-called orthogonal phases, are described. Tilted phases are derivatives of the SmC

phase and follow the same pattern as the orthogonal phases but are not mentioned further in here.

Closely related to the SmA phase is the SmB phase. It is a so-called hexatic phase because each molecule has six close in-plane neighbors, but the positional order within the layers is not long-range and decays quickly (Figure 6b).[48] Therefore, a 2D bond-orientational order is present. Upon further cooling, true translational order within the layers may manifest. Since there is 3D translational order, the phases are often referred as soft crystals rather than liquid crystals. In this crystal-smectic B phase the mesogens can still freely rotate around their long axis. This changes in the crystal-smectic E phase (SmE) where molecules stack closer and hinder their free rotation. In contrast to a real crystal, in-plane oscillations are still possible. In the case of the SmE phase the hexatic order transforms into a herringbone packing. However, even in the SmE phase the molten nature of the alkyl side chains is preserved.[48–50]

2.3 Characterization of Liquid Crystals

The exact determination of the phase geometry of a LC is often anything but trivial. For a complete understanding of the present mesophase, the combination of multiple characterization methods is crucial. This chapter describes the most common techniques when dealing with LCs.

2.3.1 Polarized Optical Microscopy

In contrast to isotropic fluids, crystals and liquid crystals are birefringent, which means that incoming light is split into an ordinary and an extraordinary ray.[51] Polarized optical microscopy (POM) takes advantage of this situation. In addition to a regular microscope, the light passes through a polarizer before it interferes with the sample. In front of the detector, a second polarizer is installed turned by 90°, the so-called analyzer. Thus, the linearly polarized light originating from the first polarizer cannot pass the analyzer. Isotropic media without birefringence appear dark under the POM. The situation changes when an optical anisotropic material such as a crystal or LC is inserted. The linearly polarized light is changed to elliptically polarized light and some part of the light will be able to pass the analyzer. Depending on the orientation and the phase geometry of the LC, characteristic textures can be observed (Figure 7a).[51] Textures observed in the POM give a first idea of the present mesophase and transition temperatures. Since textures are not always distinctive and the manual determination of phase transitions is inaccurate, further methods should be incorporated.
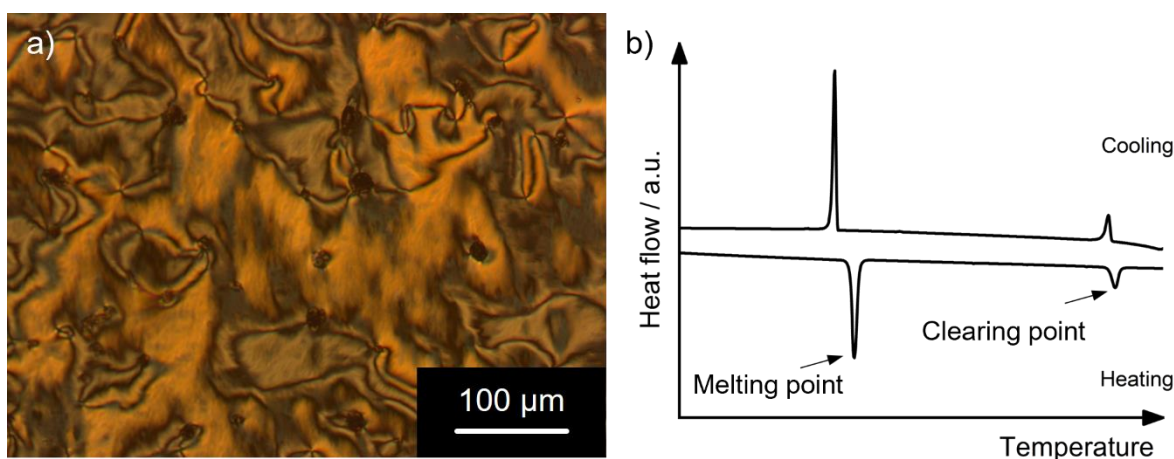
Figure 7: a) Schlieren textures of a SmC phase observed *via* POM between crossed polarizers. b) Typical thermogram of a liquid crystalline compound.

2.3.2 Differential Scanning Calorimetry

Differential Scanning Calorimetry (DSC) allows the determination of phase transition temperatures and their enthalpies.[52] In crucibles the sample and a reference compound (usually air) are heated or cooled with a certain rate. In case of an endothermic phase transition such as the melting process the sample needs more energy to keep up the temperature with the reference. For exothermic phase transitions, the sign of the energy is reversed. The energy difference can be determined and plotted against the temperature to form a thermogram. First order phase transitions are visible as peaks and second order transitions such as glass transition have a step-like appearance (Figure 7b). Integration of the peaks results in the transition enthalpy; the exact transition temperatures are usually determined by the onset values of the peak. DSC is the means of choice when it comes to analyzing phase transitions. However, especially in the case of LCs some phase transitions might be too weak to be detected. In this case the texture change under the POM should be considered. Furthermore, DSC does not give a hint towards the mesophase geometry.[52]

2.3.3 X-ray Diffractometry

Single crystal X-ray diffractometry is a powerful tool to investigate periodic systems in the size of molecules. Since liquid crystals show periodicity and are crystalline to some point, X-ray diffractometry can help to analyze the structure of a mesophase.[53]

When X-ray radiation of a certain wavelength meets an organic (or inorganic) sample, electrons with the same energy as the X-ray beam are excited from their orbitals. Upon relaxation, the electrons release an X-ray of the same wavelength λ and start a spherical wavelet that interferes with neighboring wavelets. In other words, the radiation is scattered at the lattice planes of

regularly positioned particles. For this scattering, λ must be in the same order of magnitude as the molecular distance. Constructive interference between the single wavelets takes place at certain angles to give detectable X-ray deflections, at all other angles destructive interference extinguishes the wave. The conditions for constructive interference are described by the Bragg equation (1):

$$n \cdot \lambda = 2d \cdot \sin(\Theta) \qquad (1)$$

Usually, the wavelength λ = 1.54 Å of the copper K_α line is used. Θ is the angle of the incoming beam relative to the lattice plane and *d* describes the distance between two parallel lattice planes e.g., of smectic phases. The diffraction order *n* is an integer number.
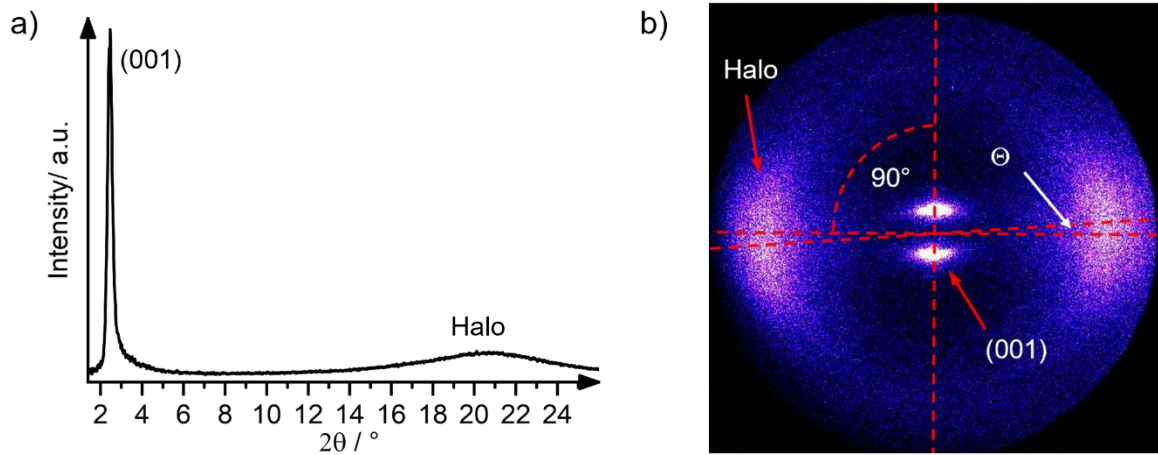

Figure 8: a) Diffractogram of a SmA or SmC phase. b) Diffraction pattern of an oriented sample of a SmC phase.

When using X-ray diffractometry on liquid crystals, usually only few signals are observed. For example, in smectic phases, a sharp Bragg-like reflex indicates the layer spacing (Figure 8a). It is often assigned the Miller index (001). Since, smectics only have quasi-long range translational order, this reflex has a Lorentz form and not a Gauss form. A broad signal in the wide angle region indicates the in-plane distance between mesogens. Due to the liquid-like nature within the layers, this halo is typically broad and at least one order of magnitude weaker than the layer reflex. When the X-ray passes through multiple domains with different orientation, the measurement equals a powder diffraction experiment. In a 2D diffractogram only rings are observed. A differentiation between SmA and SmC phases is not possible in this case. More information can be gained with a sample consisting of large monodomains, which can be prepared by fiber extrusion or slow cooling in a magnetic field (Figure 8b). In a SmA phase the layer reflex and halo are tilted by 90°. In SmC phases the tilt angle Θ can be

determined from the diffractogram by the deviation from the 90° angle. X-ray diffractometry is the most powerful tool for an exact determination of the mesophase geometry. In combination with POM and DSC a detailed picture of the liquid crystalline phase can be drawn.[53]

2.4 Liquid Crystals for Organic Field Effect Transistors

Transistors might be the most important element in today's semiconductors. They are used to amplify and switch electrical signals and usually consist of metalloids like silicon. These inorganic transistors have long been used in industry. While being state of the art, they lack the flexibility for some applications where organic field effect transistors (OFETs) might fill the niche application.[54] Further, the processing of organic molecules is more convenient and use in printed electronics is also possible. The typical design principle of a top contact bottom gate OFET is shown in Figure 9a. The organic semiconductor is applied on a substrate, which usually consists of silicon topped with a small layer of insulating SiO_2. When voltage is applied at the gate, an electrical field is formed which leads to an enrichment of charge carriers in the semiconductor. Therefore, the resistance between the electrodes (source and drain) shrinks resulting in a conducting channel. Hence, current flow in the semiconductor can be controlled by regulating the voltage at the gate. The most important indicator of the quality of an FET is the carrier mobility, but unfortunately, organic molecules typically behave like insulators and show low carrier mobilities. Large aromatic systems are commonly used to generate conductive or semiconductive organic molecules. First investigations for the manufacturing of OFETs started with molecules with an extended π-system like pentacene **22** (Figure 9b), achieving a FET mobility of over $1\,cm^2Vs^{-1}$ which can be compared to amorphous silicon FETs.[55] However, low solubility of those compounds hampered the processing. The implementation of long alkyl chains to the aromatic core **23**[56] or bulky lateral substituents[57] improved the solubility and allowed solution processing while keeping the mobility on the same level. Unfortunately, during solvent evaporation random crystallization led to a poor surface morphology and uniformity.[58] Therefore, the performance of OFETs strongly varies in large-scale synthesis. Additionally, side chain modified π-systems normally show lower melting points due to reduced π-stacking which decreases the thermal stability of films.

The design principle of soluble OFET materials with an aromatic core and flexible side chains resembles the design of liquid crystals, hence compounds used for the manufacturing of OFETs often showed mesophases. However, the promising self-assembly of mesophases was mostly overlooked. In 2015, Iino and Hanna harnessed the assembly of benzothiophene derivative **Ph-BTBT-8** forming SmE phases and produced well orientated polycrystalline films of

molecular thickness by simple solution processing on a substrate at mesophase temperature. Due to the low volume contraction at the crystallization point, the uniformity of the film remained even in the crystal. The mobility was increased from 2.1 to 22.4 cm^{2}Vs^{-1} after annealing at 120 °C for 5 min.[59] These results showed the powerful potential of SmE phases for device manufacturing.
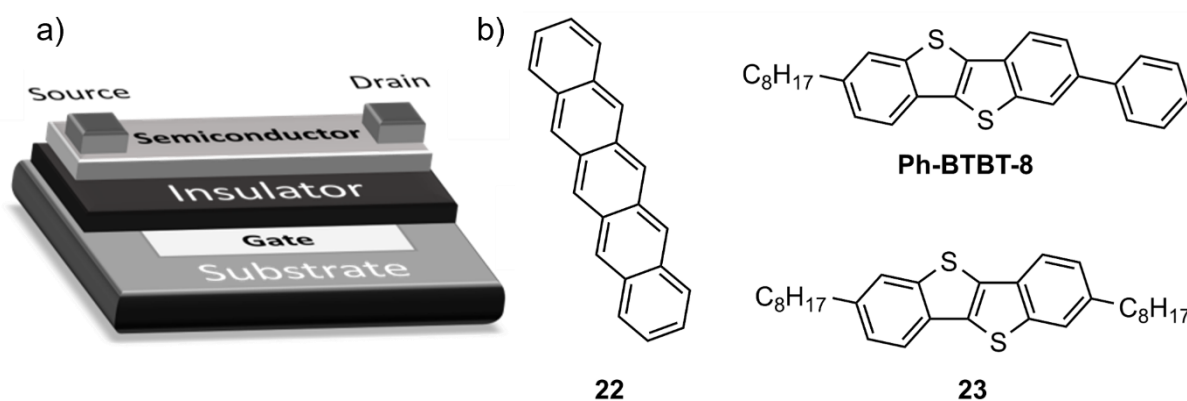

Figure 9: a) Design of a top contact bottom gate OFET. b) Previously used molecules for OFET manufacturing.

2.4.1 Determination of Transistor Properties

Depending on the sign of the gate voltage V_g, a transistor is either conductive for positively charged holes or for electrons.[60] At a negative bias, the OFET operates as a p-channel transistor and in the case of a positive V_g, an n-channel transistor is present. Most OFETs are operated under p-channel conditions. At a low voltage between source and drain V_{ds}, the current between the electrodes I_{ds} behaves linearly to V_g. In this linear region I_{ds} can be described with formula (2).

$$I_{ds} = \frac{\mu W C_i}{L}\left(V_g - V_{th} - \frac{V_{ds}}{2}\right)V_{ds} \tag{2}$$

W describes the channel width and L the channel length of the transistor. C_i is the capacity of the gate insulator. The threshold voltage V_{th} describes the required gate voltage for the formation of a conducting channel. The carrier mobility μ can be calculated from the slope of a linear plot from I_{ds} versus V_g, when V_{ds} is kept constant. This type of OFET operation yields the so-called transfer characteristics.

At higher V_{ds}, the current flow is limited only by the size of the conducting layer and thus by V_g. Further increasing V_{ds} does not affect the I_{ds} anymore, therefore it is called saturation region. The relation between I_{ds} and V_g is then described by equation (3):

$$I_{ds} = \frac{\mu W C_i}{L}\left(V_g - V_{th}\right)^2 \tag{3}$$

In this case, a plot of the square root of I_{ds} against V_g is necessary to calculate mobility and threshold voltage. Another important characteristic number for OFETs is the on/off-ratio of I_{ds}.[60]

2.5 Characterization of thin films

Before the transfer characteristics of a manufactured transistor can be measured, the quality of the materials thin film should be evaluated. For optimal conditions, films should be uniformly thin and have a good orientation on a molecular level.[58]

2.5.1 Confocal Laser Scanning Microscopy

Optical microscopy can show whether the substrate is equally distributed on the entire waver (Figure 10a).[61] Another useful tool is confocal laser scanning microscopy (CLSM) which, in contrast to conventional optical microscopy, only illuminates a single point of the sample at a time. The full picture is assembled after the whole sample has been scanned. With the help of a pinhole and a lens the incoming light can be focused on a plane in the sample. It is then possible to only detect light of a certain plain and thus get detailed information on the morphology of the film. Since the whole sample has to be scanned for different plane levels and the pinhole blocks a lot of the signal intensity, CLSM needs longer exposure times than optical microscopy. However, the resolution of the picture is improved. Further, computer assisted reconstruction allows 3D representations of the sample, and hence the thickness of the film can be measured (Figure 10a).[61]

2.5.2 Atomic force microscopy

Atomic force microscopy (AFM) is one of the microscopic techniques with the highest resolution where, in the best case, even single atoms can be resolved. A small tip is fixed at the open end of a cantilever.[62] The tip is carefully brought in direct proximity to the sample so that the atomic forces come to pass. The distance between tip and surface is then controlled by the interaction of attractive Van der Waals forces and Coulomb repulsion, which is known as the Lennard-Jones potential. The deviation of the tip and the cantilever can be measured with various methods. In the beam-deflection method, a laser is reflected from the back of the cantilever and detected by a so-called position-sensitive detector.[63] Cross sectional profiles of AFM pictures are well suited to observe the uniformity of the sample. In highly crystalline samples, molecular steps of the layers can be observed (Figure 10b).[59]
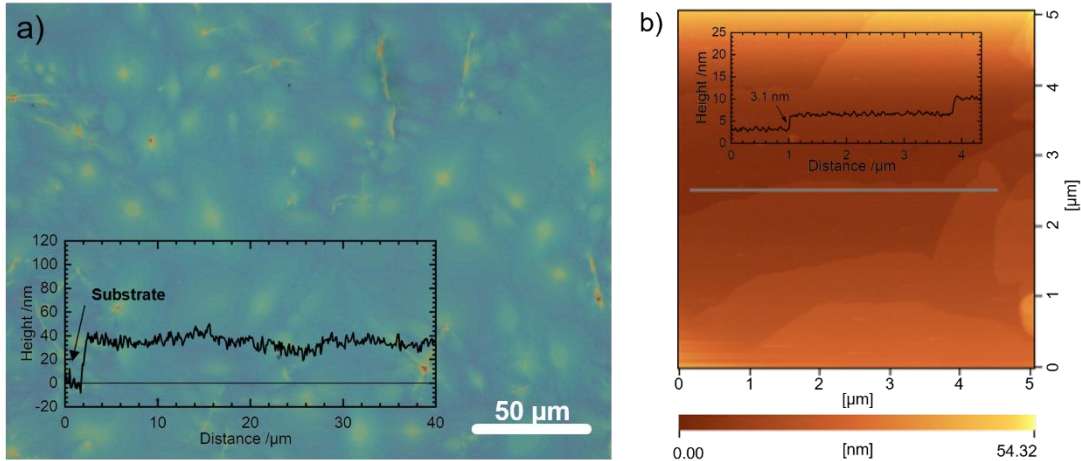
Figure 10: Images of a polycrystalline thin film fabricated by spin-coating a) Optical micrograph and b) film observed *via* AFM. The cross-sectional profiles were observed by a) CLSM and b) AFM. This figure was reproduced with permission from ref[3].

2.5.3 In-plane and Out-of-plane Diffractometry

The quality of the alignment in films can be observed by out-of-plane and in-plane X-ray diffractometry (XRD).[64] A well oriented thin film can be compared with an aligned sample of a liquid crystalline smectic phase, given the layer structure is kept in the crystalline film. Reflexes of the layer spacing will be scattered towards the top and bottom, while in-plane lattice structures cause scattering to the sides (compare Figure 8b). With exact control of the angle of the incoming X-ray beam in respect to the film, only one of the two modes can be measured. The absence of in-plane reflexes in out-of-plane measurements and vice versa indicates a well oriented film.[64–66]

2.6 The Ferroelectric SmC Phase

In addition to achiral LC phases there exist also chiral counterparts given the mesogens incorporate chirality. The chirality of a mesophase is indicated with an asterisk *. Another possibility to incorporate chiral information in the mesophase is adding a small amount of an enantiomerically enriched compound. Such compounds are called chiral dopants and are often preferred in place of expensive enantiopure mesogens.[67]

Due to the chirality, the ferroelectric SmC* phase loses the mirror plane present in the achiral counterpart. Hence, a spontaneous electric polarization P_S perpendicular to $\hat{n}$ and $\hat{k}$ may occur. The system escapes from a macroscopic polarization by forming a helix along $\hat{k}$. The tilt direction of the mesogens and therefore $\hat{n}$ and P_s spiral around $\hat{k}$ and average out the polarization. In 1980, Clark and Lagerwall invented a method to suppress helix formation by

filling the LC in a so-called SSFLC-cell (surface stabilized ferroelectric liquid crystal cell).[68] The surfaces are coated with a polymer and allow only two possible orientations of the mesogens. They differ from each other by the tilting direction and thus have opposing polarization directions. Without external stimulus, both domains form. However, when an electric field is applied, one orientation is preferred and forms over the entire cell. By changing the electric field, it is possible to switch between the two orientations resulting in switching times of microseconds which is significantly faster than nematic LCs used in commercial LC-displays. Unfortunately, the commercial success of the SSFLC-displays is prevented by defects that reduce the display quality drastically.[69,70]

This problem results from cooling a SmA phase into the required SmC phase and concomitant layer shrinkage due to the tilting of the mesogens of about 7-10 % (Figure 11a). This behavior can be described with the rigid-rod model.[69] In a SSFLC-cell, the mesogens at the surface are fixed in position and cannot follow the shrinking layer. Buckling of the layers allows for a smaller layer thickness while the surface molecules remain in position. Therefore, the bookshelf configuration from the SmA phase is changed into a chevron configuration (Figure 11c).

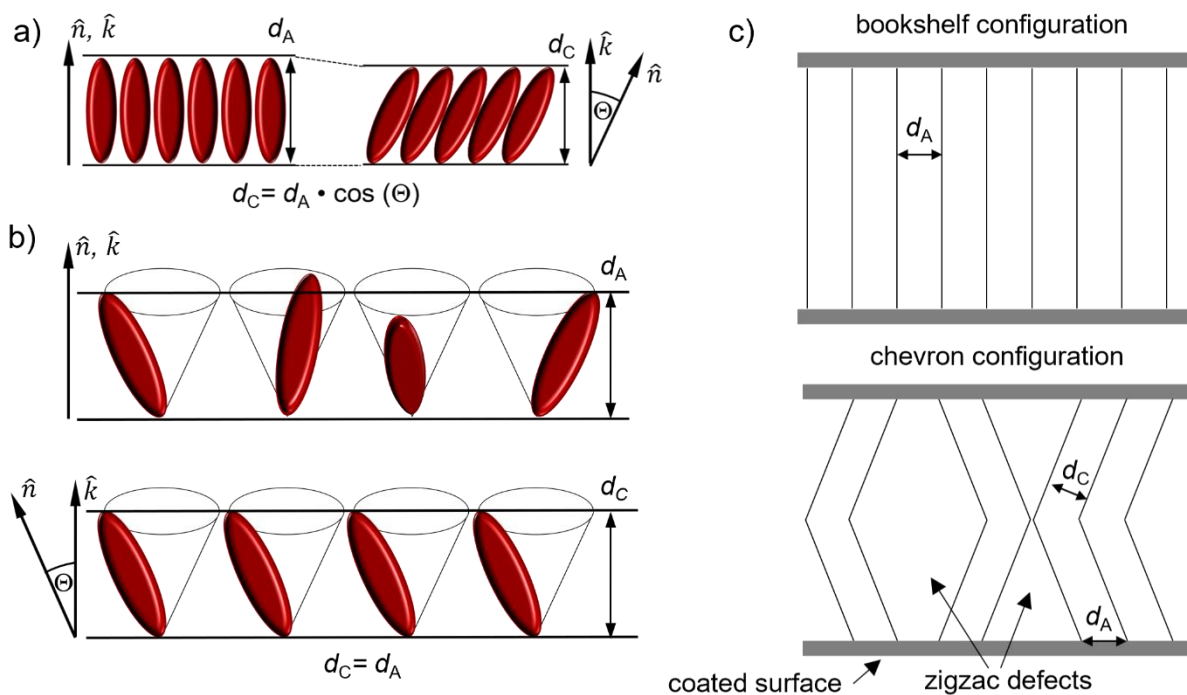**Figure 11:** a) Schematic representation of the rigid-rod model and the consequent layer shrinkage. b) Schematic representation of the diffuse cone model without layer shrinkage. The figures were adapted from ref[74]. c) Alignment of the layers under surface anchored conditions and the resulting zigzag defects due to layer shrinkage at the SmA-SmC transition. The figure was adapted from ref[69].

However, the tilting direction during the SmA-SmC transition is not defined and two directions are possible. So-called zigzag defects form at the domain boundaries and remain visible in the display. Different techniques have been proposed to circumvent this problem. One of them is to use LCs with close to no layer shrinkage during the SmA-SmC transition and these LCs are referred to as de Vries-like liquid crystals.[69,70]

2.7 De Vries-like Liquid Crystals

In 1979, Adrian de Vries described a different model for the SmA phase and the transition into the SmC phase, known as the diffuse cone model (Figure 11b).[71] He assumed that the molecules are already tilted in the SmA phase and rotate on a cone around $\hat{k}$. Since the direction of the tilting is randomly distributed, it is not observed at the macroscopic level. At the phase transition, the value of the angle does not change, but all molecules tilt to the same direction. This second order transition would be disorder to order driven and does not require layer shrinkage. Even though the diffuse-cone model does not fully reflect reality, it is often used to easily explain the behavior of de Vries-like materials during the SmA-SmC transition.[72]

Roughly speaking, LCs with a maximum layer shrinkage $lc_{max} < 1 \%$ are called de Vries-like. For a more exact description the reduction value R was described that considers the ratio between lc_{max} and tilt angle Θ (equation 4):[73]

$$R\,(T) = \frac{\cos^{-1}(lc_{max})}{\Theta\,(T)} \tag{4}$$

R can take values between 0 and 1. Perfect de Vries-like materials would assume 0, and phases following the rigid rod model would have the value 1.

Seminal work by Giesselmann and Lemieux proposed that a frustration between SmA and SmC promoting elements in a mesogen would be beneficial for good de Vries-like materials.[74] They combined SmC promoting siloxane or carbosilane side chains with the SmA promoting phenyl-pyrimidine core (e.g. **24**) and achieved very low reduction values (Figure 12).[75] A more

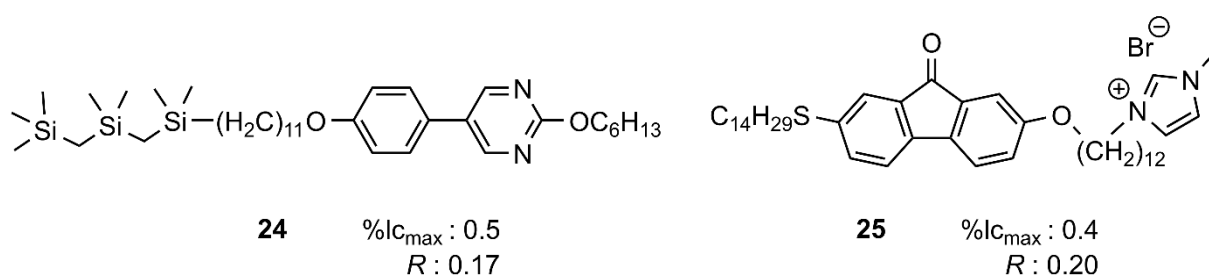| **24**	%lc_max : 0.5	**25**	%lc_max : 0.4
	R : 0.17		R : 0.20

Figure 12: State of the art de Vries-like materials based on carbosilane and imidazolium headgroups.

general approach identified the combination of high translational order between the layers and low orientational order within in the layers as the key factor for de Vries-like behavior.[69] High translational order equals well defined layers that can be achieved by nanosegregating elements. In addition to the already mentioned silicon-based side chains, perfluorinated chains[76] and ionic head groups (e.g. **25**)[77] have been reported. Usually, mixtures of numerous different liquid crystals are used to tune the properties for display applications. Therefore, the design of further de Vries-like materials is necessary for an expansion of the library. Furthermore, de Vries-like materials are also interesting for the general understanding of phase transition in LC phases.[70]

For the determination of R, the temperature dependent layer thickness d and tilt angle Θ is required. Both parameters can be determined by XRD. However, the tilt angle Θ_{XRD} does not necessarily equal the optical tilt Θ_{opt} which should be measured by POM using a SSFLC cell. The sample is rotated until one of the two opposite tilt domains is at its darkest position. The difference between the darkest positions of each domain equals $2\,\Theta$ (Figure 13).
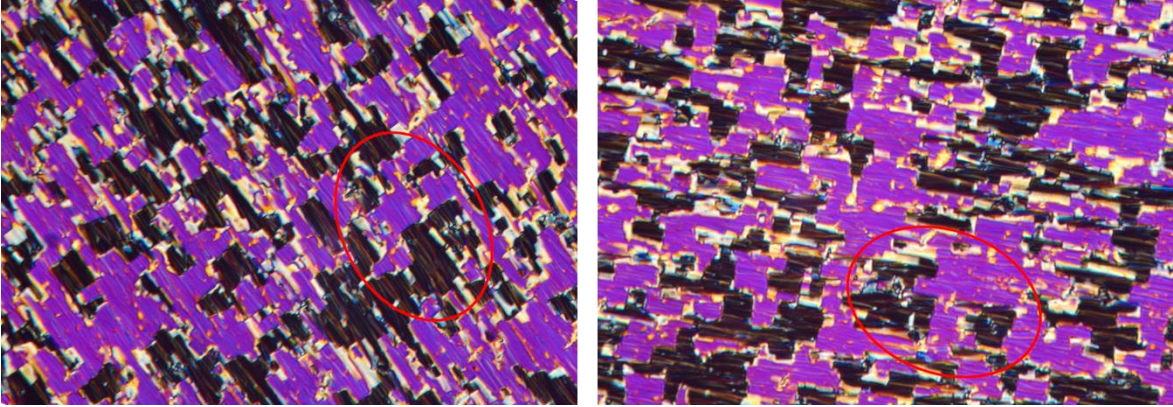

Figure 13: Micrographs of a planarly oriented SmC phase between crossed polarizers. The sample is rotated that one of two neighboring domains (red circle) appears black.

Since translational order and orientational order have been identified as important factors for de Vries-like behavior, it is crucial to quantify these properties. The translational order parameter Σ can be described with the following formula (5):[69,70]

$$\Sigma = \left\langle \cos\left(\frac{2\pi z_i}{d}\right)\right\rangle \tag{5}$$

z is the position of a molecule along $\hat{k}$. On $\Sigma = 1$ perfect translational order is present, which equals the crystalline state. For $\Sigma = 0$, the translational order is non-existent, this is the case in the nematic phase and the isotropic liquid. Measuring Σ experimentally is difficult and therefore rarely done.[69] But there are procedures that give approximations for Σ, at least for the SmA

phase.[78] In contrast, the orientational order parameter S_2 can be measured by various methods like solid state NMR spectroscopy, IR dichroism[79,80] or oriented X-ray samples.[81] S_2 is defined as:

$$S_2 = \frac{1}{2} \langle 3 \cos^2 \Theta_i - 1 \rangle \tag{6}$$

Instead of directly measuring S_2, it is also possible to measure the birefringence Δn, which behaves proportional to S_2 in uniaxial LC phases.[82] The biaxial SmC phase can still be regarded as uniaxial in good approximation.[69] The Phi-Viz imaging system offers a convenient method for the determination of Δn.[79] The retardance Γ between the ordinary and extraordinary ray is measured automatically. When Γ becomes larger than $\lambda/2$ of the used light source, the measured value is shrinking. Postprocessing of the data is performed by adding or subtracting Γ from the λ to obtain the real Γ. After this unfolding process Δn can be calculated from the real retardance when the thickness of the cell d is known:

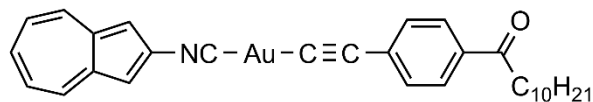$$\Delta n = \frac{\Gamma}{2d} \tag{7}$$

2.8 Azulene-based Liquid Crystals

The combination of the unique electronic structure of azulene with the self-aligning and self-healing properties of liquid crystals might furnish potent mesogens for electronic applications. Therefore, it is not surprising that numerous groups have already investigated the azulene moiety in combination with liquid crystallinity. In 1981, first mesomorphic azulene derivatives were described by Praefcke where the azulene moiety was attached to nematogenic phenyl-cyclohexyl core **26** (Figure 14).[83]. By the incorporation of the azulene into the mesogens, Praefcke aimed for applications in colored LC-displays. First smectic azulene LCs were synthesized by Estdale in 1997 by introducing a substituted dioxane ring in 6-position of **27**.[84] In the early 2000s, Ito synthesized discotic azulene derivatives e.g., hexakis(6-azuleneylethynyl)benzene derivatives **28** and investigated their multielectron redox properties by cyclic voltammetry (CV).[85] He also described numerous hexakis(azulen-2yl)benzene derivatives like **29** and suggested to use the columnar mesophases for electronic devices.[86–88] Further he discovered that 6-octyl-2-phenylazulene **8-Az-Ph** forms a SmE phases. This might be due to the dipolar character of the azulene moiety in combination with only one side chain. Interlocked layers might cause high translational order and consequently, the SmE phase is formed. Recent studies even showed that organometallic azulene mesogens are possible.[89] Isocyanoazulene-gold derivatives **30** showed SmA phases and were suggested to be a potential candidate for display applications or in sensors. While there is a systematic approach towards
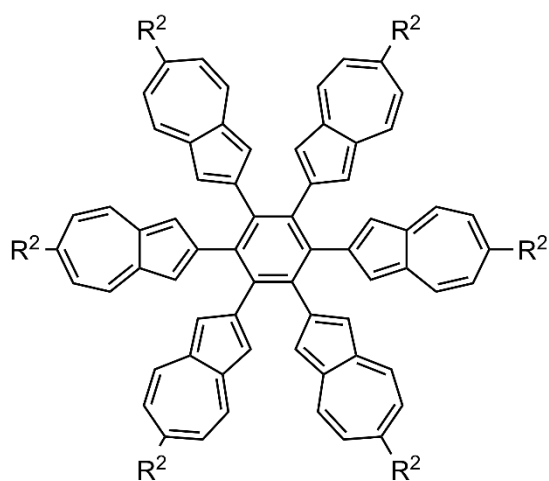
discotic azulene mesogens, calamitic azulenes are known but have not been investigated systematically. One reason for that might be the lack of a convenient synthetic route.
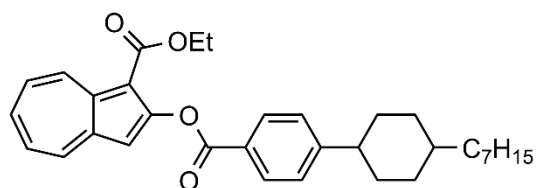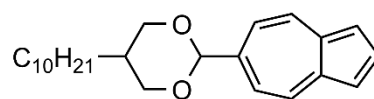
26   Cr 86 N 153 I   ref [83]

27   Cr 77 SmA 84 I   ref [84]

8-Az-Ph   Cr 110 SmE 181 I   ref [86]

30   Cr 106 SmA 150 I   ref [89]

$R^2 = C_{16}H_{33}$ ref [87]
29   Cr 97 Col$_h$ 143 I
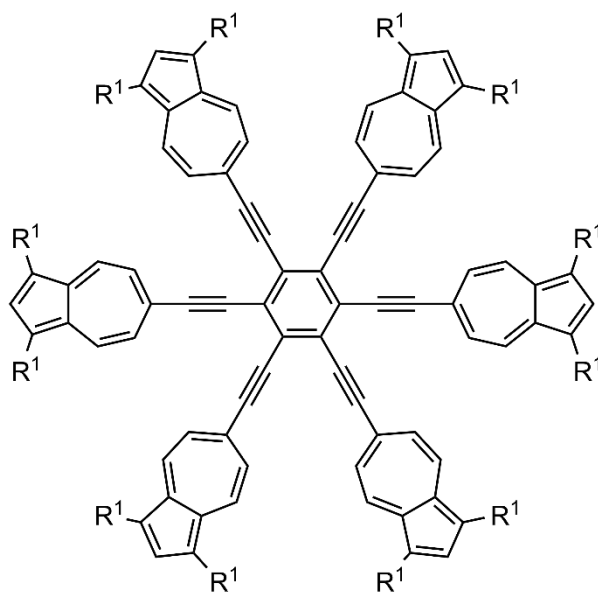
$R^1 = CO_2C_6H_{13}$ ref [85]
28   Cr 77 Col$_h$ 173 Col$_r$ 270 dec.

Figure 14: Examples for literature known liquid crystalline azulene derivatives. Cr: crystal, Col$_h$: columnar hexagonal phase, Col$_r$: columnar rectangular phase, I: isotropic liquid, dec: decomposition.

Redox properties have often been investigated for mesomorphic azulene derivatives.[86,88] The standard characterization method for redox behavior is cyclic voltammetry. Furthermore, determination of HOMO and LUMO level from the oxidation and reduction potential is possible. Therefore, cyclic voltammetry will be shortly explained.

2.8.1 Cyclic voltammetry

Cyclic voltammetry (CV) investigates the electrochemical oxidation or reduction of a compound.[90] Usually, experiments are performed in solution with electrolytes like tetrabutylammonium hexafluorophosphate added to ensure conductivity. The experimental set-

up consists of three electrodes where at the working electrode the redox reaction takes place. The current I is measured between the working electrode and the counter electrode which is used to close the circuit. The potential E is measured between the working electrode and the reference electrode. For CV, the potential is ramped in a triangular function at a certain rate. If an oxidation process is to be investigated, the potential is increased at first and the analyte is oxidized at a certain potential E_{OX}. This is depicted in a plot of I versus E (Figure 15). Since E_{Ox} depends on the scan rate, E_{Ox} does not equal the standard potential of the redox reaction. On lowering the potential after oxidation, the analyte is reduced to its neutral form at the potential E_{Red}. Since the same effects apply for E_{Ox} and E_{Red}, the half-cell potential $E_{1/2}$ can be easily calculated by taking the mean between the values (equation 10). When calculating the standard potential E_0 of the redox reaction, it should be noted that the ferrocene/ferrocenium redox couple is often used as a reference for the potential.

$$E_{1/2} = 0.5 \ (E_{Ox} - E_{Red}) \qquad (10)$$

After measuring the oxidation process and reduction process of an analyte, the HOMO and LUMO levels can be determined to a good approximation. Reversible reactions are characterized by the symmetrical wave forms of the oxidation and reduction processes. Organic analytes often show quasi-reversible or irreversible redox-reactions due to the instability of the intermediate species. In this case other techniques like the differential pulse voltammetry can be used for HOMO and LUMO determination.[90–92]
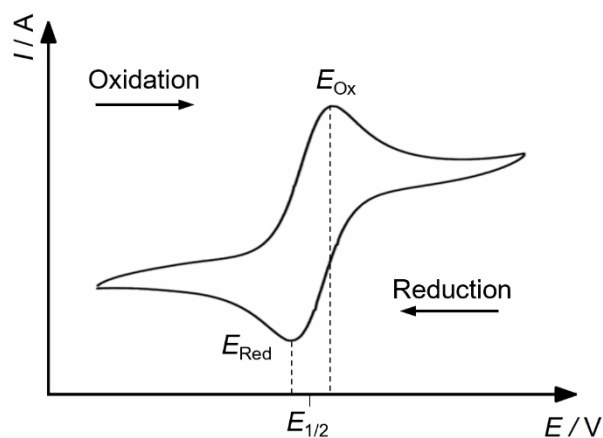
Figure 15: Schematic representation of a reversible oxidation process investigated by cyclic voltammetry.

2.9   Excursus: Hydropentalene Based Ligands

Chiral diene ligands are an important compound class in asymmetric catalysis.[93] Rhodium catalysis with hydropentalene based ligands **34** gained attention due to the highly

enantioselective 1,4-addition of organoboronic acids **32** to enones **31** and the 1,2-addition of boroxines **36** to *N*-tosylimines **35** (Figure 16a,b).[94–99] When attaching side chains to the chiral backbone, it is possible to either link the ligands to a solid support or carry out the catalysis in the confinement of a microemulsion.[99,100] In case of the PEGylated hydropentalenes **Pent-ODegYne**, the molecular scaffold resembles a calamitic mesogen with a rigid core and flexible side chains (Figure 16c). However, mesomorphic hydropentalenes are not known in the literature. Given the molecular analogy and the lack of knowledge on mesomorphism of this scaffold, calamitic hydropentalenes should be investigated regarding their mesomorphic properties.

Figure 16: a,b) Examples for highly enantioselective Rhodium catalyzed additions, using the hydropentalene ligand **34**.[95,99] c) Hydropentalene ligands with side chains resemble the blueprint for liquid crystals.

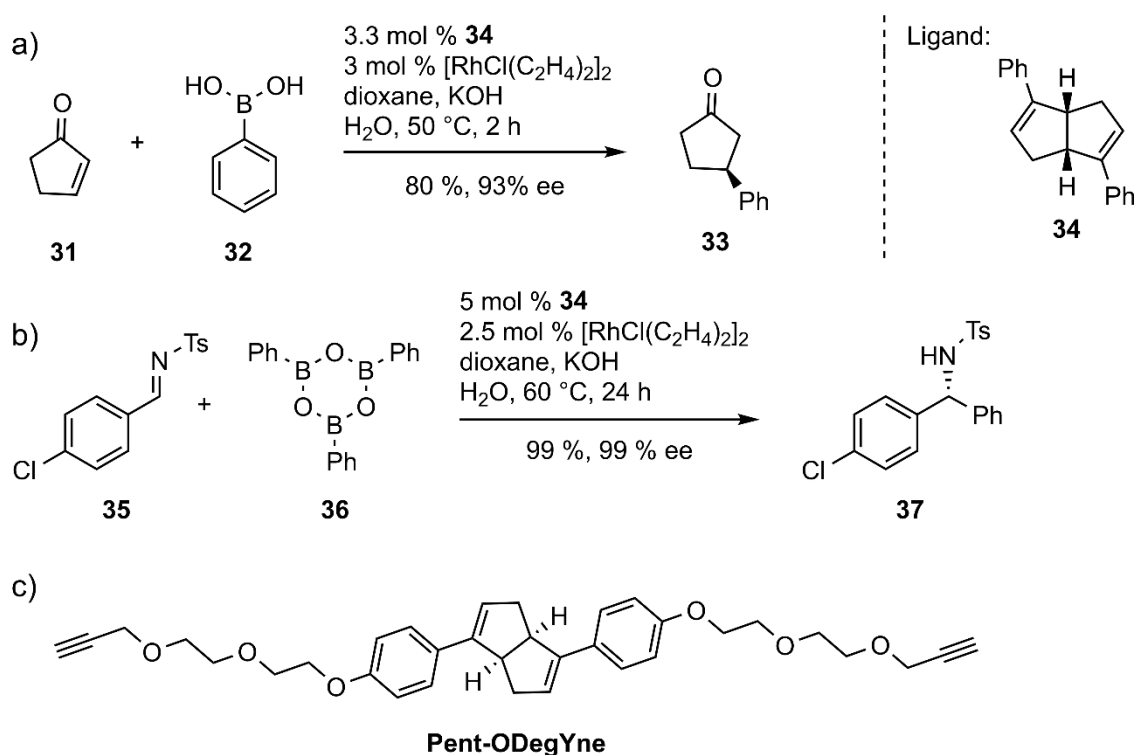# 3 Aim of the Work

The azulene moiety is known for its unique electronic properties and, consequently, often used in organic devices, such as OFETs and OLEDs.[101] However, not only the molecular structure but also orientation is crucial for optimal device performance. The molecular orientation can be controlled by self-assembly of liquid crystals. While discotic azulene mesogens are well explored,[85–88] calamitic azulenes have not been investigated in a systematic fashion.[102] Detailed understanding of the structure-property relationship of calamitic azulene mesogens would enable the tailoring of molecules for electronic applications. Therefore, the focus of this work lies in the divergent synthesis of novel azulene derivatives and their physical characterization regarding mesomorphic behavior. In addition, the mesogens should be investigated with respect to possible applications. A stepwise examination of azulenes equipped with different numbers of side chains would allow a deeper understanding of their structure-property relationship.

The first task focuses on calamitic azulenes with only one side chain which are known to form soft-crystalline phases. The 6-octyl-2-phenylazulene **8-Az-Ph** forms the SmE phase, but this fact has not been further pursued. By replacing the alkyl chain with an alkoxy chain, 6-alkoxy-2-bromoazulenes might be readily available from the literature-known **Br-Az-Br** by nucleophilic substitution in 6-position (Figure 17, top). Materials that show a SmE mesophase can be used for the creation of uniform thin films, which were shown to be an excellent basis for OFETs (Figure 17, bottom).[58] In addition, thiophene derivatives are widely used in organic semiconductors due to the high performance of thiophene containing OFETs. Thus, it might be beneficial to incorporate thiophene moieties into the azulenes. Further manipulation of the 6-
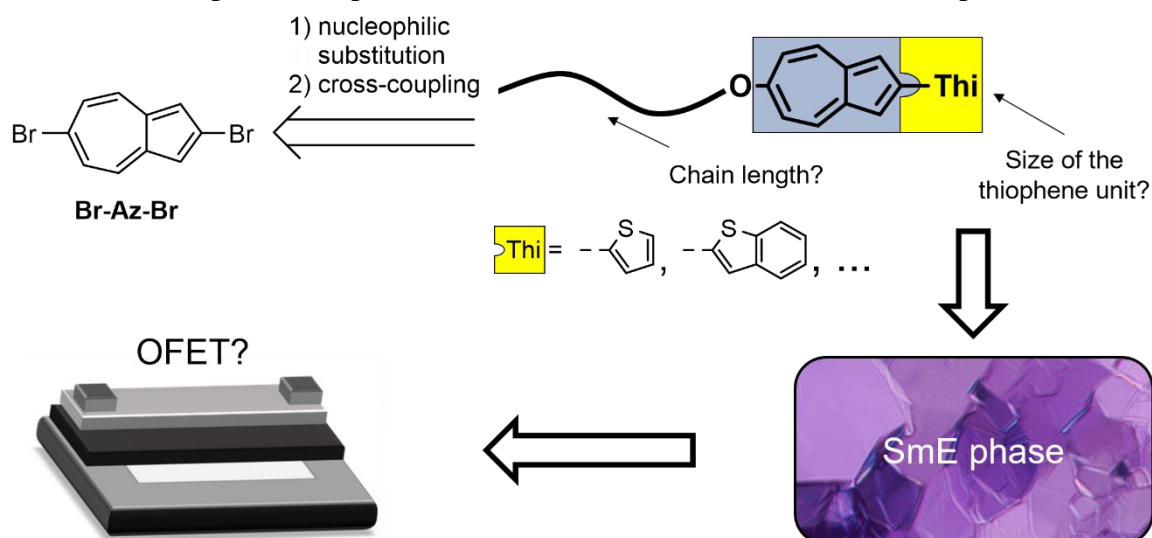

Figure 17: Retrosynthetic approach to azulene derivatives substituted with a single side chain in 6-position and thiophene derivatives in 2-position for soft crystalline materials.

alkoxy-2-bromoazulenes by Suzuki cross-coupling would install the heteroaryl moiety. By varying the size of the thiophene moiety, the solubility, melting point, and conductivity might be adjusted to the needs of applying those derivatives in OFETs.

On the other hand, grafting a second chain to the azulene core would give rise to conventional calamitic mesogens potentially forming more fluid mesophases like SmA and SmC phases (Figure 18). The synthesis could be performed in three divergent steps, starting with the implementation of the side chain at the azulene. The nucleophilic substitution is not limited to ether groups. Rather, attempts should also be made to introduce thioethers or alkynes. For lower phase transition temperatures and an additional cross-dipole moment, it might be advantageous to introduce a lateral substituent at the 5-membered ring *via* electrophilic substitution. A (hetero)aromatic moiety might be inserted to enlarge the aromatic core and could be installed with a cross-coupling reaction. Starting from **Br-Az-Br** a compound library would be unlocked that might be ideally suited for the understanding of structure-property relations. Ideally, the systematic variation of the molecular structure leads to the identification of critical parameters for the mesophase geometry.

Special attention should be paid to the effect of the lateral functionalization combined with the zwitterionic azulene moiety. While the azulene moiety might ensure high translational order, the lateral substituent could disturb orientational order within the layers. This combination resembles the known design principles of de Vries-like materials and potential SmA-SmC phase transitions should be probed for potential de Vries-like behavior.
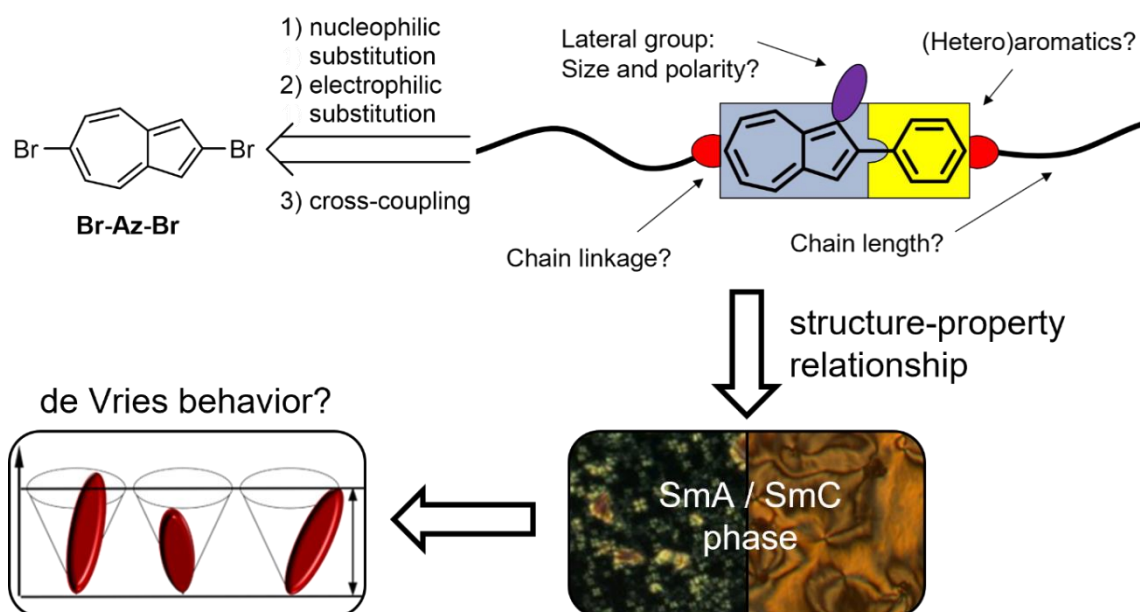

Figure 18: Retrosynthetic approach to azulene derivatives with side chains on both sides and a lateral substituent as mesogens that form fluid smectic mesophases.

4 Discussion

4.1 Synthesis

4.1.1 Synthesis of the Dibromoazulene Precursor

For this work, the method of Nozoe was chosen to build up the azulene scaffold due to the easy ways of post modification at the backbone.[41] Therefore, the commercially available tropolone **38** was transformed to 2-chlorotropone **17** in 85 % yield by treatment with thionyl chloride in benzene (Figure 19a).[103] The condensation of tropone **17** with diethyl acetone dicarboxylate **18** required 12 equiv. of sodium ethoxide to form the Nozoe azulene **19**. Recrystallization from ethanol afforded **19** as orange needles in moderate yields. While the 5-membered ring in **19** is highly functionalized, the 7-membered ring does not bear any groups. Usually, electrophilic substitutions would target the 1- and 3-position at the 5-membered ring. However, in the case of Nozoe azulene **19**, the esters acted as protecting groups and the 6-position was brominated with elemental bromine in the presence of NaOAc. The weak base reacts with the forming HBr and buffers the solution. Interestingly, the reaction performed best without stirring for two days. The brominated azulene **39** was isolated in 85 % yield from the crude mixture by simple filtration.[104]
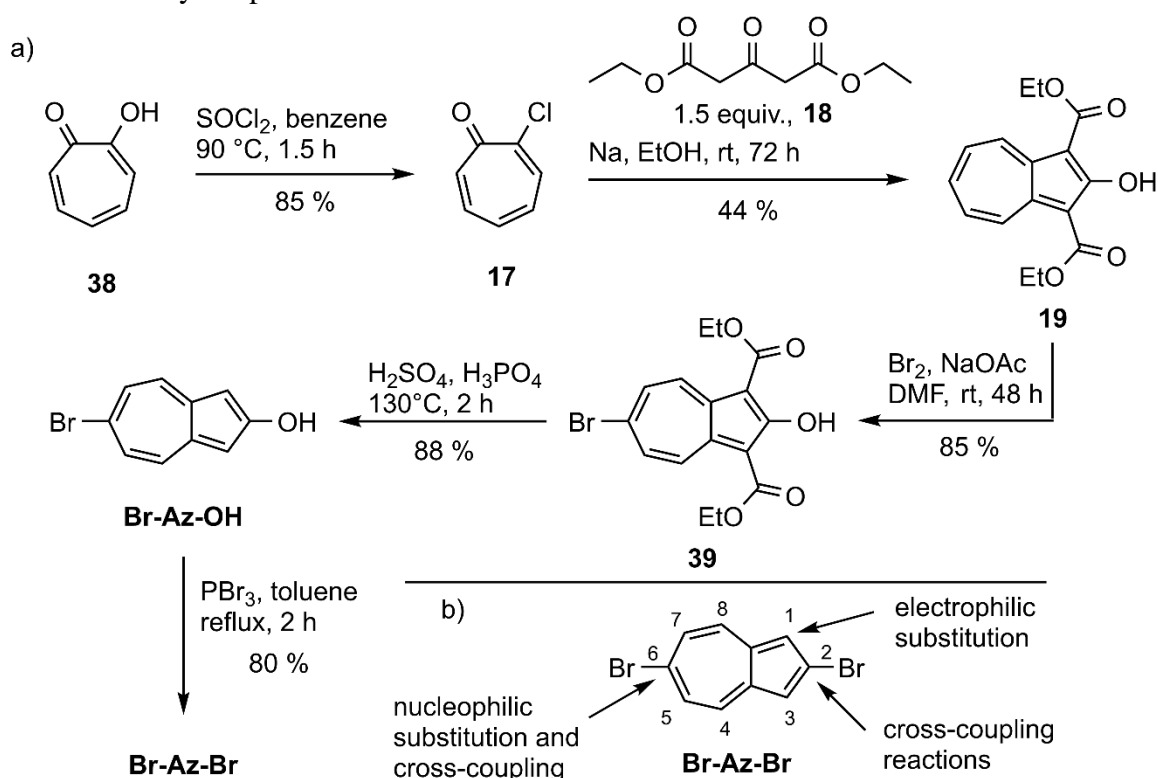

Figure 19: a) Literature known synthesis of the 2,6-dibromoazulene precursor *via* the Nozoe method.[22] b) **Br-Az-Br** as a versatile building block for rapid functionalization of the azulene motif.

To obtain a calamitic geometry of the azulene core, the esters in 1- and 3- position had to be removed. Following a method from Schwarz, **39** was heated in a mixture of conc. sulfuric acid and conc. phosphoric acid for 2 h at 130 °C.[22] Despite the harsh conditions, **Br-Az-OH** was isolated in 88 % after simple flash column chromatography. The desired dibromoazulene precursor **Br-Az-Br** was consequently synthesized in 80 % by treatment with PBr$_3$. Moreover, **Br-Az-Br** can be synthesized on a multi-gram scale and readily further functionalized at different positions (Figure 19b). Both bromo-substituents are reactive in cross-coupling reactions e.g., Suzuki-Miyaura or Sonogashira couplings. However, due to the low electron density at the 7-membered ring, the bromo-substituent can be selectively substituted in the presence of strong nucleophiles.[105] If necessary, lateral substituents can be implemented at 1-position by electrophilic aromatic substitutions.[104]

4.1.2 Synthesis of Azulene Target Molecules with one Side Chain

During own previous work, a dodecyloxy side chain was successfully introduced at the 7-membered ring.[106] The work was originally published in ref [1] and [3]. Surprisingly, **12O-Az-Br** already formed a SmE phase. For deeper understanding of the mesomorphic behavior, azulenes with different chain lengths *n*O-Az-Br were synthesized (Figure 20). Furthermore, the precursor **Br-Az-OH** was etherified under Williamson's conditions and the azulene with 'inverted' substituents **Br-Az-O*n*** was received in good yields.

compound	yield
4O-Az-Br	78 %
8O-Az-Br	90 %
12O-Az-Br	95 %
16O-Az-Br	92 %
Br-Az-O4	76 %
Br-Az-O8	80 %
Br-Az-O12	84 %
Br-Az-O16	82 %
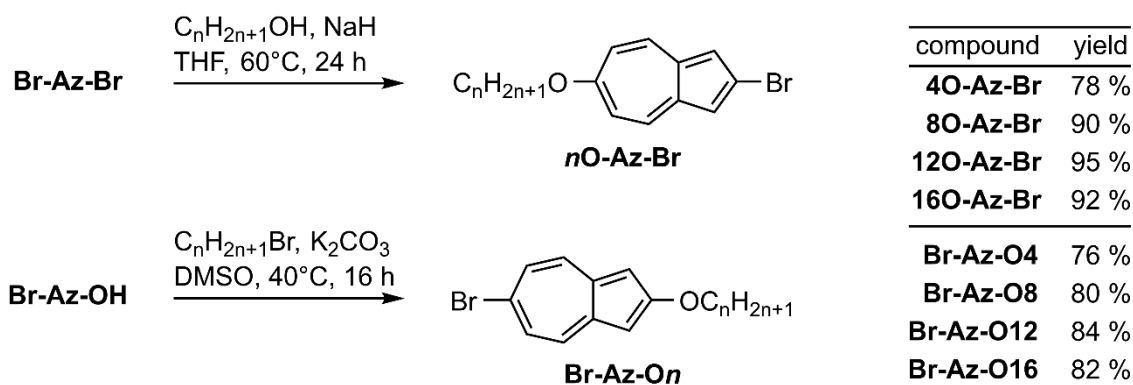
Figure 20: Synthesis of a series of 6-alkoxy-2-bromoazulenes *n*O-Az-Br and their 'inversed' structures **Br-Az-O*n***.

Since a C$_{12}$ chain length is usually a good starting point for mesomorphic behavior,[92] **12O-Az-Br** was chosen for further functionalization. The Suzuki-Miyaura coupling was identified as the best cross-coupling reaction due to its low toxicity and good availability of the boronic coupling partners. In view of good conductivity for potential applications in OFETs, various commercially available thiophene boronic acids were used in Suzuki-Miyaura reactions

(Figure 21). 2-Thienylboronic acid and 3-thienylboronic acid were converted to **12O-Az-T** and **12O-Az-iT** respectively in good yields using 10 mol% of Pd(PPh$_3$)$_4$ and dioxane as a solvent. In the case of benzo[b]thiophene-2-boronic acid the yield dropped to 25 %, which might be due to the fast deboronation reaction under basic conditions.[107] To impede deboronation, the pinacolato ester was used instead of the free boronic acid. Indeed, the yield increased to 72%, which is comparable to the smaller thiophene moieties. The benzothiophene **12O-Az-BT** showed low solubilities in common organic solvents at room temperature, therefore further experiments with larger derivatives were abandoned. The synthesis of the azulene thiophene hybrids took eight steps starting from tropolone. However, due to good yields these derivatives could be synthesized on a 500 mg scale, which is necessary for the detailed investigation of mesomorphic and electronic properties. After the successful synthesis of azulene-thiophene hybrids with one side chain, the focus changed to molecules with chains on both sides of the rigid core.
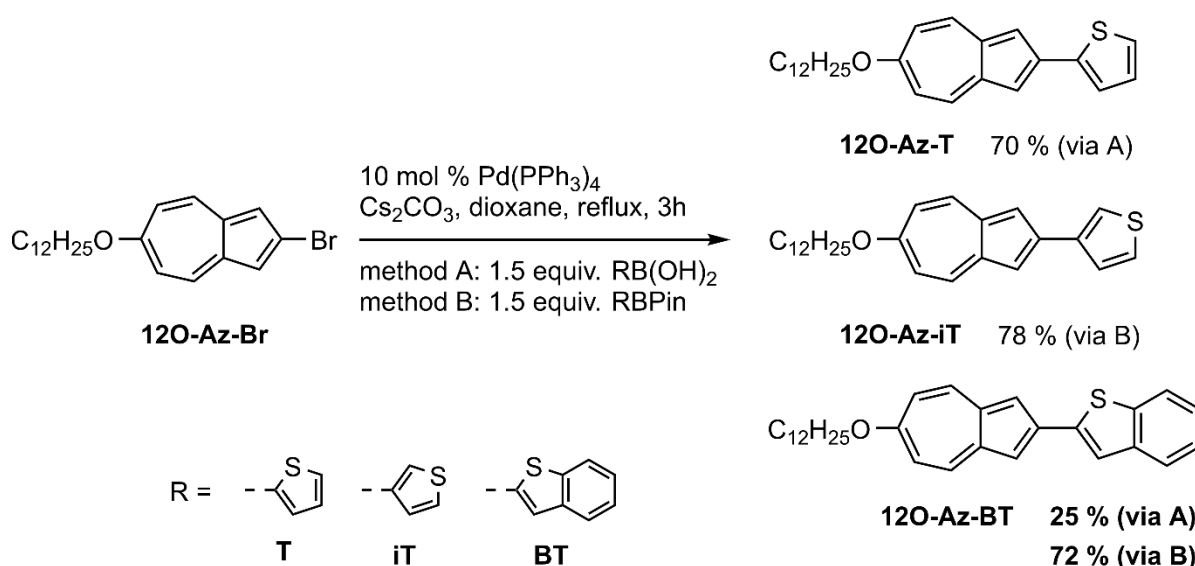
Figure 21: Synthesis of azulene thiophene hybrids under Suzuki-Miyaura conditions using either free boronic acid or pinacolato ester as coupling partner.

4.1.3 Synthesis of Azulene Target Molecules with two Side Chains.

The availability of a broad scope of azulene derivatives is crucial for the exact understanding of structure-property relationships. Thus, different chains were introduced at the 6-position (Figure 22a). The results of this chapter were originally published in ref [4] and [5]. In addition to the already described ether chains, the bromo-substituent was also substituted by a thioether under same conditions to yield **12S-Az-Br** in 56 %.[105] Another possibility for chain insertion is the Sonogashira coupling that links aromatic systems with alkynes. Investigations of the alkyne substituted azulenes were performed by Daniel Rück[108] during his bachelor thesis and

by Derman Batman[109] as part of a research internship. For the sake of completeness, these results will also be discussed here. An exact listing of the contributions is found in the contribution report preceding this work. As already seen during the nucleophilic substitutions, the bromo-substituents showed different reactivities also under Sonogashira conditions. Therefore, the mono alkyne-azulene **12Yne-Az-Br** was isolated in 85 % after reacting **Br-Az-Br** for 16 h in triethylamine at room temperature.[86]
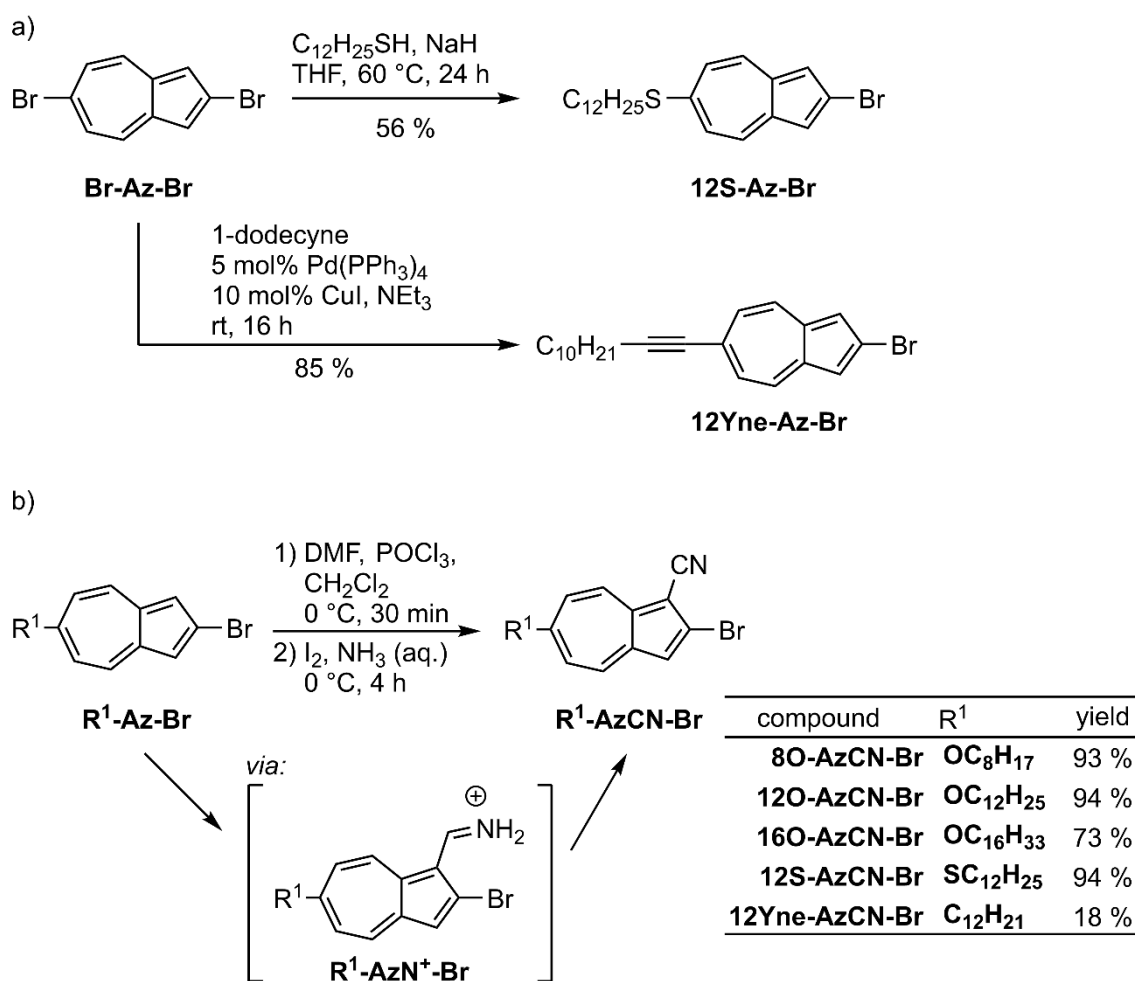
Figure 22: a) Implementation of different side chains at 6-position *via* nucleophilic substitution or Sonogashira coupling. b) Lateral substitution of calamitic azulene derivatives by Vilsmeier-Haack reaction and subsequent oxidation.

In a next step, lateral substituents were introduced *via* electrophilic substitution. Due to their rigidity and polarity, nitriles are one of the most important functionalities in liquid crystal research.[110] While the substitution of various functional groups is readily feasible, the nitrile group had to be attached by indirect methods. Most of the time the Rosenmund- von Braun reaction is used to substitute a halide with a cyano group.[111] However, this reaction requires pre-functionalization and harsh conditions.[112] In 2010, Ushijima and Togo described a

26

procedure for a one pot implementation of the cyano group.[113] In a Vilsmeier-Haack reaction, the intermediately formed iminium ion R^1-AzN^+-Br is directly oxidized with NH_3 and I_2 (Figure 22b). Bianca Wank transferred this procedure to the azulene scaffold as part of her bachelor thesis and synthesized **12O-AzCN-Br** in 94 % yield.[114] The alkoxy azulenes with different chain length **8O-AzCN-Br** and **16O-AzCN-Br** were analogously synthesized in 93 % and 73 %, respectively, whereas the thioether derivative **12S-AzCN-Br** was also isolated in 94 %. In contrast, alkyne **12Yne-AzCN-Br** was only received in low yields. Presumably, the alkyne moiety was not compatible with the oxidative conditions I_2/NH_3.
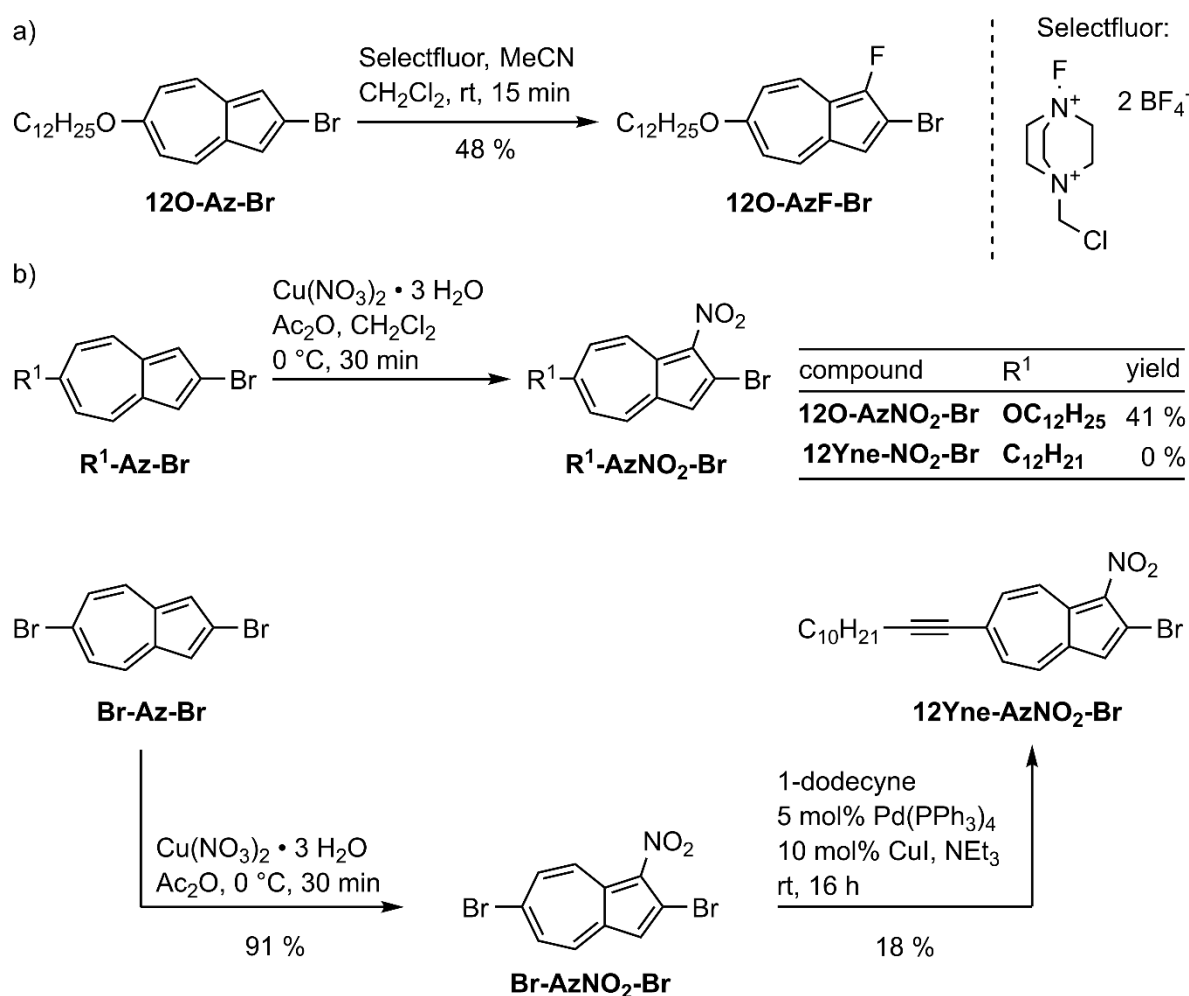
Figure 23: Lateral electrophilic aromatic substitutions of calamitic azulenes: a) fluorination and b) nitration.

In general, the lateral group is expected to have a major impact on the mesophase behavior since the mesogen deviates from the perfect rigid rod and a cross-dipole moment is added. In order to investigate its influence more precisely, further azulenes with side groups of different size and polarity were synthesized (Figure 23a). While fluoro-substituents are sought-after groups in liquid crystal research and medicinal chemistry, fluorination is often unselective.

27

Nonetheless, fluoroazulene **12O-AzF-Br** could be prepared selectively with help of the electrophilic fluorinating reagent Selectfluor® in 48 % in only 15 min reaction time.[115] Further, the nitro group was chosen as a larger and highly polar group to complement the variation of the lateral group (Figure 23b). Unfortunately, classic nitration conditions failed due to the instability of **12O-Az-Br** in acidic media. Only by applying a recently published method by Swager with $Cu(NO_3)_2$ in Ac_2O as the nitrating agent, **12O-AzNO2-Br** was synthesized in moderate yield.[116] However, the method was not compatible with the alkyne group of **12Yne-Az-Br**, thus a different approach was tested. First, **Br-Az-Br** was nitrated to **Br-AzNO2-Br** in 91 % followed by Sonogashira reaction as second step. It turned out that the electron-withdrawing nitro group changed the reactivity of the bromo-substituents compared to **Br-Az-Br**. As a result, both halides were reactive, and the mono alkyne derivative **12Yne-AzNO2-Br** was only isolated in 18 % yield.

As a result, three different substituents were prepared, differing in size and polarity, although the alkyne derivatives were prepared only in low yields. However, since the focus was on structure-property relationships, further optimization experiments were abandoned. With fluoro- nitrile- and nitro substituents as lateral group, it is possible to investigate its influence on the mesophase behavior.

In a third step, a second side chain was implemented. The azulene moiety is rather small to act as the rigid core of a liquid crystal. A larger π-system should increase the dispersion interaction and thus enhance nanosegregation. Both problems can be solved when coupling azulene with an aryl substituent that already bears a side chain (Figure 24). As in the synthesis of the azulene-thiophene hybrids, a Suzuki-Miyaura coupling was performed. The synthesis of the boronic coupling partners is widely known and described in the supporting information of the publications attached to this work.[4,5] Then, the azulene bromide was reacted with 2.0 equiv. of the boronic acid coupling partner in presence of 2.0 equiv. Cs_2CO_3 and 10 mol% $Pd(PPh_3)_4$ in dioxane. After refluxing for 16 h, the target compounds were usually isolated by column chromatography on silica without a previous aqueous work-up. For optimal purity, the desired products were recrystallized from isopropylic alcohol or ethyl acetate.

Bianca Wank synthesized in her bachelor thesis the target structure **12O-AzCN-PhO12** in 63 % yield.[114] For an independent interpretation of different influences on the mesomorphic properties, only one parameter was changed at a time. Hence, the ether groups in **12O-AzCN-PhO12** were substituted to thioethers step by step forming the first series of target

structures (Figure 24, left). Yields varied between 58 % for **12S-AzCN-PhO12** and 94 % for **12O-AzCN-PhS12**. Further, the length of the side chains might also play a prominent role on the mesophase behavior. Therefore, target structures with short side chains (**8O-AzCN-PhO8**) and long side chains (**16O-AzCN-PhO16**) were synthesized (Figure 24, right). Additionally, compounds **8O-AzCN-PhO16** and **16O-AzCN-PhO8** with both short and long side chains were isolated in 75 % and 99 %, respectively. These side chains were attached in a way that the total length of the molecule remained constant, but the position of the core shifted.

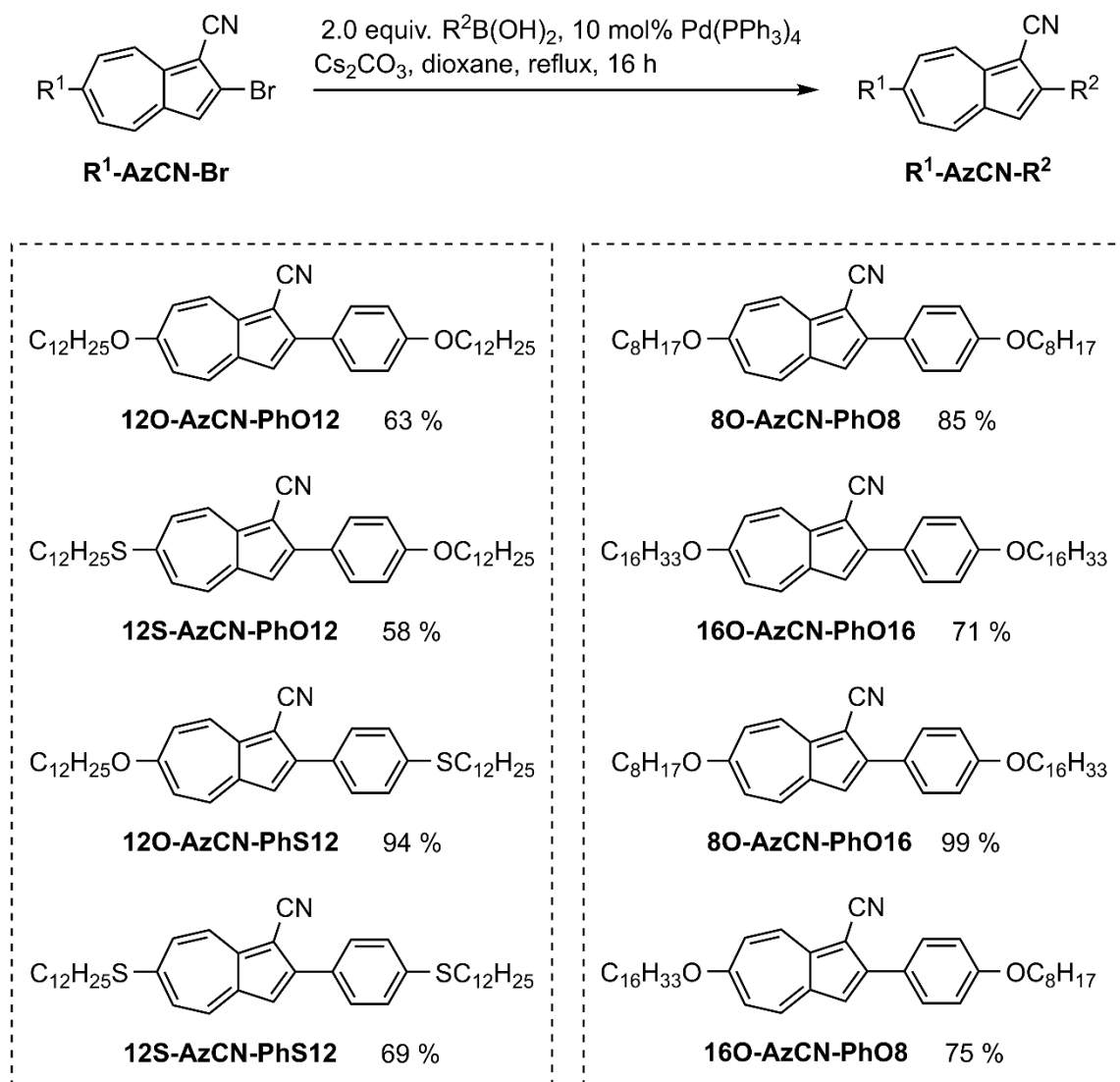**Figure 24:** Synthesis of the target compounds with chains on both sides of the core with lateral nitrile substituent and ether or thioether side chains.

To investigate the influence of the lateral group X on the mesomorphic properties, dodecyloxy groups as side chains were kept constant in the next series of target compounds (Figure 25, left). **12O-AzF-PhO12** and **12O-AzNO₂-PhO12** were synthesized following the same procedure in

68 % and 95 %, respectively. As part of a Bachelor thesis, Bettina Lutz expanded the library of target compounds and varied the azulene coupling partner.

In one approach the position of the nitro group was shifted from the azulene moiety to the phenyl ring and **12O-Az-NO₂PhO12** was isolated in 71 % yield. In this case, the pinacolato ester was used due to the easier synthetic accessibility. Additionally, compound **12O-AzNO₂-MePhO12** with two lateral groups was synthesized in 88 % yield. Furthermore, the phenyl ring was substituted with the heteroaryl moieties thiophene and pyrimidine (Figure 25, right). This work was performed by Bettina Lutz[117] and Derman Batman.[109] On the one hand known azulene motif with cyano group in 2-position was coupled with heteroaryl partner to **12O-AzCN-Thi12** and **12O-AzCN-PyriO12** in 26 % and 86 %, respectively. In addition, the pure azulene backbone was combined with the heteroaryl building blocks. **12O-Az-PyriO12** was synthesized in 30 % yield, but **12O-Az-Thi12** was not isolated under these conditions. Therefore, **12O-Az-Br** was borylated in a Miyaura-coupling and subsequently reacted with the bromo-thiophene derivative under Suzuki-Miyaura conditions. By switching the functional groups, **12O-Az-Thi12** was isolated in 10 % over 2 steps.

Daniel Rück[108] and Derman Batman[109] exchanged the alkoxy chains of **12O-AzCN-PhO12** systematically with alkyne chains (**12O-AzCN-PhYne12**, **12Yne-AzCN-PhO12** and **12Yne-AzCN-PhYne12** in Figure 25, bottom). With **12Yne-AzNO₂-PhO12** an additional derivative was synthesized that combined an alkyne chain with the lateral nitro group.

Starting from **Br-Az-Br** two different approaches have been successfully pursued. On the one hand, azulene thiophene hybrids with only one side chain were synthesized in 2 steps. On the other hand, the divergent 3 step synthesis of azulene mesogens with two side chains resulted in 22 derivatives. These compounds were partially synthesized as part of bachelor theses and a research internship. In the next step, the mesomorphic properties have been investigated for all compounds of both approaches.

Method A: 2.0 equiv. $R^2B(OH)_2$, 10 mol% $Pd(PPh_3)_4$
Cs_2CO_3, dioxane, reflux, 3 h
Method B: 2.0 equiv. R^2BPin, 10 mol% $Pd(PPh_3)_4$
Cs_2CO_3, dioxane, reflux, 3 h
Method C: 1) 20 mol% $Pd(dppf)Cl_2$, 2.0 equiv. $(Bpin)_2$
KOAc, dioxane, reflux, 16 h
2) R^2Br, 10 mol% $Pd(PPh_3)_4$
Cs_2CO_3, dioxane, reflux, 16 h

R^1-AzX-Br

R^1-AzX-R^2

12O-AzF-PhO12   68 % (via A)

12O-AzNO₂-PhO12   95 % (via A)

12O-Az-NO₂PhO12   71 % (via B)

12O-AzNO₂-MePhO12   88 % (via A)

12O-AzCN-Thi12   26 % (via A)

12O-Az-Thi12   10 % (via C)

12O-AzCN-PyriO12   86 % (via B)

12O-Az-PyriO12   30 % (via B)

12Yne-AzCN-PhO12   44 % (via A)

12Yne-AzCN-PhYne12   69 % (via A)

12O-AzCN-PhYne12   92 % (A)
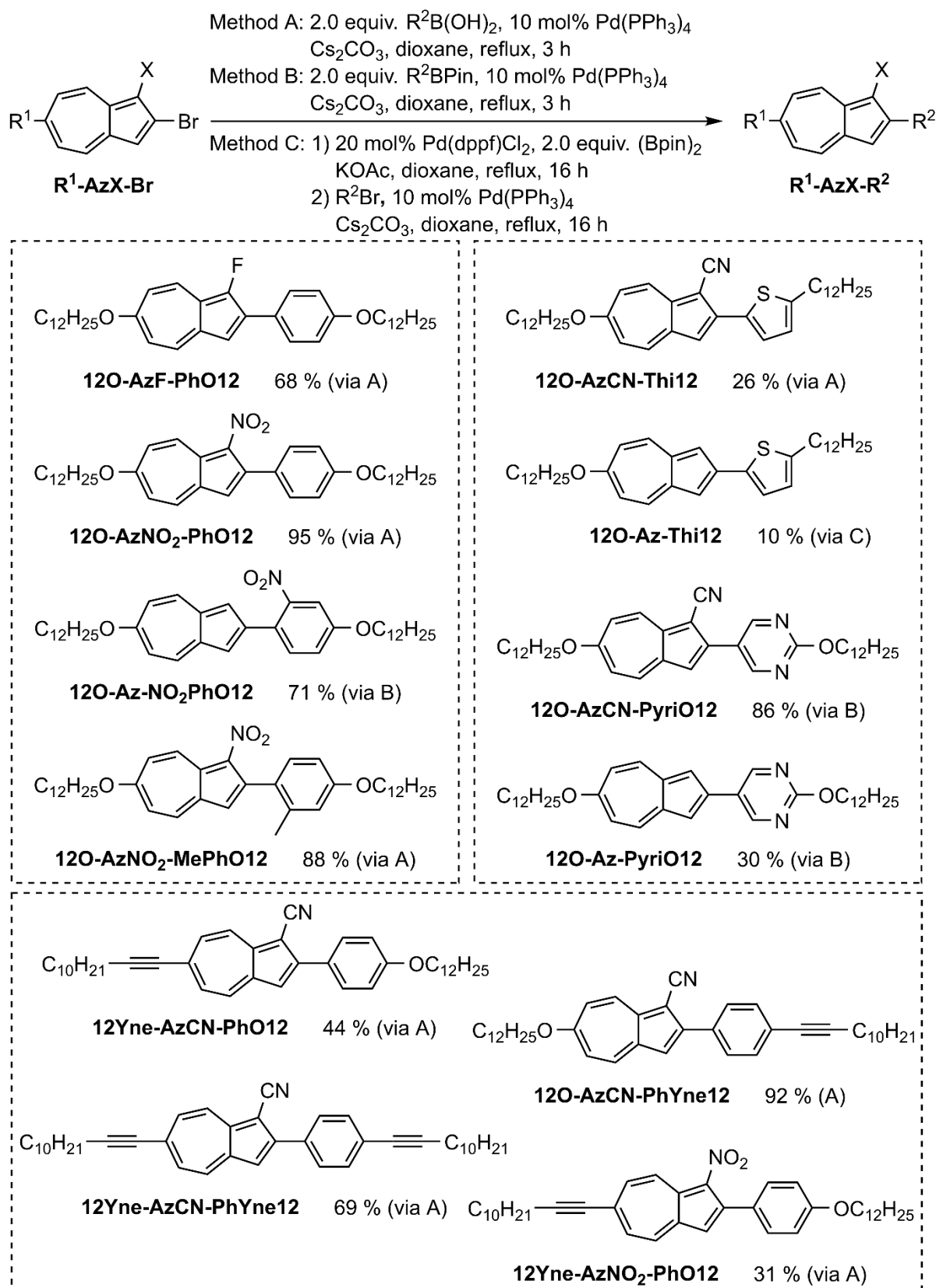
12Yne-AzNO₂-PhO12   31 % (via A)

Figure 25: Divergent synthesis of the target compounds with focus on the effect of the lateral group (left), the (hetero)aryl substituent (right) or the alkyne linked side chains (bottom).

4.2   Mesomorphic Properties

In this chapter the phase width and geometry of occurring mesophases are discussed. The assignment of the mesophase by combination of DSC, POM and XRD methods is detailed in the corresponding publications and will not be discussed here.

4.2.1   Mesomorphic Properties of Azulenes with one Side Chain

The properties of mesomorphic azulenes with one side chain was published in reference [1] and [3]. **12O-Az-Br** was originally synthesized as a precursor of azulene thiophene hybrids. Surprisingly, it already exhibited a 12 K broad SmE phase during heating that enlarged to 42 K during cooling (Figure 26a). For comparison, the isomeric naphthalene derivative **12O-Naph-CN** and the widely known cyanobiphenyl mesogen **12OCB** that also bear two aromatic cycles should be looked at. Even when using the highly polar cyano group instead of the bromine, **12O-Naph-CN** does not form mesophases while **12OCB** forms a 20 K broad SmA phase.[118,119] However, the strong interactions of the cyano group are crucial for the mesomorphic behavior in **12OCB** which form a dynamic monomer/ dimer equilibrium in the mesophase. When changing the nitrile to a bromo substituent (**12O-Ph-Ph-Br**), the mesophase disappears and the crystal directly melts into the isotropic liquid at 120 °C.[120]
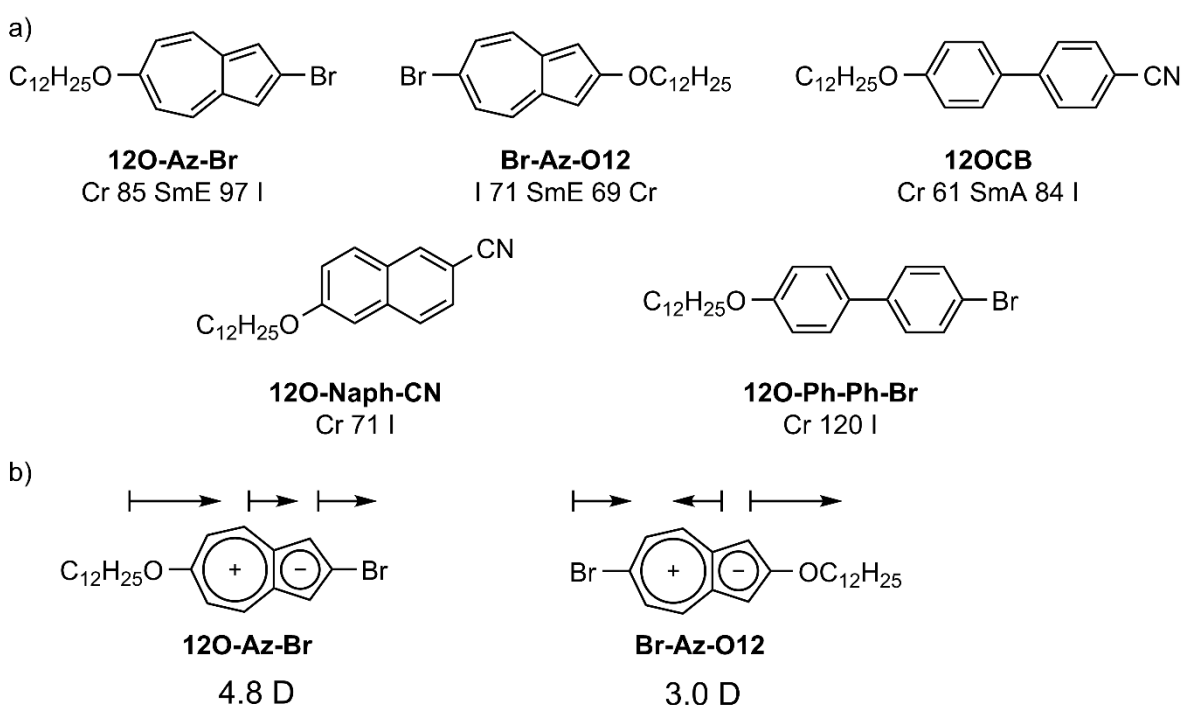
Figure 26: a) Comparison of melting and clearing points of the azulene derivative **12O-Az-Br** and related mesogens. b) Interaction of the dipole of the azulene core with the qualitative dipole moment of the substituents illustrated by means of different resonance structures of **12O-Az-Br** and **Br-Az-O12**. DFT calculations of the dipole moment were performed with the BP-86 functional and def2-SVP basis set with ethyl chains instead of dodecyloxy chains.

In the case of the azulene derivative a weakly electron withdrawing bromo substituent sufficed for the formation of a mesophase. The zwitterionic character of the azulene moiety might have enhanced dipole-dipole interactions of the π-system and therefore caused mesophase formation (Figure 26b). The dipole moment of **12O-Az-Br** might be increased by the electron donating character of the ether and the electron withdrawing character of the bromo substituent. In fact, theoretical calculations showed that the push-pull system by oxygen donor and weak bromine acceptor contributed more to the overall dipole moment than the azulene core. Thus, the direction of the overall dipole was turned in the case of **Br-Az-O12**. Even though the SmE phase of **Br-Az-O12** was monotropic and only 2 K broad, a mesophase was present. Therefore, the intrinsic azulene dipole moment could not be the only reason for the unexpected mesophase formation. In contrast to **12O-Naph-CN**, the azulenes are perfectly calamitic and C_2-symmetric. Thus, enhanced stacking of the fused rings was possible and caused mesophase behavior in both, **12O-Az-Br** and **Br-Az-O12**. The two phenyl rings of **12O-Ph-Ph-Br** could rotate freely and therefore did not interact sufficiently with neighboring π-systems to induce a mesophase. Variation of the chain length revealed that derivatives with smaller chains formed broader mesophases (Figure 27). The trend was observed in both series with **nO-Az-Br** showing larger phase widths than **Br-Az-On** which was attributed to the higher dipole moment.
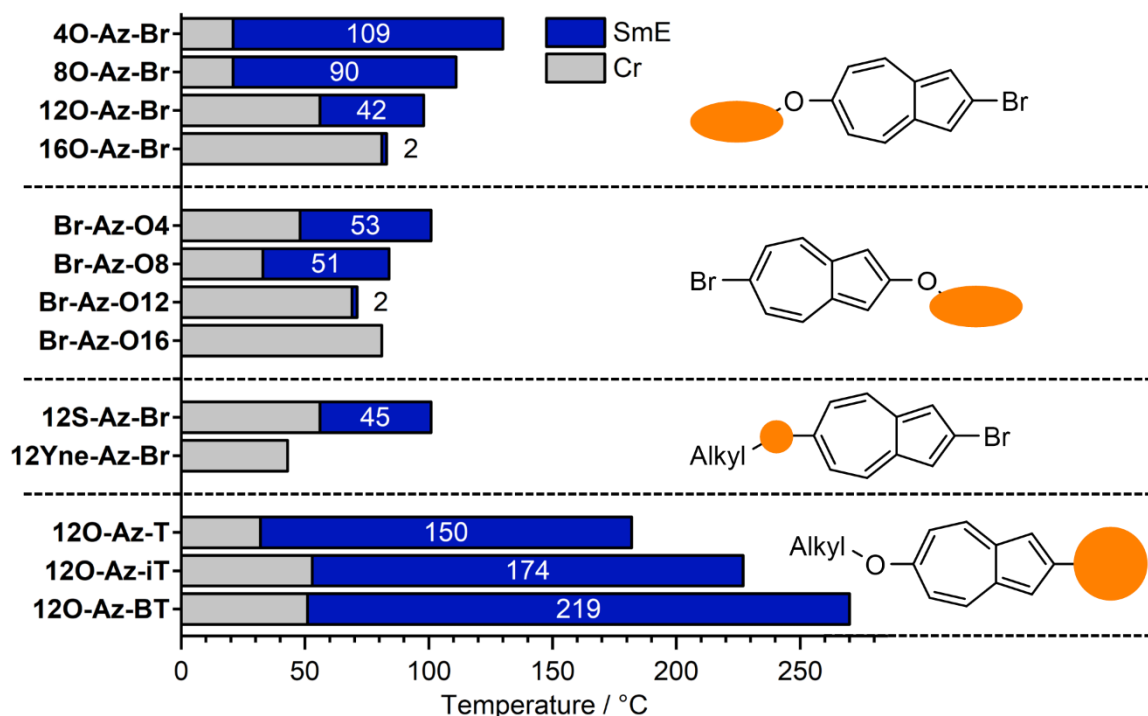

Figure 27: Phase widths of azulene mesogens with one side chain determined by the second cooling cycle of the DSC measurements. The orange markings indicate the position that was varied in this series. Yne = alkyne unit, T = 2-thienyl, iT = 3-thienyl; BT = 2-benzothienyl.

While thioether **12S-Az-Br** behaved similarly to **12O-Az-Br**, alkyne **12Yne-Az-Br** formed no mesophase at all. It was concluded that an electron donating group is crucial for mesophase behavior.

When substituting the bromine with thiophene derivatives (**12O-Az-T, 12O-Az-iT** and **12O-Az-BT**), clearing temperatures and thus the mesophase widths increased drastically (Figure 27). While the derivatives with a single thiophene unit **12O-Az-T** and **12O-Az-iT** cleared at 182 °C and 228 °C respectively, the benzothiophene **12O-Az-BT** remained in the mesophase up to a temperature of 270 °C. A closer look at the interactions of the aromatic core might help to understand the different clearing points. In **12O-Az-T** and **12O-Az-iT** the dipolar azulene moieties can stack in *anti*-fashion with the thiophene units not having an aromatic stacking partner (Figure 28a). Alternatively, the whole aromatic core could overlap. This would increase the dispersion interactions of the thiophene but bring the electron-dense 5-membered azulene rings close to each other, increasing disfavorable electrostatic interactions. The system must compromise between two non-perfect options and therefore cannot optimize intermolecular core interactions. For **12O-Az-BT**, the situation is different since the larger benzothiophene unit consists of two fused rings and is thus an adequate stacking partner for azulene (Figure 28b). As a result, the core-core interactions in the mesophase of **12O-Az-BT** are likely higher than in the mesophases of the shorter **12O-Az-T** and **12O-Az-iT** derivatives. The effects stabilized the mesophase of **12O-Az-BT** at higher temperatures and increased the clearing temperature.
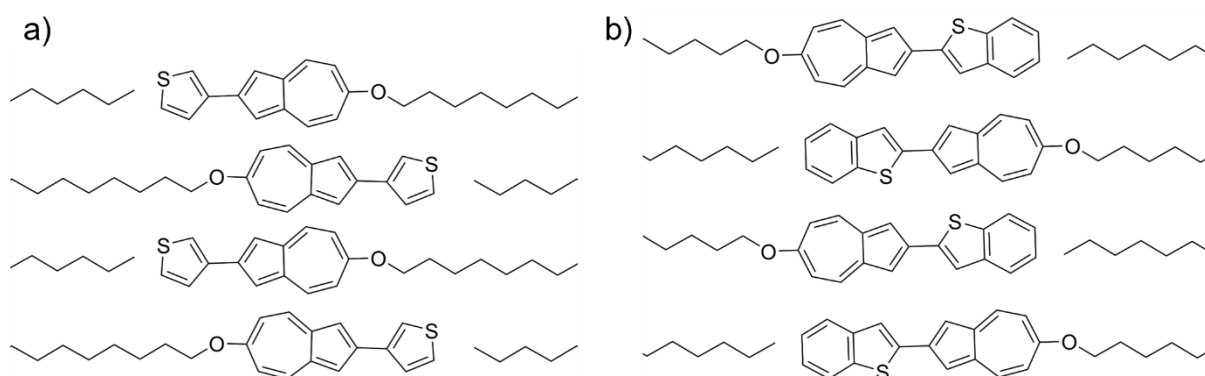
Figure 28: Proposed alignment of the rigid core in the SmE phase of azulene thiophene hybrids for a) **12O-Az-iT** and b) **12O-Az-BT**. The figure was adapted from ref [3].

All azulene mesogens with one side chain exhibited only soft crystalline SmE phases. On the one hand this might be caused by the strong interlocking in the bilayer structure. Another reason might be found in the nature of the azulene interactions. The dipole-dipole interactions of

azulenes are not directed like hydrogen-bonds and therefore might prefer the herringbone packing of the SmE phase over a dimerized form like it is known for cyanobiphenyl compounds that form nematic and SmA phases.

4.2.2 Mesomorphic Properties of Azulenes with two Side Chains

Azulene mesogens with one side chain have been shown to solely form SmE phases. When attaching a second side chain and a lateral substituent more fluid phases became prominent. An overview of the mesophase behavior of azulenes with two side chains is found in Figure 29. The research was originally published in reference [4] and [5].

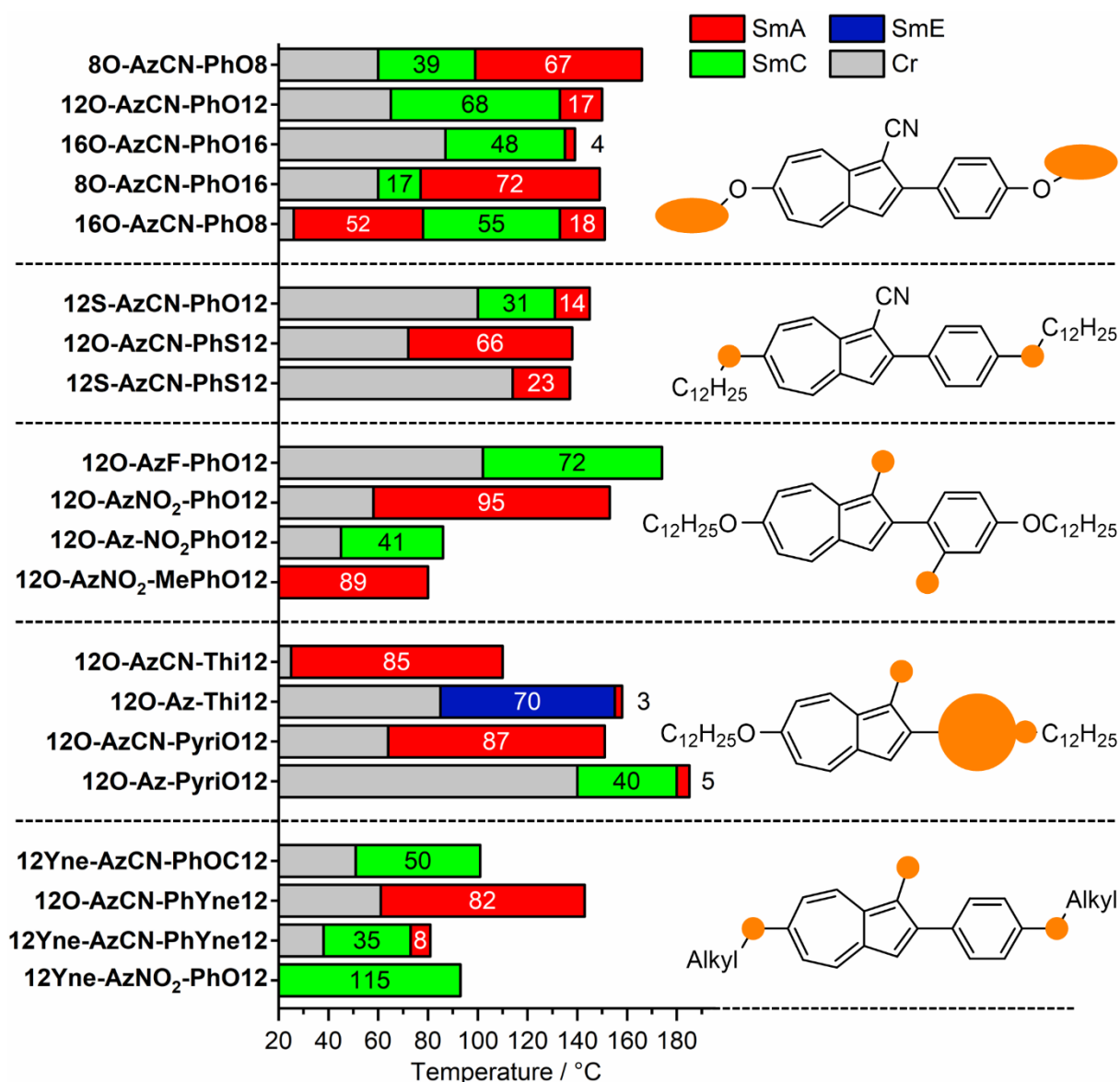
Figure 29: Phase widths of azulene mesogens with two side chains determined by the second cooling cycle of the DSC measurements and POM observations. The orange markings indicate the position that was varied in this series. Yne = alkyne unit.

The 1-cyano-2-phenyazulene derivative **12O-AzCN-PhO12** with dodecyloxy chains on both sides synthesized by Bianca Wank showed an enantiotropic SmA-SmC phase sequence.[114] During cooling, the orthogonal SmA phase formed at 150 °C from the isotropic liquid. At 133 °C, the mesophase transitioned into the tilted SmC phase which remained stable for 68 K until it crystallized at 65 °C. For detailed understanding of the structure-property relationship and thus, control of phase transition temperatures, different structural parameters were systematically varied, using **12O-AzCN-PhO12** as a reference.

For **8O-AzCN-PhO8** with shorter side chains, clearing point slightly increased to 155 °C. The SmA phase became the broader phase and the transition to the SmC phase shifted to 88 °C. Since the melting point was observed at 99 °C, a monotropic SmC phase was present. When elongating the chains, the opposite effect was observed. **16O-AzCN-PhO16** formed a 48 K broad SmC phase, followed by an only 4 K broad SmA phase. The clearing transition was slightly reduced to 139 °C. In two further derivatives, the total length of the side chains was kept constant, but distributed differently between the side chains. For **8O-AzCN-PhO16** the SmA phase was the prominent phase and only a monotropic SmC phase was observed. The clearing point was detected at 149 °C an thus very close to the 150 °C of **12O-AzCN-PhO12**. The same was true for **16O-AzCN-PhO8** which cleared at 151 °C but showed a rather small SmA phase of 18 K. Surprisingly, the SmC phase between 133 °C and 78 °C was not followed by crystallization but rather transformed into an re-entrant SmA phase (SmA$_{re}$), which crystallized at 26 °C.

While the overall chain length appeared to control the clearing temperature, the chain at the azulene determined which phase geometry was more pronounced. Shorter chains prefered the SmA phase with monotropic SmC phases while longer chains only showed small SmA phases and larger SmC phases. The origin of the unexpected re-entrant phase will be discussed later.

Next, the ether chains were systematically replaced by thioethers. **12S-AzCN-PhO12** also showed a SmA-SmC phase sequence, but the width of the SmC phase shrank to 31 K. When substituting the ether at the phenyl ring (**12O-AzCN-PhS12**), the SmC phase disappeared completely. Only a 66 K broad SmA phase was retained. In case of the dithioether derivative **12S-AzCN-PhS12**, the mesophase was further destabilized. A sole SmA phase with a width of 23 K was observed. The observation that thioethers are more likely to form orthogonal phases, while more polar ether groups induce tilted phases was already described by Goodby.[110] Since

dipolar interactions are a cornerstone for mesomorphic behavior, it appears logical that the less polar thioether derivatives showed smaller phase widths.

Lateral substituents have a strong impact on mesophase behavior. In the present system the lateral group was positioned in the center of the aromatic core and might drastically hinder the close interactions of neighboring cores. However, a polar group also introduces a cross-dipole moment that might enhance interactions in form of quadrupole couplings. Therefore, variation of size and polarity of lateral substituents was expected to be an effective tool for the manipulation of phase geometries and transition temperatures. When changing the polar cyano group with a polar but small fluorine atom, the SmA phase in **12O-AzF-PhO12** disappeared and a SmC was detected between 174 °C and 102 °C. The clearing point increased by 24 K compared to **12O-AzCN-PhO12** and solubility in common organic solvents was reduced.

The nitro group is one of the most polar groups available for organic compounds. While bulkier and less rigid than the cyano group, the diameter of the round-shaped group roughly equals the length of the rigid nitrile. Where **12O-AzF-PhO12** showed the tilted SmC phase, for **12O-AzNO$_2$-PhO12** solely the SmA phase was observed. The isotropic liquid to mesophase transition at 152 °C lay close to the cyano derivative **12O-AzCN-PhO12**. It should be mentioned that crystallization was delayed by 36 K compared to the melting point at 94 °C. The hysteresis increased from only 3 K in **12O-AzF-PhO12** to over 25 K in **12O-AzCN-PhO12** with increasing size of the lateral group.

Multiple observations can be drawn from the described series. In terms of phase geometry, small, less polar lateral substituents prefer the SmC phase, while bulky and polar groups induce formation of a SmA phase. The cyano group seems to have the right properties to induce formation of SmA and SmC phases. Clearing temperatures are reduced with larger, more polar substituents, and small substituents impede solubility. Both observations are explained by closer core-core interactions due to lower steric hindrance of the smaller lateral substituent. Crystallization seems to be kinetically hindered with bulky side groups, and hysteresis is observed.

The influence of the position and number of lateral substituents were investigated by Bettina Lutz exemplarily for the nitro derivatives.[117] When shifting the lateral nitro group from the 5-membered ring of the azulene to the phenyl ring (**12O-Az-NO$_2$PhO12**), the phase geometry changed from a SmA phase to a SmC phase, the clearing temperatures dropped to 86 °C and the phase width was reduced to 10 K during heating. A strong hysteresis was observed during

cooling, broadening the SmC phase to a width of 41 K. Presumably, the unsubstituted azulene moieties could interact closely and therefore, a SmC phase formed. In **12O-AzNO₂-MePhO12** a methyl group was added as second lateral substituent at the phenyl ring. The double substituted system showed a SmA phase, presumably due to the hindered azulene-azulene interactions. Secondary lateral substitution prevented crystallization during cooling and the mesophase vitrified at 9 °C.

Heteroaromatics differ from phenyl substituents in their electronic structure. In case of the 5-membered thiophene, they add a small kink to the calamitic mesogen. Bettina Lutz[117] and Derman Batman[109] investigated the influence of the heteroaromatics thiophene and pyrimidine on the mesomorphic properties. The thiophene derivative **12O-AzCN-Thi12** only formed the orthogonal SmA phase. When removing the cyano group in **12O-Az-Thi12**, the SmC phase was expected to reappear due to improved stacking. Instead, a small SmA phase was followed by an orthogonal SmE phase. The deviation from the perfectly linear molecular geometry presumably suppressed the formation of a tilted phase.

The pyrimidine derivative **12O-AzCN-PyriO12** has the exact same molecular geometry as **12O-AzCN-PhO12**. Indeed, the clearing temperature (151 °C) and crystallization point (64 °C) of **12O-AzCN-PyriO12** only deviated by 1 K from the transition temperatures of **12O-AzCN-PhO12**. But the SmA phase extended over the whole mesophase width and the SmC disappeared. The preference of the pyrimidine moiety to form orthogonal phases was already reported by Goodby.[110] Without the lateral substituent **12O-Az-PyriO12** once again exhibited a SmA-SmC phase sequence. However, transition temperatures were high, and decomposition occurred upon clearing at 185 °C. Surprisingly, **12O-Az-PyriO12** crystallized already at 144 °C which is far higher than any other investigated compound. The unhindered stacking of the azulene moieties probably favored the SmC phase as well as to the high crystallization temperature.

As a last variation, electron donating and flexible ether chains were stepwise substituted with moderately electron withdrawing and more rigid alkyne chains. The work was performed by Daniel Rück[108] and Derman Batman[109]. When the alkyne was introduced at the azulene (**12Yne-AzCN-PhO12**), a SmC was formed between 102 °C and 52 °C. In contrast, substitution of the other ether chain in **12O-AzCN-PhYne12** led to a sole SmA phase clearing at 143 °C and crystallizing at 61 °C. In **12Yne-AzCN-PhYne12** with alkynes on both sides, the

SmA-SmC phase sequence reappeared. In general, transition temperatures are reduced upon introduction of alkyne groups.

The position of the alkyne chain has a huge influence on the mesophase geometry. To understand the distinct behavior, the situation should be considered on a molecular level. Alkyne moieties are less polar than ether groups and increase the free volume due to their linear geometry (Figure 30a). Both effects contribute to the low transition temperature of alkyne substituted derivatives. Additionally, alkynes enlarge the π-system and might contribute to the core interactions even though an alkyne to aromatic interaction might be considered weak due to the deviating geometry. In **12Yne-AzCN-PhO12**, the phenyl ring can interact with neighboring alkynes and the interactions of the zwitterionic azulenes are optimized (Figure 30b). As a result, the lateral cyano groups do not get in each other's way and a close stacking
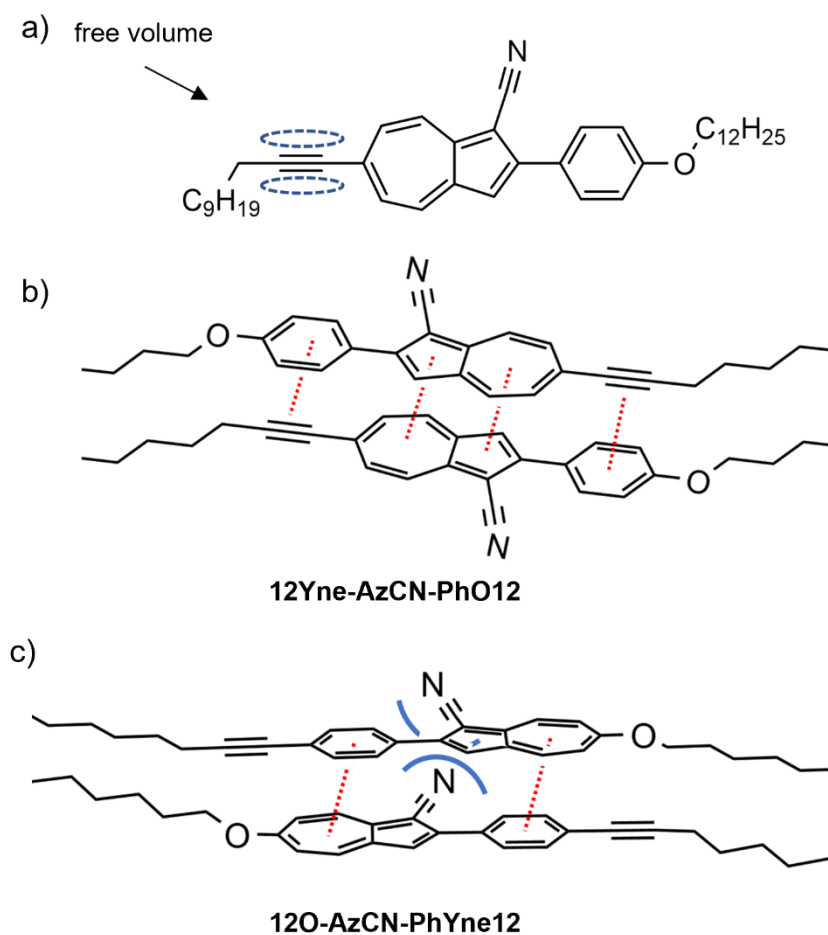

12Yne-AzCN-PhO12

12O-AzCN-PhYne12

Figure 30: Considerations of the alignment in mesogens with one alkyne unit. a) Free volume caused by alkyne groups. b) Schematic stacking of the freely rotating cores of **12Yne-AzCN-PhO12** and c) of **12O-AzCN-PhYne12**. The figure was reproduced with permission from ref [5].

of the cores is possible which is known to prefer the SmC phase. The situation changes for **12O-AzCN-PhYne12**. If the alkyne participated in the core interactions, the azulene rings had weak stacking partners. Thus, it is more likely that the alkyne is part of the chain and stacking happens between phenyl and azulene moieties (Figure 30c). In this case, lateral cyano groups are forced on each other. The azulenes cannot stack closely, which leads to a SmA phase. In **12Yne-AzCN-PhYne12** the extension of the π-system is balanced and the SmA-SmC phase sequence is kept.

It was shown that an alkyne chain at the azulene reduced the phase transition temperatures and preferred the SmC phase. For a liquid crystal with low transition temperatures, the alkyne moiety was combined with the SmA-promoting nitro group that was previously shown to prevent crystallization (*vide supra*). Indeed, **12Yne-AzNO$_2$-PhO12** showed a SmC mesophase between 96 °C and 22 °C during cooling. Only a SmC phase was observed, despite the SmA promoting nitro group. When applying the model from Figure 30b, it becomes apparent that the nitro groups are too far from each other to interact and do not prevent the close stacking necessary for the SmC phase.

Azulenes with two side chains were shown to form fluid SmA and SmC phases. In general, derivatives with unhindered interactions of the azulene cores rather exhibit SmC phase, while steric hindrance or electronic anomalies like heteroaromatics or thioethers tend to form SmA phases.

After general characterization of the mesomorphic properties, selected mesogens were further investigated for potential applications. Azulene-thiophene hybrids with one side chain were tried in OFETs and azulenes with two side chains and a SmA-SmC phase sequence were investigated for de Vries-like behavior.

4.2.3 Mesomorphic Properties of Tetrahydropentalene-based Liquid Crystals

Max Deimling synthesized chiral bicyclo[3.3.0]octa-1,4-diene ligands with chains on both sides.[2] The form of the ligands resembles the building strategy for calamitic liquid crystals and thus, the compounds were investigated for potential mesomorphic behavior. An overview of all derivatives and the nomenclature is shown in Figure 31a. Due to rapid decomposition of some derivatives at elevated temperature, the first heating cycle of the DSC was used for the determination of phase widths (Figure 31b).

The tetrahydropentalene derivative with two hexyl chains **Pent-O6** melted at 77 °C into a SmA phase and cleared at 108 °C. Since the mesogens were originally used for click-coupling
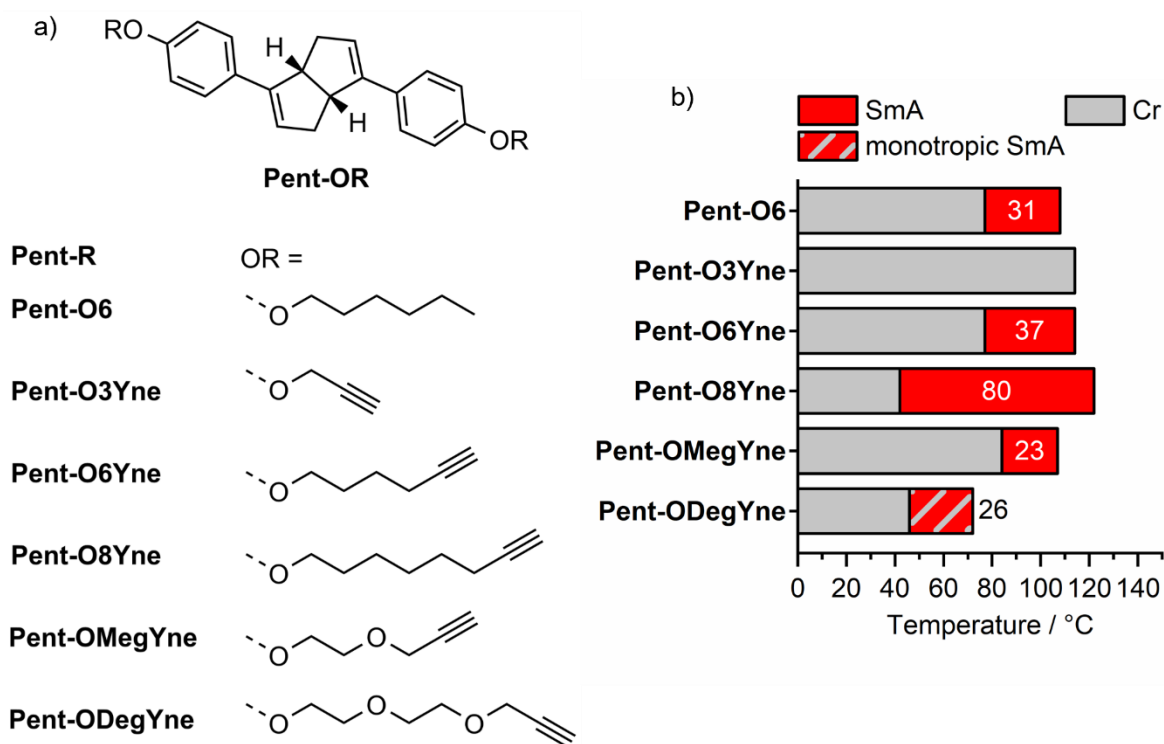
Figure 31: a) Molecular structure of calamitic tetrahydropentalene derivatives **Pent-OR** investigated for mesomorphic behavior and b) phase widths of the investigated compounds determined by the first heating cycle of the DSC.

reactions on heterogenic support, different chain lengths with terminal alkynes were available. The shortest derivative **Pent-O3Yne** did not exhibit mesomorphic behavior but cleared directly into the isotropic liquid at 114 °C. Upon repeated heating and cooling, phase transitions shifted to lower temperatures, indicating decomposition reactions. In fact, all derivatives with alkyne end groups were instable at elevated temperatures. **Pent-O6Yne** with the same chain length as **Pent-O6** showed similar phase widths. Clearing was observed at 114 °C which is slightly higher than the corresponding alkyl derivative. **Pent-O8Yne** already melted at 42 °C and exhibited a SmA phase width of 80 K. In addition to hydrocarbon derived side chains, more polar ethylene glycol chains were also investigated. The monoethylene glycol derivative **Pent-OMegYne** showed a SmA phase between 84 °C and 107 °C while the diethylene glycol derivative **Pent-ODegYne** exhibited no mesophase and melted at 72 °C. However, upon cooling a monotropic SmA was phase was observed for **Pent-ODegYne** that crystallized at 46 °C.

Since **Pent-O6** and **Pent-O6Yne** behaved very similar, it can be concluded that terminal alkyne chains affect mesomorphic behavior only marginally in this system (save for thermal stability). **Pent-O8Yne** showed the largest phase width of all investigated derivatives. Thus, the optimal

chain length in terms of SmA phase width might be even higher. When changing to ethylene glycol-based chains, phase widths shrank, presumably due to increasing polarity of the side chains contradicting nanosegregation and therefore weakening the smectic layers. The investigated compounds might be applied as potential chiral doping agents for achiral mesogens.

4.3 Application of Azulene-Thiophene Hybrids in Thin Films and OFETs

Organic semiconductors are promising candidates for numerous applications due to their light and flexible properties. Furthermore, they can potentially be used in printed electronics.[58] Various methods are known for the processing of organic semiconductors in devices, e.g. in organic field effect transistors (OFETs). Vacuum deposition of organic semiconductors allows production of uniform films resulting in high performance of related OFETs. However, the procedure requires a demanding set-up and is characterized by a low space-time yield. Thus, solution-processing (e.g. via spin-coating) of organic thin films has been developed as a method for the low-cost production of organic devices.[121] When spin-coating liquid crystalline compounds at mesophase temperature, their self-assembly can be exploited and highly ordered thin films are readily prepared.[59] This procedure should be applied for the azulene-thiophene hybrids **12O-Az-T**, **12O-Az-iT** and **12O-Az-BT** (Figure 32a). The results were originally published in reference [3].

a)

12O-Az-T
Heating: Cr_1 51 Cr_2 95 SmE 186 I
Cooling: I 182 SmE Cr_1 32

12O-Az-iT
Heating: Cr_1 63 Cr_2 104 SmE 228 I
Cooling: I 227 SmE Cr_1 53

12O-Az-BT
Heating: Cr_1 76 SmE 270 I
Cooling: I 270 SmE Cr_1 51
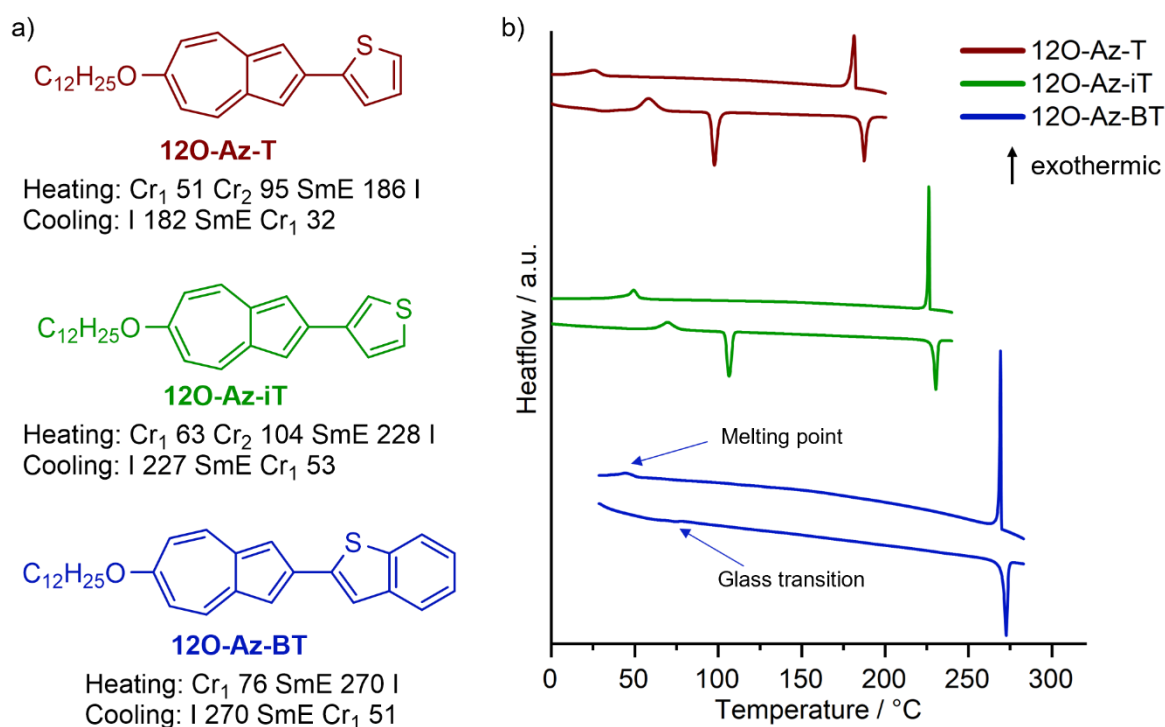
Figure 32: a) Molecular structure of azulene-thiophene hybrids used for thin film preparation and b) the second cycle of the DSC traces.

For a trouble-free use of the method described by Iino and Hanna,[59] several parameters should be checked prior to spin-coating experiments. Since the process is solution-based, a sufficient solubility of the mesogen is crucial, which is usually 5 mg/mL in toluene or *p*-xylene. **12O-Az-T** and **12O-Az-iT** showed already good solubility at room temperature. In contrast,

12O-Az-BT was not soluble until the mixture was heated to 60 °C. Since spin-coating should be performed at mesophase temperature, the solubility of all three compounds should be sufficient.

A drastic increase of the charge carrier mobilities in OFETs based on **Ph-BTBT-10** was reported after short thermal annealing which was explained by a change from a monolayer to a bilayer crystal structure in the thin film.[59] **12O-Az-T** and **12O-Az-iT** showed an exothermic crystal to crystal transition during the heating cycle of the DSC measurement (Figure 32b) that might indicate a similar behavior to **Ph-BTBT-10**. For **12O-Az-BT**, no crystal to crystal transition was detected during our DSC measurements. However, it might still be possible to induce the bilayer crystal structure by thermal annealing.

Spin-coating of the polycrystalline thin films was performed at 60 °C in *p*-xylene either on glass substrates or on silicon wafers coated with insulating SiO_2 layers. When choosing the best coating conditions, the phase transitions during cooling should be regarded, allowing lower coating temperatures due to hysteresis of the crystallization.[58] The exact procedure is detailed in the corresponding publication and will not be discussed here.[3] Alignment of the coated films was controlled with in-plane and out-of-plane XRD (Figure 33). During in-plane measurements, no layer reflexes were observed, indicating a uniform orientation of the thin film. In-plane measurements confirmed the observation but were also used to distinguish between monolayer and bilayer crystal structures. Interestingly, the film of **12O-Az-T** directly crystallized in the bilayer crystal structure and was not further influenced by annealing. In case of **12O-Az-iT** the monolayer from the SmE phase was preserved in the structure of the polycrystalline thin film. However, annealing at 80 °C for 5 min sufficed for the thin film to transform into a bilayer crystal structure. A monolayer crystal structure was also observed for **12O-Az-BT** after spin-coating and 19 h of annealing at 85 °C were necessary to achieve a full transformation into a bilayer crystal structure.

All three compounds formed well-oriented thin films upon spin-coating and thermal treatment. Thus, they might be suitable for OFET applications. While the bilayer crystal structure seems to be thermodynamically preferred for all compounds, the stimulus for the monolayer to bilayer transformation deviates strongly. Calculations from XRD measurements in the mesophase revealed a higher density of **12O-Az-BT** (1.02 g/cm^3) than **12O-Az-T** and **12O-Az-iT** (each 0.76 g/cm^3). This reflects the more efficient stacking of **12O-Az-BT** compared to**12O-Az-T** and **12O-Az-iT** as discussed in chapter 4.2.
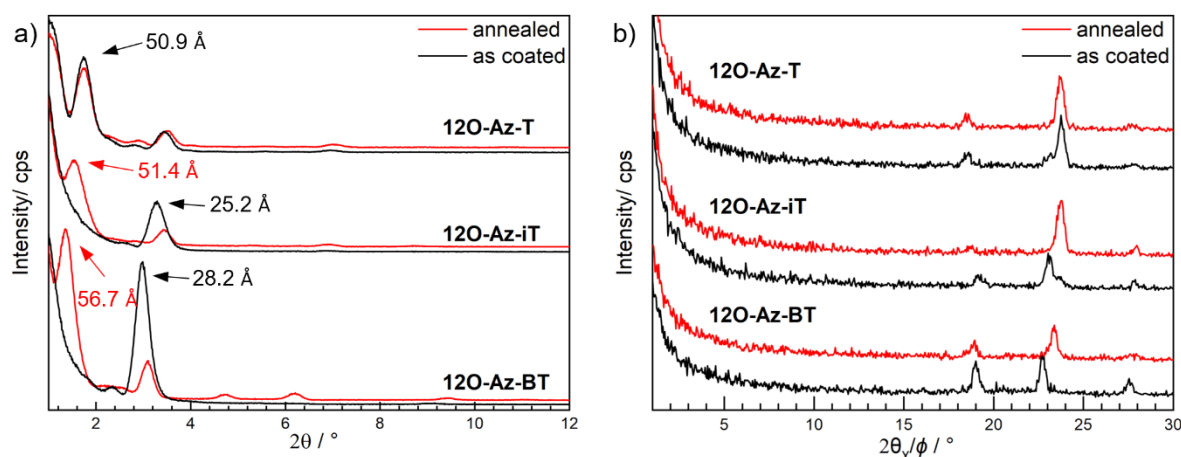
Figure 33: X-ray diffraction experiments of thin films before and after annealing a) out-of-plane XRD and b) in-plane XRD. Annealing conditions: **12O-Az-T** and **12O-Az-iT**: 80 °C, 5 min; **12O-Az-BT**: 85 °C, 19 h. The figure was reproduced with permission from ref [3].

Besides good molecular orientation, a uniform thickness and high crystallinity of the prepared thin films is also important for the charge carrier properties of the organic thin-films and their application in OFETs. Different microscopy techniques were applied to ensure the uniformity of the film. The techniques are exemplarily shown for **12O-Az-BT**. The experimental data of **12O-Az-iT** and **12O-Az-BT** are presented in the supporting information of the corresponding publication.[3] Optical microscopy gave a first glance over the morphology of the film (Figure 34a). Dark spots would have been observed if the silicon waver had not been completely coated with the organic compound. After annealing, the surface became rougher, but the waver was still coated homogenously (Figure 34e). Cross-sectional profiles taken with confocal laser scanning microscopy (CLSM, Figure 34c,g) are suited for thickness determination of the films. Before annealing, the film exhibited a uniform thickness of ca. 40 nm, after annealing the uniformity is slightly reduced and the film thickness varied between 20 nm and 40 nm. Another tool for the investigation of surfaces is atomic force microscopy (AFM).The images showed a terrace structure with clear transitions between the different molecular layers (Figure 34b,d,f,h). In the as coated film, steps between two levels equaled the layer spacing of the monolayer crystal structure (3.1 nm) while the film after annealing showed steps that confirmed the presence of the bilayer crystal structure (5.7 nm). The terrace structure of the polycrystalline thin films was also observed for **12O-Az-T** and **12O-Az-iT**, but crystallinity and uniformity were reduced after annealing.

After the uniform morphology and homogeneous orientation of the polycrystalline thin films of all compounds were ensured, the interaction between organic semiconductor and electrodes
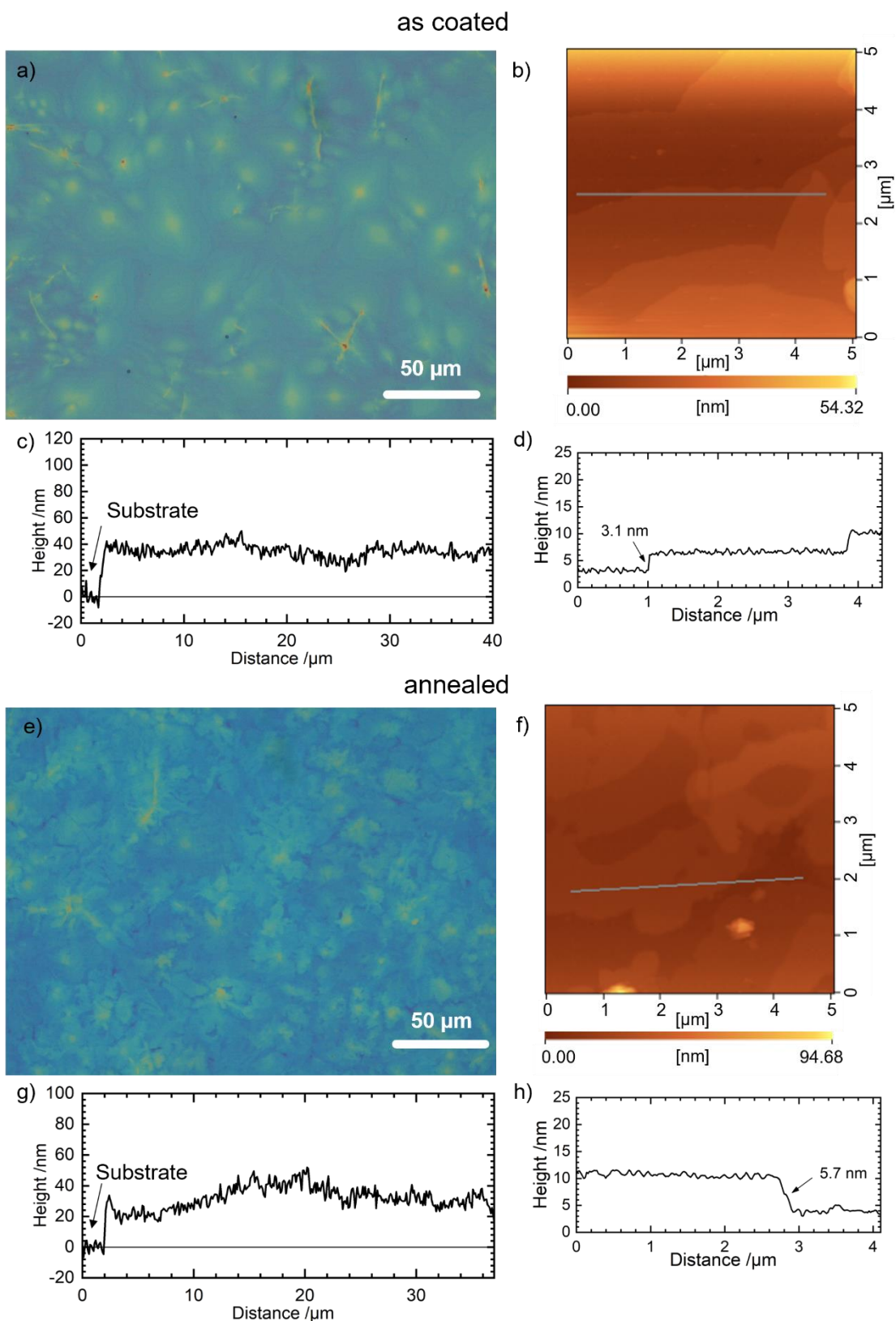
as coated

annealed

Figure 34: Images of polycrystalline thin films of **12O-Az-BT** fabricated by spin-coating. Top: as coated and bottom after annealing. a), e) Textures determined by optical microscopy and b),f) film observed via AFM. c),g) Cross-sectional profiles observed by CLSM and d),h) AFM. The figure was adapted from ref [3].

was investigated. For optimal charge carrier injection from the electrode to the organic film, the HOMO level of the compound should match with the working function of the electrode metal (5.1 eV for gold).[122] HOMO energies were determined by DFT calculations using the B3LYP functional and def2-TZVP basis set.[123] Additionally, cyclic voltammetry (CV) measurements performed by Tobias Bens were also used to calculate the HOMO levels (Table 1). The calculations based on DFT and CV both are close to 5.1 eV, suggesting an easy carrier injection. Top contact bottom gate transistors with heavily p-doped silicon substrates topped with 300 nm of SiO_2 as gate and insulator and gold electrodes were manufactured. The whole manufacturing process is explained in the publication.

Table 1: HOMO levels of azulene-thiophene hybrids calculated by cyclic voltammetry and DFT.

Compound	HOMO (CV) / eV	HOMO (DFT) / eV
12O-Az-T	–5.4	–5.3
12O-Az-iT	–5.4	–5.4
12O-Az-BT	–5.5	–5.3
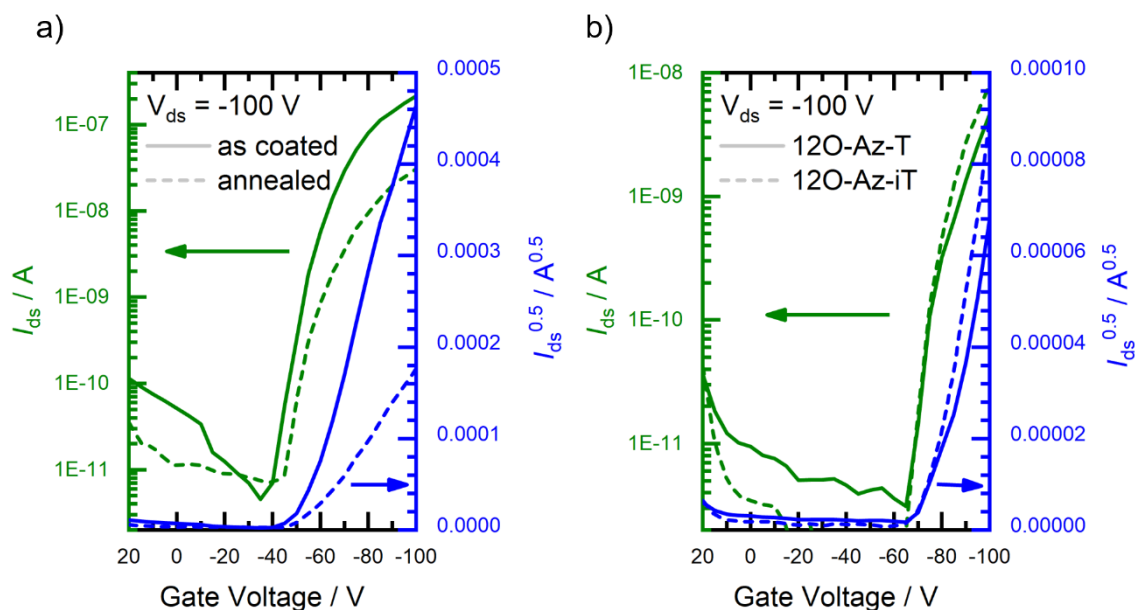
Figure 35: a) p-channel transfer characteristics of polycrystalline thin films of **12O-Az-BT** as coated and after annealing and b) transfer characteristics of as coated films of **12O-Az-T** and **12O-Az-iT**. The figure was reproduced with permission from ref [3].

For transfer characteristics of the **12O-Az-BT**-based OFETs, 10 transistors were manufactured on 2 substrates. Hole mobilities of $\mu^+ = (3.1 \pm 0.5) \cdot 10^{-3} \text{cm}^2\text{V}^{-1}\text{s}^{-1}$ and a threshold voltage of

V_{th} = -52 ± 2 V were calculated (Figure 35a). After annealing, a lower mobility of μ^+ = (5.1 ± 0.8)·10^{-4}cm^{2}V^{-1}s^{-1} and higher V_{th} = -57 ± 3 V were observed. The variance of μ and V_{th} is relatively low which is caused by the liquid crystalline self-assembly during spin-coating at mesophase temperatures.[58] The derivatives with smaller aromatic cores **12O-Az-T** and **12O-Az-iT** showed lower mobilities of μ = 2.2·10^{-4}cm^{2}V^{-1}s^{-1} and 4.1·10^{-4}cm^{2}V^{-1}s^{-1}, respectively and V_{th} = 74 V in both cases (Figure 35b). After annealing, no transistor properties were observed, which might be caused by the decrease of uniformity and crystallinity of the thin films.
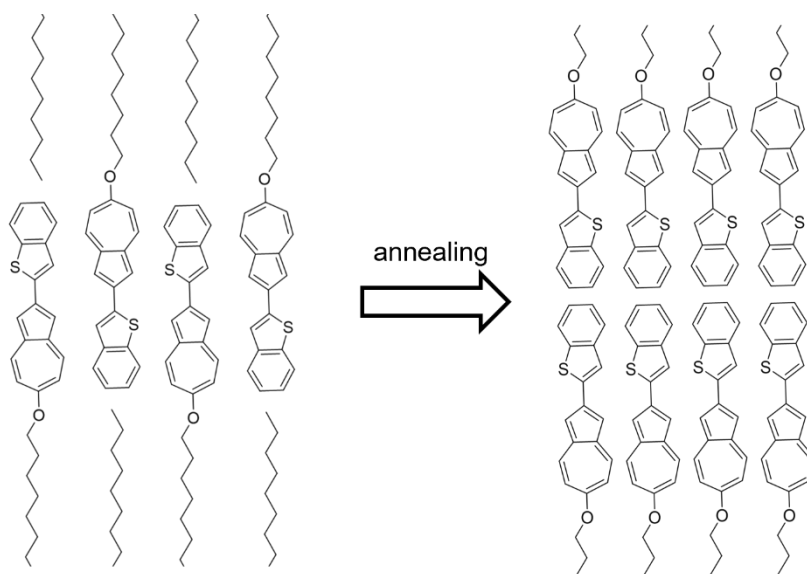

Figure 36: Comparison between the monolayer crystal structure and the bilayer crystal structure of **12O-Az-BT**. The figure was adapted from ref [3].

In contrast to **Ph-BTBT-10**, the transition from a monolayer crystal structure to a bilayer crystal structure did not boost transistor performance. Since it is not possible to achieve a single crystal structure of the thermodynamically less stable monolayer crystals it is difficult to clearly identify the reasons for the enhanced mobility of **Ph-BTBT-10** and the reduced mobility of **12O-Az-BT** after annealing. However, the schematic comparison of the monolayer and bilayer structures of **12O-Az-BT** in Figure 36 might give a hint. In the bilayer structure, azulenes stack parallel to each other which leads to a row of 5-membered rings and a row of 7-mebered rings. The dispersion interaction of the aromatic system might thus be reduced by the repulsion of equally charged dipoles. As a result, stacking might not be as tight as in the monolayer crystal structure and carrier mobilities are reduced.

In summary, thin films of azulene-thiophene hybrids **12O-Az-T**, **12O-Az-iT** and **12O-Az-BT** were prepared by spin-coating during mesophase temperature. The films turned out to be well-

oriented with a uniform morphology. For all compounds top contact bottom gate OFETs were manufactured whereby **12O-Az-BT** showed best charge carrier mobilities with $\mu^+ = (3.1 \pm 0.5)\cdot10^{-3}\,cm^2V^{-1}s^{-1}$. Even though it was possible to transform the monolayer crystal structure into a bilayer crystal structure by thermal annealing, carrier mobilities did not improve. The surprising fact was explained with the zwitterionic nature of the azulene core and the resulting weaker π-interactions in the bilayer crystal.

4.4 De Vries Properties and Re-entrant Behavior of Azulenes with two Side Chains

The SSFLC-display is a potential next generation display based on the ferroelectric SmC* phase. However, usual layer shrinkages of over 10 % of mesogens following the rigid rod model during cooling in the SmC* cause defects that impede the broad application of those displays.[69] Liquid crystals that exhibit SmA-SmC phase sequences and show exceptionally low temperature dependent layer shrinkage in the SmC phase are often referred to as de Vries-like materials and might help to overcome the limitations of SSFLCDs. De Vries-like behavior is often linked to the diffuse cone model.[71] Furthermore, understanding of the unusual behavior might help to improve the fundamental understanding of transitions between liquid crystalline phases. The findings of this chapter were originally published in ref [4] and [5].

De Vries-like LCs are often characterized by exceptionally low orientational and high translational order. Since the zwitterionic azulene moiety is expected to promote well-ordered layers, azulene mesogens with a SmA-SmC phase sequence were investigated for de Vries-like behavior. The compounds discussed in this chapter are shown in Figure 37. The whole series of **nO-AzCN-PhOm, 12S-AzCN-PhO12**, **12Yne-AzCN-PhYne12** and **12O-Az-PyriO12** exhibited the sought-after SmA-SmC phase sequence. However, **16O-AzCN-PhO8** showed a SmA$_{re}$ phase below the SmC phase.

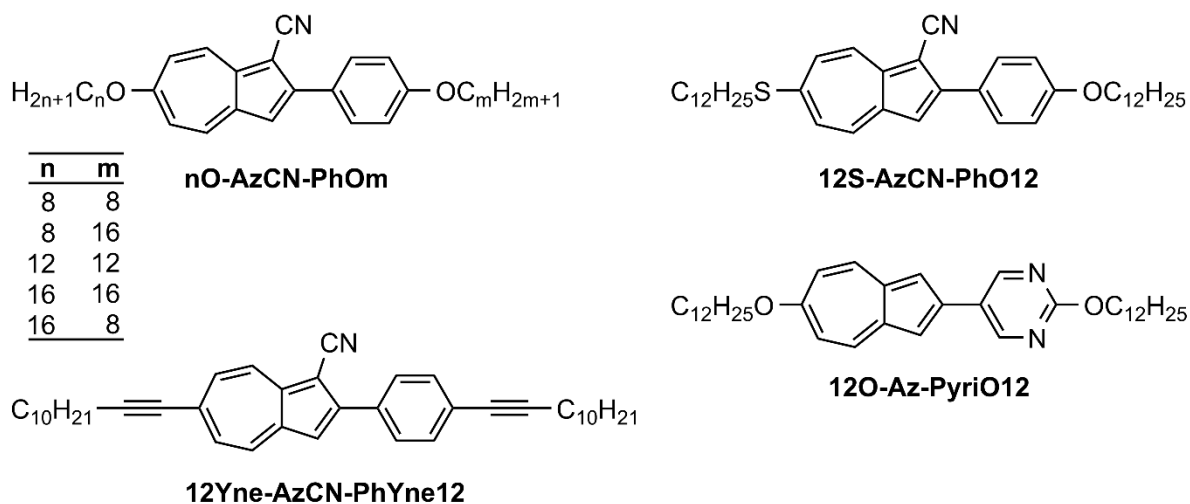**Figure 37:** Azulene compounds exhibiting a SmA-SmC phase sequence that were investigated for de Vries-like behavior.

Temperature dependent layer spacing d was measured by XRD (Figure 38). For better comparability, the layer spacing was normalized relative to the layer spacing at the SmA-SmC transition d/d_{AC} and was plotted *versus* the reduced temperature $T - T_{AC}$. Layer spacing of

compounds with octyloxy chains tethered to the azulene core (**8O-AzCN-PhO8** and **8O-AzCN-PhO16**) shrank upon with decreasing temperature (Figure 38a,c). In contrast, d/d_{AC} of mesogens with longer chain lengths at the azulene passed through a minimum after the SmA-SmC transition and increased again upon cooling in the SmC phase which is typical for de Vries-like behavior. Maximum layer shrinkages lc_{max} are summarized in Table 2.
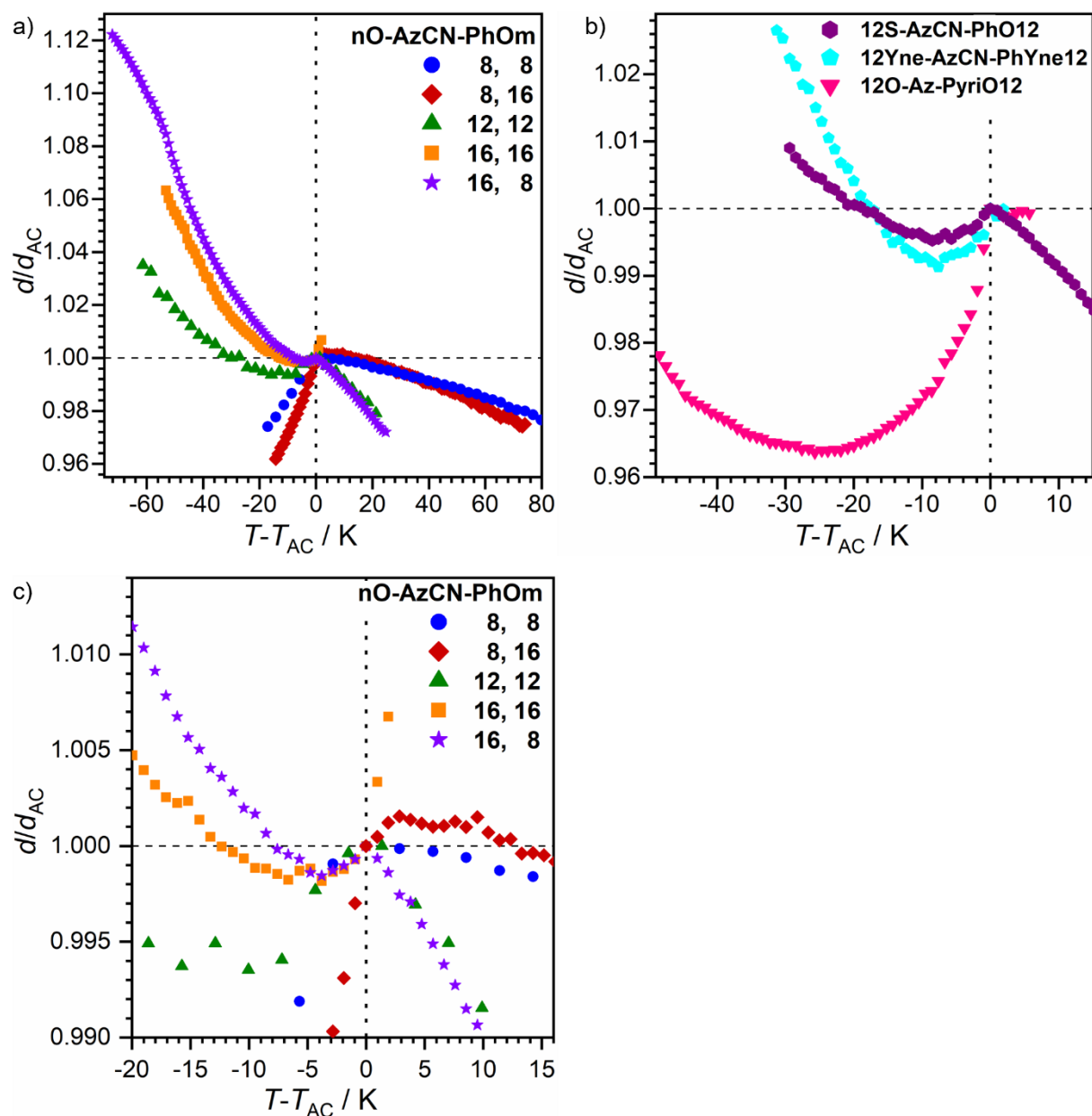
Figure 38: Plot of the relative layer spacing d/d_{AC} as a function of $T - T_{AC}$ for a) **nO-AzCN-PhOm** and b) other azulene compounds with a SmA-SmC phase sequence. c) zoom of a) close to the SmA-C transition. The figure was adapted from ref [4] and ref [5].

While **12O-AzCN-PhO12** had a moderate lc_{max} of 0.65 %, both compounds with C_{16} chain at the azulene possessed exceptionally low lc_{max} of 0.18 % for **16O-AzCN-PhO16** and 0.16 % for

16-AzCN-PhO8. Upon further cooling, d increases over the value of d_{AC} for all three compounds. When exchanging the ether chain with a thioether in **12S-AzCN-PhO12**, lc_{max} is reduced to 0.43 % and lc_{max} of alkyne derivative **12Yne-AzCN-PhYne12** was determined to 0.87 % (Figure 38b). Even though the layer spacing of pyrimidine derivative **12O-Az-PyriO12** without lateral substituent also passed through a minimum, lc_{max} was much higher with 3.63 %. As de Vries-like materials are often defined as $lc_{max} < 1$ %, **12O-Az-PyriO12** cannot not be regarded to be part of this group despite the non-classical behavior of d.

Table 2: Maximum layer contraction lc_{max} measured by XRD, tilt angles determined by POM and R-values of de Vries-like liquid crystals at $T - T_{AC} = -10$ K of the characterized compounds.

Compound	lc_{max} / %	Θ_{opt}/ °	R
12O-AzCN-PhO12	0.65	15	0.43
16O-AzCN-PhO16	0.18	24	0.14
16O-AzCN-PhO8	0.16	18	0.18
12S-AzCN-PhO12	0.48	16	0.35
12Yne-AzCN-PhYne12	0.87	13	0.58
12O-Az-PyriO12	3.63	21	0.74

Measuring the temperature dependent layer spacings revealed de Vries-like behavior. For closer understanding of the underlying cause, further measurements were performed. The reduction value R indicates the quality of de Vries-like materials. To calculate R according to equation (4), the optical tilt angle Θ_{opt} was measured (Figure 39). For better comparability, the tilt angles in **Table 2** are given at 10 K below the SmA-SmC transition. In the **nO-AzCN-PhOm** series, Θ_{opt} increased with increasing chain length on the azulene core (Figure 39a). **16O-AzCN-PhO16** and **16O-AzCN-PhO8** showed similar tilt angles close to the SmA-SmC transition. However, Θ_{opt} of **16O-AzCN-PhO8** passed through a maximum at $T - T_{AC} = -10$ K and shrank afterwards which can be seen as a harbinger for the SmA$_{re}$ phase. Substitution of the ether group from **12O-AzCN-PhO12** to a thioether in **12S-AzCN-PhO12** barely affected the tilt angle of the mesogens with $\Theta_{opt} = 15°$ and $\Theta_{opt} = 16°$, respectively (Figure 39b). For **12Yne-AzCN-PhYne12** a low Θ_{opt} of 13° was measured, while **12O-Az-PyriO12** exhibited the second highest value of the series with $\Theta_{opt} = 21°$ only topped by 24° of **16O-AzCN-PhO16**. After determination of Θ_{opt} and lc_{max}, R was calculated for the investigated series. **12O-Az-PyriO12** and **12Yne-AzCN-Yne12** showed R-values of 0.74 and 0.58, respectively and thus seemed to follow the rigid rod model than the diffuse cone model. **12O-AzCN-PhO12** and **12S-AzCN-PhO12** had moderate R-values of 0.43 and 0.35, with the

thioether derivative being the slightly better de Vries-like material. With $R = 0.14$, **16O-AzCN-PhO16** showed the best de Vries-like behavior, even surpassing **16O-AzCN-PhO8** ($R = 0.18$) due to the higher tilt angle Θ_{opt}.
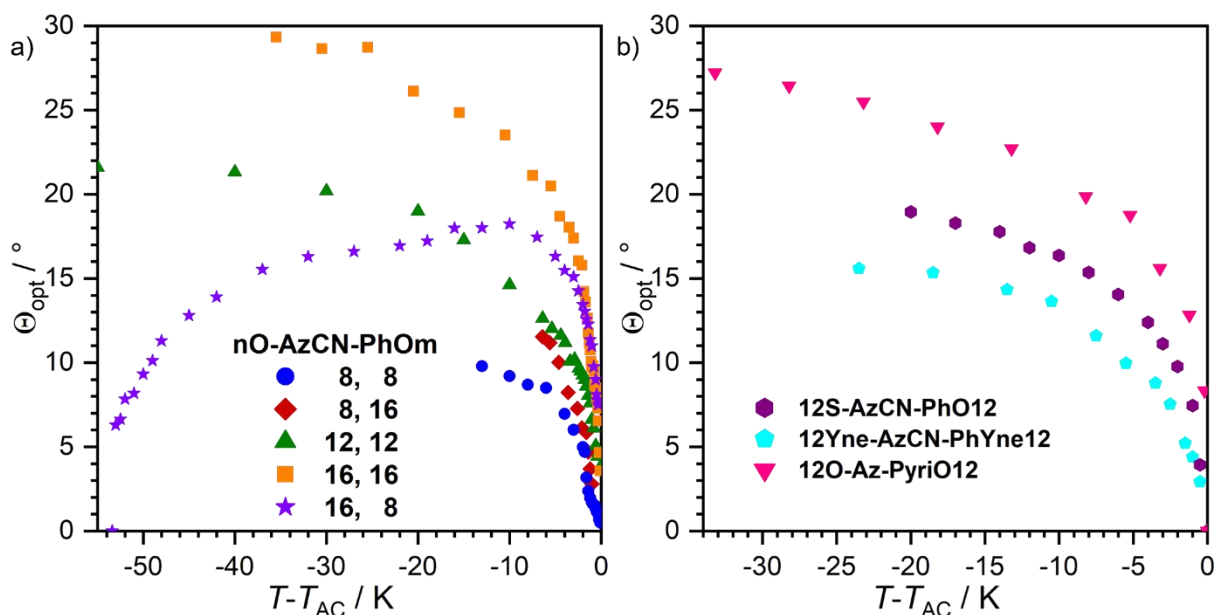

Figure 39: Optical tilt angle Θ_{opt} determined by POM. The figure was adapted from ref [4] and ref [5].

SmC phases following the rigid rod model exhibit higher layer shrinkages with higher tilt angles due to their geometry. It is worth mentioning that, except for **12O-Az-PyriO12**, lower lc_{max} are accompanied by higher Θ_{opt}. Θ_{opt} and lc_{max} both seem to be affected mainly by the length of the chain at the azulene moiety. While the long C_{16} chain causes the highest tilt angles and lowest layer shrinkages, the C_8 chain does not even show de Vries-like behavior and exhibits low tilt angle Θ_{opt}. When the alkynes in **12Yne-AzCN-PhYne12** are seen as part of the core, side chains would only be C_{10} and therefore explain the high R-value. The observations seem to be limited to azulenes with lateral substituents, since the unsubstituted derivative **12O-Az-PyriO12** has a large lc_{max} and high Θ_{opt}.

Low layer shrinkage of de Vries-like materials is often explained with a strong increase of the orientational order parameter S_2 that compensates for the layer shrinkage due to tilting of the molecules.[69] S_2 can be determined from oriented WAXS samples that are best prepared by very slow cooling from the isotropic liquid in a magnetic field. Unfortunately, due to proximity of the clearing temperature of the liquid crystals and the Curie-temperature of the magnet, magnetic alignment was not possible. Aligning without a magnetic field was tedious but the achieved orientation was partly lost during the experiments because of the fluidity of the

samples. Alternatively, the birefringence Δn in the **nO-AzCN-PhOm** series behaving proportional to S_2 was measured *via* the Phi-Viz (Figure 40a).

Δn mainly originates from the aromatic part of the molecule. Therefore, molecules with smaller side chains are expected to show higher Δn and the absolute value should not be regarded. The more important aspect is the behavior of Δn shortly after the SmA-SmC transition.[69] **8O-AzCN-PhO8** only showed a small increase of Δn upon entering the SmC phase. In contrast, Δn of **16O-AzCN-PhO16** increases strongly at the SmA-SmC transition. Both observations are in accordance with the theory that the layer shrinkage of the tilt is compensated for by increasing molecular order. However, **16O-AzCN-PhO8** only had a moderate increase of Δn at the phase transition and **8O-AzCN-PhO16** showed a huge increase of Δn but did not behave de Vries-like. While an increasing Δn and thus S_2 might contribute to the de Vries-like behavior it cannot be the only factor in the present system.
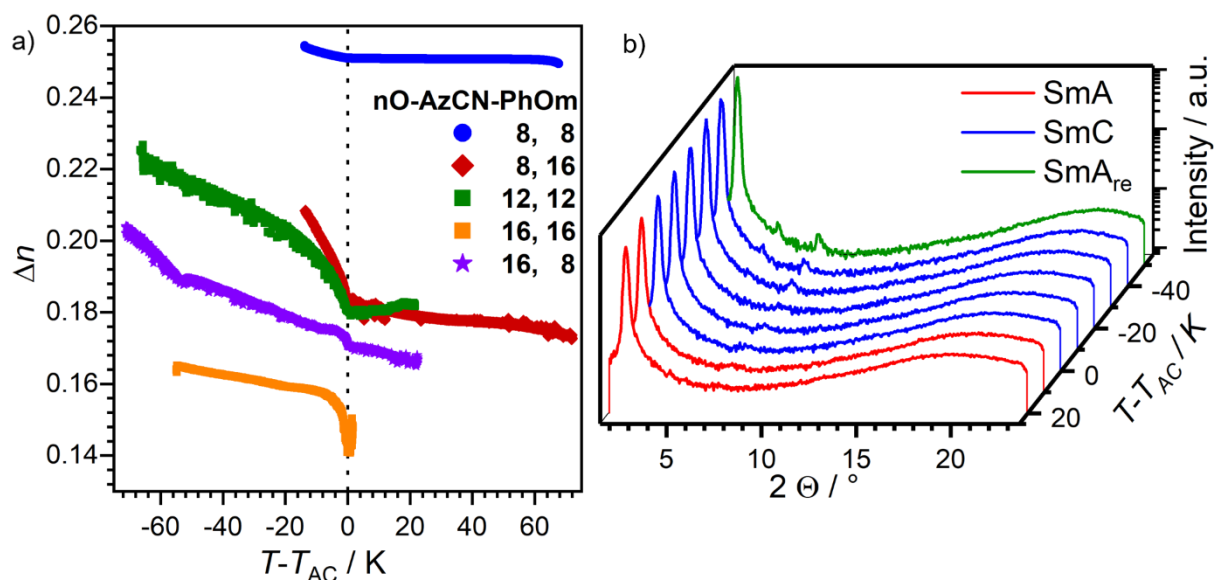

Figure 40: a)Temperature dependence of birefringence Δn for compounds **nO-AzCN-PhOm** and b) temperature dependent WAXS measurements of **16O-AzCN-PhO8**. The figure was adapted from ref [4].

Another aspect might be found when closely examining the SmA$_{re}$ phase of **16O-AzCN-PhO8**. To ensure that the mesophase is really a SmA phase and not a higher order orthogonal phase, temperature dependent WAXS measurements were performed (Figure 40b). The absence of any sharp reflexes in the wide angle region ruled out the presence of a SmB or SmE phase.

Re-entrant behavior is often caused by frustration between different effects. Orthogonal re-entrant phases following a SmC phase are only known for bent-mesogenic dimers and chiral rod-like molecules.[124,125] A SmA*-SmC*-SmA* phase sequence was reported by Novotna *et*

al. for **9ZBL** (Figure 41).[126,127] They argued that upon cooling quadrupolar ordering increased. Steric repulsion of the lateral chloro substituent prevented close packing of the core. The system avoids the steric hindrance by a shift of mass centers which increases the layer spacing. In the case of **16O-AzCN-PhO8**, the cyano group takes over the role of the chloro substituent (Figure 42). Analogous to Novotna, the quadrupolar ordering increases upon cooling and the molecules try to stack closer which is prevented by the steric repulsion of the nitrile groups. Shifting of the mass centers lowers the steric interactions between the cyano groups and thus allows closer stacking. Simultaneously, the side chains slowly approach the *all-trans* configuration. The resulting stacking mode seems to prefer an SmA phase over the SmC phase and thus a re-entrant phase appears. In **16O-AzCN-PhO8** the shift of mass centers partially compensates for the different length of the chains. This might be the reason why the SmA$_{re}$ phase is only observed for the derivative with long chains at the azulene and short chains at the phenyl ring.
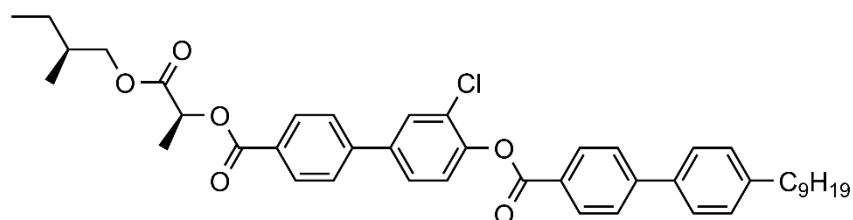
9ZBL

I 175 BP 174 N* 160 TGBA 158 SmA* 96 SmC* 58 SmAre* 31 Cr

Figure 41: Molecular structure of **9ZBL** that also exhibits a SmA$_{re}$ phase.[126,127]

The described shift of mass centers not only caused the re-entrant phase in **16O-AzCN-PhO8** but also contributed to the compensation of the tilt caused layer shrinkage in our de Vries materials. It therefore seems to be the cornerstone for the observed de Vries-like behavior. Upon reversion, the high lc$_{max}$ of **12O-Az-PyriO12** can be explained. Because there is no lateral substituent in **12O-Az-PyriO12** , the system does not need to shift mass centers and the layer spacing shrinks, preventing de Vries behavior.

Drawing a close analogy between the re-entrant phases of **9ZBL** and **16O-AzCN-PhO8** explained not only the anomalous phase behavior but also showed another reason for de Vries-like behavior of the investigated mesogens. Multiple factors have been identified the cause de Vries-like behavior: The strong influence of the chain lengths on *d* indicated an active part of the side chains as already described by Novotna[126] and Merkel.[128] Furthermore, it was shown that Δ*n* and thus orientational order increased at the SmA-SmC transition which is

beneficial for de Vries-like behavior.[79] Both aspects are known in literature and are complemented by the described, novel shift of mass centers.

Normally, nanosegregating head groups are necessary for high-performance de Vries-like materials. In the described system, the zwitterionic azulene moiety acts as a nanosegregating core and thus replaces the usual head groups. Even though the color of azulene derivatives will impede the application in non-monochromic displays, the system is useful to closely understand re-entrant and de Vries-like behavior.

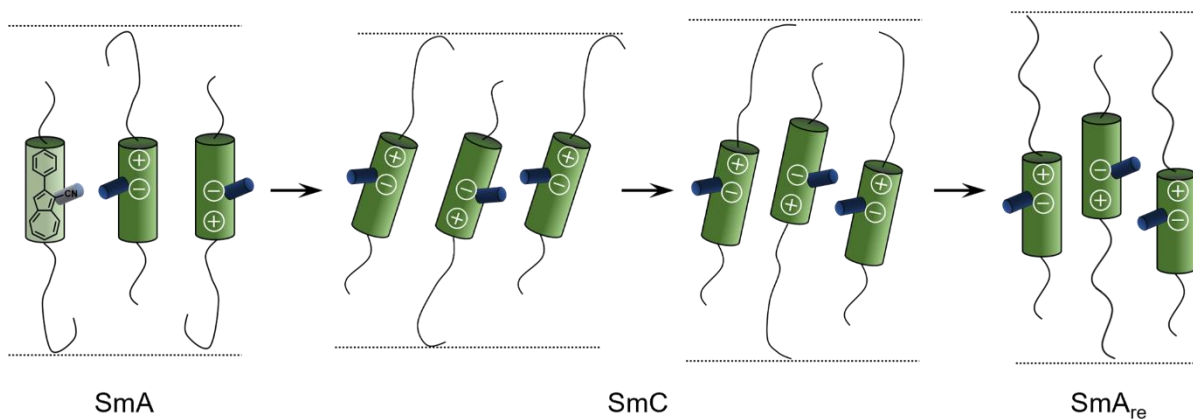
Figure 42: Proposed mechanism for the formation of the SmA_{re} phase of **16O-AzCN-PhO8** due to a shift of mass centers based on a model by Novotná et al. ref [126]. The figure was reproduced with permission from ref [4].

5 Summary

Due to its inherent dipole moment and unique electronic character, the azulene moiety is often tried in optoelectronic applications. The aim of this work was the understanding of the structure-property relationship of novel calamitic azulenes towards their liquid crystalline properties. Mesomorphic compounds would combine the unique properties of azulene with the self-aligning nature of liquid crystals and should be investigated regarding potential applications. For this purpose, a divergent synthesis route was designed starting from the literature known dibromoazulene **Br-Az-Br** (Figure 43). Two different blueprints have been pursued. On the one hand, calamitic azulenes with one side chain were prepared. The π-system of the target molecules **12O-Az-Thi** was extended at the 5-membered ring with thiophene-based heteroaromatics. On the other hand, azulene derivatives **R^1-AzX-(Het)ArR^2** with two side chains, a lateral substituent X, and an incorporated (hetero)aryl moiety were synthesized. The three-step synthesis allowed for an easy combination of the three parameters and yielded a compound library with 22 derivatives.
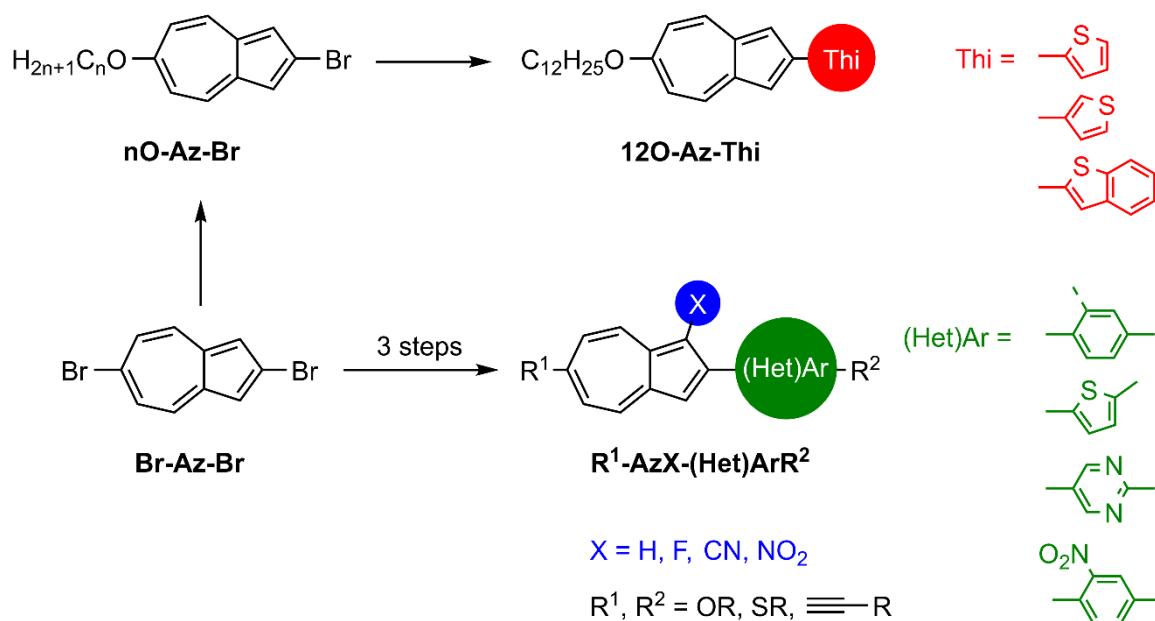
Figure 43: Divergent synthesis route for azulene based target molecules starting from **Br-Az-Br**.

All compounds were investigated for their potential mesomorphic properties by POM, DSC and XRD. Azulenes with one side chain formed the soft-crystalline SmE phase. Not only the target compounds **12O-Az-Thi**, but also the precursor **nO-Az-Br** showed mesomorphic properties despite the small size of the aromatic core (Figure 44). The surprising mesomorphic properties were explained by additional Coulomb interactions originated from the zwitterionic

resonance structure and the small spheroid caused by the rotating azulene moiety compared to other mesogenic cores.

Figure 44: a) Molecular structure of azulene compounds with one side chain and b) corresponding mesophase widths during cooling.
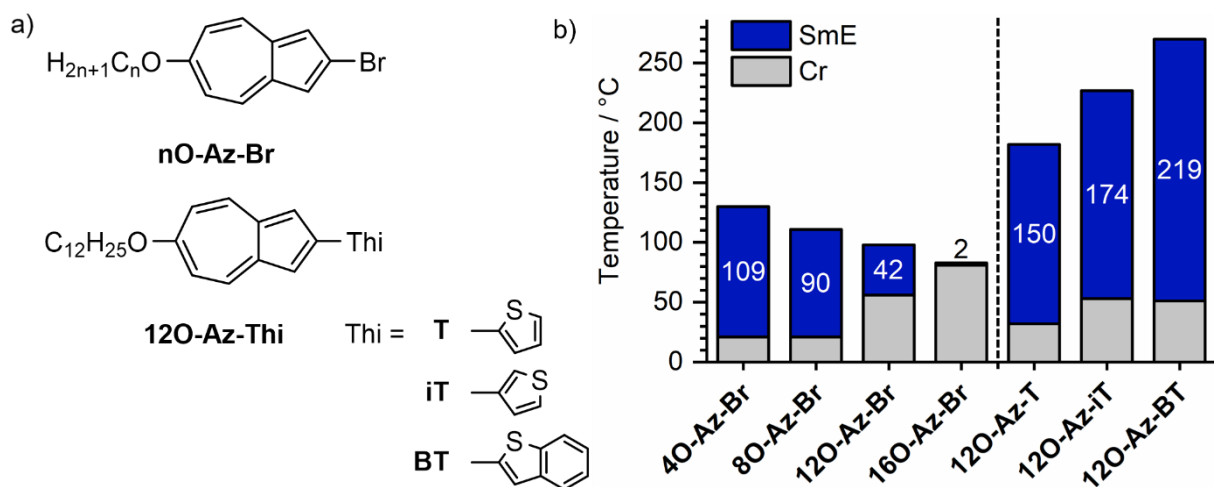
Azulene thiophene hybrids were used for the spin-coating of uniform thin films at mesophase temperature, exploiting the self-aligning behavior of the SmE phase. The polycrystalline thin films were investigated by optical microscopy, AFM, CLSM, as well as in-plane and out-of-plane XRD to guarantee the uniform alignment. Based on the thin films, top contact bottom gate OFETs were manufactured with hole carrier mobilities of up to $\mu^+ = (3.1 \pm 0.5) \cdot 10^{-3} \text{cm}^2\text{V}^{-1}\text{s}^{-1}$ for **12O-Az-BT**. The low deviation reflects the homogeneity of the alignment due to the templating effect of the mesophase. Subsequent thermal annealing changed the monolayer crystal structure of **12O-Az-BT** into a bilayer crystal structure. In contrast to cases in the literature, the transformation did not boost OFET characteristics. It was argued that the repulsion of partial charges with same sign prevented close π-π stacking.

Azulene mesogens with two side chains and a lateral substituent formed fluid smectic phases. The series of **nO-AzCN-PhOm** showed SmA-SmC phase sequences and was studied in detail (Figure 45a,b). Long chain lengths (n = 12,16) at the azulene led to de Vries-like properties while short chains (n = 8) followed the rigid rod model and exhibited monotropic SmC phases. The exceptionally low lc_{max} of **16-AzCN-PhO16** (0.18 %) and **16O-AzCN-PhO8** (0.16 %) were the reason for very low *R*-values of 0.14 and 0.18, respectively. De Vries-like behavior was explained by interaction of increasing order within the layers, elongating side chains and shift of mass centers to avoid the steric repulsion of the lateral cyano group upon cooling. In the case of **16O-AzCN-PhO8**, the shift induced a SmA_{re} phase below the SmC phase. By

closely studying the present system, deeper insights into the origin of de Vries-like and re-entrant behavior were gained.
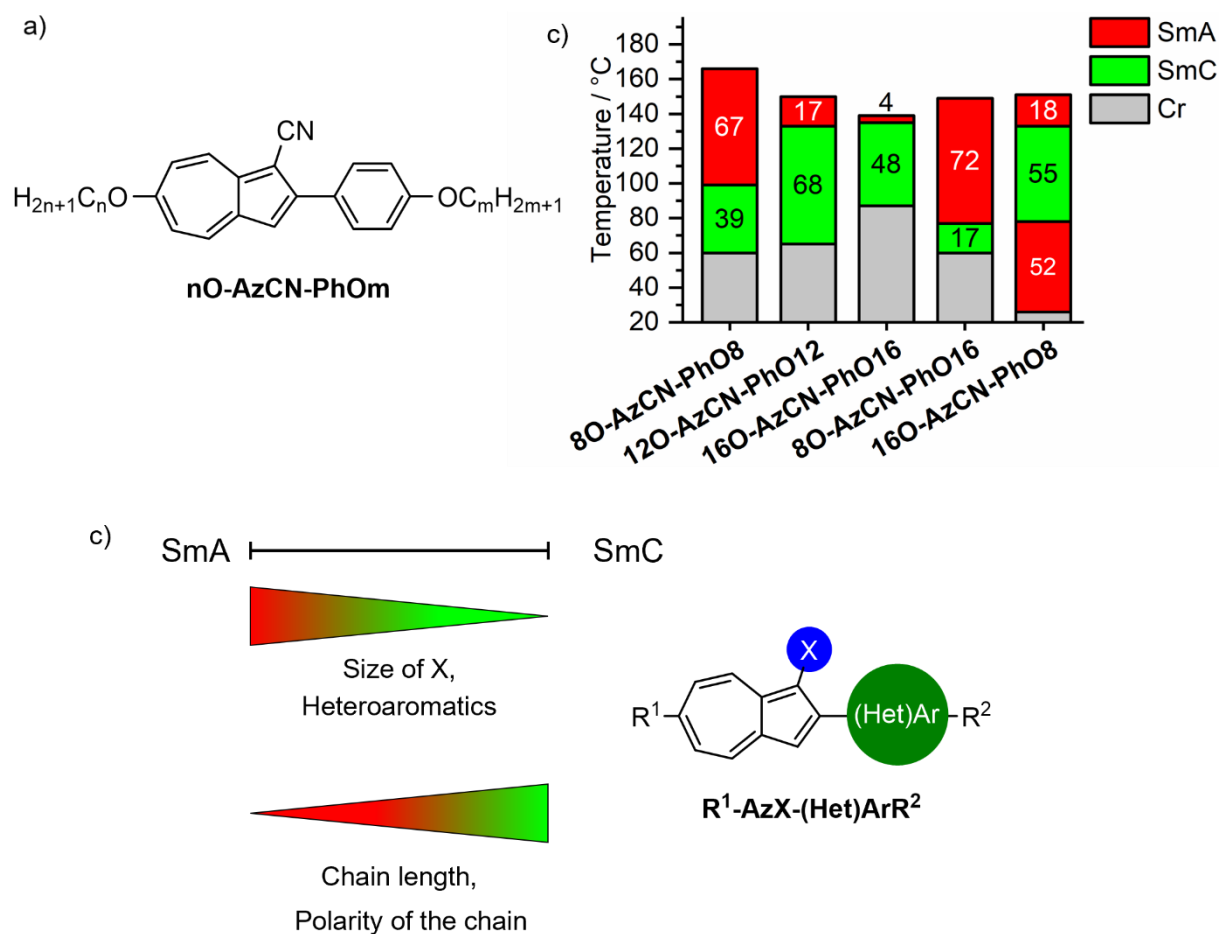

Figure 45: a) Molecular structure of the **nO-AzCN-PhOm** series and b) corresponding mesophase widths during cooling. c) Trends observed in the mesogenic system of **R^1-AzX-(Het)ArR^2** upon systematic variation of the parameters.

The phase geometry changed between SmA and SmC upon variation of the lateral substituent, the chain linkage or the (hetero)aryl moiety (Figure 45c). Smaller, less polar lateral substituents like a fluorine preferred the SmC phase, while larger, highly polar units e.g., a nitro group, formed SmA phases. When moving the lateral group away from the molecule center, only the SmC phase appeared. The heteroaromatic moieties thiophene and pyrimidine, as well as thioether chains destabilized the SmC phase and mostly the SmA phase occurred. Alkyne chains reduced the phase transition temperatures. The different trends can be summarized that whenever the azulene moiety is allowed to stack without hindrance, a SmC phase is preferred. Once the stacking is influenced by large substituents or heteroaromatic moieties, SmA phases become more prominent. Understanding of the preference in the phase geometry might help to

closely control the molecular orientation which is a crucial task during the preparation of organic optoelectronic devices. The herein described trends might also be applied to mesogens beyond the azulene system and will help to predict and understand occurring phase geometries.

In this work, a compound library of calamitic azulenes was constructed that was used to gain deep understanding in the structure-property relationship of mesomorphic azulene compounds with one and two chains. Furthermore, azulenes with SmE phases were used for thin film preparation and implemented in OFETs. Azulenes with two side chains turned out to be potent de Vries-like materials and one derivative showed a rare SmA$_{re}$ phase.

6 References

[1]   F. Schulz, P. Ehni, B. Wank, A. Bauer, W. Frey, S. Laschat, *Liq. Cryst.* **2021**, *48*, 832–843.

[2]   F. Schulz, M. Deimling, S. Laschat, *Liq. Cryst.* **2021**, *48*, 1575–1580.

[3]   F. Schulz, S. Takamaru, T. Bens, J. Hanna, B. Sarkar, S. Laschat, H. Iino, *Phys. Chem. Chem. Phys.* **2022**, *24*, 23481–23489.

[4]   F. Schulz, B. Wank, P. Nacke, W. Frey, S. Laschat, *Mater. Adv.* **2023**, *4*, 1306–1313.

[5]   F. Schulz, B. Lutz, D. Rück, D. Batman, W. Frey, S. Laschat, *Soft Matter* **2023**, *13*, 2397–2406.

[6]   E. Steinegger, R. Hänsel, in *Lehrb. Allg. Pharmakogn.* (Eds.: E. Steinegger, R. Hänsel), Springer, Berlin, Heidelberg, **1963**, pp. 399–479.

[7]   https://pixabay.com/de/photos/kamille-blumen-pflanze-wei%C3%9Fe-blumen-3489847/, 25.01.2023; 13:54.

[8]   S. Piesse, *Chem. News* **1863**, 245.

[9]   A. E. Sherndal, *J. Am. Chem. Soc.* **1915**, *37*, 167–171.

[10]   A. S. Pfau, P. Plattner, *Helv. Chim. Acta* **1936**, *19*, 858–879.

[11]   F. Vögtle, F. Alfter, *Reizvolle Moleküle der organischen Chemie*, Teubner, Stuttgart, **1989**.

[12]   R. S. H. Liu, *J. Chem. Educ.* **2002**, *79*, 183.

[13]   A. G. Anderson, B. M. Steckler, *J. Am. Chem. Soc.* **1959**, *81*, 4941–4946.

[14]   H. Nakamura, M. Sekido, Y. Yamamoto, *J. Med. Chem.* **1997**, *40*, 2825–2830.

[15]   T. Tomiyama, M. Yokota, S. Wakabayashi, K. Kosakai, T. Yanagisawa, *J. Med. Chem.* **1993**, *36*, 791–800.

[16]   A. E. Asato, A. Peng, M. Z. Hossain, T. Mirzadegan, J. S. Bertram, *J. Med. Chem.* **1993**, *36*, 3137–3147.

[17]   J. Zhang, S. Petoud, *Chem. Eur. J.* **2008**, *14*, 1264–1272.

[18]   Y. Zhou, Y. Zhuang, X. Li, H. Ågren, L. Yu, J. Ding, L. Zhu, *Chem. Eur. J.* **2017**, *23*, 7642–7647.

[19]   E. Puodziukynaite, H.-W. Wang, J. Lawrence, A. J. Wise, T. P. Russell, M. D. Barnes, T. Emrick, *J. Am. Chem. Soc.* **2014**, *136*, 11043–11049.

[20]   H. Xin, C. Ge, X. Jiao, X. Yang, K. Rundel, C. R. McNeill, X. Gao, *Angew. Chem. Int. Ed.* **2018**, *57*, 1322–1326.

[21]   H. Xin, C. Ge, X. Jiao, X. Yang, K. Rundel, C. R. McNeill, X. Gao, *Angew. Chem.* **2018**, *130*, 1336–1340.

[22]   F. Schwarz, M. Koch, G. Kastlunger, H. Berke, R. Stadler, K. Venkatesan, E. Lörtscher, *Angew. Chem. Int. Ed.* **2016**, *55*, 11781–11786.

[23]   F. Schwarz, M. Koch, G. Kastlunger, H. Berke, R. Stadler, K. Venkatesan, E. Lörtscher, *Angew. Chem.* **2016**, *128*, 11956–11961.

[24]   T. Tsuchiya, R. Umemura, M. Kaminaga, S. Kushida, K. Ohkubo, S.-I. Noro, Y. Mazaki, *ChemPlusChem* **2019**, *84*, 655–664.

[25]   Q. Fan, D. Martin-Jimenez, D. Ebeling, C. K. Krug, L. Brechmann, C. Kohlmeyer, G. Hilt, W. Hieringer, A. Schirmeisen, J. M. Gottfried, *J. Am. Chem. Soc.* **2019**, *141*, 17713–17720.

[26]   Z. Chen, J. Droste, G. Zhai, J. Zhu, J. Yang, M. R. Hansen, X. Zhuang, *Chem. Commun.* **2019**, *55*, 9047–9050.

[27]   H. Xin, X. Gao, *ChemPlusChem* **2017**, *82*, 945–956.

[28]   C. Duan, J. Zhang, S. Cai, J. Xiang, X. Yang, X. Gao, *Eur. J. Org. Chem.* **2023**, DOI 10.1002/ejoc.202201347.

[29]   Z. Zhao, M. E. El-Khouly, Q. Che, F. Sun, B. Zhang, H. He, Y. Chen, *Angew. Chem. Int. Ed.* **2023**, DOI 10.1002/anie.202217249.

[30]   P. Mathey, F. Lirette, I. Fernández, L. Renn, T. Weitz, J.-F. Morin, *Angew. Chem. Int. Ed.* **2023**, anie.202216281.

[31]   Y. Yamaguchi, K. Ogawa, K. Nakayama, Y. Ohba, H. Katagiri, *J. Am. Chem. Soc.* **2013**, *135*, 19095–19098.

[32]   Y. Yamaguchi, M. Takubo, K. Ogawa, K. Nakayama, T. Koganezawa, H. Katagiri, *J. Am. Chem. Soc.* **2016**, *138*, 11335–11343.

[33]   Y. Yamaguchi, Y. Maruya, H. Katagiri, K. Nakayama, Y. Ohba, *Org. Lett.* **2012**, *14*, 2316–2319.

[34]   X.-H. Zhang, C. Li, W.-B. Wang, X.-X. Cheng, X.-S. Wang, B.-W. Zhang, *J. Mater. Chem.* **2007**, *17*, 642–649.

[35]   T. Umeyama, Y. Watanabe, T. Miyata, H. Imahori, *Chem. Lett.* **2015**, *44*, 47–49.

[36]   K. Hafner, *Angew. Chem.* **1958**, *70*, 419–430.

[37]   K. Ziegler, K. Hafner, *Angew. Chem.* **1955**, *67*, 301–301.

[38]   K. Hafner, *Justus Liebigs Ann. Chem.* **1957**, *606*, 79–89.

[39]   K. Hafner, H. Kaiser, *Org. Synth.* **1964**, *44*, 94.

[40]   T. Nozoe, K. Takase, N. Shimazaki, *Bull. Chem. Soc. Jpn.* **1964**, *37*, 1644–1648.

[41] T. Nozoe, S. Seto, S. Matsumura, Y. Murase, *Bull. Chem. Soc. Jpn.* **1962**, *35*, 1179–1188.

[42] H. Langhals, M. Eberspächer, *Synthesis* **2018**, *50*, 1862–1866.

[43] T. Shoji, S. Ito, M. Yasunami, *Int. J. Mol. Sci.* **2021**, *22*, 10686.

[44] S. Kramer, Y. Odabachian, J. Overgaard, M. Rottländer, F. Gagosz, T. Skrydstrup, *Angew. Chem. Int. Ed.* **2011**, *50*, 5090–5094.

[45] V. Claus, M. Schukin, S. Harrer, M. Rudolph, F. Rominger, A. M. Asiri, J. Xie, A. S. K. Hashmi, *Angew. Chem. Int. Ed.* **2018**, *57*, 12966–12970.

[46] F. Reinitzer, *Monatsh. Chem.* **1888**, *9*, 421–441.

[47] G. W. Gray, in *Handb. Liq. Cryst. Set*, John Wiley & Sons, Ltd, **1998**, pp. 1–16.

[48] J. W. Goodby, R. J. Mandle, E. J. Davis, T. Zong, S. J. Cowling, *Liq. Cryst.* **2015**, *42*, 593–622.

[49] T. Adachi, H. Saitoh, Y. Yamamura, M. Hishida, M. Ueda, S. Ito, K. Saito, *Bull. Chem. Soc. Jpn.* **2013**, *86*, 1022–1027.

[50] N. Shioya, M. Yoshida, M. Fujii, T. Shimoaka, R. Miura, S. Maruyama, T. Hasegawa, *J. Phys. Chem. Lett.* **2022**, *13*, 11918–11924.

[51] I. Dierking, *Textures of Liquid Crystals*, John Wiley & Sons, **2006**.

[52] J. W. Goodby, in *Handb. Liq. Cryst.* (Eds.: J.W. Goodby, C. Tschierske, P. Raynes, H. Gleeson, T. Kato, P.J. Collings), Wiley-VCH Verlag GmbH & Co. KGaA, Weinheim, Germany, **2014**, pp. 1–18.

[53] D. M. Agra-Kooijman, S. Kumar, in *Handb. Liq. Cryst.* (Eds.: J.W. Goodby, C. Tschierske, P. Raynes, H. Gleeson, T. Kato, P.J. Collings), Wiley-VCH Verlag GmbH & Co. KGaA, Weinheim, Germany, **2014**, pp. 1–38.

[54] H. Ma, H.-L. Yip, F. Huang, A. K.-Y. Jen, *Adv. Funct. Mater.* **2010**, *20*, 1371–1388.

[55] S. F. Nelson, Y.-Y. Lin, D. J. Gundlach, T. N. Jackson, *Appl. Phys. Lett.* **1998**, *72*, 1854–1856.

[56] H. Ebata, T. Izawa, E. Miyazaki, K. Takimiya, M. Ikeda, H. Kuwabara, T. Yui, *J. Am. Chem. Soc.* **2007**, *129*, 15732–15733.

[57] C. D. Sheraw, T. N. Jackson, D. L. Eaton, J. E. Anthony, *Adv. Mater.* **2003**, *15*, 2009–2011.

[58] H. Iino, J. Hanna, *Polym. J.* **2017**, *49*, 23–30.

[59] H. Iino, T. Usui, J. Hanna, *Nat. Commun.* **2015**, *6*, 6828.

[60] G. Horowitz, *Adv. Mater.* **1998**, *10*, 365–377.

[61] C. Sheppard, D. Shotton, *Confocal Laser Scanning Microscopy*, BIOS Scientific Publishers In Association With The Royal Microscopical Society, Oxford, **1997**.

[62] G. Binnig, C. F. Quate, Ch. Gerber, *Phys. Rev. Lett.* **1986**, *56*, 930–933.

[63] F. Ohnesorge, G. Binnig, *Science* **1993**, *260*, 1451–1456.

[64] S. Kobayashi, *The Rigaku Journal* **2010**, *26*, 1–11.

[65] K. Inaba, S. Kobayashi, K. Uehara, A. Okada, S. L. Reddy, T. Endo, *Adv. Mater. Phys. Chem.* **2013**, *3*, 72–89.

[66] T. Mitsunaga, *The Rigaku Journal* **2009**, *25*, 7–12.

[67] W. Kuczyński, H. Stegemeyer, *Chem. Phys. Lett.* **1980**, *70*, 123–126.

[68] N. A. Clark, S. T. Lagerwall, *Appl. Phys. Lett.* **1980**, *36*, 899–901.

[69] J. P. F. Lagerwall, F. Giesselmann, *ChemPhysChem* **2006**, *7*, 20–45.

[70] K. Bader, *Dissertation*, Stuttgart, **2019**.

[71] A. de Vries, *J. Chem. Phys.* **1979**, *71*, 25–31.

[72] P. Rudquist, M. A. Osipov, F. Giesselmann, *Liq. Cryst.* **2018**, *45*, 2097–2108.

[73] M. D. Radcliffe, M. L. Brostrom, K. A. Epstein, A. G. Rappaport, B. N. Thomas, R. Shao, N. A. Clark, *Liq. Cryst.* **1999**, *26*, 789–794.

[74] J. C. Roberts, N. Kapernaum, F. Giesselmann, R. P. Lemieux, *J. Am. Chem. Soc.* **2008**, *130*, 13842–13843.

[75] C. P. J. Schubert, C. Müller, A. Bogner, F. Giesselmann, R. P. Lemieux, *Soft Matter* **2017**, *13*, 3307–3313.

[76] J. P. F. Lagerwall, F. Giesselmann, M. D. Radcliffe, *Phys. Rev. E* **2002**, *66*, 031703.

[77] K. Bader, C. Müller, Y. Molard, A. Baro, P. Ehni, J. Knelles, S. Laschat, *RSC Adv* **2020**, *10*, 23999–24016.

[78] N. Kapernaum, F. Giesselmann, *Phys. Rev. E* **2008**, *78*, 062701.

[79] Z. Ahmed, C. Müller, J. J. Johnston, K. Nguyen, C. P. J. Schubert, K. Abitaev, S. Marino, F. Giesselmann, R. P. Lemieux, *Liq. Cryst.* **2019**, *46*, 896–904.

[80] F. Jenz, M. A. Osipov, S. Jagiella, F. Giesselmann, *J. Chem. Phys.* **2016**, *145*, 134901.

[81] P. Davidson, D. Petermann, A. M. Levelut, *J. Phys. II* **1995**, *5*, 113–131.

[82] C. Müller, Dissertation, Universität Stuttgart, **2019**.

[83] K. Praefcke, *Z Naturforsch* **1981**, *36 b*, 375–378.

[84] S. E. Estdale, R. Brettle, D. A. Dunmur, C. M. Marson, *J. Mater. Chem.* **1997**, *7*, 391–401.

[85] S. Ito, H. Inabe, N. Morita, K. Ohta, T. Kitamura, K. Imafuku, *J. Am. Chem. Soc.* **2003**, *125*, 1669–1680.

References

[86] S. Ito, M. Ando, A. Nomura, N. Morita, C. Kabuto, H. Mukai, K. Ohta, J. Kawakami, A. Yoshizawa, A. Tajiri, *J. Org. Chem.* **2005**, *70*, 3939–3949.

[87] K. Nakagawa, T. Yokoyama, K. Toyota, N. Morita, S. Ito, S. Tahata, M. Ueda, J. Kawakami, M. Yokoyama, Y. Kanai, K. Ohta, *Tetrahedron* **2010**, *66*, 8304–8312.

[88] S. Ito, M. Ueda, R. Sekiguchi, J. Kawakami, *Tetrahedron* **2013**, *69*, 4259–4269.

[89] E. de Domingo, M. Barcenilla, J. M. Martín-Alvarez, J. A. Miguel, S. Coco, *Dyes Pigments* **2020**, *176*, 108195.

[90] J. Heinze, *Angew. Chem.* **1984**, *96*, 823–840.

[91] A. M. Bond, R. G. Compton, D. A. Fiedler, F. Scholz, *Electroanalytical Methods: Guide to Experiments and Applications*, Springer Berlin / Heidelberg, Berlin, Heidelberg, **2013**.

[92] J. C. Haenle, *Dissertation*, Stuttgart, **2017**.

[93] Y. Huang, T. Hayashi, *Chem. Rev.* **2022**, *122*, 14346–14404.

[94] M. Nagamoto, T. Nishimura, *ACS Catal.* **2017**, *7*, 833–847.

[95] S. Helbig, S. Sauer, N. Cramer, S. Laschat, A. Baro, W. Frey, *Adv. Synth. Catal.* **2007**, *349*, 2331–2337.

[96] S. Helbig, K. V. Axenov, S. Tussetschläger, W. Frey, S. Laschat, *Tetrahedron Lett.* **2012**, *53*, 3506–3509.

[97] T. Mühlhäuser, A. Savin, W. Frey, A. Baro, A. J. Schneider, H.-G. Döteberg, F. Bauer, A. Köhn, S. Laschat, *J. Org. Chem.* **2017**, *82*, 13468–13480.

[98] Z.-Q. Wang, C.-G. Feng, M.-H. Xu, G.-Q. Lin, *J. Am. Chem. Soc.* **2007**, *129*, 5336–5337.

[99] M. Deimling, M. Kirchhof, B. Schwager, Y. Qawasmi, A. Savin, T. Mühlhäuser, W. Frey, B. Claasen, A. Baro, T. Sottmann, S. Laschat, *Chem. Eur. J.* **2019**, *25*, 9464–9476.

[100] M. Deimling, S. R. Kousik, K. Abitaev, W. Frey, T. Sottmann, K. Koynov, S. Laschat, P. Atanasova, *ChemCatChem* **2021**, *13*, 2242–2252.

[101] H. Xin, B. Hou, X. Gao, *Acc. Chem. Res.* **2021**, *54*, 1737–1753.

[102] For the few reported examples see ref [83, 84, 86, 89]

[103] R. Brettle, D. A. Dunmur, S. Estdale, C. M. Marson, *J. Mater. Chem.* **1993**, *3*, 327–331.

[104] T. Nozoe, T. Asao, M. Oda, *Bull. Chem. Soc. Jpn.* **1974**, *47*, 681–686.

[105] E. v Dehmlow, D. Balschukat, *Chem. Ber.* **1985**, *118*, 3805–3816.

[106] F. Schulz, *Master Thesis*, Stuttgart, **2018**.

[107] T. Kinzel, Y. Zhang, S. L. Buchwald, *J. Am. Chem. Soc.* **2010**, *132*, 14073–14075.

[108] D. Rück, *Bachelor Thesis*, Stuttgart, **2021**.

[109] D. Batman, *Research Internship*, Stuttgart, **2023**.

[110] J. W. Goodby, in *Handb. Liq. Cryst.*, John Wiley & Sons, Ltd, **2014**, pp. 1–39.

[111] K. W. Rosenmund, E. Struck, *Berichte Dtsch. Chem. Ges. B Ser.* **1919**, *52*, 1749–1756.

[112] J. Zanon, A. Klapars, S. L. Buchwald, *J. Am. Chem. Soc.* **2003**, *125*, 2890–2891.

[113] S. Ushijima, H. Togo, *Synlett* **2010**, 1067–1070.

[114] B. Wank, *Bachelor Thesis*, Stuttgart, **2020**.

[115] R. S. Muthyala, R. S. H. Liu, *J. Fluor. Chem.* **1998**, *89*, 173–175.

[116] H. Xin, J. Li, R.-Q. Lu, X. Gao, T. M. Swager, *J. Am. Chem. Soc.* **2020**, *142*, 13598–13605.

[117] B. Lutz, *Bachelor Thesis*, Stuttgart, **2021**.

[118] U. H. Lauk, P. Skrabal, H. Zollinger, *Helv. Chim. Acta* **1985**, *68*, 1406–1426.

[119] A. J. Leadbetter, J. C. Frost, J. P. Gaughan, G. W. Gray, A. Mosley, *J. Phys.* **1979**, *40*, 375–380.

[120] S. Sandhu, R. Kumar, P. Singh, S. Kumar, *J. Mater. Chem. C* **2016**, *4*, 3209–3216.

[121] H. Wu, H. Iino, J. Hanna, *ACS Appl. Mater. Interfaces* **2020**, *12*, 29497–29504.

[122] C.-W. Chu, S.-H. Li, C.-W. Chen, V. Shrotriya, Y. Yang, *Appl. Phys. Lett.* **2005**, *87*, 193508.

[123] R. H. Hertwig, W. Koch, *Chem. Phys. Lett.* **1997**, *268*, 345–351.

[124] W. Weissflog, Ch. Lischka, S. Diele, I. Wirth, G. Pelzl, *Liq. Cryst.* **2000**, *27*, 43–50.

[125] C. Tschierske, *Liq. Cryst.* **2022**, *49*, 1043–1077.

[126] V. Novotná, V. Hamplová, N. Podoliak, M. Kašpar, M. Glogarová, D. Pociecha, E. Gorecka, *J. Mater. Chem.* **2011**, *21*, 14807.

[127] V. Novotná, M. Glogarová, M. Kašpar, V. Hamplová, E. Gorecka, D. Pociecha, M. Cepic, *Phys. Rev. E* **2011**, *83*, 020701.

[128] K. Merkel, A. Kocot, J. K. Vij, P. J. Stevenson, A. Panov, D. Rodriguez, *Appl. Phys. Lett.* **2016**, *108*, 243301.

Paper I

Taylor & Francis
Taylor & Francis Group

Check for updates

Alkoxy-bromo-azulenes displaying ambient temperature smectic E-phases

Finn Schulz, Philipp Ehni, Bianca Wank, Alina Bauer, Wolfgang Frey and Sabine Laschat

Institut für Organische Chemie, Universität Stuttgart, Stuttgart, Germany

ABSTRACT

Azulenes and crystal-smectic E-phases (SmE) both have recently raised attention for the design of novel organic devices. However, the combination of self-assembly into soft-crystalline mesophases with the unique electronic properties of azulene derivatives has not been probed yet. Therefore, a convenient synthesis of 6-alkoxy-2-bromoazulenes, forming ambient temperature SmE-phases, was developed. Differential scanning calorimetry, polarising optical microscopy and X-ray diffraction provided insight into the self-assembly of the liquid crystalline phase. Comparison of experimental data and quantum chemical calculations of 6-alkoxy-2-bromoazulene with the 'inverted' 2-alkoxy-6-bromoazulene revealed large differences in polarity, which affected optical and mesomorphic properties, and provided insight into structure–property relationships enabling the design of novel thin-film devices.
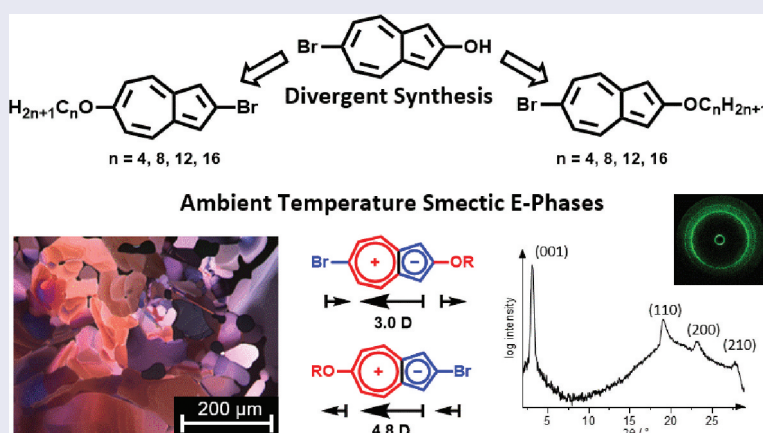
Introduction

Azulene **1** has been fascinating many scientists due to its uncommon properties and its beautiful blue colour (Scheme 1a), which make azulene derivatives highly useful for optoelectronic materials [1–4]. The surprisingly high dipole moment of 1.08 D for the parent unsubstituted hydrocarbon **1** can be explained by a zwitterionic resonance structure **1z** [5], where both rings fulfil the Hückel rule. Besides a variety of applications in medicinal and analytical chemistry [6–10], azulene derivatives were reported to be potent candidates for NIR emitters [11,12], electrochromic materials and organic electronics [13–16]. For example, recently Gottfried synthesised azulene-based ribbons as graphene-like conductor [17]. Zhuang disclosed an azulene containing polymer as a new building block for cathodes in Li-S batteries [18]. For organic

electronics, a proper alignment and uniform orientation are of utmost importance [19]. A promising strategy to achieve such uniform orientation for small molecules is their self-assembly in a liquid crystalline phase. Among the various liquid crystalline phases, the soft-crystalline E phase (SmE) is particularly attractive for device applications [20]. In a seminal study, Hanna reported high mobilities up to 13.9 cm^{2}V^{-1} s^{-1} and a good thermal durability of thin films using an SmE phase of compound **2** (Scheme 1b) [21–23]. SmE phases are usually formed by rod-like (calamitic) molecules displaying SmA or SmB phases upon cooling from these more fluid phases, as was described by Funahashi, Hanna [24] Osiecka [25] and Cozan [26]. In contrast, a direct formation of the SmE phase from the isotropic liquid is rare [27,28]. Among the few examples of low-molecular-weight liquid crystals
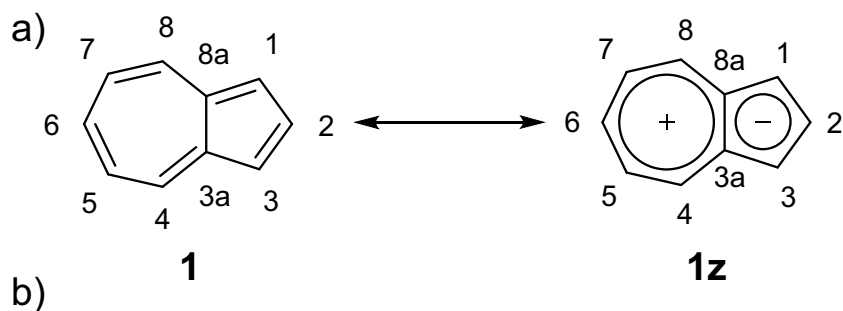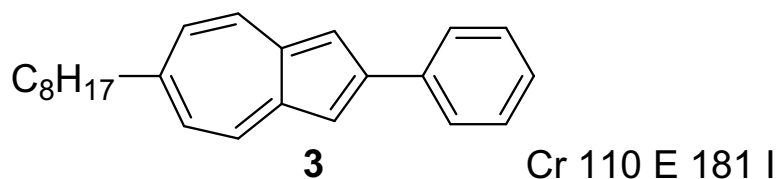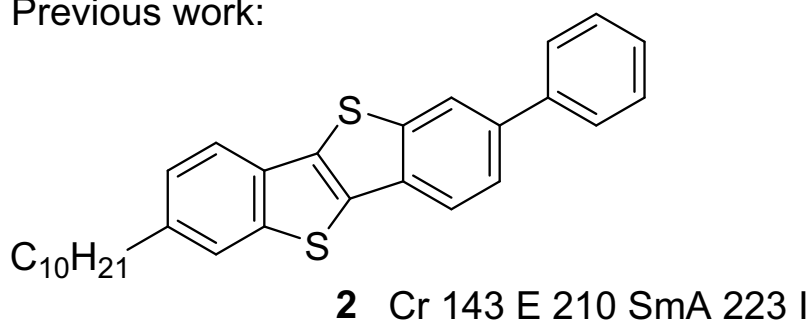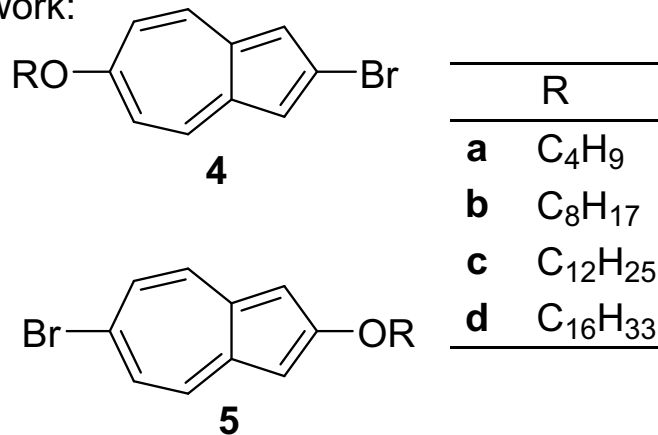

Scheme 1. (a) Localised and zwitterionic resonance structure of azulene (b) Selected examples of known compounds with SmE-phases and current target structure.

displaying only SmE phases are isothiocyanate-substituted biphenyls reported by Dabrowski [29–31], 4-alkyloxy-4′-alkynoylbiphenyls studied by Diele [32], 2-phenylindenes developed by Schultz [33], and substituted crown ethers by Cozan [34]. Despite the rich polymorphism of azulene derivatives, Ito observed only for 6-alkyl-2-phenyl azulenes **3** SmE phases at elevated temperatures which were not accompanied by another

mesophase [35,36]. An additional advantage of SmE phases as compared to other mesophases is their herringbone packing, which is maintained upon crystallisation resulting in 2D conduction beneficial for high charge carrier mobilities [37–39]. However, low-molecular-weight materials with ambient temperature SmE phases and moderate clearing temperatures suitable for organoelectronic applications are only little explored. In the

current paper, we designed 6-alkoxy-2-bromoazulenes **4** with room temperature SmE phases. By a combined experimental and theoretical approach, the self-assembly and optical properties of compounds **4** were rationalised in comparison with 2-alkoxy-6-bromoazulenes **5** possessing the 'inverted' substitution pattern.

Experimental

General methods

All chemicals were, unless otherwise stated, used without further purification. Anhydrous THF was obtained by refluxing the solvent over potassium. The eluents for chromatography (hexanes, low boiling, and ethyl acetate EtOAc) were distilled prior to use. ^{1}H NMR spectra were measured using the Bruker Avance 400, Bruker Avance 500, and Bruker Avance 700 spectrometers at 300 MHz, 400 MHz, 500 MHz and 700 MHz, as well as ^{13}C NMR spectra at 75 MHz, 76 MHz, 126 MHz, and 176 MHz, respectively. To assign the signals of the ^{1}H and ^{13}C NMR spectra, COSY, HSQC and HMBC measurements were carried out. FT-IR spectra were measured on a Bruker Vektor 22 with an MKII Golden Gate Single Reflection Diamond ATR. Absorption bands were rounded to integer wavenumbers/cm^{-1} and the absorption intensities were classified as follows: w (weak), m (medium), s (strong). Mass spectra (MS) and high-resolution mass spectra (HRMS) were measured by electrospray ionisation (ESI) or electron impact ionisation (EI) with a Bruker MicrOTOF-Q spectrometer or electron impact ionisation (EI) with a *Varian MAT 711* spectrometer. CHN analysis was performed using an Elemental Analyser Model 1106 from Carlo Erba Strumentazione. For thin-layer chromatography, silica gel 60 F254 glass plates (layer thickness of 0.25 mm) on aluminium (pore size 60 Å) from Merck were used. Column chromatography was performed using silica gel (particle diameter of 40–60 μm) from Fluka. A polarising optical microscope Olympus BX 50, equipped with a Linkam LTS heating stage, was used. Temperature regulation was carried out with the control units TP93 and LNP from Linkam (ΔT = ±1 K). Photographs were saved with a digital camera ColorView from Soft Imaging System using the software analySIS. For differential scanning calorimetry, a DSC822e from the company Mettler Toledo was employed. The compounds were analysed in 40 μL sealed aluminium pans. Heating and cooling rates of 5 K min^{-1} were employed. Phase transition temperatures and enthalpies were determined by onset values using the software STARe 7.01.

Measurements of the X-ray diffraction were performed using a Bruker AXS Nanostar C with a ceramic tube generator (1500 W) having cross-coupled Goebel mirrors providing monochromatic Cu Kα radiation (1.5405 Å). Diffraction patterns were recorded with Bruker HI-STAR or VÅNTEC 500 detectors. Calibration was carried out using the diffraction pattern of silver behenate at room temperature. The compounds were examined in sealed glass capillaries from Hilgenberg GmbH (external diameter of 0.7 mm, wall thickness 0.01 mm). Measured values were analysed with the software SAXS from Bruker. The diffraction patterns were further processed using the software Datasqueeze, Origin and LCDiXray. For UV/Vis spectroscopy solvents were obtained in spectroscopic grade from the supplier and were not further purified. For absorption spectra, a Perkin Elmer Lambda 35 spectrometer was employed. Fits were obtained using origin software and the goodness of fit judged by the reduced χ^2 value and residual plot shape.

Experimental procedures

General procedure for the syntheses of 6-alkoxy-2-bromoazulene (4a-d) by nucleophilic aromatic substitution. (GP 1): Adapting a procedure by Dehmlow [40] 2,6-dibromoazulene **9** (332 mg 1.16 mmol for **4b**) in anhydrous THF (10 mL) was added to sodium hydride (60% in mineral oil, 232 mg, 5.80 mmol for **4b**). Subsequently, a solution of octanol (1.51 g, 11.60 mmol for **4b**) in THF (20 mL) was added. After the reaction mixture was refluxed for 16 h, 2 M aqueous HCl (40 mL) was added. The phases were separated, and the aqueous phase was extracted with dichloromethane (3 x 30 mL). The combined organic layers were washed with brine (50 mL) and dried over MgSO$_4$. The solvent was removed under reduced pressure. Further purification was achieved via column chromatography on silica (hexanes).

General procedure for the syntheses of 2-alkoxy-6-bromoazulene (5a-d) via Williamson Ether Synthesis. (GP 2): 6-Bromo-2-hydroxyazulene **8** (256 mg, 1.15 mmol for **5 c**), K$_2$CO$_3$ (634 mg, 4.59 mmol for **5 c**) and dodecylbromide (286 mg, 1.15 mmol for **5 c**) were dissolved in dimethyl sulphoxide (5 mL) and the reaction mixture was stirred at 40°C for 16 h. Next water (50 mL) was added and **5** could be filtered off the brown mixture as a berry coloured solid (84%, 378 mg, 0.97 mmol). In case of traces of dimethylsulfoxide, the product was redissolved in diethyl ether (30 ml), washed with water (3 x 30 mL) and dried over MgSO$_4$. The solvent was removed under reduced pressure.

2-Bromo-6-butyloxyazulen (4a): Synthesis according to GP1; pink solid (114 mg, 408 μmol, 78%), melting point: 44°C, clearing point: 130°C; ^{1}H-NMR (500 MHz, CDCl$_3$): δ = 1.01 (t, *J* = 7.4 Hz, 3 H, CH$_3$), 1.49–1.58 (m,

2H, CH$_2$), 1.80–1.87 (m, 2H, CH$_2$), 4.09 (t, J = 6.5 Hz, 2H, OCH$_2$), 6.82–6.86 (m, 2H, 5-H, 7-H), 7.21 (s, 2H, 1-H, 3-H), 8.05–8.11 (m, 2H, 4-H, 8-H) ppm; ^{13}C-NMR (126 MHz, CDCl$_3$): δ = 13.9 (CH$_3$), 19.3, 31.2 (CH$_2$), 68.7 (OCH$_2$), 112.3 (C-5, C-7), 119.3 (C-1, C-3), 121.8 (C-2), 134.9 (C-4, C-8), 135.5 (C-3a, C-8a), 167.0 (C-6) ppm; FT-IR (ATR): ν = 2960 (w), 2935 (w), 2874 (w), 2250 (w), 1580 (m), 1543 (w), 1492 (w), 1467 (w), 1400 (m), 1380 (w), 1360 (w), 1252 (m), 1190 (m), 1065 (w), 999 (w), 966 (w), 904 (s), 865 (w), 840 (m), 789 (w), 725 (s), 688 (m), 649 (m), 593 (w), 430 (w) cm^{-1}; HRMS (EI): m/z for C$_{14}$H$_{15}$BrO$^+$ calc.: 238.0306 [M]$^+$, found: 278.0309.

2-Bromo-6-octyloxyazulene (4b): Synthesis according to GP1; pink solid (351 mg, 1.05 mmol, 90%); Melting point: 68°C, clearing point: 113°C; ^{1}H-NMR (700 MHz, CDCl$_3$): δ = 0.90 (t, J = 6.8 Hz, 3 H, CH$_3$), 1.26–1.40 (m, 8H, CH$_2$), 1.46–1.52 (m, 2H, OCH$_2$CH$_2$CH$_2$), 1.84 (tt, J = 6.8 Hz, 6.8 Hz, 2H, OCH$_2$CH$_2$), 4.08 (t, J = 6.5 Hz, 2H, OCH$_2$), 6.84 (d, J = 10.8 Hz, 2H, 5-H, 7-H), 7.20 (s, 2H, 1-H, 3-H), 8.08 (d, J = 10.8 Hz, 2H, 4-H, 8-H) ppm; ^{13}C-NMR (176 MHz, CDCl$_3$): δ = 14.1 (CH$_3$), 22.7, 26.0, 29.2, 29.2, 29.3, 31.8 (CH$_2$), 69.0 (CH$_3$), 112.3 (C-5, C-7), 119.3 (C-1, C-3), 121.8 (C-2), 134.9 (C-4, C-8), 135.5 (C-4a, C-8a), 167.0 (C-6) ppm; FT-IR (ATR): ν = 2926 (w), 2856 (w), 2250 (w), 1580 (m), 1543 (w), 1491 (w), 1468 (w), 1400 (m), 1379 (w), 1359 (w), 1296 (w), 1253 (m), 1190 (m), 1072 (w), 1008 (w), 904 (s), 863 (w), 904 (w), 863 (w), 839 (m), 821 (w), 789 (w), 727 (s), 689 (m), 649 (w), 594 (w) cm^{-1}; MS (ESI): m/z for C$_{18}$H$_{23}$BrO$^+$ calc.: 335.10 [M + H]$^+$, found: 335.10; HRMS (ESI): m/z for C$_{18}$H$_{23}$BrO$^+$ calc.: 335.1005 [M + H]$^+$, found: 335.1005.

2-Bromo-6-dodecyloxyazulene (4c): Synthesis according to GP1; pink solid (470 mg, 1.20 mmol, 92%); Melting point: 85°C, clearing point: 97°C; ^{1}H-NMR (500 MHz, CDCl$_3$): δ = 0.88 (t, J = 6.9 Hz, 3 H, CH$_3$), 1.21–1.41 (m, 16 H, CH$_2$), 1.45–1.52 (m, 2H, OCH$_2$CH$_2$CH$_2$), 1.84 (tt, J = 6.7 Hz, 6.7 Hz, 2H, OCH$_2$CH$_2$), 4.08 (t, J = 6.5 Hz, 2H, OCH$_2$), 6.84 (d, J = 11.0 Hz, 2H, C-5, C-7), 7.20 (s, 2H, C-1, C-3), 8.08 (d, J = 11.0 Hz, 2H, C-4, C-8) ppm; ^{13}C-NMR (126 MHz, CDCl$_3$): δ = 14.1 (CH$_3$), 22.7, 26.0, 29.2, 29.3, 29.4, 29.6, 29.6, 29.6, 29.7, 31.9 (CH$_2$), 69.0 (OCH$_2$), 112.2 (C-5, C-7), 119.3 (C-1, C-3), 121.8 (C-2), 134.9 (C-4, C-8), 135.5 (C-3a, C-8a), 167.0 (C-6) ppm; FT-IR (ATR): ν = 2917 (s), 2850 (s), 1585 (w), 1541 (s), 1471 (w), 1407 (m), 1378 (w), 1357 (w), 1298 (w), 1256 (m), 1235 (w), 1198 (s), 1017 (w), 996 (w), 910 (w), 841 (m), 823 (w), 797 (w), 767 (w), 728 (w), 693 (w), 596 (w) cm^{-1}; MS (EI): m/z for C$_{22}$H$_{32}$OBr$^+$ calc.: 393.16 [M + H]$^+$, found: 393.16; HRMS (EI): m/z for C$_{22}$H$_{32}$OBr$^+$ calc.: 393.1631 [M + H]$^+$, found:

393.1596; CHN-analysis. (%) for C$_{22}$H$_{32}$OBr (391.39): C 67.51, H 7.98; found: C 67.69, H 7.96.

2-Bromo-6-hexadecyloxyazulene (4d): Synthesis according to GP1; pink solid (332 mg, 0.74 mmol, 92%); ^{1}H-NMR (500 MHz, CDCl$_3$): δ = 0.88 (t, J = 6.8 Hz, 3 H, CH$_3$), 1.20–1.40 (m, 24 H, CH$_2$), 1.44–1.52 (m, 2H, OCH$_2$CH$_2$CH$_2$), 1.84 (tt, J = 6.6 Hz, 6.5 Hz, 2H, OCH$_2$CH$_2$), 4.08 (t, J = 6.5 Hz, 2H), 6.84 (d, J = 1.0 Hz, 2H, 5-H, 7-H), 7.20 (s, 2H, 1,-H, 3-H), 8.08 (d, J = 11.0 Hz, 2H, 4-H, 8-H) ppm; ^{13}C-NMR (126 MHz, CDCl$_3$): δ = 14.1 (CH$_3$), 22.7, 26.0, 29.2, 29.4, 29.4, 29.6, 29.6, 29.7, 29.7, 32.0 (CH$_2$), 69.0 (OCH$_2$), 112.3 (C-5, C-7), 119.3 (C-1, C-3), 121.8 (C-2), 134.9 (C-4, C-8), 135.5 (C-3a, C-8a), 167.0 (C-6) ppm; FT-IR (ATR): ν = 2916 (s), 2849 (m), 1586 (m), 1542 (w), 1472 (w), 1464 (w), 1408 (m), 1378 (w), 1358 (w), 1296 (w), 1257 (m), 1237 (w), 1199 (m), 1015 (w), 993 (w), 910 (w), 841 (m), 822 (w), 797 (w), 767 (w), 728 (w), 693 (w), 596 (w), 469 (w) cm^{-1}; MS (ESI): m/z for C$_{26}$H$_{40}$BrO$^+$ calc.: 447.23 [M + H]$^+$, found: 447.22, HRMS (ESI): m/z for C$_{26}$H$_{40}$BrO$^+$ calc.: 447.2257 [M + H]$^+$, found: 447.2258.

6-Bromo-2-butyloxyazulene (5a): Synthesis according to GP2; berry coloured solid (230 mg, 0.82 mmol, 76%); melting point: 87°C, clearing point: 105°C; ^{1}H-NMR (500 MHz, CDCl$_3$): δ = 1.00 (t, J = 7.4 Hz, 3 H, CH$_3$), 1.50–1.58 (m, 2H, OCH$_2$CH$_2$CH$_2$), 1.83–1.89 (m, 2H, OCH$_2$CH$_2$), 4.23 (t, J = 6.6 Hz, 2H, OCH$_2$), 6.83 (s, 2H, 1-H, 3-H), 7.49–7.53 (m, 2H, 5-H, 7-H), 7.75–7.82 (m, 2H, 4-H, 8-H) ppm; ^{13}C-NMR (126 MHz, CDCl$_3$): δ = 13.9 (CH$_3$), 19.2, 31.3 (CH$_2$), 70.4 (OCH$_2$), 103.6 (C-1, C-3), 127.5 (C-5, C-7), 128.4 (C-6), 129.7 (C-4, C-8), 138.6 (C-3a, C-8a), 169.3 (C-2) ppm; FT-IR (ATR): ν = 2957 (w), 2934 (w), 2872 (w), 1583 (w), 1562 (w), 1536 (m), 1504 (w), 1464 (w), 1407 (w), 1383 (w), 1343 (w), 1289 (w), 1222 (w), 1168 (w), 1150 (w), 1123 (w), 1065 (w), 1025 (w), 994 (w), 972 (w), 943 (w), 907 (w), 824 (s), 789 (w), 732 (m), 652 (w), 516 (w) cm^{-1}; MS (ESI): m/z für C$_{14}$H$_{16}$BrO$^+$ calc.: 279.04 [M + H]$^+$, found.: 279.04; HRMS (ESI): m/z für C$_{14}$H$_{16}$BrO$^+$ calc.: 279.0379 [M + H]$^+$, found.: 279.0384.

6-Bromo-2-octyloxyazulene (5b): Synthesis according to GP2; berry coloured solid (170 mg, 0.51 mmol, 80%); melting point: 62°C, clearing point: 82°C; ^{1}H-NMR (500 MHz, CDCl$_3$): δ = 0.78–0.86 (m, 3 H, CH$_3$), 1.16–1.34 (m, 8H, CH$_2$), 1.38–1.47 (m, 2H, OCH$_2$CH$_2$CH$_2$), 1.76–1.84 (m, 2H, OCH$_2$CH$_2$), 4.14 (t, J = 6.6 Hz, 2H, OCH$_2$), 6.76 (s, 2H, 1-H, 3-H), 7.42–7.46 (m, 2H, 5-H, 7-H), 7.68–7.73 (m, 2H, 4-H, 8-H) ppm; ^{13}C-NMR (126 MHz, CDCl$_3$): δ = 14.1 (CH$_3$), 22.7, 26.0, 29.3, 29.4, 31.8 (CH$_2$), 70.7 (OCH$_2$), 103.6 (C-1, C-3), 127.5 (C-5, C-7), 128.4 (C-6), 129.7 (C-4, C-8), 138.6 (C-3a, C-8a), 169.3 (C-2) ppm; FT-IR (ATR): ν = 2955

(m), 2925 (s), 2855 (m), 1584 (w), 1566 (m), 1532 (s), 1504 (m), 1465 (m), 1407 (w), 1381 (m), 1360 (w), 1342 (m), 1289 (w), 1223 (w), 1164 (m), 1020 (w), 996 (w), 950 (w), 908 (m), 822 (s), 789 (w), 735 (m), 651 (w), 511 (w), 408 (w), cm^{-1}; MS (ESI): m/z für $C_{18}H_{24}BrO^+$ calc.: 335.10 [M + H]$^+$, found.: 335.10; HRMS (ESI): m/z für $C_{18}H_{24}BrO^+$ calc.: 335.1005 [M + H]$^+$, found.: 335.1004

6-Bromo-2-dodecyloxyazulene (5c): Synthesis according to GP2; berry coloured solid (378 mg, 0.97 mmol, 84%); Melting point: 79°C; ^{1}H-NMR (500 MHz, CD$_2$Cl$_2$): δ = 0.88 (t, J = 6.8 Hz, 3 H, CH$_3$), 1.21–1.42 (m, 16 H, CH$_2$), 1.44–1.52 (m, 2H, OCH$_2$CH$_2$CH_2), 1.86 (tt, J = 6.8 Hz, 6.8 Hz, 2H, OCH$_2$CH_2), 4.22 (t, J = 6.8 Hz, 2H, OCH$_2$), 6.85 (s, 2H, 1-H, 3-H), 7.52 (d, J = 10.5 Hz, 2H, 5-H, 7-H), 7.80 (d, J = 10.5 Hz, 2H, 4-H, 8-H) ppm; ^{13}C-NMR (176 MHz, CD$_2$Cl$_2$): δ = 13.9 (CH$_3$), 22.7, 26.0, 29.2, 29.4, 29.4, 29.6, 29.6, 29.7, 29.7, 31.9 (CH$_2$), 70.8 (OCH$_2$), 103.7 (C-1, C-3), 127.4 (C-5, C-7), 128.1 (C-6), 129.5 (C-4, C-8), 138.6 (C-3a, C-8a), 169.5 (C-2) ppm; FT-IR (ATR): ν = 2955 (w), 2917 (s), 2850 (s), 1727 (w), 1565 (w), 1532 (s), 1505 (s), 1463 (m), 1408 (w), 1386 (m), 1339 (m), 1288 (w), 1252 (w), 1224 (w), 1169 (m), 1155 (m), 1037 (w), 1019 (w), 1006 (w), 983 (w), 951 (s), 890 (w), 824 (s), 784 (s), 713 (w), 679 (w), 653 (w), 638 (w), 542 (w), 518 (m), 492 (w), 409(w) cm^{-1}; MS (ESI): m/z for $C_{22}H_{32}OBr^+$ calc.: 391.2 [M + H]$^+$, found: 391.1; HRMS (ESI): m/z for $C_{22}H_{32}OBr^+$ calc.: 391.1631 [M + H]$^+$, found: 391.1616.

6-Bromo-2-hexadecyloxyazulene (5d): Synthesis according to GP2; berry coloured solid (190 mg, 0.42 mmol, 82%); Melting point: 86°C; ^{1}H-NMR (500 MHz, CDCl$_3$): δ = 0.92 (t, J = 6.9 Hz, 3 H, CH$_3$), 1.25–1.44 (m, 24 H, CH$_2$), 1.48–1.57 (m, 2 H OCH$_2$CH$_2$CH_2), 1.86–1.94 (m, 2 H, OCH$_2$CH_2), 4.24 (t, J = 6.6 Hz, 2 H, OCH$_2$), 6.86 (s, 2 H, 1-H, 3-H), 7.52–7.57 (m, 2 H, 5-H, 7-H), 7.78–7.84 (m, 2 H, 4-H, 8-H) ppm; ^{13}C-NMR (126 MHz, CDCl$_3$): δ = 14.2 (CH$_3$), 22.7, 26.0, 29.3, 29.4, 29.6, 29.6, 29.7, 29.7, 29.7, 32.0 (CH$_2$), 70.7 (OCH$_2$), 103.7 (C-1, C-3), 127.5 (C-5, C-7), 128.4 (C-6), 129.6 (C-4, C-8), 138.6 (C-3a, C-8a), 169.3 (C-2) ppm; FT-IR (ATR): ν = 2955 (w), 2917 (s), 2849 (m), 1567 (w), 1536 (m), 1509 (w), 1472 (w), 1463 (w), 1410 (w), 1387 (w), 1362 (w), 1339 (w), 1289 (w), 1226 (w), 1170 (w), 1156 (w), 1019 (w), 985 (w), 949 (w), 909 (m), 826 (m), 783 (w), 730 (w), 653 (w), 521 (w), 410 (w) cm^{-1}; MS (ESI): m/z für $C_{26}H_{40}BrO^+$ calc.: 447.23 [M + H]$^+$, found.: 447.23; HRMS (ESI): m/z für $C_{26}H_{40}BrO^+$ calc.: 447.2257 [M + H]$^+$, found.: 447.2259.
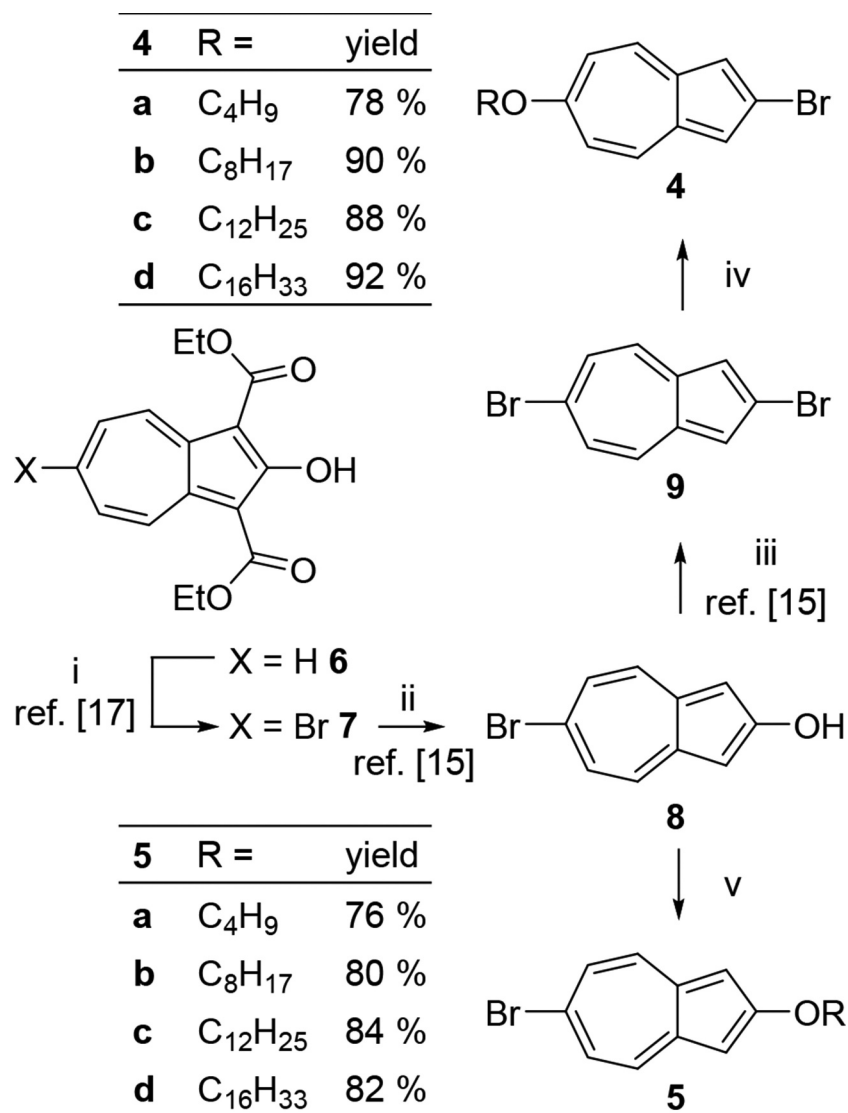
Results and discussion

Synthesis

The synthesis of calamitic azulenes **4–5** is shown in Scheme 2. The known diethyl 2-hydroxyazulene-1,3-dicarboxylate **6** [17,41] was brominated in DMF in the presence of NaOAc according to a method by Nozoe to give the 6-bromo derivative **7** in 85%. Removal of the ester groups was achieved by heating in a mixture of concentrated sulphuric acid and 85% phosphoric acid via the method of Schwarz [15]. Williamson etherification of **8** with alkyl bromide and K$_2$CO$_3$ yielded the 6-bromo-2-azulene ether **5a-e**. In order to obtain the inverse substitution pattern, intermediate **8** was treated with PBr$_3$ in refluxing toluene to give 80% of the dibromoazulene **9** [15], which was submitted to nucleophilic aromatic substitution to yield the ether **4a-e** in 77–92%. The regioselectivity of this reaction is achieved by the electronical difference between the electron-rich five-membered ring and the electron-poor seven-membered ring.

Mesomorphic properties

To investigate the mesomorphic behaviour of compounds **4a-d** and **5a-d**, they were examined with polarising optical microscopy (POM), differential scanning calorimetry (DSC) and small- and wide-angle X-ray scattering (SAXS and WAXS). For every DSC measurement, three heating and cooling cycles were performed with a heating rate of 5 K/min. The DSC curves of all compounds can be found in the SI (Figure S1). Transition temperatures and enthalpies are summarised in Table 1.

The C$_4$-derivative **4a** showed an endothermic phase transition at 45°C in the first heating cycle and cleared at 130°C into the isotropic phase (Figure S1a). In the cooling cycle, exothermic phase transitions at 130°C and 21°C were observed. In further iterations, the heating cycle showed endothermic peaks at 15°C and 130°C. The transition at higher temperatures comes along with a larger enthalpy than the crystallisation peak. This indicates a well-ordered mesophase [34].

Compounds **4b,c** with C$_8$ and C$_{12}$ side chain, respectively, showed a similar phase sequence as compared to C$_4$ derivative **4a**. With increasing chain lengths melting temperatures increased and clearing temperatures decreased in the heating cycles. However, it should be emphasised that in the cooling cycle a pronounced hysteresis of the crystallisation was detected and thus the mesophase persisted at ambient temperatures for **4a** (T$_m$ 21°C), **4b** (T$_m$ 21°C), **4c** (T$_m$ 56°C) (Figure S1a-c). The C$_{16}$-homologue **4d** only showed a small monotropic mesophase (Figure S1d). For azulenes with the inverted substitution, pattern **5a-d** reduced clearing points and

4	R =	yield
a	C_4H_9	78 %
b	C_8H_{17}	90 %
c	$C_{12}H_{25}$	88 %
d	$C_{16}H_{33}$	92 %

5	R =	yield
a	C_4H_9	76 %
b	C_8H_{17}	80 %
c	$C_{12}H_{25}$	84 %
d	$C_{16}H_{33}$	82 %

Scheme 2. Synthesis of alkoxy-bromoazulenes **4,5**: i) Br_2, NaOAc, DMF, rt, 48 h, 85% ii) H_2SO_4, H_3PO_4, 130°C, 2 h, 88% iii) PBr_3, toluene, reflux, 2 h, 80% iv) ROH, NaH, THF, 60°C, 24 h. v) RBr, K_2CO_3, DMSO, 40°C, 16 h. Details are described in the SI.

phase widths were observed and the melting points were above ambient temperature. For the C_{12}-derivative **5c**, a monotropic phase was observed. Further elongation of the chain to the C_{16}-azulene **5d** resulted in a complete loss of the mesophase (Figure S1e-h). The monotropic behaviour of azulene derivatives **4d**, **5c** with longer side chains is in good agreement with previous work by Jaffer [42] and might be rationalised by increased contributions of van der Waals interactions between the alkyl chains of neighbouring molecules disfavouring the herringbone packing of the SmE orthorhombic lattice.

The cooling from the isotropic liquid was monitored via polarising optical microscopy. C_8-substituted azulene **4b** showed dendritic growth at 111°C which developed into characteristic 'platelet textures' after completion of the phase transition (Figure 1(b,c)).

Table 1. Onset transition temperatures [°C] and enthalpies [kJ/mol] of 6-alkyloxy-2-bromoazulene 4a-d and the inverted 2-alkoxy-6-bromoazulene 5a-d.

Comp		Transition temperatures/°C (and enthalpies/kJ/mol)				Range/ K	
4a	Cr	15 (−2.7)	SmE	130 (−14.7)	I	115	h
	Cr	21 (3.1)	SmE	130 (14.5)	I	109	c
4b	Cr	57 (−19.8)	SmE	113 (−15.9)	I	56	h
	Cr	21 (11.6)	SmE	111 (15.5)	I	90	c
4c	Cr	85 (−34.5)	SmE	97 (−10.8)	I	12	h
	Cr	56 (35.0)	SmE	98 (12.0)	I	42	c
4d	Cr	92 (−58.3)	–	–	I	–	h
	Cr	81 (46.2)	SmE	83 (3.4)	I	2	c
5a	Cr	88 (−6.6)	SmE	104 (−11.6)	I	16	h
	Cr	48 (3.6)	SmE	101 (12.4)	I	53	c
5b	Cr	62 (−20.1)	SmE	82 (10.2)	I	20	h
	Cr	33 (19.1)	SmE	84 (9.4)	I	51	c
5c	Cr	79 (−41.1)	–	–	I	–	h
	Cr	69 (33.0)	SmE	71 (2.7)	I	2	c
5d	Cr	86 (−62.2)	–	–	I	–	h
	Cr	81 (63.8)	–	–	I	–	c

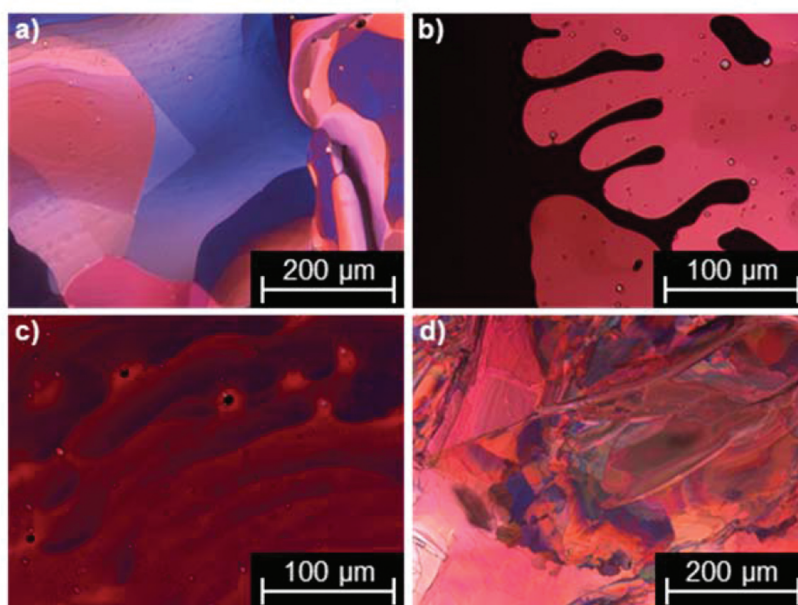Heating/Cooling rate: 5 K/min, second cycle. h: heating c: cooling.

Figure 1. (Colour online) POM micrographs of alkoxybromo- azulenes. (a) platelet textures of **4a** at 130°C, (b) dendritic growth of **4b** at 111°C that change into (c) platelet textures at 109°C. (d) Platelet textures of **5c** at 71°C. All pictures were taken upon cooling from the isotropic phases between crossed polarisers with a cooling rate of 5 K/min.

Both textures are typical for SmE phases [33,35,43,44]. During growing of platelets, they often overlap each other. Therefore, 'ghost-like' platelets were visible through upper platelets. This special case of mosaic textures is unique for SmE phases [33,43]. All derivatives **4a-d** and **5a-c** showed those characteristic textures (Figure 1(c-d) and Figure S2). However, C_{12}- and C_{16}-substituted azulenes **4c,d** initially formed needles upon cooling from the isotropic melt. From these needle-like textures the platelets formed upon further cooling (Figure S2c,d), which is in good agreement with previous observations by Cozan [34]. For the higher homologues **4c,d** a sharp crystallisation could be observed. In contrast, the crystallisation of **4a,b** could only be noticed by cracks in the platelet texture [23]. Presumably, the packing in the crystalline state of C_4- and C_8-derivatives **4a,b** is similar to the mesophase. In the case of **4b,c**, the textures changed upon shearing the top glass plate ensuring a fluid phase. This behaviour was not observed in the case of the C_4-azulene **4a**. However, textures changed over a period of 15 min at the same temperature, ensuring a certain degree of fluidity.

In order to determine the phase geometry, XRD-measurements were performed. Results are summarised in Table 2. Due to their small mesophase widths, azulenes **4d** and **5c** could not be examined with X-ray diffraction. Figure 2 shows the WAXS diffractograms and diffraction patterns of the azulenes **4a-c**. In the case of C_4 azulene **4a** an orientated sample was obtained

Table 2. Lattice constants and observed reflexes in WAXS- and SAXS measurements of the compounds **4a-c.**

Compound	Lattice constants/Å	Observed (Calculated)		Miller indices (hkl)
		Spacing/Å	
4a	(SmE at 112°C, cooling)	15.72	(15.70)	(001)
	$a = 7.76$	7.84	(7.85)	(002)
	$b = 5.77$	4.63	(4.63)	(110)
	$c = 15.70$	4.32	(4.34)	(103)
	molecular length: 13.9[a]	3.88	(3.88)	(200)
	$Z = 2.0$ $\rho = 1.3$[b]	3.76	(3.76)	(201)
		3.21	(3.22)	(210)
4b	(SmE at 104°C, heating)	21.32	(21.32)	(001)
	$a = 7.64$	10.66	(10.66)	(002)
	$b = 5.78$	4.61	(4.61)	(110)
	$c = 21.32$	3.82	(3.82)	(200)
	molecular length: 18.9[a]	3.26	(3.19)	(210)
	$Z = 2.0$ $\rho = 1.2$[b]	4.08	-	halo
4c	(SmE at 83°C, cooling)	27.25	(27.25)	(001)
	$a = 7.64$	4.62	(4.62)	(110)
	$b = 5.80$	3.82	(3.82)	(200)
	$c = 27.25$	3.20	(3.19)	(210)
	molecular length: 24.0[a]	4.25	-	halo
	$Z = 2.1$ $\rho = 1.1$[b]			
5a	(SmE at 75°C, cooling)	15.43	(15.43)	(001)
	$a = 7.78$	7.72	(7.72)	(002)
	$b = 5.76$	5.17	(5.14)	(003)
	$c = 15.43$	4.63	(4.63)	(110)
	molecular length: 13.9[a]	4.29	(4.29)	(103)
	$Z = 1.9$ $\rho = 1.3$[b]	3.89	(3.89)	(200)
		3.78	(3.77)	(201)
		3.23	(3.22)	(210)
5b	(SmE at 56°C, cooling)	20.88	(20.90)	(001)
	$a = 7.70$	10.46	(10.45)	(002)
	$b = 5.78$	4.62	(4.62)	(110)
	$c = 20.90$	4.23	(4.23)	(112)
	molecular length: 18.9[a]	3.85	(3.85)	(200)
	$Z = 2.0$ $\rho = 1.2$[b]	3.21	(3.20)	(210)

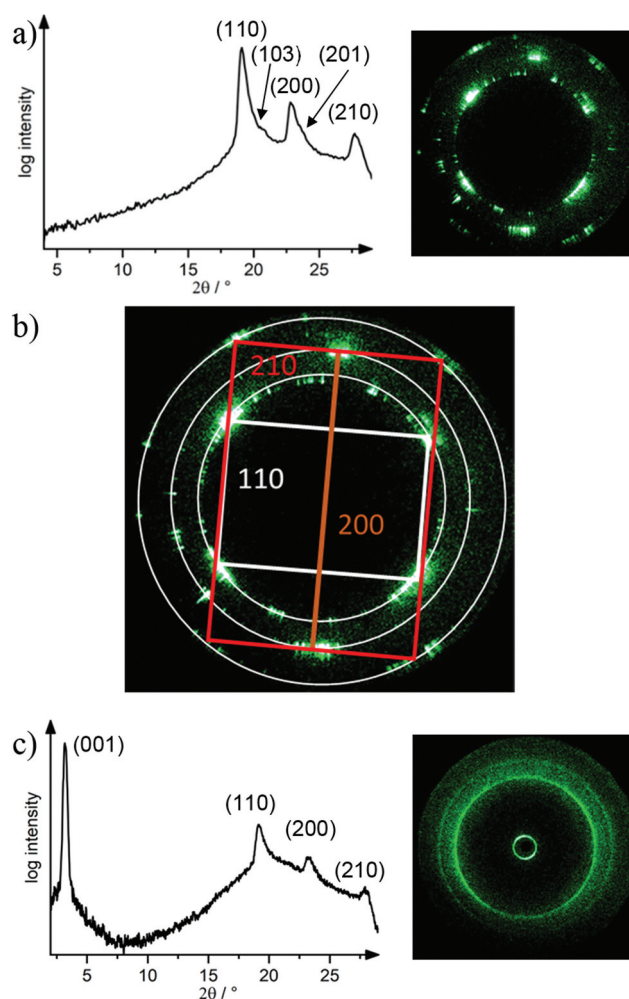[a]calculated with Chem3D [48]; [b] assumed density (g/cm³)

Figure 2. (Colour online) WAXS diffractogram and 2D diffraction pattern of (a) **4a** at 112°C (SmE). (b) zoom of (a) and assignment of the reflexes. (c) **4c** at 83°C (SmE).

(Figure 2(a)) [28,45]. In this case, the long axis of the molecules was aligned parallel to the incident X-ray beam. Therefore, the reflexes of the layer spacing were not observed. However, due to this orientation, the position of the different reflexes in the wide-angle area was observed (Figure 2(b)). This observation strongly indicates a SmE phase and clearly excludes the possibility of an SmB phase where six equidistant neighbour molecules are required. According to seminal work by Demus, the wide-angle area of a SmE phase is characterised by three characteristic reflexes (110), (200) and (210) [32]. The diffraction pattern of C_4-derivative **4a** exhibited further weak signals (Table 2), that could be assigned according to the calculated lattice parameters based on the typical reflexes of an SmE phase (Table 2) [46, p.661–668]. The broad halo is caused by the molten alkyl chains, indicating the presence of a fluid mesophase [47].

Diffractograms of the compounds **4b-c** and **5a-b** showed one or two sharp signals in the small-angle area (Figure S3-S13). In the wide-angle area, three sharp reflexes overlaying a broad halo were observed. The small-angle signals can be assigned to the smectic layer constants and their corresponding higher-order signals (00*l*). Those signals can be used to calculate the layer spacing *c*. As expected, layer spacings increased upon elongation of the side chain. However, when the spacings were compared with the calculated molecular lengths, it turns out, that layer spacing is slightly larger in comparison with the molecular length (Table 2) [48]. For unimolecular layers, the reversed effect would be expected due to random tilts of the molecules. Therefore, a bilayer arrangement was assumed in which the azulene cores most likely stack antiparallel in order to optimise dipole interactions and the free volume is filled by interdigitation of the side chains (Figure 3).
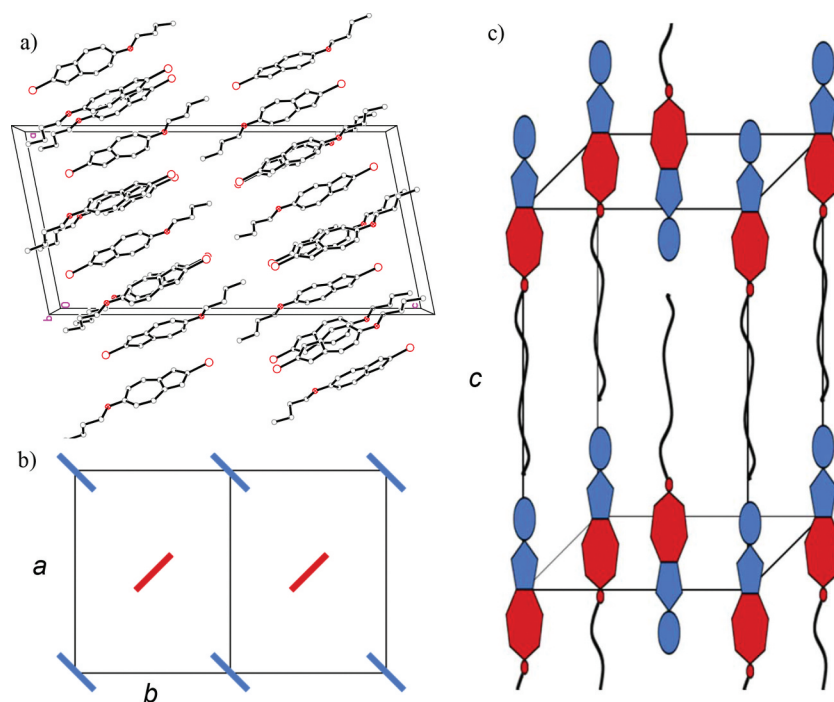
Figure 3. (Colour online) (a) Single crystal structure of the C_4-substituted azulene **4a** [49]. Important parameters: monoclinic crystal system, space group: P2$_1$/n; unit cell: a = 14.8 Å, b = 5.8 Å, c = 29.6 Å; α = 90°, β = 101.4°, γ = 90°; Z = 8; ρ = 1.49 g/cm^3 and proposed model for the arrangement of azulenes **4** in the observed SmE-phase: (b) top view of the anti-parallel herring-bone packing and (c) 3D depiction of the orthorhombic packing.

The experimental results of C_4-azulene **4a** are in accordance with the other investigated derivatives **4b,c** and support the SmE-phase assignment. However, due to the low crystallisation enthalpy and a less fluid mesophase of **4a** as compared to **4b,c**, the presence of a crystalline phase cannot fully be excluded.

Fortunately, for azulene **4a,** single crystals suitable for X-ray crystal structure analysis were obtained (Figure 3(a)) [49]. It should be emphasised that the comparison between crystalline and liquid crystalline phases should be treated with great care. However, soft-crystalline phases are more closely related to crystals than more fluid mesophases. Therefore, a careful comparison might improve the understanding of the mesophase packing. In the case of **4a** herring-bone-like layers were observed in the crystal. The monoclinic unit cell contains eight molecules. Herring-bone packing is the typical alignment of SmE phases [32]. Therefore, a similar arrangement in the mesophase can be expected. However, the layer spacing in the mesophase is slightly larger than half the height of the unit cell (15.7 Å vs. 14.8 Å) [48]. Presumably, this difference is caused by the more pronounced interdigitation of the alkyl side chains in the crystalline phase in comparison to the SmE phase. In accordance with the experimental data and the obtained crystal structure, a packing model was proposed (Figure 3(b,c)) [32,50]. Based on the

herring-bone pattern characteristic of SmE phases, the dipolar core of the azulene moiety should force the molecules in a strict anti-parallel packing. The layers can then interdigitate in order to minimise the free volume.

Absorption properties

Absorption properties of the azulenes **4a-d** and **5c** were examined in comparison with the known dibromoazulene **9** (Table 3) [40]. The UV region of the absorption spectra of azulene derivatives **4a-d, 5c, 9** was only weakly affected by the substitution pattern. Two intense peaks at around 290 and 300 nm could be observed for every derivative (Figure S14b-S19b). In the visible region compounds, **4a-d** displayed one broad absorption maximum at 500 nm with vibrational fine structure

Table 3. Absorption maxima λ_{max} and extinction coefficient ε_{vis} of the compounds **4–5** and **9**.

Compound	λ_{max}/nm (ε_{vis}/L mol^{-1} cm^{-1})			
4a	240 294 300	377		502 (341)
4b	242 294 300	377		500 (357)
4c	241 294 300	377		500 (359)
4d	241 294 301	377		500 (338)
5c	243 287 295	328 368 385		519 (127)
9[a]	242 289 297	341 355 372	416	556 (341)

[a]UV/Vis spectra of **9** were measured for comparison. For details see ref [40].
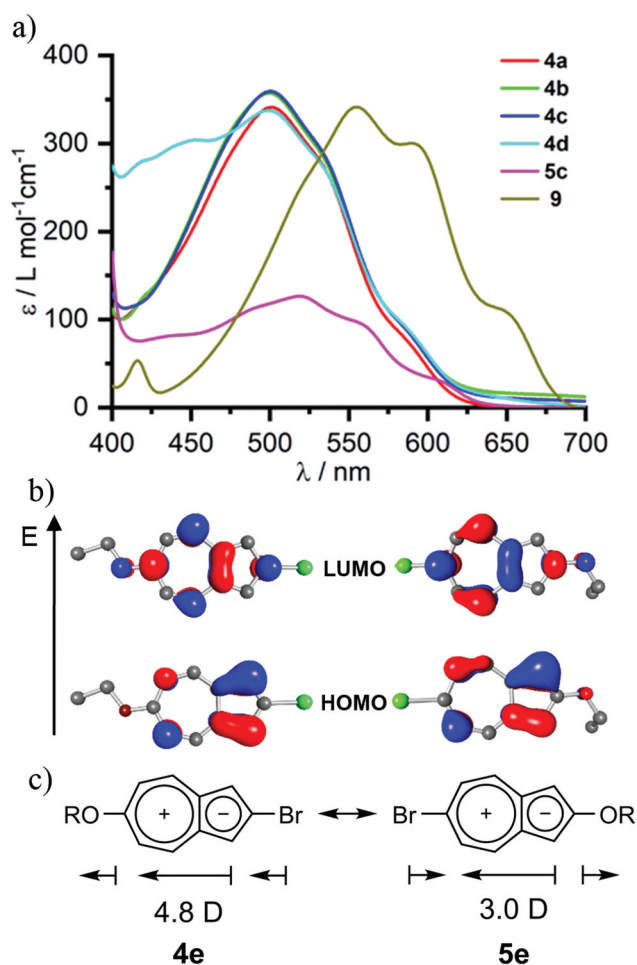
Figure 4. (Colour online) (a) Absorption spectra of the compounds **4a-d**, **5c**, **9**, measured in chloroform. (b) DFT calculated frontier orbitals of the azulenes **9e** and **10**(e and c) the dependence of the dipole moment to the substitution pattern.

(Figure 4(a)). The λ_{max} values were independent of the chain lengths. The λ_{max} value of the azulene **5c** with inverted substitution pattern shows a bathochromic shift to 519 nm. The λ_{max} value of dibromoazulene **9** was even further red-shifted to 556 nm.

In order to rationalise the influence of the substitution pattern (i.e. **4** vs. **5**) on the shift of the absorption maxima, frontier molecular orbitals were calculated by DFT methods [51]. The HOMOs and LUMOs of 2-bromo-6-ethoxyazulene **4e** and the inverted 6-bromo-2-ethoxyazulene **5e** are shown in Figure 4(b). The HOMOs have no coefficients at 2- and 6-position. Therefore, those orbitals were not affected by the substituents. The strongly electron-donating +M-effect of the oxygen raised the energy of the LUMO and led to a hypsochromic shift.

Furthermore, the dipole moments of 6-ethoxy-2-bromoazulene **4e** and its inverted counterpart 2-ethoxy-6-bromoazulene **5e** were calculated to understand the different mesomorphic properties between the substitution patterns of **4** and **5**. According to Figure 4(c), the dipole moment of **4e** (μ = 4.8 D) is significantly higher than that for **5e** (μ = 3.0 D), suggesting a better stabilisation of the SmE phase through stronger dipolar interactions in **4** as compared to **5**.

Conclusions

Efficient synthetic access has been provided to novel 6-alkoxy-2-bromoazulenes **4** and 2-alkoxy-6-bromoazulenes **5** with inverted substitution pattern in four steps starting from Nozoe azulene **6** [52] in overall yields of 47–55%. Compounds **4a-c** and **5a,b** displayed SmE phases, which were stable at remarkably low temperatures, in case of **4a,b** reaching room temperature and below. According to DFT calculations the strong dipolar interactions governed the mesophase stability of **4** as compared to **5**.

The SmE phases form directly upon cooling from the isotropic melt and the azulenes **4a-d** do not show additional less ordered phases. The ambient temperature

and broad mesophase widths of the zwitterionic aromatic system of 6-alkoxy-2-bromoazulenes **4a-d** facilitate their use in organic electronics – not least because the low-molecular weight allows their solution processing.

Acknowledgments

Disclosure statement

No potential conflict of interest was reported by the authors.

Funding

References

[1] Xin H, Gao X. Application of azulene in constructing organic optoelectronic materials: new tricks for an old dog. ChemPlusChem. 2017;82:945–956.

[2] Dong J-X, Zhang H-L. Azulene-based organic functional molecules for optoelectronics. Chin Chem Lett. 2016;27:1097–1104.

[3] Tobe Y. Non-alternant non-benzenoid aromatic compounds: past, present, and future. Chem Rec. 2015;15:86–96.

[4] Ito S, Morita N. Creation of stabilized electrochromic materials by taking advantage of azulene skeletons. Eur J Org Chem. 2009;27:4567–4579.

[5] Anderson AG, Steckler BM, Azulene A VIII. Study of the visible absorption spectra and dipole moments of some 1- and 1,3-substituted azulenes1,2. J Am Chem Soc. 1959;81:4941–4946.

[6] Asato AE, Peng A, Hossain MZ, et al. Azulenic retinoids: novel nonbenzenoid aromatic retinoids with anticancer activity. J Med Chem. 1993;36:3137–3147.

[7] Tomiyama T, Yokota M, Wakabayashi S, et al. Design, synthesis, and pharmacology of 3-substituted sodium azulene-1-sulfonates and related compounds: non-prostanoid thromboxane A2 receptor antagonists. J Med Chem. 1993;36:791–800.

[8] Nakamura H, Sekido M, Yamamoto Y. Synthesis of carboranes containing an azulene framework and in vitro evaluation as boron carriers. J Med Chem. 1997;40:2825–2830.

[9] Murfin LC, López-Alled CM, Sedgwick AC, et al. A simple, azulene-based colorimetric probe for the detection of nitrite in water. Front Chem Sci Eng. 2020;14:90–96.

[10] Ayaz F, Yuzer A, Ince T, et al. Anti-cancer and anti-inflammatory activities of bromo- and cyano-substituted azulene derivatives. Inflammation. 2020;43:1009–1018.

[11] Zhang J, Petoud S. Azulene-moiety-based ligand for the efficient sensitization of four near-infrared luminescent lanthanide cations: nd3+, Er3+, Tm3+, and Yb3+. Chem – Eur J. 2008;14:1264–1272.

[12] Zhou Y, Zhuang Y, Li X, et al. Selective dual-channel imaging on cyanostyryl-modified azulene systems with unimolecularly tunable visible–near infrared luminescence. Chem – Eur J. 2017;23:7642–7647.

[13] Puodziukynaite E, Wang H-W, Lawrence J, et al. Azulene Methacrylate Polymers: synthesis, Electronic Properties, and Solar Cell Fabrication. J Am Chem Soc. 2014;136:11043–11049.

[14] Xin H, Ge C, Jiao X, et al. Incorporation of 2,6-connected azulene units into the backbone of conjugated polymers: towards high-performance organic optoelectronic materials. Angew Chem Int Ed. 2018;57:1322–1326.

[15] Schwarz F, Koch M, Kastlunger G, et al. Charge transport and conductance switching of redox-active azulene derivatives. Angew Chem Int Ed. 2016;55:11781–11786.

[16] Tsuchiya T, Umemura R, Kaminaga M, et al. Paddlewheel complexes with azulenes: electronic interaction between metal centers and equatorial ligands. ChemPlusChem. 2019;84:655–664.

[17] Fan Q, Martin-Jimenez D, Ebeling D, et al. Nanoribbons with nonalternant topology from fusion of polyazulene: carbon allotropes beyond graphene. J Am Chem Soc. 2019;141:17713–17720.

[18] Chen Z, Droste J, Zhai G, et al. Sulfur-anchored azulene as a cathode material for Li–S batteries. Chem Commun. 2019;55:9047–9050.

[19] Yuan Y, Giri G, Ayzner AL, et al. Ultra-high mobility transparent organic thin film transistors grown by an off-centre spin-coating method. Nat Commun. 2014;5:3005.

[20] Instead of crystal-smectic E-phase, the terms Smectic E-phase and Crystal E-phase are als known in the literature. On behalf of consistency we will use the abbreviation SmE throughout the paper.

[21] Iino H, Usui T, Hanna J. Liquid crystals for organic thin-film transistors. Nat Commun. 2015;6:6828.

[22] Iino H, Hanna J. Liquid crystalline organic semiconductors for organic transistor applications. Polym J. 2017;49:23–30.

[23] Wu H, Iino H, Hanna J. Bilayered crystalline organic semiconductors for solution-processed OFETs: asymmetrically-substituted smectic liquid crystal of benzo[1,2-b:4,5-b′]dithiophene derivatives. Chem Lett. 2018;47:510–513.

[24] Funahashi M, Hanna J. Fast ambipolar carrier transport in smectic phases of phenylnaphthalene liquid crystal. Appl Phys Lett. 1997;71:602–604.

[25] Osiecka N, Massalska-Aroдź M, Galewski Z, et al. Dynamics and phase transitions of 4-Bromobenzylidene-4′-pentyloxyaniline and 4-Bromobenzylidene-4′-hexyloxyaniline as studied by dielectric spectroscopy. Acta Phys Pol A. 2013;124:913–916.

[26] Cozan V, Avadanei M, Shova S, et al. Crystal smectic E revisited for(E)-N-(biphenyl-4-ylmethylene)-4-buty-laniline – mesomorphism, crystal structure and FTIR study. Liq Cryst. 2019;46:492–501.

[27] Goodby JW. Structures and properties of smectic liquid crystals. In: Goodby JW, Collings PJ, Kato T, et al., editors. Handb Liq Cryst [Internet]. Weinheim, Germany: Wiley-VCH Verlag GmbH & Co. KGaA; 2014. pp. 1–26. [cited 2020 Mar 26]. doi:http://doi.wiley.com/10.1002/9783527671403.hlc061.

[28] Voronov VP, Muratov AR, Sulyanov SN, et al. Interplay between various crystalline and hexatic-B phases in 75OBC liquid crystal: X-ray diffraction and calorimetry study. Liq Cryst. 2020;47:1–13.

[29] Dabrowski R, Zytyński E. Mesomorphic properties of 4- n -pentylbiphenyl derivatives. Mol Cryst Liq Cryst. 1982;87:109–135.

[30] Jasiurkowska-Delaporte M, Massalska-Aroдź M. Molecular dynamics of 4-propyl-4′-thiocyanatobiphenyl (3BT) in the strong glass-forming smectic E phase. J Mol Liq. 2017;241:355–358.

[31] Saito K, Miyazawa T, Fujiwara A, et al. Reassessment of structure of smectic phases: nano-segregation in smectic E phase in 4- n -alkyl-4′-isothiocyanato-1,1′-biphenyls. J Chem Phys. 2013;139:114902.

[32] Diele S, Tosch S, Mahnke S, et al. Structure and packing in smectic E and smectic A phases in the series of 4-n-Alkyloxy-4′-alkanoylbiphenyls. Cryst Res Technol. 1991;26:809–817.

[33] Schultz SM, Kehr G, Fröhlich R, et al. Crystal-smectic E mesophases in a series of 2-(4- n -alkylphenyl) indenes. Liq Cryst. 2007;34:919–926.

[34] Cozan V, Ardeleanu R, Airinei A, et al. Crystalline smectic E phase revisited in case of symmetrical dibenzo-18-crown-6-ether azomethine dimers. J Mol Struct. 2018;1156:22–29.

[35] Ito S, Ando M, Nomura A, et al. Synthesis and properties of hexakis(6-octyl-2-azulenyl)benzene as a multielectron redox system with liquid crystalline behavior. J Org Chem. 2005;70:3939–3949.

[36] Nakagawa K, Yokoyama T, Toyota K, et al. Synthesis and liquid crystalline behavior of azulene-based liquid crystals with 6-hexadecyl

[37] Cheng YC, Silbey RJ, da Silva Filho DA, et al. Three-dimensional band structure and bandlike mobility in oligoacene single crystals: A theoretical investigation. J Chem Phys. 2003;118:3764–3774.

[38] Coropceanu V, Cornil J, da Silva Filho DA, et al. Charge transport in organic semiconductors. Chem Rev. 2007;107:926–952.

[39] Takimiya K, Shinamura S, Osaka I, et al. Thienoacene-based organic semiconductors. Adv Mater. 2011;23:4347–4370.

[40] Dehmlow EV, Balschukat D. Azulene durch Vakuumpyrolyse von Halogentricyclo[7.1.0.0]decadie-nen. Chem Ber. 1985;118:3805–3816.

[41] The synthesis is described in the supporting information.

[42] Tomi IHR, Al-Heetimi DTA, Jaffer HJ. Asymmetric 1,3,4-thiadiazole derivatives: synthesis, characterization and studying their liquid crystalline properties. J Mol Struct. 2017;1141:176–185.

[43] Gray GW, Goodby JWG. Smectic liquid crystals: textures and structures. Glasgow: Hill; 1984.

[44] Dierking I. Textures of liquid crystals. 1st ed. Weinheim, Germany: Wiley-VCH Verlag GmbH & Co. KGaA; 2003.

[45] A non-orientated WAXS sample is displayed in the supporting information.

[46] Demus D, editor. Handbook of liquid crystals. Weinheim; New York: Wiley-VCH; 1998.

[47] Adachi T, Saitoh H, Yamamura Y, et al. Universality of molten state of alkyl chain in liquid-crystalline meso-phases: Smectic E phase of 6-Alkyl-2-phenylazulene. Bull Chem Soc Jpn. 2013;86:1022–1027.

[48] Chem3D Version 18.0.0.231, PerkinElmer Informatics, Inc. Optimization via MM2 forcefields.

[49] Details of the crystal structure determination of azulene 4a have been deposited at the Cambridge Crystallographic Data Centre under CCDC 2018587 and can be obtained free of charge.

[50] Goodby JW, Mandle RJ, Davis EJ, et al. What makes a liquid crystal? The effect of free volume on soft matter. Liq Cryst. 2015;42:593–622.

[51] The BP-86 functional and def2-SVP basis set was used. Details are described in the Supporting Information.

[52] Nozoe T, Takase K, Shimazaki N. The synthesis of diethyl 2-hydroxyazulene-1, 3-dicarboxylate from tro-ponoids and some reactions of 2-Hydroxyazulene derivatives. Bull Chem Soc Jpn. 1964;37:1644–1648.

Paper II

Taylor & Francis
Taylor & Francis Group

Check for updates

Phase behaviour of alkynyl-terminated bicyclo[3.3.0]octa-1,4-diene ligands: a serendipitous discovery of novel calamitic liquid crystals

Finn Schulz*, Max Deimling* and Sabine Laschat

Institut für Organische Chemie, Universität Stuttgart, Stuttgart, Germany

ABSTRACT

Chiral bicyclo[3.3.0]octadienes carrying two alkoxy- or alkynyloxy side chains are highly valuable ligands for asymmetric catalysis but have never been explored regarding their liquid crystalline self-assembly. Therefore, a series of bicyclo[3.3.0]octadienes was synthesised and studied by differential scanning calorimetry (DSC), polarising optical microscopy (POM) and X-ray diffraction (XRD) to understand the role of the terminal alkyne unit in the side chain. Dienes with hexinyloxy or octinyloxy side chains behaved similar to the diene with hexyloxy chains, showing broad SmA phases and a pronounced tendency for supercooling. In contrast, dienes with mono- or diethylenglycolpropargylic ether chains displayed a decreased phase range and monotropic behaviour in the latter case, while the corresponding diene with propargylether side chains was non-mesomorphic.
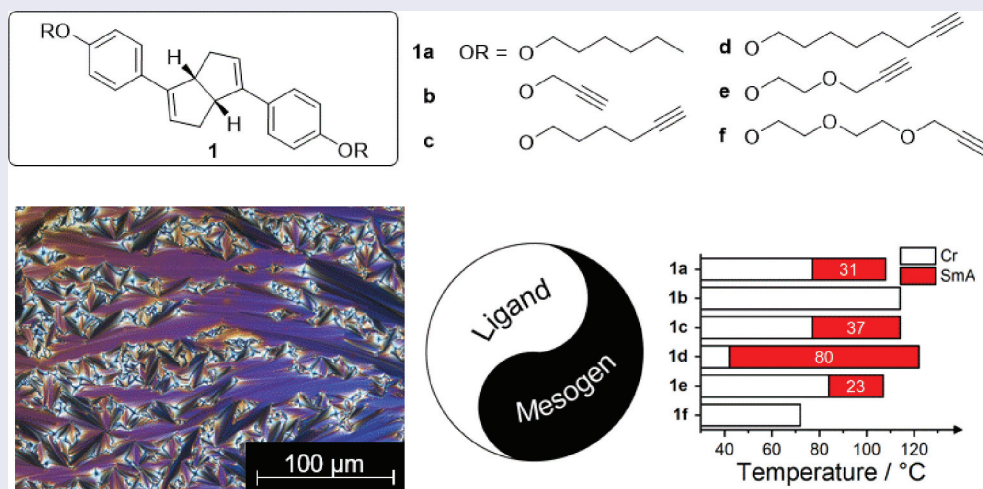
Introduction

Chiral bicyclo[3.3.0]octa-1,4-dienes (hydropentalenes) have been successfully employed as chiral steering ligands in asymmetric catalysis (Scheme 1) [1,2]. Benchmark reactions such as the Rh-catalysed 1,4-additions of organoboronic acids to enones and 1,2-additions of boroxines to N-tosylimines [1] were performed with chiral bicyclo [3.3.0]octa-1,4-dienes in high yields and excellent enantioselectivities [3–7]. More recently, we synthesised dienes 1 carrying terminal side chains of different polarity and probed their catalytic performance in microemulsions and conventional solvents (Scheme 1) [8]. During spectroscopic and analytic characterisation, we noticed

double melting of both diene **1a** carrying hexyloxy side chains and diene **1 c** with terminal alkyne moieties. We surmised that the *concave* open book-shaped hydropentalene unit promotes mesophase formation and that alkynes might further contribute to the mesophase stabilisation. Despite the wealth of information available on hydropentalenes [9], their application in liquid crystalline materials has not been studied so far. In addition, a literature survey revealed that the influence of terminal alkynes on the mesomorphic properties of thermotropic liquid crystals has only been little explored. In a seminal report on triphenylenes Stackhouse studied the influence of acetylene-containing side chains on discotic mesogens

---

CONTACT Sabine Laschat ✉ sabine.laschat@oc.uni-stuttgart.de

*These authors contributed equally to this work.

ⓘ Supplemental data for this article can be accessed here.
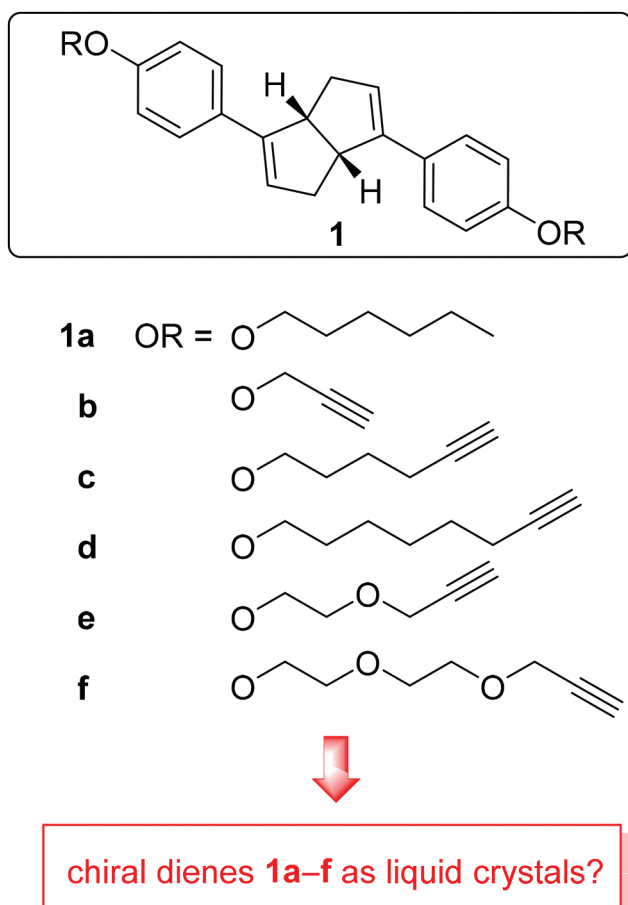
Scheme 1. (Colour online) Chiral bicyclo[3.3.0]octadienes **1** carrying alkoxy, alkinyloxy or (di)ethyleneglycolpropargylic ether side chains.

[10]. Pentaalkyloxytriphenylenes with a single alkynyl-appendage were employed by Zhao for Co-mediated [2 + 2 + 1]-cocyclizations towards discotic trimers [11]. Petrzilka studied a series of apolar bicyclic calamitics with terminal and internal alkyne units [12]. Comparison with the hydrogenated counterparts revealed that the presence of the alkyne unit generally led to mesophases with higher thermal stability and the clearing temperatures were found to be dependent on the location of C ≡ C triple bond [13][1] These precedences motivated us to investigate the calamitic bicyclo[3.3.0]octadienes **1a-f** in more detail, in order to understand the role of the side chain and in particular the terminus on the liquid crystalline self-assembly. The results are reported below.

Results and discussion

The synthesis of bicyclo[3.3.0]octa-1,4-dienes **1a,c,f** was performed as previously described [8]. Compound **1b** was synthesised via Williamson etherification from the known diol **2** [8] with propargyl bromide in DMSO in the presence of Cs₂CO₃ and KI to give the product in 75%

yield (Scheme 2). Mitsunobu reaction [14] of diol **2** with 7-octyn-1-ol and 2-(prop-2-yn-1-yloxy)ethan-1-ol, respectively, in THF in the presence of PPh₃ and DIAD provided products **1d** and **1e** in 62% and 75% isolated yield.

The liquid crystalline properties of dienes **1a-f** were examined by differential scanning calorimetry (DSC), polarising optical microscopy (POM) and X-ray diffraction (WAXS, SAXS).

Phase transition temperatures and enthalpies of dienes **1a-f** are summarised in Table 1, phase widths are shown in Figure 1. The DSC curve of hexyloxy terminated diene **1a** showed an endothermic transition at 77°C during the first heating (Figure S1a). A smaller transition at 108°C indicated a clearing into the isotropic melt. During cooling down, an isotropic to mesophase transition was observed at 105°C. Similar to other dienes **1d,e** discussed below, crystallisation did not occur until 26°C. In further heating iterations, an additional post crystallisation peak was observed at 35°C followed by the melting into the meso-phase and clearing. Diene **1b** with propargylethers did not show any mesomorphism (Figure S1b); however, diene **1c** with 5-hexynyloxy chain showed an endothermal crystal to crystal transition at 77°C as a shoulder of the larger melting peak upon 1st heating, and an endothermal clearing transition at 114°C, which was hardly visible (Figure 2). During
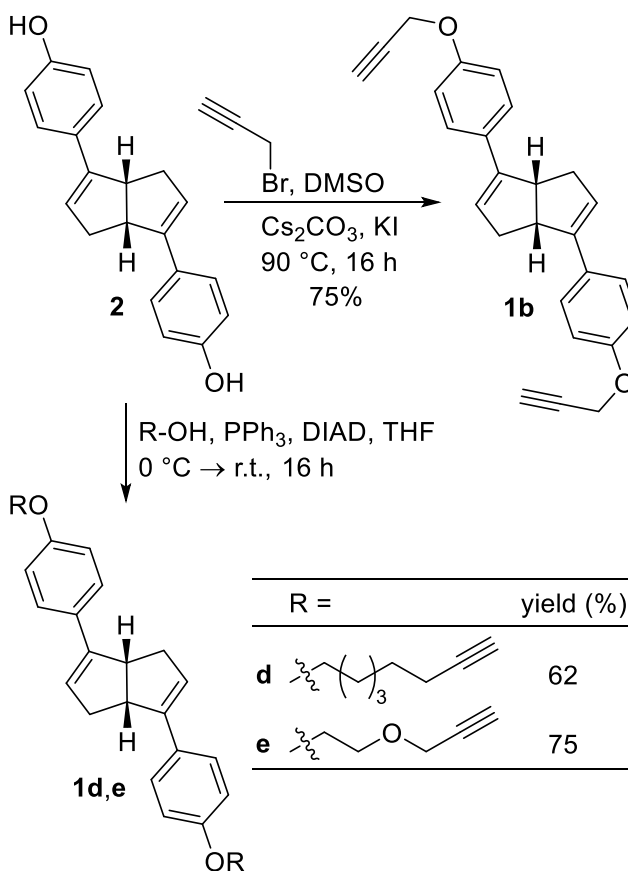
Scheme 2. Synthesis of chiral dienes **1b**, **1d** and **1e.**

Table 1. Transition temperatures [°C] and enthalpies [kJ/mol] of pentalenes **1a-f** determined by DSC. Heating/cooling rate 5 K/min.

Comp		Transition temperatures (and enthalpies)				Range/K	
1a	Cr	77 (36.4)	SmA	108 (0.2)	I	31	1st heat
	Cr	26 (−12.2)	SmA	105 (−0.3)	I	79	1st cool
1b	Cr	114 (26.3)	-	-	I	-	1st heat
	Cr	96 (−24,8)	-	-	I	-	1st cool
1 c	Cr	77 (26.7)	SmA	114 (0.2)	I	37	1st heat
	Cr	30 (−11.5)	SmA	108 (−0.2)	I	78	1st cool
1d	Cr	42 (17.5)	SmA	122 (1.3)	I	80	1st heat
	Cr	37 (−16.4)	SmA	120 (−0.3)	I	85	1st cool
1e	Cr	84 (17.4)	SmA	107 (0.1)	I	23	1st heat
	Cr	52 (−13.3)	SmA	105[a]	I	53	1st cool
1 f	Cr	72 (40.9)	-	-	I	-	1st heat
	Cr	46[a]	SmA	74[a]	I	28	1st cool

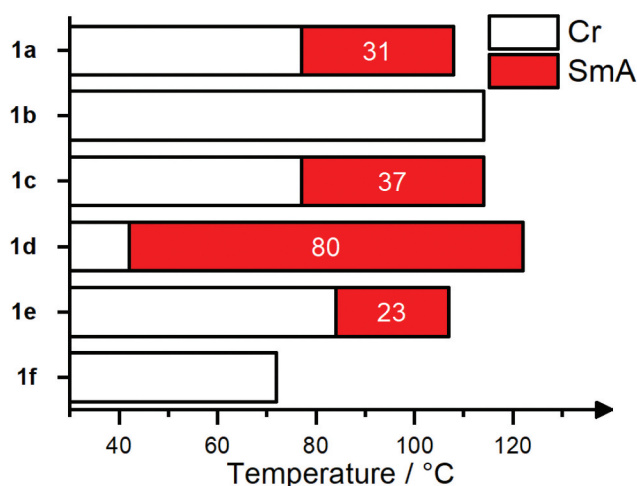[a]Phase transitions were determined by POM.

Figure 1. (Colour online) Phase widths of shown pentalene derivatives determined during the first heating cycle.
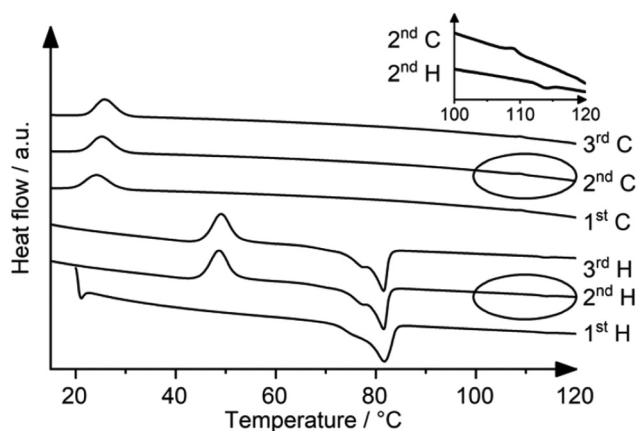

Figure 2. DSC curves of diene **1c**. Heating/cooling rates 5 K/min. The inset shows the weak transition into the isotropic liquid during the second cycle.

cooling, the isotropic to mesophase transition was observed at 108°C, and an exothermal crystallisation peak at 30°C. During 2nd heating a cold crystallisation was

detected at 45°C, followed by crystal to crystal, crystal to mesophase and clearing transitions, respectively. Further heating/cooling cycles looked similar.

Diene **1d** with 7-octinyloxy side chains showed a broad melting point between 42°C and 71°C in the first heating cycle (Figure S1c). The endothermic transition from the mesophase into the isotropic liquid at 122°C displayed two peaks, indicating decomposition. During cooling, the isotropic to mesophase transition was detected at 120°C. However, the observed enthalpy was reduced significantly as compared to the transition in the heating cycle. Crystallisation occurred at 37°C. Further iterations looked similar, but transition temperatures and enthalpies between mesophase and isotropic liquid slowly degraded during heating and cooling.

At a first glance, the DSC curves of diene **1e** with ethylenglycol spacer looked similar to **1d** (Figure S1d). Upon 1st heating compound **1e** showed an endothermal crystal to crystal transition at 75°C, an endothermal melting transition at 85°C and a very weak clearing transition at 107°C. Upon subsequent cooling the crystallisation peak at 52°C occurred. However, during 2nd and 3rd heating/cooling cycles the crystallisation peak disappeared from the cooling curve suggesting that thermal decomposition had taken place.

Diene **1f** with two ethylene glycol units and terminal alkyne chains showed a broad melting point between 72°C and 92°C during the first heating (Figure S1e), and when zoomed in, a small exothermic transition at 74°C became visible upon cooling, indicating a monotropic mesophase. Crystallisation was not visible via DSC during cooling. In further heating iterations, crystallisation was observed at 19°C followed by a broad melting transition at 72°C.

Changing from aliphatic side chains (**1a,c**) to ethylene glycol-based chains (**1e**) increased the melting point by 7 K, while the clearing temperature stayed nearly the same. Presumably, the higher polarity of the ether units leads to stronger London forces, and thus stabilising the crystalline state. In contrast to the favoured *all-trans*

conformation of alkyl chains, polyethylene glycol chains tend to have a more compact conformation [15].[2] Moreover, the repulsion between negatively charged oxygen atoms of neighbouring chains might disfavour lamellar packing. Those two aspects might be the reason for the monotropic mesophase of **1f** compared to the broad enantiotropic phase of **1d**.

It can be argued that both the sluggish tendency to crystallise and the low clearing enthalpies of compounds **1c-f** can be traced back to the particular nature of the mesogenic core. The molecular structure, which deviates from the perfect rod-like mesogen causes a high molecular biaxiality which increases the amount of free volume and therefore disfavours crystallisation. On the other hand, high biaxiality reduces the entropy change during the clearing transition [16].

During investigations by polarising optical microscopy (POM) compound **1a** showed Maltese crosses at 111°C upon cooling from the isotropic liquid, strongly hinting a SmA phase (Figure 3(a)). However, further cooling
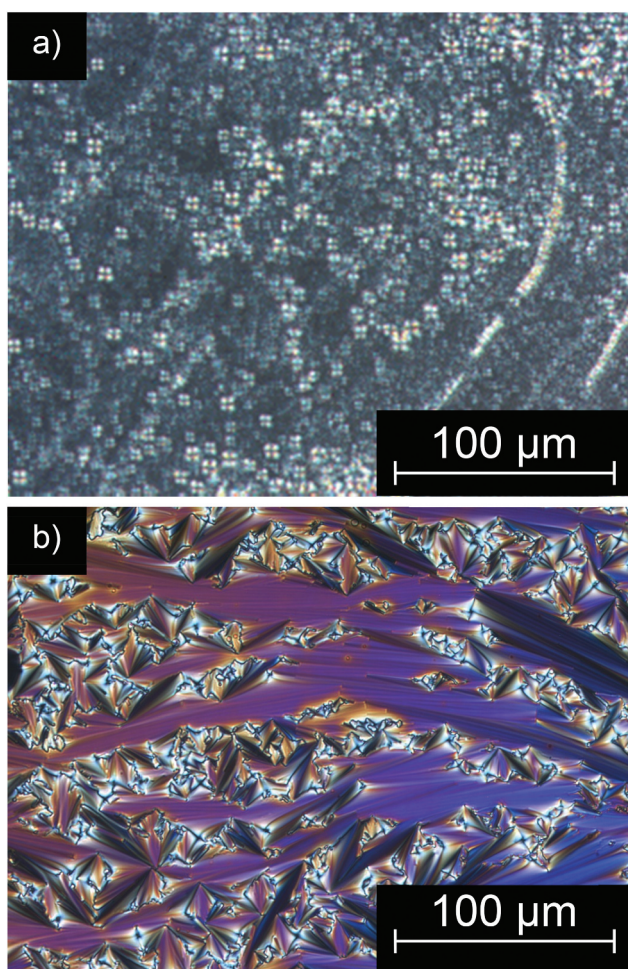
did not result in a typical crystallisation. At 26°C, the mesophase textures disappeared and a homeotropically aligned glass formed. Analogous to the observations by DSC this glass transformed into a crystal when reheated to 35°C (Figures S1 and S2d-g). For compound **1c** with alkyne terminated side chains fan-shaped textures were observed at 91°C (Figure 3(b)), again indicating a SmA phase. Similar textures were observed in the case of compounds side **1e,f** with (di)ethylenglycol side chains (Figure S2b,c). In the case of **1d** only uncharacteristic textures were observed (Figure S2a); however, due to the structural similarities with the other compounds, a SmA phase was assumed.

In order to gain further understanding of the mesophase, XRD measurements were performed. Wide-angle X-ray scattering (WAXS) of diene **1a** with alkyl chain and **1c** with alkyne chain revealed a sharp signal at $2\Theta = 3.2°$ for **1a** and 3.3° for **1c** and a broad reflex in the wide-angle range with the maximum at 20.2° in both cases (Figures 4 (a) and S3). These results matched very well with the proposed lamellar phase. The sharp reflexes can be assigned to the lamellar layers of a smectic phase (001), while the broad signal represents the molten alkyl chains (halo). The XRD data of **1a** and **1c** are summarised in Table 2. Due to trigonometric reasons, the layer spacing d of **1a** is about 1 Å larger than d of alkyne derivative **1c**. The linear geometry of the alkyne unit in **1a** leads to a longer sidechain despite the shorter bond length. However, in both cases d is about 1 Å smaller than the calculated molecular length [17]. This might be due to random tilts of the molecules and indicates a monolayer. Temperature-dependent SAXS measurements revealed a slight increase of the smectic layer spacing of ca. 0.8% throughout the mesophase (Figure 4(b,c)) contradicting the expected SmA phase. In most cases, orthogonal mesophases decrease their layer spacing upon heating. With higher temperatures, the smectic order partner decreases, and the molecules possess a larger tilt. However, on average, the molecules are still orthogonally aligned with respect to the layer direction. In our case, there must be an antagonistic effect to the diffuse cone model [18]. This phenomenon might be caused by the particular nature of the core. The bicyclo[3.3.0]octadiene unit is rigid, but not planar and behaves like an open book scaffold. The angle between the two five-membered rings might change depending on the temperature. This would have a big impact on the overall molecular geometry and therefore counterbalance the expected layer shrinkage caused by a reduced smectic order parameter.

The resulting packing model (Figure 5) is supported by the previously reported solid state data of diene **1f** [8]. As shown in Figure S4, in the solid state the acetylene moieties of neighbouring layers are not coplanar oriented; thus, π-
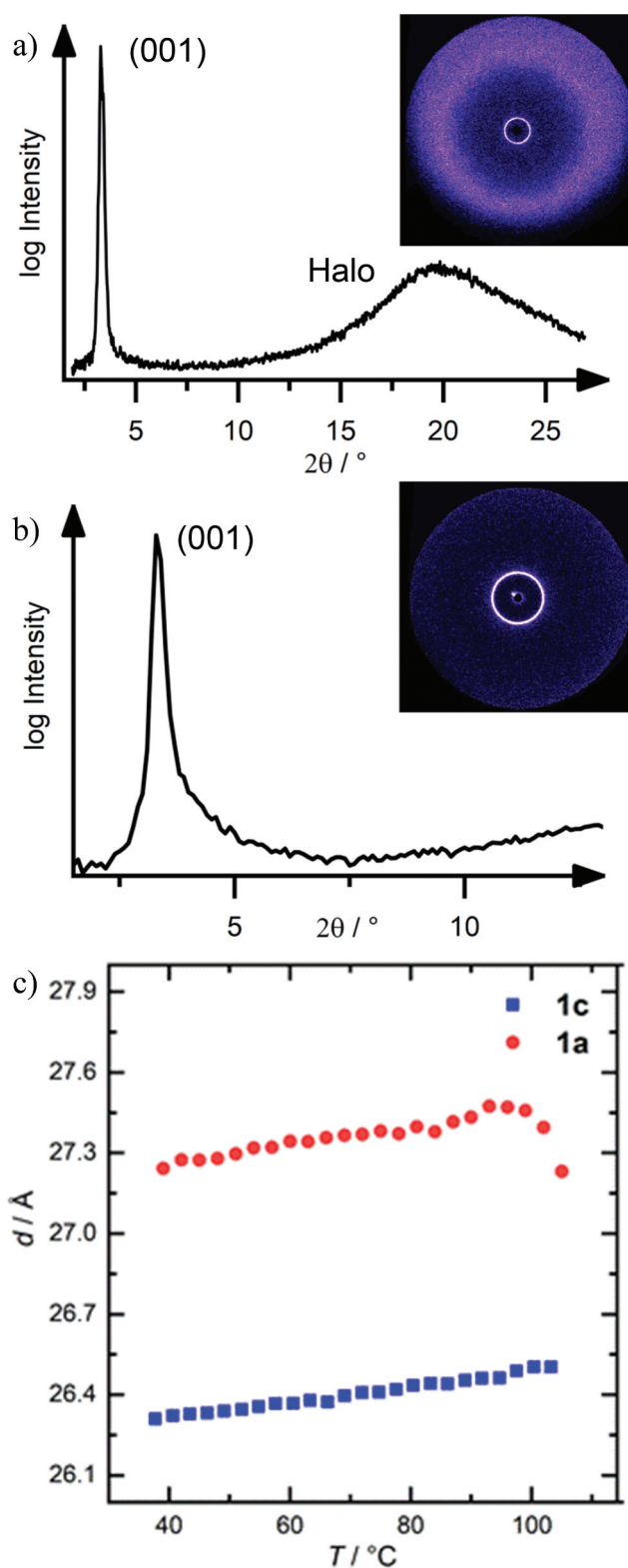
Figure 3. (Colour online) (a) Maltese crosses of **1a** at 111°C and (b) fan textures of **1c** at 91°C under the POM upon cooling from the isotropic liquid (cooling rate: 5 K/min).

Table 2. X-ray diffraction data of dienes **1a** and **1c**.

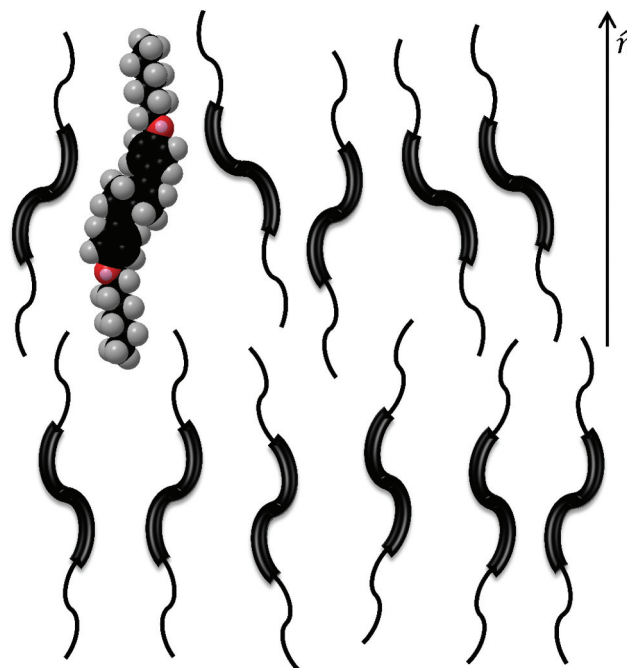| Diene	Mesophase	d-values/Å	Miller Indices
1a	SmA at 93°C	27.5	(001)
		4.4	halo
1c	SmA at 93°C	26.5	(001)
		4.4	halo

Figure 5. (Colour online) Proposed packing model of liquid crystalline pentalene derivatives, exemplary shown for diene **1a**.

π-stacking interaction is only partially possible due to the laterally shifted C≡C triple bonds. The molecules stack by minimising the free volume. However, the serpentine geometry of the mesogen disfavours a tight packing, which results in low clearing enthalpies. Nanosegregation between the rigid core and the flexible side chains enforces the formation of layers leading in a SmA phase.

Conclusion

A series of chiral bicyclo[3.3.0]octadienes **1** carrying alkoxy, alkinyloxy or (di)ethyleneglycolpropargylic ether side chains, which were originally intended as ligands for asymmetric catalysis have been synthesised and probed for their mesomorphic properties. Dienes **1c,d** with alkinyloxy side chains behaved similarly as compared to diene **1a** with alkoxy side chains yielding enantiotropic SmA phases. In contrast, propargylether side chains compromised mesophase formation either fully, when directly bound to the diene core (**1b**) or reduced the temperature range and mesophase stability when tethered via a mono- or

Figure 4. (Colour online) (a) WAXS XRD profile of diene **1c** in a glass capillary at 93°C (inset: 2-dimensional diffraction pattern). (b) Exemplary SAXS XRD profile of diene **1c** in a glass capillary at 92°C (inset: 2-dimensional diffraction pattern). (c) Temperature dependent layer spacing d of diene **1a** and **1c** determined by SAXS results.

diethyleneglycol unit (**1e,f**). Besides providing insight into the influence of terminal alkyne moieties on the mesomorphic properties of calamitic liquid crystals this work introduced open book-shaped bicyclo[3.3.0]octadienes as novel calamitic mesogens. Future work must demonstrate whether this unique carbobicyclic scaffold can be used for other liquid crystalline compounds or as potential chiral doping agents for known mesogens.

Notes

1. For other terminal group modifications.
2. One could compare this carefully with our crystal structure in Figure S4.

Acknowledgments

Disclosure statement

No potential conflict of interest was reported by the author(s).

Funding

References

[1] Nagamoto M, Nishimura T. Asymmetric transformations under Iridium/Chiral diene catalysis. ACS Catal. 2017;7:833–847.

[2] Feng CG, Xu MH, Lin GQ. Development of bicyclo [3.3.0]octadiene- or dicyclopentadiene-based chiral diene ligands for transition-metal-catalyzed reactions. Synlett. 2011;10:1345–1356.

[3] Helbig S, Sauer S, Cramer N, et al. Chiral bicyclo[3.3.0] octa-2,5-dienes as steering ligands in substrate-dependent rhodium-catalyzed 1,4-addition of arylboronic acids to enones. Adv Synth Catal. 2007;349(14–15):2331–2337.

[4] Wang ZQ, Feng CG, Xu MH, et al. Design of C_2-symmetric tetrahydropentalenes as new chiral diene ligands for highly enantioselective Rh-catalyzed arylation of *N*-tosylarylimines with arylboronic acids. J Am Chem Soc. 2007;129:5336–5337.

[5] Helbig S, Axenov KV, Tussetschläger S, et al. Application of chiral tetrahydropentalene ligands in rhodium-catalyzed 1,4-addition of (*E*)-2-phenylethenyl- and (*Z*)-propenylboronic acids to enones. Tetrahedron Lett. 2012;53:3506–3509.

[6] Mühlhäuser T, Savin A, Frey W, et al. Role of regioisomeric bicyclo[3.3.0]octa-2,5-diene ligands in Rh catalysis: synthesis, structural analysis, theoretical study, and application in asymmetric 1,2- and 1,4-additions. J Org Chem. 2017;82(24):13468–13480. .

[7] Pecchioli T, Christmann M. Synthesis of highly enantioenriched propelladienes and their application as ligands in asymmetric Rh-catalyzed 1,4-additions. Org Lett. 2018;20(17):5256–5259.

[8] Deimling M, Kirchhof M, Schwager B, et al. Asymmetric catalysis in liquid confinement: probing the performance of novel chiral rhodium–diene complexes in microemulsions and conventional solvents. Chem Eur J. 2019;25(40):9464–9475. .

[9] Deimling M, Zens A, Park N, et al. Adventures and detours in the synthesis of hydropentalenes. Synlett. 2020;31:A–U.

[10] Stackhouse PJ, Hird M. Influence of acetylene-containing peripheral chains on the mesomorphic properties of triphenylene-based liquid crystals. Liq Cryst. 2009;36 (9):953–965.

[11] Han B, Hu P, Wang BQ, et al. Triphenylene discotic liquid crystal trimers synthesized by $Co_2(CO)_8$-catalyzed terminal alkyne [2 + 2 + 2] cycloaddition. Beilstein J Org Chem. 2013;9:2852–2861.

[12] Petrzilka M. Apolar acetylenic liquid crystals. Mol Cryst Liq Cryst. 1984;111(3–4):347–358.

[13] Zhu S, Zhu Y, Chigan J, et al. The effect of terminal epoxy modification on the mesomorphic and thermal stability of biphenyl ester liquid crystals. Liq Cryst. 2019;46(15):2149–2158. .

[14] Lee M, Nguyen M, Brandt C, et al. Catalytic hydroalkylation of allenes. Angew Chem Int Ed. 2017;56 (49):15703–15707. .

[15] Sasanuma Y, Sugita K. The attractive Gauche effect of ethylene oxides. Polym J. 2006;38(9):983–988.

[16] Chan TN, Lu Z, Yam WS, et al. Non-symmetric liquid crystal dimers containing an isoflavone moiety. Liq Cryst. 2012;39:393–402.

[17] Chem3D. Version 18.0.0.231, PerkinElmer Informatics, Inc. Optimization via MM2 forcefields.

[18] de Vries A. The description of the smectic *A* and *C* phases and the smectic *A*–*C* phase transition of TCOOB with a diffuse-cone model. J Chem Phys. 1979;71:25–31.

Paper III

PAPER

Check for updates

Liquid crystalline self-assembly of azulene–thiophene hybrids and their applications as OFET materials†

Finn Schulz, [ab] Shun Takamaru, [b] Tobias Bens, [c] Jun-ichi Hanna, [b] Biprajit Sarkar, *[c] Sabine Laschat *[a] and Hiroaki Iino *[b]

Orientational control within thin films is crucial for the preparation of organic field effect transistors (OFETs). The highly ordered liquid crystalline smectic E phase (SmE) is known as a powerful template for solution processed thin films. Here, we describe the synthesis and characterization of three novel azulene–thiophene hybrid materials. Liquid crystalline characterization showed the presence of wide SmE phases. Thin films were prepared by spin-coating at mesophase temperature. Due to the self-aligning properties of the SmE phase uniformly flat films with good molecular alignment were manufactured. Top contact bottom gate OFETs showed mobilities up to $(3.3 \pm 0.5) \times 10^{-3}$ cm^2 V^{-1} s^{-1}.

Introduction

In materials chemistry, the azulene moiety **Az** has received a lot of attention due to its unusual properties.[1–5] Owing to Hückel's rule, this aromatic isomer of naphthalene has a positively charged seven-membered ring and a negatively charged five-membered ring (Fig. 1(a)). The resulting permanent dipole moment of 1.08 D is combined with a deep blue color due to the non-alternant character of both aromatic rings.[6–8] Thus, the azulene moiety seems to mimic a larger polycyclic aromatic hydrocarbon in terms of the π-conjugation and HOMO–LUMO gap.[9,10]

Liquid crystalline (LC) materials are valued due to self-assembly and self-healing behavior while possessing a fluidity that can readily react to applied forces. Therefore, they are used in numerous applications like displays, smart windows and biosensors.[11,12] LC phases can further be used as templates for well orientated crystalline structures. Due to the intrinsic self-assembly of LCs a high degree of orientation and a molecular flatness in the films is achieved.[13,14] The self-assembly process

is not limited to a certain mesophase and applies generally to various LCs.[15] When cooled down, the LC film should crystallize to a uniform polycrystalline film. However, liquid-like phases such as the smectic A phase (SmA) and the crystalline phase have rather different thermal expansion-coefficients and structures. Volume contraction and reorientation during crystallization
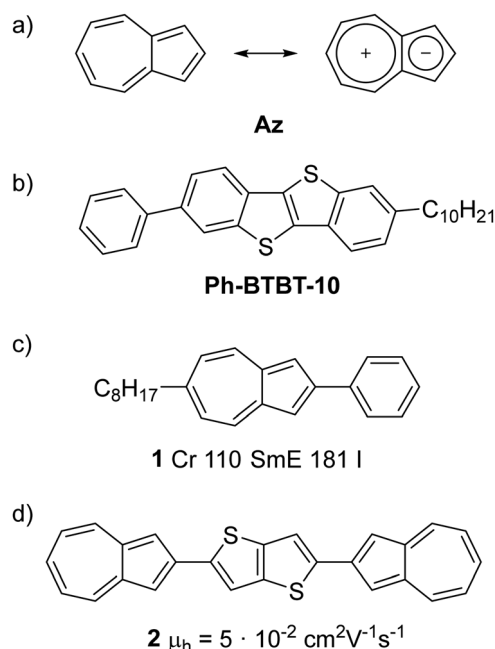
a Institut für Organische Chemie, Universität Stuttgart, Pfaffenwaldring 55, D-70569 Stuttgart, Germany. E-mail: sabine.laschat@oc.uni-stuttgart.de

b Imaging Science and Engineering Research Center, Tokyo Institute of Technology, J1-2, 4259 Nagatsuta, Midori-ku, Yokohama 226-8503, Japan. E-mail: iino@isl.titech.ac.jp

c Institut für Anorganische Chemie, Universität Stuttgart, Pfaffenwaldring 55, D-70569 Stuttgart, Germany. E-mail: sarkar@iac.uni-stuttgart.de

Fig. 1 (a) Resonance structures of azulene **Az** (b) structure of **Ph-BTBT-10**. (c) Example LCs and (d) OFETs **1–2** bearing azulene moieties.[26,32]

This journal is © the Owner Societies 2022

Phys. Chem. Chem. Phys., 2022, **24**, 23481–23489 | 23481

reduces the quality of the resulting crystalline film. Thus, mesophases whose molecular packing is more closely related to the crystalline phase, like the soft-crystalline smectic E phase (SmE), are more suitable.[16] Similar to the SmA phase, the SmE phase is based on a layered ordering of calamitic mesogens. But instead of a liquid-like ordering within the layers, a long-range translational order and a herringbone packing are present. Nevertheless, oscillations around the long axis of the molecules are possible.[17] Due to the close structural relationship between the SmE phase and the crystalline phase, minimum volume contraction and optimal transfer of molecular orientation during crystallization is possible. Iino *et al.* demonstrated the templating effect of the SmE phase by preparing molecularly flat thin films of **Ph-BTBT-10** (Fig. 1(b)).[18] They also showed that the herringbone pattern was conserved in the crystallized film and fabricated potent organic field effect transistors (OFETs) with great application potential.[19–23]

Although there have been several reports on azulene-based liquid crystals[24–28] and OFETs (Fig. 1(c) and (d)),[29–37] the combination of the unique properties of azulene **Az** and the strong templating effect of the SmE phase remains unknown. In our research we focused on the combination of azulene with small thiophene derivatives, a non-alternant heteroaromatic moiety successfully used in organic electronics.[38–40] Herein, we report novel calamitic mesogens with azulene cores **12O-Az-T**, **12O-Az-iT** and **12O-Az-BT** (Fig. 2). All compounds displayed broad SmE phases, that were suitable for the easy preparation of polycrystalline thin films. The thermal rearrangement of these films into a bilayer crystal structure was investigated and the films were integrated in OFETs.
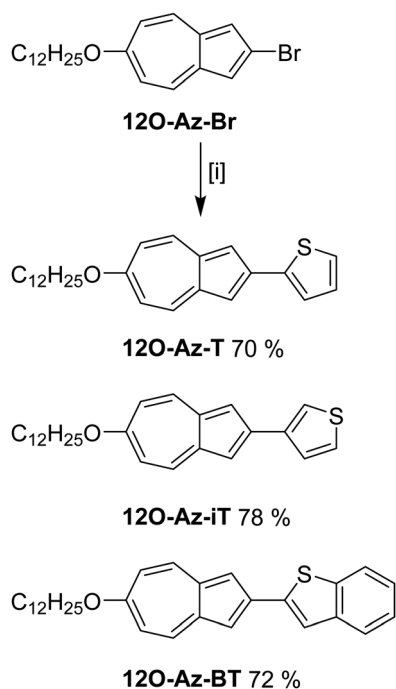

Fig. 2 Synthesis of azulene–thiophene hybrids *via* Suzuki cross-coupling. [i] RB(OH)$_2$ or RBpin, Pd(PPh$_3$)$_4$, Cs$_2$CO$_3$, dioxane, reflux, 3 h.

Synthesis

We recently reported on a series of 6-alkoxy-2-bromoazulenes **12O-Az-Br** forming SmE phases.[41] Expansion of the aromatic core *via* Suzuki-coupling with thiophene derivatives should increase the clearing temperature of the soft-crystalline phase and enforce a moderate conductivity. Alkoxy chains are rarely used in OSCs. This might be due to more complicated synthesis routes compared to simple alkyl chains. However, the mesomeric effect of the ether group increases the HOMO level of the target molecule and therefore reduces contact resistances at the electrodes.[42]

Three different azulene–thiophene hybrids were synthesized with commercially available thiophene boronic acids (Fig. 2). Aside from thiophene rings with connections in the 2-position (**12O-Az-T**) and the 3-position (**12O-Az-iT**), a benzo[*b*]thiophene (**12O-Az-BT**) moiety was also introduced. In this case the pinacol boronic ester gave better yields. This might be due to slower deboronation during the reaction conditions.[43]

Liquid crystalline properties

The mesomorphic properties of the azulene compounds were characterized by differential scanning calorimetry (DSC), polarizing optical microscopy (POM) and wide-angle X-ray scattering (WAXS). The thermograms of all compounds are shown in Fig. S1 (ESI†) and the transition temperatures are summarized in Table 1. **12O-Az-T** and **12O-Az-iT** displayed two endothermic first-order transitions during the heating cycles, which were assigned as melting and clearing point. During cooling strong hysteresis of the crystallization was observed. In subsequent heating cycles an exothermic crystal–crystal transition indicated a crystal-to-crystal transition before entering the mesophase. The second crystalline phase (Cr$_2$) seems to be the thermodynamically stable structure and might also be the reason for different melting points during the first heating cycle, as after recrystallization Cr$_2$ is present. **12O-Az-BT** showed similar melting behavior in the first heating cycle and cleared into the isotropic melt at 270 °C. During cooling a weak exothermic transition (3.0 kJ mol^{-1}) indicated the crystallization of the sample at 51 °C. In contrast to the other azulene derivatives no cold crystallization was observed. As a result, the Cr$_1$ phase directly melted into the mesophase through a second-order transition at 76 °C. The phase width of the mesophase increased throughout the series from **12O-Az-T** (150 K) over **12O-Az-iT** (174 K) and peaked at **12O-Az-BT** at 219 K during cooling.

For assignment of the mesophases the compounds were examined between crossed polarizers using POM. Platelet textures strongly hinted the presence of a soft-crystalline SmE phase in all cases (Fig. 3 and Fig. S2, ESI†).[44]

WAXS is a powerful tool for the characterization of the mesophase geometry. The diffraction pattern and diffractogram of **12O-Az-T** is shown in Fig. 4 (Fig. S3 for all X-ray data, ESI†). The layer like-structure of the SmE phase causes an intensive

23482 | *Phys. Chem. Chem. Phys.*, 2022, **24**, 23481–23489

This journal is © the Owner Societies 2022

Compound		$T/$°C (ΔH/kJ mol^{-1})							Range/K	
12O-Az-T	Cr$_1$	51 (−15.7)	Cr$_2$	95 (23.5)	SmE	186 (17.4)	I		91	2nd heat
	Cr$_1$	32 (−7.9)	—	—	SmE	182 (−17.4)	I		150	2nd cool
12O-Az-iT	Cr$_1$	63 (−15.5)	Cr$_2$	104 (34.0)	SmE	228 (29.1)	I		114	2nd heat
	Cr$_1$	53 (−15.6)	—	—	SmE	227 (−29.6)	I		174	2nd cool
12O-Az-BT	Cr$_1$	76^a	—	—	SmE	270 (30.0)	I		194	2nd heat
	Cr$_1$	51 (−3.0)	—	—	SmE	270 (−28.1)	I		219	2nd cool

Heating/cooling rate: 5 K min^{-1}. ^{a} Second order transition.
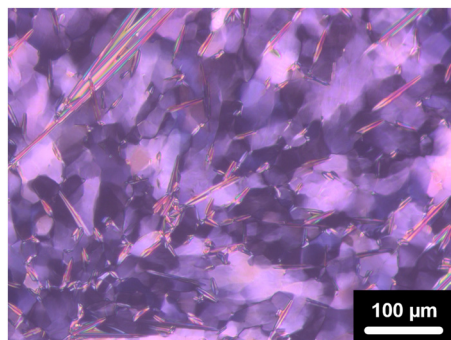

Fig. 3 Platelet textures of **12O-Az-iT** at 222 °C between crossed polarizers.

Bragg-like reflex in the small angle area. At larger angles, the broad halo of the molten side chains is overlayed by three signals. This characteristic pattern for herringbone packing of SmE phases was observed for all compounds (Table 2).[45] The layer spacings of the SmE phases are slightly longer than the calculated molecular lengths. This can be explained by a strongly interdigitating bilayer. It is noteworthy that **12O-Az-BT** shows a 2 Å shorter layer spacing despite the molecule being 2 Å longer. However, the most remarkable difference between the packing of

12O-Az-BT and those of **12O-Az-T** and **12O-Az-iT** is found within the layer: while the lattice parameters of **12O-Az-BT** a = 7.88 Å and b = 5.82 Å are relatively close to each other, in case of **12O-Az-T** and **12O-Az-iT** a is more than two times larger than b (Fig. 5(a)). The resulting packing resembles a herringbone packing with a dihedral angle of 120° instead of the usual 60° (Fig. 5(a)). According to Desiraju and Gavezzotti such packing has been designated as a γ-structure.[46] Additionally, alkyl–alkyl distances in **12O-Az-BT** are 0.6 Å smaller. To rationalize these observations, we took a closer look at the molecular structure. Due to the double bicyclic core of **12O-Az-BT**, improved overlap of the whole π-system in an anti-parallel packing results in minimization of free volume and enforces nanophase segregation (Fig. 5(b)). Such overlap is much weaker for the derivatives carrying only a monocyclic thiophene unit. In this case only the zwitterionic azulene moiety stacks with each other and the thiophene ring has no adequate partner left (Fig. 5(c)). A smaller π-overlap decreases the attractive interactions, expanding the lattice in one dimension. Therefore, the tilt in the herringbone packing might be reduced, allowing tighter stacking along b. As a result, the density of **12O-Az-BT** (1.02 g cm^{-3}) is much higher than of the other azulene–thiophene hybrids (0.76 g cm^{-3}). The higher degree of space filling might also explain the reluctance to form a bilayer crystal structure in agreement with the above discussed DSC data.

Thin film characterization

Having secured the phase geometry in the LC state, we investigated the LC to crystal transition in thin films. All derivatives had a sufficient solubility in *p*-xylene and therefore, could be spin-coated as a 0.5 wt% solution at 60 °C substrate temperature. We used in-plane and out-of-plane X-ray diffractometry (XRD) to evaluate the molecular orientation. In general, for molecules with only one alkyl chain, the monolayer crystal structure similar to the liquid crystalline phase can be changed into a bilayer crystal structure by thermal annealing, which also might boost the mobility of the OTFT.[18,47–49] As the investigated compounds showed an exothermic crystal to crystal transition during heating in DSC, a monolayer crystal structure to bilayer crystal structure transformation might also take place in our case. Surprisingly, films of **12O-Az-T** directly transformed into a bilayer crystal structure during spin-coating because the layer spacing is 50.9 Å (Fig. 6(a)). Subsequent annealing at 80 °C for 5 min did not affect the film any further. **12O-Az-iT** and **12O-Az-BT** showed
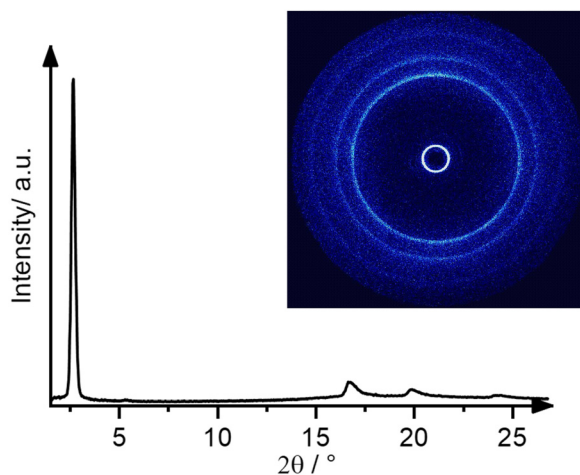

Fig. 4 WAXS diffraction pattern and diffractogram of the SmE phase of **12O-Az-T** at 115 °C.

Table 2 Lattice constants and observed reflexes in WAXS measurements (SmE) and XRD measurements of thin films (crystalline phase) of the compounds **12O-Az-Ar**

Compound	Lattice constants/Å	Spacing/Å		Miller indices (hkl)
		Observed	(calculated)	
12O-Az-T	(SmE at 115 °C, heating)	33.16	(33.16)	(001)
	$a = 10.54$	16.59	(16.58)	(002)
	$b = 4.94$	5.27	(5.27)	(200)
	$c = 33.16$	4.44	(4.47)	(110)
	Molecular length: 26.7[a]	3.62	(3.60)	(210)
	$Z = 2.0$, $\rho = 0.76$[b]	4.45	—	Halo
12O-Az-iT	(SmE at 118 °C, cooling)	33.56	(33.56)	(001)
	$a = 10.46$	16.79	(16.78)	(002)
	$b = 4.88$	5.23	(5.23)	(200)
	$c = 33.56$	4.41	(4.42)	(110)
	Molecular length: 26.7[a]	3.58	(3.57)	(210)
	$Z = 2.0$, $\rho = 0.76$[b]	4.43	—	Halo
12O-Az-BT	(SmE at 143 °C, heating)	31.58	(31.50)	(001)
	$a = 7.88$	15.74	(15.75)	(002)
	$b = 5.82$	10.48	(10.50)	(003)
	$c = 31.58$	4.67	(4.68)	(110)
	Molecular length: 29.0[a]	3.94	(3.94)	(200)
	$Z = 2.0$, $\rho = 1.02$[b]	3.27	(3.26)	(210)
		3.78	—	Halo
12O-Az-T	(Thin film, bilayer crystal structure)	50.92	(50.92)	(001)
	$a = 7.50$	25.68	(25.46)	(002)
	$b = 6.24$	12.72	(12.72)	(004)
	$c = 50.92$	4.80	(4.80)	(110)
	Molecular length: 26.7[a]	3.75	(3.75)	(200)
	$Z = 4.0$, $\rho = 1.10$[b]	3.21	(3.21)	(210)
12O-Az-iT	(Thin film, monolayer crystal structure)	25.22	(25.22)	(001)
	$a = 7.69$	12.84	(12.61)	(002)
	$b = 5.79$	4.63	(4.63)	(110)
	$c = 25.22$	3.85	(3.85)	(200)
	Molecular length: 26.7[a]	3.20	(3.20)	(210)
	$Z = 2.0$, $\rho = 1.17$[b]			
12O-Az-iT	(Thin film, bilayer crystal structure)	57.99	(51.35)[c]	(001)
	$a = 7.48$	25.73	(25.68)	(002)
	$b = 6.12$	12.82	(12.84)	(004)
	$c = 51.35$	4.74	(4.74)	(110)
	Molecular length: 26.7[a]	3.74	(3.74)	(200)
	$Z = 4.0$, $\rho = 1.12$[b]	3.19	(3.19)	(210)
12O-Az-BT	(Thin film, monolayer crystal structure)	30.51	(28.17)[c]	(001)
	$a = 7.82$	9.39	(9.39)	(003)
	$b = 5.82$	4.67	(4.67)	(110)
	$c = 28.17$	3.91	(3.91)	(200)
	Molecular length: 29.0[a]	3.24	(3.25)	(210)
	$Z = 2.0$, $\rho = 1.15$[b]			
12O-Az-BT	(Thin film, bilayer crystal structure)	65.77	(56.70)[c]	(001)
	$a = 7.69$	28.63	(28.35)	(002)
	$b = 5.79$	18.70	(18.90)	(003)
	$c = 56.70$	14.28	(14.18)	(004)
	Molecular length: 29.0[a]	9.39	(9.45)	(006)
	$Z = 4.0$, $\rho = 1.15$[b]	4.70	(4.70)	(110)
		3.80	(3.80)	(200)
		3.22	(3.21)	(210)

[a] Calculated with Chem3D. [b] Density calculated for $Z = 2$ or 4 (g cm^{-3}). [c] The strong deviation of the (001) reflex is due to the intensity strongly increasing when 2θ approaches 0°.

the expected monolayer crystal structure after coating with layer spacings being 25.3 Å and 30.5 Å, respectively. Under the same annealing conditions **12O-Az-iT** smoothly underwent a transition into a bilayer crystal structure. **12O-Az-BT** was reluctant to form a bilayer crystal structure under these conditions. This might be contributed to the already high degree of space filling in the monolayer crystal structure. However, annealing at 85 °C for 19 h was sufficient to enforce the thermodynamically favored bilayer crystal structure. For the bilayer

crystal structures more and stronger higher ordered layer reflexes were observed, indicating an increase of crystallinity during the transition.

No layer reflexes were visible in in-plane XRD measurements (Fig. 6(b)). Spin-coating at mesophase temperature ensured the alignment of the long molecular axis to be perpendicular to the surface. It should be noted that the crystal structures of all compounds seem to follow the herringbone packing similar to the mesophase of **12O-Az-BT**. The lattice constants of the

23484 | *Phys. Chem. Chem. Phys.*, 2022, **24**, 23481–23489
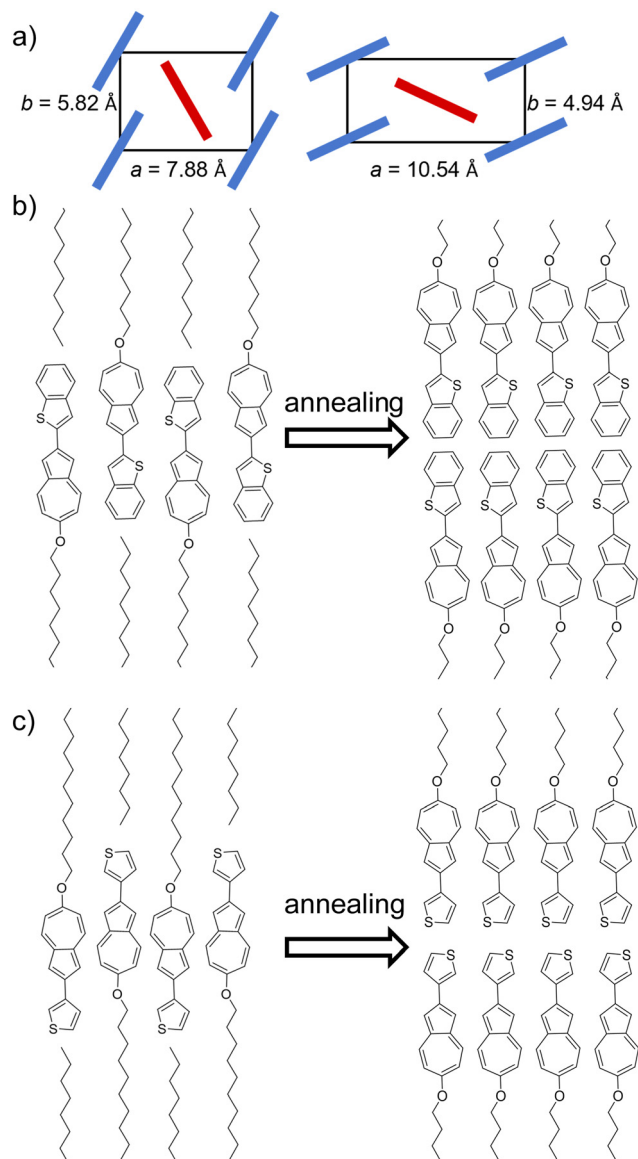
This journal is © the Owner Societies 2022

Fig. 5 (a) Top view of the anti-parallel herringbone packing of **12O-Az-BT** (left) and **12O-Az-T** (right) in the SmE phase. (b) Assumed packing model of **12O-Az-BT** in the SmE-phase and monolayer crystal structure (left) and after annealing in the bilayer crystal structure (right). (c) Corresponding packing model for **12O-Az-iT** and **12O-Az-T**.
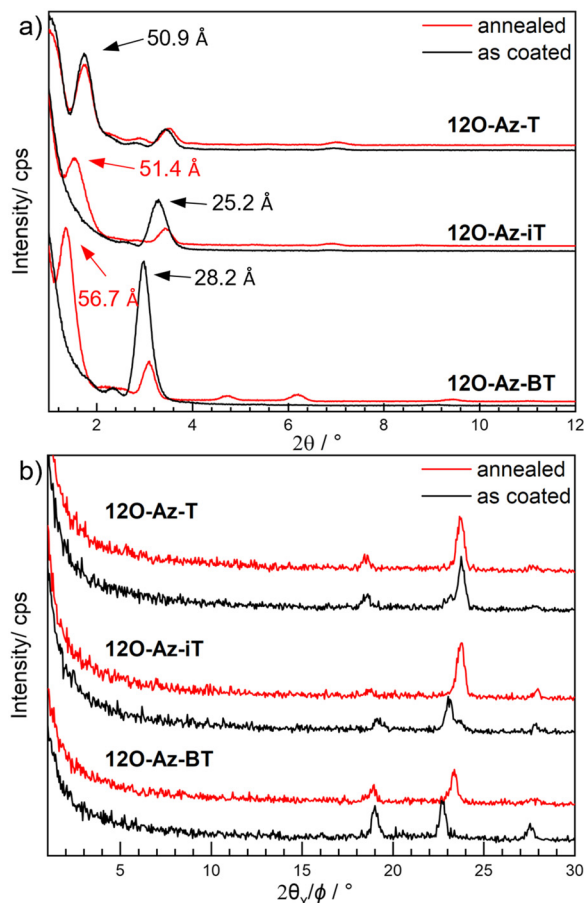

Fig. 6 X-ray diffraction experiments of thin films of **12O-Az-Ar** before and after annealing: (a) out-of-plane XRD and (b) in-plane XRD. Annealing conditions: **12O-Az-T** and **12O-Az-iT**: 80 °C, 5 min; **12O-Az-BT**: 85 °C, 19 h.

crystalline thin films in Table 2 revealed, that no γ-structure was observed for the crystalline phase.

Uniformity and thickness of the films were evaluated by optical microscopy, confocal laser scanning microscopy and atomic force microscopy (AFM). The as coated film of **12O-Az-BT** is uniform with a thickness of about 40 nm (Fig. 7(a)). After annealing the uniformity is slightly reduced and the film thickness decreased. Films of **12O-Az-iT** and **12O-Az-T** were only 20 nm thick. The decrease of uniformity during annealing had a stronger effect on the thin films of **12O-Az-iT** (Fig. S10a and b, ESI†). AFM images of **12O-Az-BT** showed a terrace structure with steps of 3.1 nm, which resemble the molecular layer spacing (Fig. 7(b)). After annealing the steps changed to the molecular layer spacing of the bilayer

(Fig. S11, ESI†). For **12O-Az-T** and **12O-Az-iT** these steps were also observed. But after annealing the terrace areas became smaller (Fig. S11, ESI†).

OFET properties

For optimum carrier injection, the HOMO level of the OSCs should match the working function of the electrode metal (5.1 eV for gold[50]). HOMO energies were determined by cyclic voltammetry (CV) (Fig. S4–S9, ESI†) and DFT calculations with the B3LYP functional and def2-TZVP basis set (Table 3).[51] The estimated HOMO levels are very close to the optimal values, suggesting an easy charge injection. It should be noted that Yamaguchi *et al.* reported, that different regioisomers of ter-azulenes showed drastically different HOMO shapes and charge carrier properties.[34] Since azulene is a non-alternant hydrocarbon, we expected a similar behavior in all π-elongated azulene derivatives. According to a report by Ran *et al.* better results regarding transistor properties were reported for terminal azulene units connected in 2-position compared to 6-connected units.[37] Therefore, we decided to focus on the 2-connected azulenes. However, in our case the small number of studied
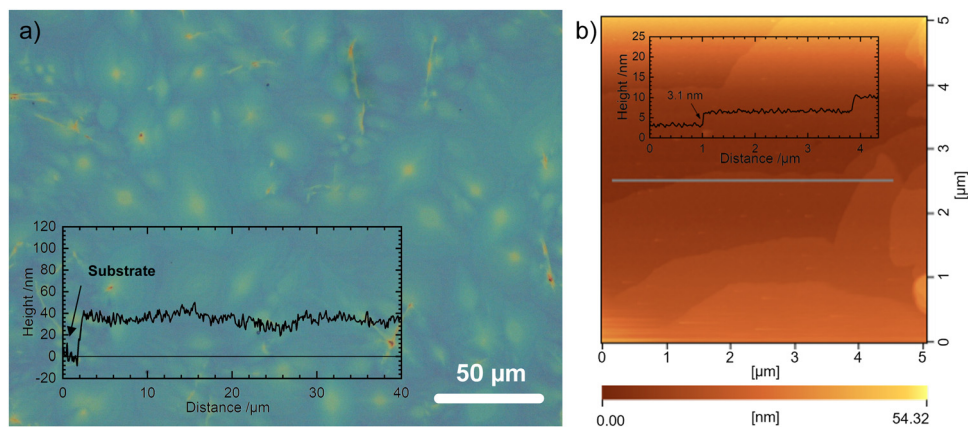
Fig. 7 Images of polycrystalline thin films of **12O-Az-BT** fabricated by spin-coating a 0.5 wt% solution in *p*-xylene at 60 °C. (a) Textures determined by optical microscopy and (b) film observed *via* AFM. Insets show cross-sectional profiles observed by (a) confocal laser scanning microscopy and (b) AFM.

Table 3 HOMO levels of **12O-Az-Ar** calculated *via* cyclic voltammetry or DFT

Compound	HOMO (CV)/eV	HOMO (DFT)/eV
12O-Az-T	−5.4	−5.3
12O-Az-iT	−5.4	−5.4
12O-Az-BT	−5.5	−5.3

azulene derivatives does not allow a more detailed discussion of HOMO shapes and their relation to the transistor properties.

After characterizing the thin film and electronic properties of **12O-Az-Ar**, we examined our compounds in transistors. Top contact bottom gate transistors were manufactured by spin-coating the organic solution on a silicon substrate with 300 nm silicon dioxide as gate electrode and insulator. For p-channel transfer characteristics of **12O-Az-BT** 10 transistors on 2 substrates were measured (Fig. 8(a)). The hole mobility was calculated to be $\mu^+ = (3.1 \pm 0.5) \times 10^{-3}$ cm^2 V^{-1} s^{-1} with a threshold voltage of $V_{th} = -52 \pm 2$ V and a subthreshold swing

of 6.6 V decade^{-1}. The low variance of the FET performance is caused by the templating effect of the SmE phase during spin-coating. After annealing, a lower mobility of $\mu^+ = (5.1 \pm 0.8) \times 10^{-4}$ cm^2 V^{-1} s^{-1} and higher $V_{th} = -57 \pm 3$ V were observed. This decay of performance could be caused by nanophase segregation within the aromatic area. In the monolayer crystal structure azulene moieties interact with benzothiophene units (Fig. 5(b)). In the bilayer crystal structure, the azulene bicycle is neighbored by other azulenes. The identical partial charge might slightly repulse each other and therefore, change the transfer integral and the mobility of the transistor. Transistors of **12O-Az-T** and **12O-Az-iT** with a smaller core showed lower mobilities of $\mu = 2.2 \times 10^{-4}$ cm^2 V^{-1} s^{-1} for **12O-Az-T** and 4.1×10^{-4} cm^2 V^{-1} s^{-1} for **12O-Az-iT**. In both cases, V_{th} was 74 V (Fig. 8(b)).

We used the transfer length method (TLM) to estimate the impact of contact resistance between electrodes and the as coated thin film of **12O-Az-BT** (Fig. 8(c)).[52] The sum of both contact resistances seems to be 1.8 MΩ cm. This is only a small proportion of the resistance of the transistor. So, charge injections do not seem to impede the carrier mobility.
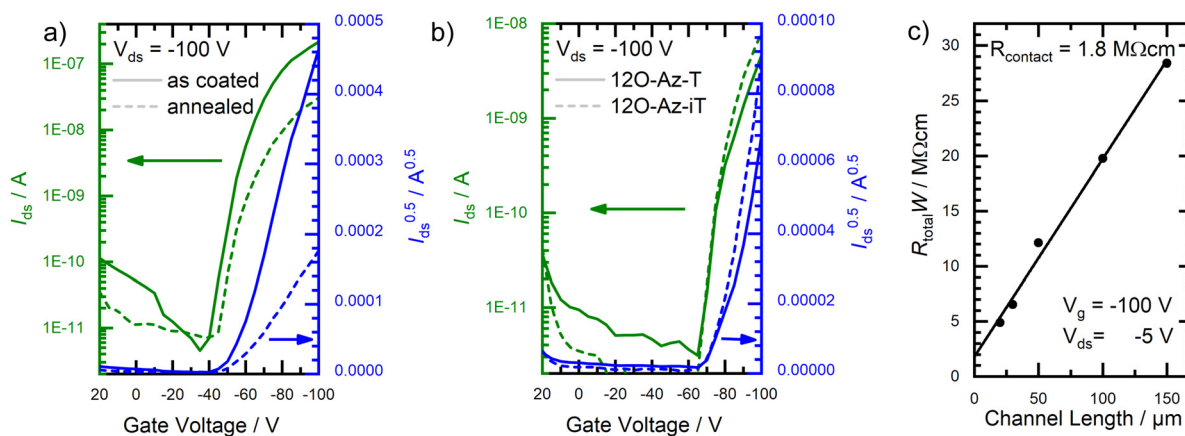

Fig. 8 (a) Transfer characteristics of polycrystalline thin films **12O-Az-BT** as coated and after annealing; (b) transfer characteristics of as coated films of **12O-Az-T** and **12O-Az-iT**. (c) Evaluation of the contact resistance of **12O-Az-BT** using the transfer length method (TLM).

23486 | *Phys. Chem. Chem. Phys.*, 2022, **24**, 23481–23489

This journal is © the Owner Societies 2022

Summary

In summary, we synthesized three novel azulene thiophene hybrids starting from the literature known **12O-Az-Br**. All compounds turned out to show the highly ordered SmE phase. X-ray analysis of the mesophase confirmed the presence of the sought-after herringbone-like packing. Spin-coating at liquid crystalline temperature resulted in well-orientated and reproducible poly-crystalline thin films. OFETs of the **12O-Az-BT** showed the best mobilities of $\mu = 3.1 \times 10^{-3}$ cm^2 V^{-1} s^{-1} with a low variance. Even though it was possible to enforce a bilayer-structure by consequent thermal annealing after spin-coating, this fact could not be used to improve FET performances. This might be caused by weak repulsive forces between partial charges on the azulene core. These results underline the importance of a deep understanding and a careful molecular design on the way to potent organic semiconductors.

Author contributions

Finn Schulz: conceptualization, formal analysis, investigation, funding acquisition, writing – original draft. Shun Takamaru: resources, validation, writing – review and editing. Tobias Bens: investigation, writing – review and editing. Jun-ichi Hanna: supervision, writing – review and editing. Biprajit Sarkar: funding acquisition, supervision, writing – review and editing. Sabine Laschat: conceptualization, funding acquisition, supervision, writing – review and editing. Hiroaki Iino: conceptualization, funding acquisition, supervision, writing – review and editing.

Conflicts of interest

There are no conflicts to declare.

Acknowledgements

References

1 H. Xin and X. Gao, Application of azulene in constructing organic optoelectronic materials: New tricks for an old dog, *ChemPlusChem*, 2017, **82**, 945–956.

2 Q. Fan, D. Martin-Jimenez, D. Ebeling, C. K. Krug, L. Brechmann, C. Kohlmeyer, G. Hilt, W. Hieringer, A. Schirmeisen and J. M. Gottfried, Nanoribbons with non-alternant topology from fusion of polyazulene: Carbon allotropes beyond graphene, *J. Am. Chem. Soc.*, 2019, **141**, 17713–17720.

3 E. Puodziukynaite, H.-W. Wang, J. Lawrence, A. J. Wise, T. P. Russell, M. D. Barnes and T. Emrick, Azulene methacrylate polymers: Synthesis, electronic properties, and solar cell fabrication, *J. Am. Chem. Soc.*, 2014, **136**, 11043–11049.

4 F. Schwarz, M. Koch, G. Kastlunger, H. Berke, R. Stadler, K. Venkatesan and E. Lörtscher, Charge transport and conductance switching of redox-active azulene derivatives, *Angew. Chem., Int. Ed.*, 2016, **55**, 11781–11786.

5 J. Yao, Z. Cai, Z. Liu, C. Yu, H. Luo, Y. Yang, S. Yang, G. Zhang and D. Zhang, Tuning the semiconducting behaviors of new alternating dithienyldiketopyrrolopyrrole–azulene conjugated polymers by varying the linking positions of azulene, *Macromolecules*, 2015, **48**, 2039–2047.

6 R. S. H. Liu, Colorful azulene and its equally colorful derivatives, *J. Chem. Educ.*, 2002, **79**, 183.

7 B. P. Klein, N. J. van der Heijden, S. R. Kachel, M. Franke, C. K. Krug, K. K. Greulich, L. Ruppenthal, P. Müller, P. Rosenow, S. Parhizkar, F. C. Bocquet, M. Schmid, W. Hieringer, R. J. Maurer, R. Tonner, C. Kumpf, I. Swart and J. M. Gottfried, Molecular topology and the surface chemical bond: Alternant *versus* nonalternant aromatic systems as functional structural elements, *Phys. Rev. X*, 2019, **9**, 011030.

8 A. G. Anderson and B. M. Steckler, Azulene. VIII. A study of the visible absorption spectra and dipole moments of some 1- and 1,3-substituted azulenes1,2, *J. Am. Chem. Soc.*, 1959, **81**, 4941–4946.

9 K. Kurotobi, K. S. Kim, S. B. Noh, D. Kim and A. Osuka, A quadruply azulene-fused porphyrin with intense near-IR absorption and a large two-photon absorption cross section, *Angew. Chem., Int. Ed.*, 2006, **45**, 3944–3947.

10 A. Muranaka, M. Yonehara and M. Uchiyama, Azulenocyanine: A new family of phthalocyanines with intense near-IR absorption, *J. Am. Chem. Soc.*, 2010, **132**, 7844–7845.

11 A. Hemaida, A. Ghosh, S. Sundaram and T. K. Mallick, Evaluation of thermal performance for a smart switchable adaptive polymer dispersed liquid crystal (PDLC) glazing, *Sol. Energy*, 2020, **195**, 185–193.

12 H. K. Bisoyi and Q. Li, Liquid crystals: Versatile self-organized smart soft materials, *Chem. Rev.*, 2022, **122**, 4887–4926.

13 H. Iino and J. Hanna, Availability of liquid crystalline molecules for polycrystalline organic semiconductor thin films, *Jpn. J. Appl. Phys.*, 2006, **45**, L867.

14 H. Iino and J. Hanna, Availability of liquid crystallinity in solution processing for polycrystalline thin films, *Adv. Mater.*, 2011, **23**, 1748–1751.

15 H. Iino and J. Hanna, Polycrystalline organic TFT fabricated by solution process using liquid crystalline material, *Mol. Cryst. Liq. Cryst.*, 2009, **510**, 259–267.

16 H. Iino and J. Hanna, Liquid crystalline organic semiconductors for organic transistor applications, *Polym. J.*, 2017, **49**, 23–30.

17 J. W. Goodby, R. J. Mandle, E. J. Davis, T. Zong and S. J. Cowling, What makes a liquid crystal? The effect of free volume on soft matter, *Liq. Cryst.*, 2015, **42**, 593–622.

18 H. Iino, T. Usui and J. Hanna, Liquid crystals for organic thin-film transistors, *Nat. Commun.*, 2015, **6**, 6828.

19 P. Mittal, S. Yadav and S. Negi, Advancements for organic thin film transistors: Structures, materials, performance parameters, influencing factors, models, fabrication, reliability and applications, *Mater. Sci. Semicond. Process.*, 2021, **133**, 105975.

20 T. Minami, Organic transistor-based chemical sensors with self-assembled monolayers, *J. Inclusion Phenom. Macrocyclic Chem.*, 2021, **101**, 1–18.

21 X. Guo, L. Han and X. Hou, Insights into the device structure, processing and material design for an organic thin-film transistor towards functional circuit integration, *Mater. Chem. Front.*, 2021, **5**, 6760–6778.

22 R. Kubota, Y. Sasaki, T. Minamiki and T. Minami, Chemical sensing platforms based on organic thin-film transistors functionalized with artificial receptors, *ACS Sens.*, 2019, **4**, 2571–2587.

23 H. Wang, Q. Wang and Y. Li, Two-dimensional organic materials and their electronic applications, *Chem. Lett.*, 2019, **48**, 14–21.

24 K. Praefcke, Erste flüssigkristalline Azulen-Derivate, *Z. Naturforsch.*, 1981, **36 b**, 375–378.

25 R. Brettle, D. A. Dunmur, S. Estdale and C. M. Marson, Synthesis, linear dichroism and mesogenic properties of substituted azulenes, *J. Mater. Chem.*, 1993, **3**, 327–331.

26 S. Ito, M. Ando, A. Nomura, N. Morita, C. Kabuto, H. Mukai, K. Ohta, J. Kawakami, A. Yoshizawa and A. Tajiri, Synthesis and properties of hexakis(6-octyl-2-azulenyl)benzene as a multielectron redox system with liquid crystalline behavior, *J. Org. Chem.*, 2005, **70**, 3939–3949.

27 S. E. Estdale, R. Brettle, D. A. Dunmur and C. M. Marson, The azulene ring as a structural element in liquid crystals, *J. Mater. Chem.*, 1997, **7**, 391–401.

28 E. de Domingo, M. Barcenilla, J. M. Martín-Alvarez, J. A. Miguel and S. Coco, The 2-isocyanoazulene-gold(I) fragment as a versatile element for organometallic dyes and liquid crystals, *Dyes Pigm.*, 2020, **176**, 108195.

29 E. C. P. Smits, S. Setayesh, T. D. Anthopoulos, M. Buechel, W. Nijssen, R. Coehoorn, P. W. M. Blom, B. de Boer and D. M. de Leeuw, Near-infrared light-emitting ambipolar organic field-effect transistors, *Adv. Mater.*, 2007, **19**, 734–738.

30 H. Xin, J. Li, R.-Q. Lu, X. Gao and T. M. Swager, Azulene–pyridine-fused heteroaromatics, *J. Am. Chem. Soc.*, 2020, **142**, 13598–13605.

31 P. H. Wöbkenberg, J. G. Labram, J.-M. Swiecicki, K. Parkhomenko, D. Sredojevic, J.-P. Gisselbrecht, D. M. de Leeuw, D. D. C. Bradley, J.-P. Djukic and T. D. Anthopoulos, Ambipolar organic transistors and near-infrared phototransistors based on a solution-processable squarilium dye, *J. Mater. Chem.*, 2010, **20**, 3673.

32 Y. Yamaguchi, Y. Maruya, H. Katagiri, K. Nakayama and Y. Ohba, Synthesis, properties, and OFET characteristics of 5,5′-di(2-azulenyl)-2,2′-bithiophene (DAzBT) and 2,5-di(2-azulenyl)-thieno[3,2-b]thiophene (DAzTT), *Org. Lett.*, 2012, **14**, 2316–2319.

33 Y. Yamaguchi, K. Ogawa, K. Nakayama, Y. Ohba and H. Katagiri, Terazulene: A high-performance n-type organic field-effect transistor based on molecular orbital distribution control, *J. Am. Chem. Soc.*, 2013, **135**, 19095–19098.

34 Y. Yamaguchi, M. Takubo, K. Ogawa, K. Nakayama, T. Koganezawa and H. Katagiri, Terazulene isomers: Polarity change of OFETs through molecular orbital distribution contrast, *J. Am. Chem. Soc.*, 2016, **138**, 11335–11343.

35 H. Xin, C. Ge, X. Yang, H. Gao, X. Yang and X. Gao, Biazulene diimides: A new building block for organic electronic materials, *Chem. Sci.*, 2016, **7**, 6701–6705.

36 H. Xin, J. Li, C. Ge, X. Yang, T. Xue and X. Gao, 6,6′-Diaryl-substituted biazulene diimides for solution-processable high-performance n-type organic semiconductors, *Mater. Chem. Front.*, 2018, **2**, 975–985.

37 H. Ran, X. Duan, R. Zheng, F. Xie, L. Chen, Z. Zhao, R. Han, Z. Lei and J.-Y. Hu, Two isomeric azulene-decorated naphthodithiophene diimide-based triads: Molecular orbital distribution controls polarity change of OFETs through connection position, *ACS Appl. Mater. Interfaces*, 2020, **12**, 23225–23235.

38 F. A. Larik, M. Faisal, A. Saeed, Q. Abbas, M. A. Kazi, N. Abbas, A. A. Thebo, D. M. Khan and P. A. Channar, Thiophene-based molecular and polymeric semiconductors for organic field effect transistors and organic thin film transistors, *J. Mater. Sci.: Mater. Electron.*, 2018, **29**, 17975–18010.

39 K. Feng, H. Guo, H. Sun and X. Guo, n-Type organic and polymeric semiconductors based on bithiophene imide derivatives, *Acc. Chem. Res.*, 2021, **54**, 3804–3817.

40 Y.-J. Zhong, K.-Q. Zhao, B.-Q. Wang, P. Hu, H. Monobe, B. Heinrich and B. Donnio, 2-Phenylbenzothiophene-based liquid crystalline semiconductors, *Dyes Pigm.*, 2020, **173**, 107964.

41 F. Schulz, P. Ehni, B. Wank, A. Bauer, W. Frey and S. Laschat, Alkoxy-bromo-azulenes displaying ambient temperature smectic E-phases, *Liq. Cryst.*, 2021, **48**, 832–843.

42 S. Guo, Y. He, I. Murtaza, J. Tan, J. Pan, Y. Guo, Y. Zhu, Y. He and H. Meng, Alkoxy substituted [1]benzothieno[3,2-b][1]benzothiophene derivative with improved performance in organic thin film transistors, *Org. Electron.*, 2018, **56**, 68–75.

43 T. Kinzel, Y. Zhang and S. L. Buchwald, A new palladium precatalyst allows for the fast Suzuki−Miyaura coupling reactions of unstable polyfluorophenyl and 2-heteroaryl boronic acids, *J. Am. Chem. Soc.*, 2010, **132**, 14073–14075.

44 S. M. Schultz, G. Kehr, R. Fröhlich, G. Erker, N. Kapernaum, C. Hägele, F. Giesselmann, S. Laschat, R. Judele and A. Baro, Crystal-smectic E mesophases in a series of 2-(4-n-alkylphenyl)indenes, *Liq. Cryst.*, 2007, **34**, 919–926.

45 S. Diele, S. Tosch, S. Mahnke and D. Demus, Structure and packing in smectic E and smectic A phases in the series of 4-n-alkyloxy-4′-alkanoylbiphenyls, *Cryst. Res. Technol.*, 1991, **26**, 809–817.

46 G. R. Desiraju and A. Gavezzotti, Crystal structures of polynuclear aromatic hydrocarbons. Classification, rationalization and prediction from molecular structure, *Acta Crystallogr., Sect. B: Struct. Sci.*, 1989, **45**, 473–482.

23488 | *Phys. Chem. Chem. Phys.*, 2022, **24**, 23481–23489

This journal is © the Owner Societies 2022

47 Y. Wang, Y. He, A. Li, X. Zhang, L. Zhang, C. He and H. Meng, Inverted annealing enhanced performance of organic thin-film transistors and phototransistors based on 2-(4-dodecylphenyl)[1]benzothieno[3,2-b]benzothiophene, *Org. Electron.*, 2020, **85**, 105791.

48 H. Wu, H. Iino and J. Hanna, Thermally induced bilayered crystals in a solution-processed polycrystalline thin film of phenylterthiophene-based monoalkyl smectic liquid crystals and their effect on FET mobility, *RSC Adv.*, 2017, **7**, 56586–56593.

49 H. Wu, H. Iino and J. Hanna, Bilayered crystalline organic semiconductors for solution-processed OFETs: Asymmetrically-substituted smectic liquid crystal of benzo[1,2-*b*:4,5-*b'*]dithiophene derivatives, *Chem. Lett.*, 2018, **47**, 510–513.

50 C.-W. Chu, S.-H. Li, C.-W. Chen, V. Shrotriya and Y. Yang, High-performance organic thin-film transistors with metal oxide/metal bilayer electrode, *Appl. Phys. Lett.*, 2005, **87**, 193508.

51 R. H. Hertwig and W. Koch, On the parameterization of the local correlation functional. What is Becke-3-LYP?, *Chem. Phys. Lett.*, 1997, **268**, 345–351.

52 S. Takamaru, J. Hanna and H. Iino, Use of doping to achieve low contact resistance in bottom-gate top-contact type organic transistor with liquid-crystalline organic semiconductor, Ph-BTBT-10, *Jpn. J. Appl. Phys.*, 2021, **60**, SBBG08.

Paper IV

PAPER

Check for updates

First azulene liquid crystal with de Vries behavior and a SmA re-entrant phase†

Finn Schulz, [iD] [a] Bianca Wank,[a] Pierre Nacke, [iD] [b] Wolfgang Frey[a] and Sabine Laschat [iD] *[a]

De Vries-like materials show small layer shrinkages at the SmA to SmC transition and can therefore be applied in surface-stabilized ferroelectric liquid crystal displays. Here we report the synthesis and characterization of a new class of de Vries mesogens with a simple 2-phenylazulene-1-carbonitrile-based core. These materials exhibit an exceptionally small lower threshold for the maximum layer shrinkage of only 0.16%. One of the investigated compounds shows an orthogonal SmA re-entrance phase below the tilted SmC phase. This behavior has not been observed for achiral calamitic molecules before. The rationalization of the anomalous phase behavior might lead to a new design principle for liquid crystalline compounds showing re-entrant phases and de Vries behavior.

Introduction

Liquid crystalline phases differ from each other by the degree of orientational and positional order. In the nematic (N) phase the mesogenic molecules orientate along the director $\hat{n}$.[1] In contrast, smectic phases behave like 2D fluids where the molecules form layers. When $\hat{n}$ is parallel to the layer normal $\hat{k}$ a smectic A (SmA) phase is present. An additional tilt of the molecules at the angle Θ leads to a SmC phase. The tilt-direction in a SmC phase can be controlled by an external electric field. When anchored between planar surfaces of a liquid crystal cell, a macroscopic polarization is exhibited by ferroelectric SmC* phases. This effect is exploited in surface-stabilized ferroelectric liquid crystal displays (SSFLCDs).[2,3]

SSFLCDs outperform liquid crystal displays based on nematic mesogens in terms of switching time and offer bistable modes of operation.[2,3] However, the SSFLCD technology is limited to specific applications due to fabrication difficulties. The major problem is the layer contraction that occurs at the SmA–SmC transition due to tilting of the mesogens which can be rationalized by the rigid rod model (Fig. 1a).[3] Buckling of the layers causes chevron structures, which lower the quality of the display. So-called zigzag defects at the boundary of domains with different fold directions are visible as image irregularities in the display. A possible solution to this problem is the use of materials with SmC phases with low or no layer contraction during cooling, which are called de Vries-like materials.[3] This behavior is often explained by the diffuse cone model (Fig. 1b), where the SmA–SmC transition is characterized by a change from disorder to order according to seminal work by de Vries in 1979.[4] It suggests that the molecules are already tilted in the SmA phase but have a random azimuthal distribution.[5] During formation of the SmC phase the molecules tilt in the same direction, increasing the order while maintaining the layer spacing

[a] *Institut für Organische Chemie, Universität Stuttgart, Pfaffenwaldring 55, D-70569 Stuttgart, Germany. E-mail: sabine.laschat@oc.uni-stuttgart.de*

[b] *Institut für Physikalische Chemie, Universität Stuttgart, Pfaffenwaldring 55, D-70569 Stuttgart, Germany*

† Electronic supplementary information (ESI) available: Synthetic protocols and characterization data, ^{1}H and ^{13}C NMR spectra for all new compounds. Liquid crystalline characterization (DSC, POM) and UV/Vis spectra for all investigated compounds are presented (pdf). CCDC 2215784, 2215785 and 2215787–2215789. For ESI and crystallographic data in CIF or other electronic format see DOI: https://doi.org/10.1039/d2ma01055k
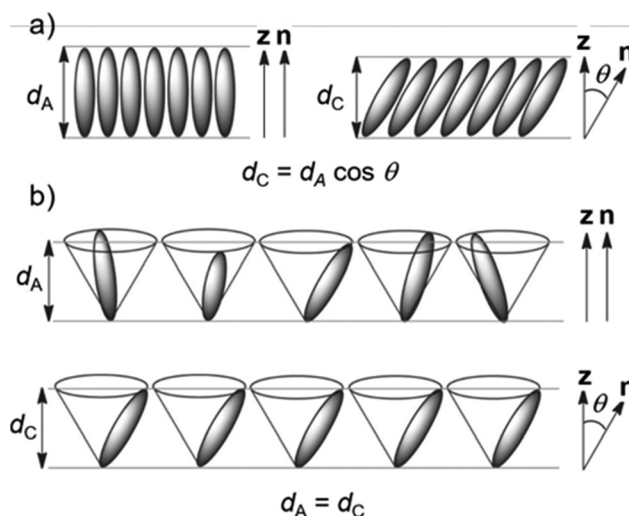

Fig. 1 Models for the behavior during the SmA–SmC transition. (a) Rigid rod model and (b) diffuse cone model. Reproduced from ref. 9 with permission from the Royal Society of Chemistry.

d. Experimental temperature-dependent XRD studies of compounds possessing a SmA phase at higher temperatures and a de Vries-like SmC phase at lower temperatures reveal that *d* passes through a minimum and increases again upon cooling in the SmC phase.[3] The ratio between the lowest value of *d* and the layer spacing at the SmA–SmC transition d_{AC} is defined as the maximum layer contraction lc_{max}. Both the rigid rod model and the diffuse cone model are ideal cases and usually a mixture of both cases is observed. Besides lc_{max}, the reduction factor *R* is defined to quantify the degree of de Vries-like behavior:[6]

$$R(T) = \frac{\cos^{-1}(lc_{max})}{\Theta_{opt}(T)}$$

R can assume values between 1 and 0, whereby *R* = 0 describes perfect de Vries-like and *R* = 1 classic rigid rod behavior. For comparison purposes, the optical tilt angle Θ_{opt} is given at 10 K below the SmA–SmC-transition.

Roberts *et al.* claimed that a frustration between SmA and SmC promoting elements within one molecule establishes de Vries-like properties.[7] In a more general approach, a combination of a low orientational order parameter S_2 and very well-defined layers lead to the sought-after de Vries-like properties. Usually nano-segregating elements like perfluorated side chains,[8] carbosilane[5,9] units or ionic headgroups[10] were chosen to acquire the necessary degree of translational order. However, materials with ordinary alkyl chains and very low lc_{max} have also been reported.[11,12] The rapid availability and chemical inertness of those side chains renders them attractive for potential applications.

Frustration is an important concept not only in creating materials with de Vries-like properties. The appearance of re-entrant phases can also be explained by a frustration between different effects.[13] Re-entrant phases form on cooling and are characterized by a less-ordered phase geometry than the corresponding higher temperature phase.[14] Often, re-entrant phases appear in mixtures of liquid crystals.[15,16] On the other hand, pure compounds with re-entrance behavior are also known.[17–19] Orthogonal re-entrant phases following a tilted SmC phase are rare and limited to bent mesogenic dimers and rod-like molecules with permanent chirality.[20,21] Novotná *et al.* found a SmA*–SmC*–SmA*$_{re}$ phase sequence for **9ZBL** (Fig. 2a).[14,22] Among a homologous series, the anomalous phase behavior did only occur for this derivative and was explained by the interaction of multiple effects such as dipolar interactions, packing arrangements and the rotational distribution of various conformers.[14] It was further argued that the presence of multiple chiral centers might be important for the re-entrant phase. More recent studies showed that racemic mixtures with only one chiral center would also form the SmA re-entrance phase.[23]

Azulene **Az** has been highlighted as a potential candidate for numerous applications due to its optoelectronic properties.[24–31] As a non-alternant isomer of naphthalene, azulene **Az** consists of a five-membered and a seven-membered ring (Fig. 2b). Owing to Hückel's rule, a zwitterionic resonance structure can be drawn which explains the dipole moment of 1.08 D. Embedded in a calamitic molecule, the polar aromatic motif improves translational order in smectic phases. Therefore, the soft crystalline SmE
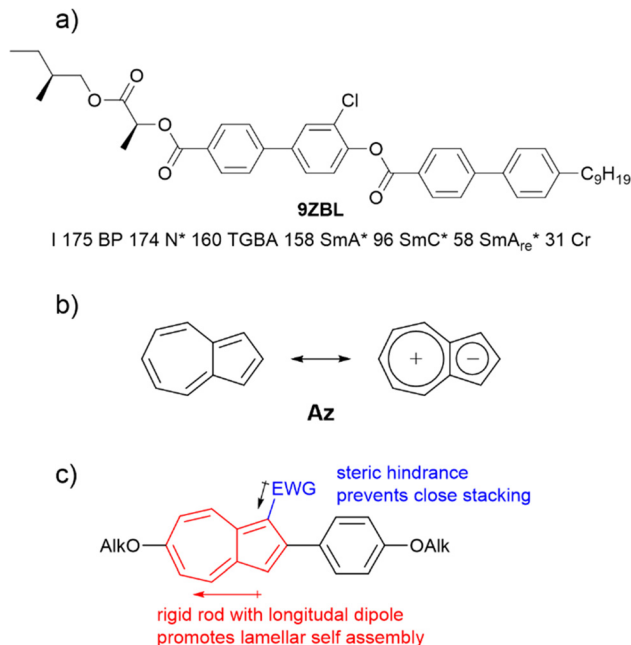

Fig. 2 (a) Structure of **9ZBL** exhibiting a SmA$_{re}$ phase (b) Localized and zwitterionic resonance structure of azulene **Az**. (c) Design concept for azulene derivatives with de Vries and re-entrant behavior.

appears frequently in those systems.[32–34] We recently described a series of 2-bromo-6-alkyloxyazulenes **nO-Az-Br** forming those highly ordered SmE phases.[32] From these results we anticipated that lateral substitution at the azulene moiety should reduce the order within the layers while preserving the translational order induced by the phenyl azulene core (Fig. 2c). Adapting the concept of Lagerwall and Giesselmann this could result in de Vries behavior.[3] Indeed, as detailed below azulene derivatives with de Vries behavior were identified. Surprisingly, one of the investigated compounds displayed a SmA$_{re}$ phase below the tilted SmC phase.

Results and discussion

The synthesis of azulene target compounds is detailed in Fig. 3. Starting from the known 2-bromo-6-alkyloxyazulene **nO-Az-Br**,[32] implementation of a nitril substituent in the 1-position of the azulene moiety was achieved *via* Vilsmeier–Haack reaction with DMF and POCl$_3$, followed by direct oxidation with iodine in aqueous ammonia to yield **nO-AzCN-Br** (n = 8, 12, 16) in 73–94%.[35] The target compounds **nO-AzCN-PhOm** were prepared by a Suzuki–Miyaura cross-coupling with arylboronic acids in 64–99% yield (*n*, *m* = 8, 12, 16).

Fortunately, single crystal structures of all five compounds were obtained, allowing a close comparison between the solid state interactions. In the solid state structure of the shortest member **8O-AzCN-PhO8** (Fig. 4a) only little nanosegregation was observed. Thus, the alkyl side chains of a certain molecule are located between the aromatic units of neighboring molecules. Along the *a* axis phenylazulene cores are oriented in a *syn-periplanar* fashion, while neighboring phenylazulenes
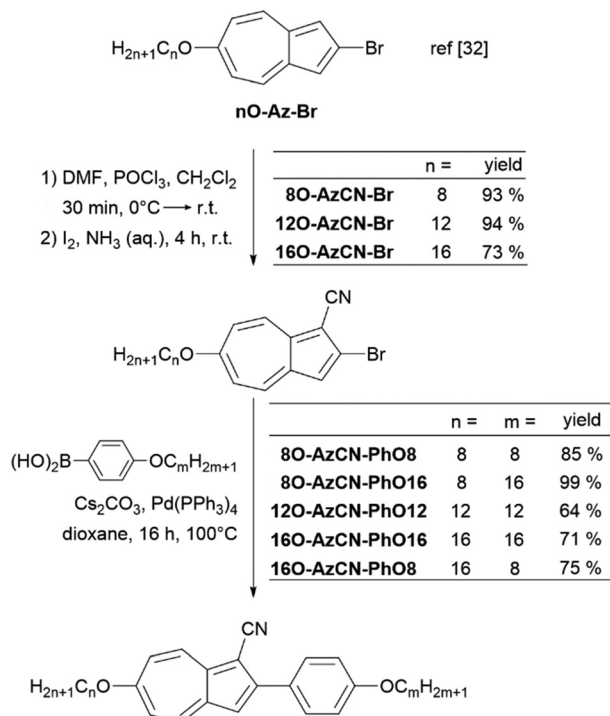
Fig. 3 Synthesis of the target compounds **nO-AzCN-PhOm**.

the *b* axis in a *syn-periplanar* fashion. Within the *ac* plane dimers are formed due to the non-classical hydrogen bond CN···H–C(azulene). In these dimers the phenylazulenes are oriented *antiperiplanar* with a parallel shift along the *a* axis (*i.e.* parallel to the long molecular axis) so that the dipole interaction between azulene moieties is maximized. For **12O-AzCN-PhO12** nanosegregation and interdigitation of alkyl chains is further improved (Fig. 4c). Phenylazulene cores are stacked along the *a* axis *antiperiplanar* and the nearest neighbors within such stack are shifted along the *b* axis (*i.e.* perpendicular to the long molecular axis), so that the π–π interaction of the phenyl ring is lost. Non-classical H-bonded dimers are formed within the *bc* plane. For **16O-AzCN-PhO8** nanosegregation and interdigitation of side chains is visible (Fig. 4d). Phenylazulene cores are stacked along the *a* axis in *antiperiplanar* manner. However, in contrast to the symmetrical derivative **12O-AzCN-PhO12** with C_{12} chains at both ends of the phenylazulene core, in **16O-AzCN-PhO8** nearest neighbors are stacked along the *a* axis in such a manner, that the 7-membered ring of the ''upper'' azulene core is positioned at the center of the ''lower'' azulene core, *i.e.* the connecting bond between 5- and 7-membered ring of the ''lower'' azulene. In addition, the H-bonded dimers are visible in the *bc* plane. For the symmetrical member **16O-AzCN-PhO16** with C_{16} chains on both ends perfect nanosegregation and interdigitation of alkyl chains was observed (Fig. 4e). Phenylazulene cores are oriented along the *a* axis in an *syn-periplanar* fashion, however the neighboring phenylazulenes are tilted with respect to each other, thus reducing π–π interactions. Clusters composed of four conformers including *pseudo*-dimers are formed in the *bc* plane. The
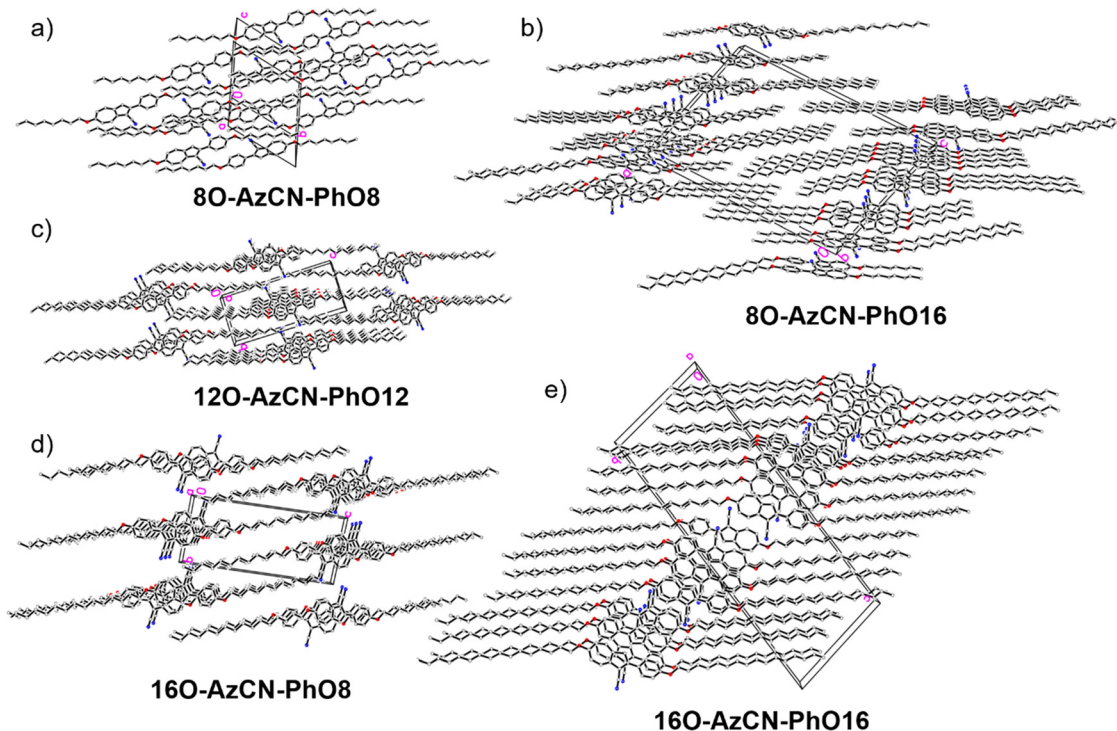
within the *bc* plane are oriented *anti-periplanar*. However, no dimers are formed. In contrast, for **8O-AzCN-PhO16** nanosegregation and interdigitation of side chains is clearly visible in the solid state (Fig. 4b). Phenylazulene cores are stacked along

Fig. 4 Single crystal structures of all compounds. (a), (c)−(e) View along the *a* axis and (b) view along the *b* axis.

unit cell of **16O-AzCN-PhO16** bears four independent molecules and crystallizes in the chiral space group *P*1.

Mesomorphic properties were characterized first by polarizing optical microscopy (POM). All compounds showed Maltese crosses and fan textures when cooling down from the isotropic liquid. On further cooling, these textures changed to Schlieren and broken fans indicating a SmA–SmC phase sequence (see Fig. S8, ESI†).[36] Phase transition temperatures were determined by differential scanning calorimetry (DSC). For **8O-AzCN-PhO8**, an endothermic peak at 99 °C indicated the entrance into the mesophase (Table 1 and Fig. S6, ESI†). At 154 °C, **8O-AzCN-PhO8** cleared into the isotropic yield. Due to supercooling, crystallization was detected at 60 °C. The transition from the SmA to SmC phase was not visible in the thermogram for any compound and therefore was determined *via* POM. In the case of **8O-AzCN-PhO8**, the SmC phase formed at 88 °C during cooling, thus only showing a monotropic phase. When extending the length of the chain at the phenyl ring from C_8 to C_{16}, transition temperatures of **8O-AzCN-PhO16** hardly changed. Clearing was observed at 148 °C and the monotropic SmA to SmC transition took place at 77 °C. **12O-AzCN-PhO12** melted at 90 °C and formed an enantiotropic SmC phase that changed into the SmA phase at 133 °C. Further elongation of the side chains to **16O-AzCN-PhO16** resulted in a lower clearing temperature at 139 °C. The SmA–SmC transition was detected at 135 °C, thus the phase width of the SmA phase was only 4 K. During heating, the transition temperatures of **16O-AzCN-PhO8** were similar to those of **12O-AzCN-PhO12**. To our astonishment, during cooling a rare monotropic SmA re-entrance (SmA$_{re}$) phase beneath the SmC phase was detected, leading to a SmA–SmC–SmA phase sequence (Fig. S7, ESI†).

The layer spacing *d* as a function of temperature was measured by small angle X-ray scattering (SAXS) (Fig. 5). In the SmA phase, an increase of *d* with decreasing temperature is expected.[7] However, **16O-AzCN-PhO16** displayed a linear correlation between *T* and *d*. This might be due to the small phase width of the observed orthogonal SmA phase. The phase might not have fully developed from the isotropic liquid before the transition to the SmC phase occurred. The monotropic SmC phases of **8O-AzCN-PhO8** and **8O-AzCN-PhO16** revealed typical rigid rod-like behavior with a linear layer shrinkage during cooling. In contrast, layer thicknesses of compounds **12O-AzCN-PhO12**, **16O-AzCN-PhO16**, and **16O-AzCN-PhO8**

passed through a minimum and increased again. This behavior is typical for de Vries-like liquid crystals.[7] In fact, an overcompensation of the tilt-caused layer shrinkage is observed in our case. The maximum layer contraction lc$_{max}$ was as low as 0.16% for **16O-AzCN-PhO8** compared with *d* at the SmA–SmC-transition (Table 2). To the best of our knowledge this is the lowest value reported in the literature. Upon entering the SmA$_{re}$ phase, **16O-AzCN-PhO8** showed another discontinuity by changing back to a linear relation between *d* and *T*. This fits well with the SmA$_{re}$ phase observed by POM.

The ratio between *d* and the molecular length *L* is usually between 0.95 and 1 for smectic monolayers due to orientational disorder within the layers.[37] The compounds **8O-AzCN-PhO8** and **8O-AzCN-PhO16** that follow the rigid rod model have a low d_{AC}/L ratio of 0.93 at the SmA–SmC transition (Table 2 and Fig. S9, ESI†). With d_{AC}/L = 0.86, **12O-AzCN-PhO12** and **16O-AzCN-PhO8** are far out of the usual range. The ratio for **16O-AzCN-PhO16** is even lower (d_{AC}/L = 0.78). This observation suggests that the all-*trans*-configuration is not present at the SmA–SmC transition at least for the de-Vries compounds.

Temperature dependent WAXS measurements were performed to ensure that the unusual phase of phase of **16O-AzCN-PhO8** was indeed a SmA$_{re}$ phase rather than a higher order orthogonal SmB phase (Fig. 6a). The absence of sharp reflexes in the wide-angle region confirms the proposed smectic phase without positional order in the layers. However, the halo in the partially orientated 2D WAXS diffractogram becomes sharper and more focused, indicating an increasing orientational order upon cooling (Fig. 6a and b). At short angles, higher ordered layer reflexes become more pronounced upon cooling, indicating an increase in translational order. It is worth noting that the third order diffraction peak of the layer spacing is stronger than the second order peak. In agreement with Davidson and Strzelecki, in such cases the electron density along the director $\hat{n}$ cannot be described with a single sinusoidal modulation.[38] In our case, the second function might be assigned to the electron density of the nitrile substituent.

With the temperature dependent layer thickness in hand, we determined the optical tilt angle Θ as a function of *T via* POM in a glass cell with rubbed nylon layers (Fig. 7). Compounds with linear layer shrinkage in the SmC-phase showed smaller tilt angles compared to their de Vries-like behaving

Table 1 Onset transition temperatures [°C] and enthalpies [kJ mol^{-1}] of azulenes *n*O-AzCN-PhO*m* determined by DSC

Compound		Transition temperatures/°C (and enthalpies/kJ mol^{-1})								
8O-AzCN-PhO8	Cr	99 (31.8)	—	—	—	—	SmA	154 (7.3)	I	h
	Cr	60 (−21.3)	—	—	SmC	88[a]	SmA	155 (−7.1)	I	c
8O-AzCN-PhO16	Cr	95 (51.4)	—	—	—	—	SmA	148 (8.4)	I	h
	Cr	60 (−48.3)	—	—	SmC	77[a]	SmA	149 (−8.3)	I	c
12O-AzCN-PhO12	Cr	90 (31.8)	—	—	SmC	133[a]	SmA	149 (9.9)	I	h
	Cr	65 (−46.9)	—	—	SmC	133[a]	SmA	150 (−9.9)	I	c
16O-AzCN-PhO16	Cr	95 (62.6)	—	—	SmC	135[a]	SmA	138 (10.9)	I	h
	Cr	87 (−75.3)	—	—	SmC	135[a]	SmA	139 (−9.2)	I	c
16O-AzCN-PhO8	Cr	86 (41.0)	—	—	SmC	133[a]	SmA	151 (11.5)	I	h
	Cr	26 (−3.5)	SmA$_{re}$	78[a]	SmC	133[a]	SmA	151 (−11.9)	I	c

Heating/cooling rate: 5 K min^{-1}, h: 2nd heating, c: 2nd cooling. Crystal-crystal transitions are not listed. [a] Determined *via* POM.
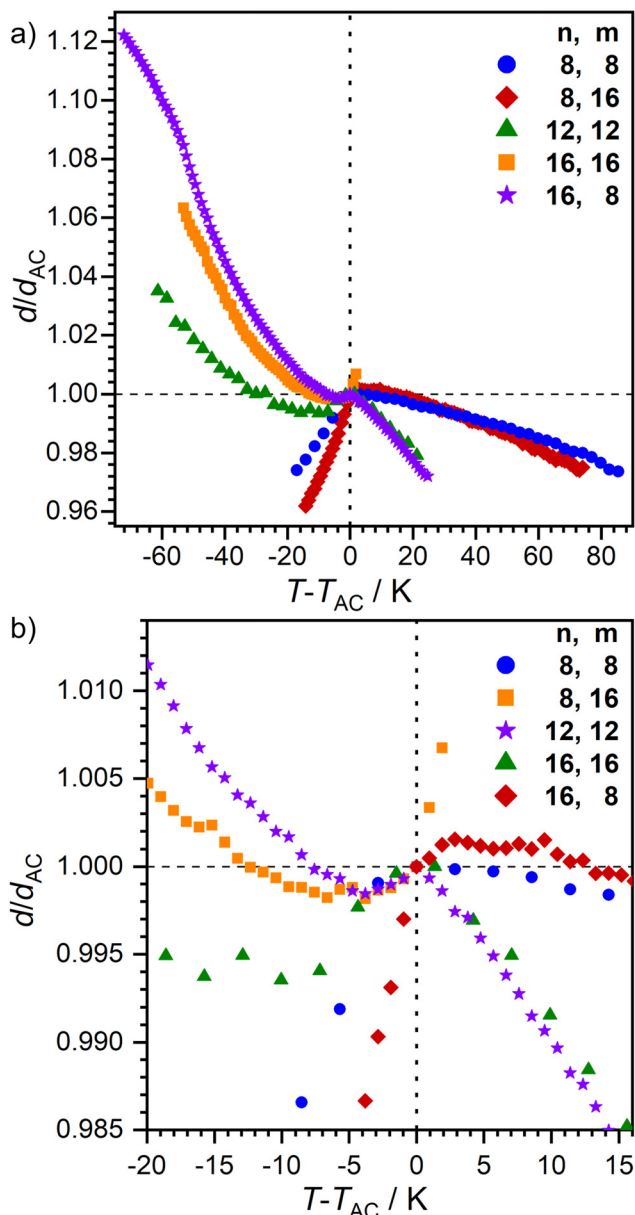
Fig. 5 Plot of the relative layer spacing d/d_{AC} as a function of $T - T_{AC}$ for **nO-AzCN-PhOm**. (a) Full size and (b) close to the SmA–C transition.
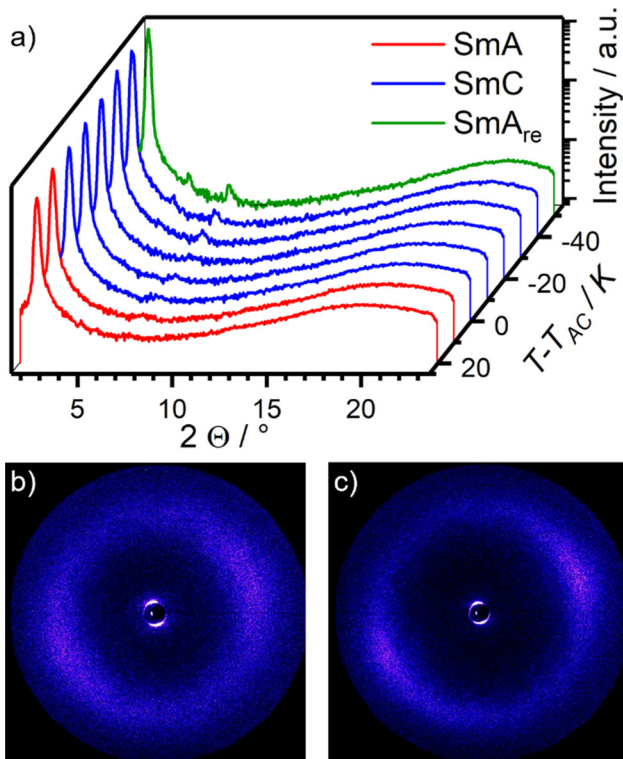

Fig. 6 (a) Temperature dependent WAXS measurements of **16O-AzCN-PhO8**. (b) 2D diffractogram of the WAXS measurement of the SmA phase at $T - T_{AC} = 20$ K and (c) of the SmA$_{re}$ phase at $T - T_{AC} = -50$ K.

of **16O-AzCN-PhO8** with a SmA re-entrance phase peaked 10 K beneath the SmA–SmC transition and decreased while approaching the SmA$_{re}$ phase. Similar behavior was observed in an SmA–SmC-SmA$_{re}$ phase sequence reported by Novotná et al.[22]
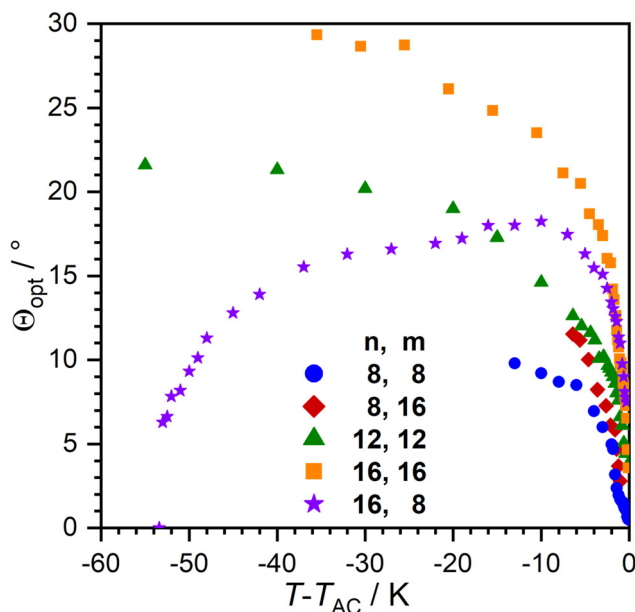
counterparts. **16O-AzCN-PhO16** had the largest tilt angle with $\Theta = 24°$ 10 K beneath the SmA–SmC transition. The optical tilt

Table 2 Layer spacing at the SmA–SmC transition d_{AC}, ratio of the layer to molecular length d/L and maximum layer contraction lc$_{max}$ measured with SAXS, tilt angles determined by POM and R-values of de-Vries like liquid crystals at $T - T_{AC} = -10$ K of the characterized compounds

Compound	$d_{AC}/$Å	d_{AC}/L^a	lc$_{max}$/%	$\Theta_{opt}/°$	R
8O-AzCN-PhO8	30.8	0.93	—	—	—
8O-AzCN-PhO16	40.2	0.93	—	—	—
12O-AzCN-PhO12	37.2	0.86	0.65	15	0.43
16O-AzCN-PhO16	41.4	0.78	0.18	24	0.14
16O-AzCN-PhO8	37.2	0.86	0.16	18	0.18

^{a} Calculated for the all-*trans*-configuration *via* Chem3D.

Fig. 7 Temperature dependence of the optical tilt angle Θ during the SmC phase.

With knowledge of Θ and lc_{max}, the R-value could be calculated (Table 2). The lowest value was achieved by **16O-AzCN-PhO16** with $R = 0.14$, which is similar to state of the art de Vries-like materials.[10,11,39] The fact that longer side chains improve de Vries-like properties is in good accordance with a model by Merkel *et al.*, who showed that the layer contraction caused by the tilting of the core can be compensated for only by increasingly ordered side chains.[40]

Ahmed *et al.* argued that the layer shrinkage caused by tilting of the molecule is compensated for either by a decrease in interdigitation and/or by an increase of orientational order within the layers.[39] Since interdigitation plays only a minor role in smectic monolayers, compensation should arise through increasing order. The molecules do not have nanosegregating head groups that are commonly associated with de Vries-like behavior. They usually cause high translational order between the layers which compensate for a low order within the layers in the SmA phase. It might be argued that the dipolar azulene core mimics such a headgroup, therefore acting as a nanosegregating core.

Order within the layers can be quantified by the nematic order parameter S_2. Unfortunately, even after repeated attempts it was not possible to achieve completely orientated WAXS samples. Therefore, determination of S_2 *via* X-ray diffraction was not possible. Instead, we measured the birefringence Δn which is closely related to S_2 using a Phi-Viz Imaging System (Polaviz, APSYS Inc.).[3,5] As seen in Fig. 8, all compounds showed a discontinuity of Δn at the SmA–SmC transition, followed by a rise of Δn. **8O-AzCN-PhO8** showed the highest overall Δn, but only a small increase when entering the SmC phase. Since Δn is mainly caused by the aromatic moiety of the molecules, it is expected that the birefringence decreases with increasing chain length in the homologous series. As expected,
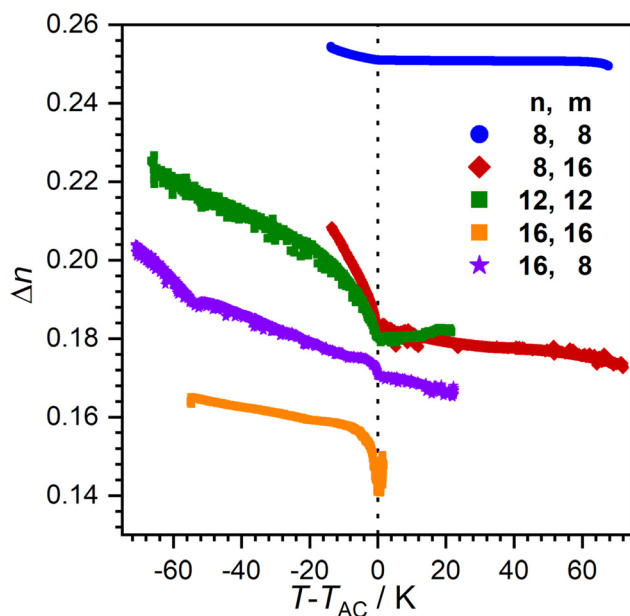
16O-AzCN-PhO16 has the lowest birefringence which, however, increases strongly after the SmA–SmC transition. Those observations suggest the compensation of the layer shrinkage through increasing order. However, **8O-AzCN-PhO16** also has a strong increase in Δn while following classic behavior. Furthermore, **16O-AzCN-PhO8** has the lowest lc_{max} while only showing a moderate increase in Δn. Therefore, it might be argued that the increasing S_2 cannot be the only factor contributing to the observed compensation.

The X-ray data reported by Novotná *et al.* suggest, that compound **9ZBL** behaves like a de Vries material (Fig. 2a), albeit with a moderate R-value of about 0.8 due to the low tilt angle.[22] However, the qualitative behavior of d and Θ during the SmA–SmC–SmA$_{re}$ phase sequence is similar to our observations. They reasoned that quadrupolar ordering increases on cooling. With higher order the lateral chloro substituent of **9ZBL** hinders closer packing. The system avoids the steric hindrance by a shift of mass centers and so, increases the layer spacing.[14] Taking inspiration by Novotná *et al.*, we propose a related packing model for **16O-AzCN-PhO8** in which the nitrile group sterically hinders the packing similar to the lateral chloro substituent in **9ZBL** (Fig. 9). In addition, the nitrile group contributes a lateral dipole moment and enhances the dipole caused by the zwitterionic resonance structure of the azulene moiety. This combination of lateral and axial dipoles might be important for the strong increase in quadrupolar ordering on cooling. Re-entrance phases purely driven by steric frustration have been predicted.[41] In our case the steric frustration is intrinsically entangled with dipole–dipole interactions since the nitrile is a key element to both. The reinforcement between those two effects might be crucial for the anomalous behavior.

During the first SmA phase, the low d/L ratio of **16O-AzCN-PhO16** suggests that the long C_{16} chain is not present in the all-*trans* configuration (Fig. 9a). The entangled chain fills up the free volume left by the shorter C_8 chain. The shift of mass centers slightly compensates for the different length of the side chains allowing the C_{16} chain to adopt a more linear configuration (Fig. 9d). This might be a reason why the SmA$_{re}$ phase is only present for **16O-AzCN-PhO8**. In **8O-AzCN-PhO16**, the shifting would further unbalance the already different chain lengths, thus the shifting seems not to take place. This might be the reason why classical behavior was observed for **8O-AzCN-PhO16**. The active role of the side chains on the appearance of re-entrancy was also highlighted by Novotná.[14]

Although comparisons of single crystal structures with mesophase packing geometries should be handled with great care, solid structures might give some useful hints about the specific interactions relevant for the packing in the mesophase, particularly where solid state structures of a whole series are available. The solid state structure of **16O-AzCN-PhO8** in Fig. 5d resembles the model of the SmA$_{re}$ phase in Fig. 9d. As discussed above, the loss of the π–π interaction of the phenyl ring is compensated for by dipolar interactions, and strong van der Waals interactions of the interdigitated alkyl chains. In both, the mesophase and the crystalline phase subtle changes of the chain lengths lead to completely different behavior of the phase.
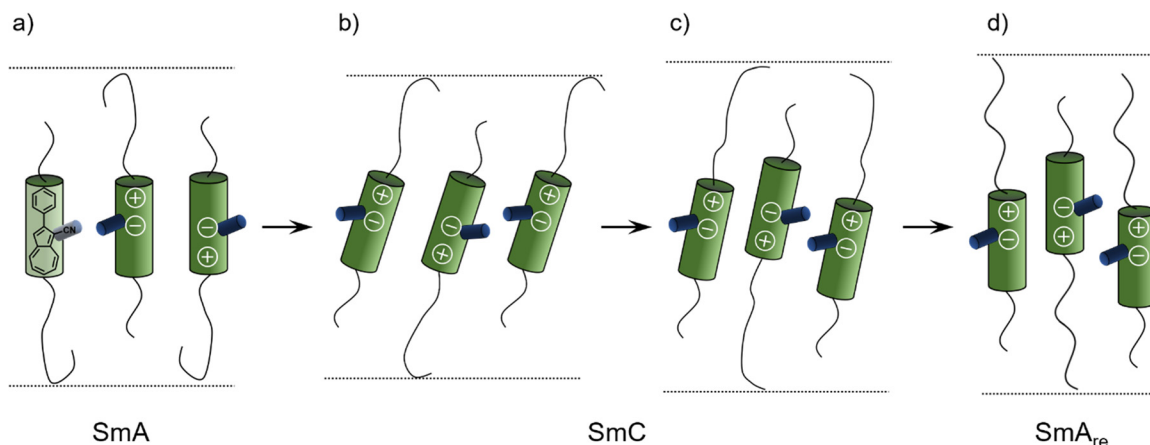

Fig. 8 Temperature dependence of birefringence Δn for compounds *n*O-AzCN-PhO*m*.

Fig. 9 Proposed mechanism for the formation of the SmA$_{re}$ phase of **16O-AzCN-PhO8** due to a shift of mass centers based on a model by Novotná *et al.*[14] (a) The SmA phase is present. (b) Tilting of the mesogens in the SmC phase leads to layer contraction. (c) A shift of mass centers is induced by the hindrance of the nitrile group and the layer thickness increases. (d) Mesogens lose their tilt in the SmA$_{re}$ phase, the layer thickness further increases.

In summary, we synthesized a new class of liquid crystals based on the azulene core. These readily available compounds turned out to be potent de Vries-like materials with very low maximum layer shrinkages and R-values as low as 0.14 for **16O-AzCN-PhO16**. The overcompensation of the layer shrinkage might be a useful property when creating mixtures with other de Vries behaving compounds in order to achieve minimal layer shrinkages. It was suggested that the layer shrinkage caused by the molecular tilt is compensated for not only by an increase of the molecular order, but also by a shift of mass center in the aromatic core. In the case of **16O-AzCN-PhO8** the frustration between shift of mass center, good van der Waals interaction, but reduced dipole and π–π interaction might have led to the orthogonal SmA$_{re}$ phase below the tilted SmC phase. The observations are in close analogy to the re-entrance phase of **9ZBL**.[14,22] However, in contrast to **9ZBL** azulene compound **16O-AzCN-PhO8** does not have chiral centers, indicating that anomalous phase behavior can exist without chirality. These observations might lead to a new design principle for achiral liquid crystalline compounds showing re-entrant phases and de Vries behavior. Further work to understand this behavior in more detail is currently in progress and will be reported in due course.

Author contributions

FS and SL conceived and designed this research. FS and BW synthesized the compounds and did the liquid crystalline characterization. FS performed the X-ray and birefringence measurements. PN contributed their expertise to the evaluation of the results. WF performed and evaluated the single crystal measurements. FS wrote the first draft of the manuscript, SL PN and BW co-wrote the manuscript. All authors approved the final version of the manuscript.

Conflicts of interest

There are no conflicts to declare.

Acknowledgements

References

1 in *Handbook of liquid crystals*, J. W. Goodby, P. J. Collings, T. Kato, C. Tschierske, H. Gleeson and P. Raynes, ed., Wiley-VCH, Weinheim, 2., completely rev. and greatly enlarged ed., 2014, vol. 1.

2 N. A. Clark, M. A. Handschy and S. T. Lagerwall, *Mol. Cryst.*, 1983, **94**, 213–233.

3 J. P. F. Lagerwall and F. Giesselmann, *ChemPhysChem*, 2006, **7**, 20–45.

4 A. de Vries, *J. Chem. Phys.*, 1979, **71**, 25–31.

5 Z. Ahmed, C. Müller, J. J. Johnston, K. Nguyen, C. P. J. Schubert, K. Abitaev, S. Marino, F. Giesselmann and R. P. Lemieux, *Liq. Cryst.*, 2019, **46**, 896–904.

6 M. D. Radcliffe, M. L. Brostrom, K. A. Epstein, A. G. Rappaport, B. N. Thomas, R. Shao and N. A. Clark, *Liq. Cryst.*, 1999, **26**, 789–794.

7 J. C. Roberts, N. Kapernaum, F. Giesselmann and R. P. Lemieux, *J. Am. Chem. Soc.*, 2008, **130**, 13842–13843.

8 J. P. F. Lagerwall, F. Giesselmann and M. D. Radcliffe, *Phys. Rev. E: Stat., Nonlinear, Soft Matter Phys.*, 2002, **66**, 031703.

9 Q. Song, D. Nonnenmacher, F. Giesselmann and R. P. Lemieux, *J. Mater. Chem. C*, 2013, **1**, 343–350.

10 K. Bader, C. Müller, Y. Molard, A. Baro, P. Ehni, J. Knelles and S. Laschat, *RSC Adv.*, 2020, **10**, 23999–24016.

11 H. K. Singh, S. K. Singh, R. Nandi, D. S. S. Rao, S. K. Prasad, R. K. Singh and B. Singh, *RSC Adv.*, 2016, **6**, 57799–57802.

12 A. Sanchez-Castillo, M. A. Osipov, S. Jagiella, Z. H. Nguyen, M. Kašpar, V. Hamplová, J. Maclennan and F. Giesselmann, *Phys. Rev. E: Stat., Nonlinear, Soft Matter Phys.*, 2012, **85**, 061703.

13 P. E. Cladis, R. J. Mandle and J. W. Goodby, in *Handbook of Liquid Crystals*, ed. J. W. Goodby, C. Tschierske, P. Raynes, H. Gleeson, T. Kato and P. J. Collings, Wiley-VCH Verlag GmbH & Co. KGaA, Weinheim, Germany, 2014, pp. 1–30.

14 V. Novotná, V. Hamplová, N. Podoliak, M. Kašpar, M. Glogarová, D. Pociecha and E. Gorecka, *J. Mater. Chem.*, 2011, **21**, 14807.

15 P. E. Cladis, *Phys. Rev. Lett.*, 1975, **35**, 48–51.

16 S. Diele, G. Pelzl, A. Humke, S. Wünsch, W. Schäfer, H. Zaschke and D. Demus, *Mol. Cryst. Liq. Cryst. Inc. Nonlinear Opt.*, 1989, **173**, 113–119.

17 P. E. Cladis, R. J. Mandle and J. W. Goodby, *Handbook of Liquid Crystals*, John Wiley & Sons, Ltd, 2014, pp. 1–30.

18 W. Weissflog, G. Pelzl and D. Demus, *Mol. Cryst. Liq. Cryst.*, 1981, **76**, 261–268.

19 F. Hardouin and A. M. Levelut, *J. Phys.*, 1980, **41**, 41–46.

20 W. Weissflog, Ch Lischka, S. Diele, I. Wirth and G. Pelzl, *Liq. Cryst.*, 2000, **27**, 43–50.

21 C. Tschierske, *Liq. Cryst.*, 2022, **49**, 1043–1077.

22 V. Novotná, M. Glogarová, M. Kašpar, V. Hamplová, E. Gorecka, D. Pociecha and M. Cepic, *Phys. Rev. E: Stat., Nonlinear, Soft Matter Phys.*, 2011, **83**, 020701.

23 V. Novotná, S. Stulov, M. Cigl, V. Hamplová, E. Gorecka and D. Pociecha, *Liq. Cryst.*, 2020, **47**, 1516–1527.

24 J. Zhang and S. Petoud, *Chem. – Eur. J.*, 2008, **14**, 1264–1272.

25 Y. Zhou, Y. Zhuang, X. Li, H. Ågren, L. Yu, J. Ding and L. Zhu, *Chem. – Eur. J.*, 2017, **23**, 7642–7647.

26 E. Puodziukynaite, H.-W. Wang, J. Lawrence, A. J. Wise, T. P. Russell, M. D. Barnes and T. Emrick, *J. Am. Chem. Soc.*, 2014, **136**, 11043–11049.

27 H. Xin, C. Ge, X. Jiao, X. Yang, K. Rundel, C. R. McNeill and X. Gao, *Angew. Chem., Int. Ed.*, 2018, **57**, 1322–1326.

28 H. Xin, C. Ge, X. Jiao, X. Yang, K. Rundel, C. R. McNeill and X. Gao, *Angew. Chem.*, 2018, **130**, 1336–1340.

29 F. Schwarz, M. Koch, G. Kastlunger, H. Berke, R. Stadler, K. Venkatesan and E. Lörtscher, *Angew. Chem., Int. Ed.*, 2016, **55**, 11781–11786.

30 F. Schwarz, M. Koch, G. Kastlunger, H. Berke, R. Stadler, K. Venkatesan and E. Lörtscher, *Angew. Chem.*, 2016, **128**, 11956–11961.

31 T. Tsuchiya, R. Umemura, M. Kaminaga, S. Kushida, K. Ohkubo, S.-I. Noro and Y. Mazaki, *ChemPlusChem*, 2019, **84**, 655–664.

32 F. Schulz, P. Ehni, B. Wank, A. Bauer, W. Frey and S. Laschat, *Liq. Cryst.*, 2021, **48**, 832–843.

33 S. Ito, M. Ando, A. Nomura, N. Morita, C. Kabuto, H. Mukai, K. Ohta, J. Kawakami, A. Yoshizawa and A. Tajiri, *J. Org. Chem.*, 2005, **70**, 3939–3949.

34 F. Schulz, S. Takamaru, T. Bens, J. Hanna, B. Sarkar, S. Laschat and H. Iino, *Phys. Chem. Chem. Phys.*, 2022, **24**, 23481–23489.

35 S. Ushijima and H. Togo, *Synlett*, 2010, 1067–1070.

36 I. Dierking, *Textures of liquid crystals*, Wiley-VCH, Weinheim, 1st edn, 2003.

37 A. De Vries, A. Ekachai and N. Spielberg, *Mol. Cryst. Liq. Cryst.*, 1979, **49**, 143–152.

38 P. Davidson and L. Strzelecki, *Liq. Cryst.*, 1988, **3**, 1583–1595.

39 C. P. J. Schubert, A. Bogner, J. H. Porada, K. Ayub, T. Andrea, F. Giesselmann and R. P. Lemieux, *J. Mater. Chem. C*, 2014, **2**, 4581–4589.

40 K. Merkel, A. Kocot, J. K. Vij, P. J. Stevenson, A. Panov and D. Rodriguez, *Appl. Phys. Lett.*, 2016, **108**, 243301.

41 R. J. Mandle, N. Stock, S. J. Cowling, R. R. Parker, S. Hart, A. C. Whitwood and J. W. Goodby, *Liq. Cryst.*, 2019, **46**, 114–123.

Paper V

PAPER

Check for updates

Tailoring liquid crystalline self-assembly and de Vries behavior of azulenes *via* lateral and core substitution†

Finn Schulz, [ID] Bettina Lutz, Daniel Rück, Derman Batman, Wolfgang Frey and Sabine Laschat [ID] *‡

The azulene moiety is a highly attractive building block in optoelectronic applications due to its unique properties. For high-performing devices, the molecular orientation is crucial and can be controlled through liquid-crystalline self-assembly. Recent work showed that liquid crystalline derivatives bearing the 2-phenyl-azulene-1-nitrile core formed broad de Vries-type SmA and SmC phases. For exact understanding of the structure–property relationship, a series of 2-(hetero)aryl-azulenes has been synthesized varying the chain linkage, the lateral substituent, and the aromatic ring. Small changes of the molecular structure determined whether the orthogonal SmA phase or the tilted SmC phase is predominant. Implementation of alkyne chains instead of alkoxy chains resulted in the reduction of phase transition temperatures and formation of mesophases at room temperature. Furthermore, de Vries-like behavior was investigated and reduction values between $R = 0.35$ and 0.74 were measured which supported the hypothesis that in this system de Vries-like behavior is caused by steric repulsion of the lateral substituent. The control of the phase geometry by the molecular structure might be used for improved molecular orientation in optoelectronic materials.

Introduction

Azulene **Az** is a non-alternating hydrocarbon consisting of a 5- and a 7-membered ring. The isomer of naphthalene has special properties such as non-symmetric frontier orbitals and a permanent dipole moment of 1.08 D caused by a zwitterionic resonance structure (Fig. 1(a)).[1,2] Due to those characteristics, numerous publications focused on the azulene moiety regarding their electronic and optoelectronic applications such as near infrared emitters, electrochromic materials and organic electronics.[3–12] Furthermore, azulene derivatives have been suggested for a variety of applications in medicinal and analytical chemistry.[13–17] Due to their self-aligning properties, special attention was paid to liquid crystalline azulene derivatives. Ito *et al.* proposed a series of columnar phenylazulenes **1** as semiconductors or for electrochromic applications (Fig. 1(b)).[18–21] Domingo *et al.* synthesized isocyanoazulene gold complexes forming smectic A (SmA) phases. The organometallic dyes might be used in sensors.[22] We could recently show that the soft crystal E phase

(SmE) of calamitic thiophene–azulene hybrids can be used to manufacture well-orientated and molecularly thin films.[23]

Previously, we established the 2-phenyl azulene core as a potent de Vries promoting element (Fig. 1(b), **12O-AzCN-PhO12**).[24] Materials with de Vries-like behavior possess a smectic A – smectic C (SmC) phase sequence and a unique temperature-dependent behavior of the smectic layer spacing d. During cooling in the SmC phase, d of ordinary calamitic liquid crystals (*i.e.* non de Vries-like materials) decreases due to an increasing tilt angle θ of the molecules by about 10%.[25] This behavior is often rationalized by the rigid rod model (Fig. 2(a)).[26] In de Vries-like materials the layer spacing d rather passes through a minimum and increases again upon further cooling. This phenomenon can be explained with the diffuse cone model, where the mesogens are randomly tilted in the SmA phase and synchronize the direction of the tilt once entering the SmC phase (Fig. 2(b)).[26] In this case no layer shrinkage is observed. Typical de Vries-like materials show layer shrinkages below 1%.[25] Materials with very low layer shrinkage are sought-after for novel display applications.[25,27] In order to quantify the layer shrinkage, the reduction value R was defined:[28]

$$R(T) = \frac{\cos^{-1}(\mathrm{lc_{max}})}{\theta_{\mathrm{opt}}(T)}$$

The maximum layer shrinkage $\mathrm{lc_{max}}$ is defined as the ratio between the minimum d value and the layer spacing at the SmA

Institut für Organische Chemie, Universität Stuttgart, Pfaffenwaldring 55, D-70569 Stuttgart, Germany. E-mail: sabine.laschat@oc.uni-stuttgart.de

a)

Az

b) Previous work:

1: R = C$_{16}$H$_{33}$ Cr 97 Col$_h$ 143 I   ref [20]

12O-AzCN-PhO12: Cr 90 SmC 133 SmA 150 I   ref [24]

c) This work:

X = H, F, CN, NO$_2$

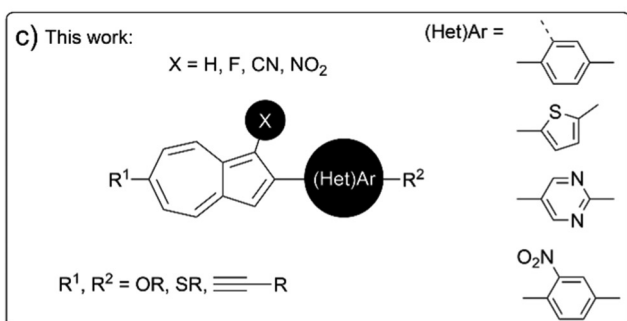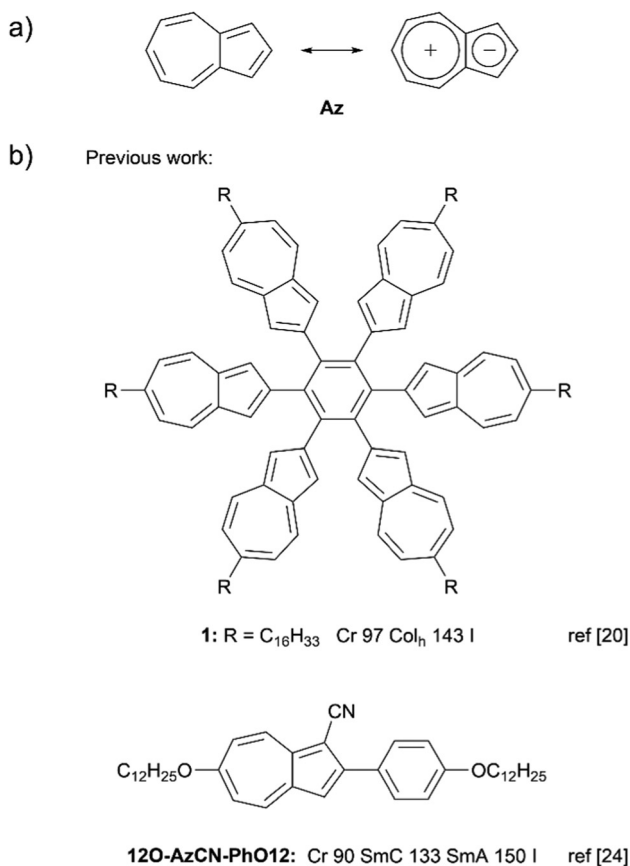(Het)Ar =

R^1, R^2 = OR, SR, ≡—R

Fig. 1 (a) Localized and zwitterionic resonance structure of azulene **Az**. (b) Previous work on azulene liquid crystals. (c) Topic of this work.

Fig. 2 Models for the behavior during the SmA–SmC transition. (a) Rigid rod model and (b) diffuse cone model. Figure was adapted from ref. 27.

to SmC transition d_{AC}. R can assume values between 0 and 1, whereas 0 equals perfect de Vries-like behavior and 1 describes the classical behavior following the rigid rod model.

Even though our previously reported compounds *e.g.*, **12O-AzCN-PhO12** showed good de Vries-like behavior, their melting points were at elevated temperatures and therefore not suitable for applications such as displays. A strategy to overcome this limitation is the use of mixtures of liquid crystals. Thus, we anticipated that in order to obtain suitable mixtures of liquid crystals showing both de Vries-like behavior and phase transition temperatures in a certain range, it might be desirable to prepare derivatives of **12O-AzCN-PhO12** and to study their structure–property relationships. A compound
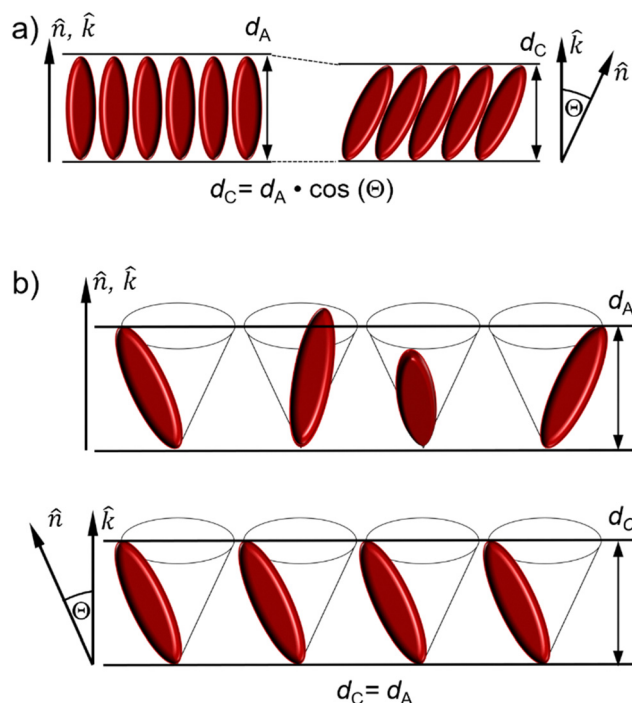
library could help to reduce phase transition temperatures of both, single compounds, and mixtures. In this work we describe the synthesis and characterization of novel azulene mesogens derived from the phenylazulene core (Fig. 1(c)).

Results and discussion

Synthesis

The divergent synthesis of the target compounds started from the literature known **Br-Az-Br** (Fig. 3(a)).[10] The C-Br unit at the 7-membered ring is prone to nucleophilic substitution, while the brominated position at the 5-membered ring does not react under these conditions.[29] Thus, alkoxy side chains can be inserted in a regioselective way on the 7-membered ring. Analogous to the known **12O-Az-Br**,[30] the nucleophilic attack was also possible with thiododecanolate in THF affording **12S-Az-Br** in 56% yield. As an alternative to the ether- and thioether-based side chains, dodecyne was introduced *via* Sonogashira coupling. While both bromides can be substituted at room temperature in the presence of 5 mol% Pd(PPh$_3$)$_4$, 10 mol% of CuI and triethylamine, the bromide at the 7-membered ring reacted fast and **12Yne-Az-Br** was isolated in 85% yield.

Next, we focused on azulenes with lateral substituent at the 5-membered ring (X = CN, F, NO$_2$; Fig. 3(b)). The nitrile group was implemented by Vilsmeier–Haack reaction with subsequent oxidation *via* our previously reported method[24] to yield the azulene derivative **12S-AzCN-Br** with thioether side chain in 94%. In contrast, the corresponding azulene with alkyne unit **12Yne-AzCN-Br** was isolated in only 18% yield. Presumably, the
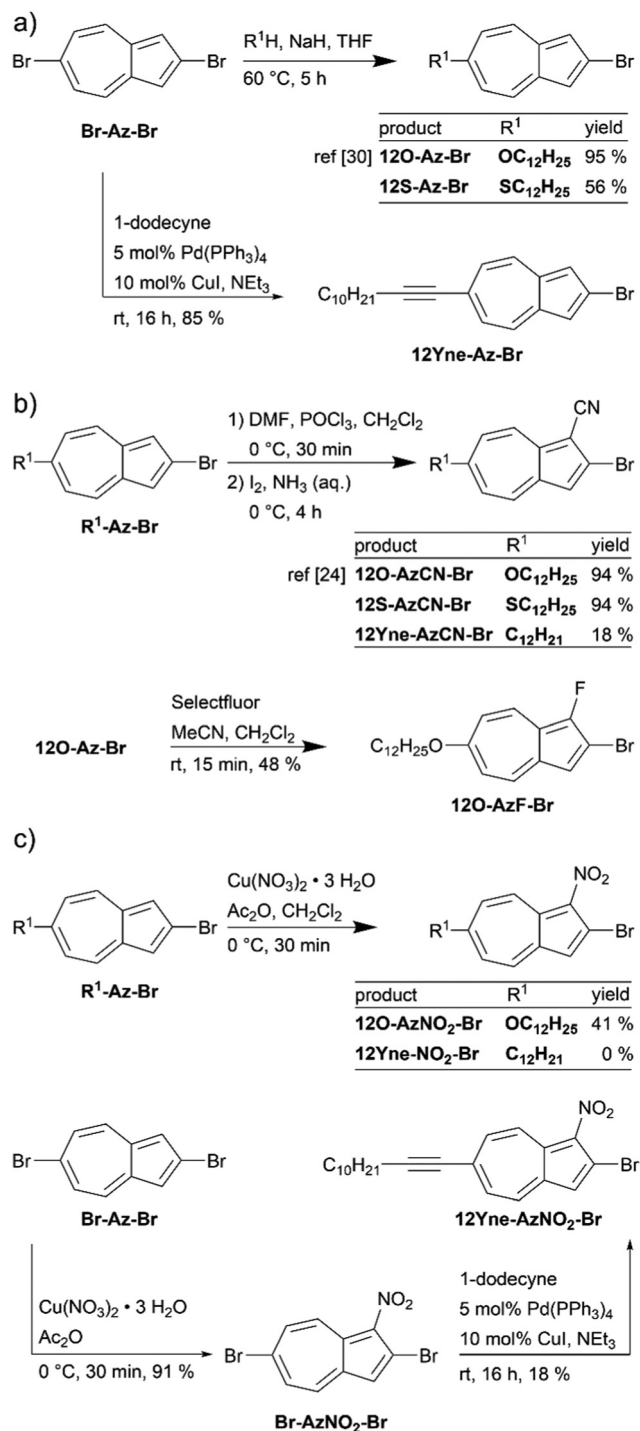
Fig. 3 Synthesis of the azulene precursors. (a) Insertion of the side chain and (b), (c) implementation of the lateral group. Selectfluor®: 1-chloromethyl-4-fluoro-1,4-diazoniabicyclo[2.2.2]octane bis(tetrafluoroborate).

alkyne moiety was not compatible with the oxidative conditions I_2/NH_3. As alternative for the polar cyano substituents, we aimed at introducing fluoro substituents at the azulene. Following a procedure by Muthyala and Liu,[31] **12O-Az-Br** was fluorinated with Selectfluor® in 15 min reaction time and

yielded **12O-AzF-Br** in 48%. Next, the highly polar nitro group should be implemented on the azulene core (Fig. 3(c)). While common nitration conditions failed due to decomposition of the protonated azulene compounds, **12O-Az-Br** was successfully converted to **12O-AzNO2-Br** under Menke conditions[32] with $Cu(NO_3)_2$ in Ac_2O in 48%. Unfortunately, the analogous nitration of **12Yne-Az-Br** failed. Hence, we decided to change the order of steps, firstly performing the nitration, followed by the subsequent Sonogashira coupling as the second step. Whereas nitration of **Br-Az-Br** gave **Br-AzNO2-Br** in 91% yield, the Sonogashira coupling provided **12O-AzNO2-Br** in only 16%. Presumably, the electron-withdrawing nitro group changed the reactivity of the C-Br units at the azulene.

In order to expand to further expand the azulene library, the different azulene bromides were coupled under Suzuki–Miyaura conditions with aryl and heteroaryl boronic acids or the corresponding pinacolato esters (Fig. 4). For comparison, the length of the side chains was not varied and always kept at C_{12}. In the case of thiophene derivatives, alkyl instead of alkoxy chains were used due to the synthetic availability. The synthesis of those coupling partners is detailed in the ESI† (Fig. S1). In the presence of 10 mol% $Pd(PPh_3)_4$ and Cs_2CO_3, the target compounds **R^1-AzX-R^2** were synthesized in 31–95% yield. The reaction of the thiophene boronic acid derivative with the unsubstituted **12O-Az-Br** was not successful. In this case the functional groups were switched. Under Miyaura coupling conditions **12O-Az-Br** was transformed to **12O-Az-BPin** in 30% yield.[33] The pinacol ester was then coupled with the bromo thiophene derivative **Br-Thi12**, yielding **12O-Az-Thi12** in 33%.

Mesomorphic properties

After successfully synthesizing the target compounds, their liquid crystalline properties were characterized by differential scanning calorimetry (DSC), polarized optical microscopy (POM) and X-ray diffractometry (XRD). First the intermediate azulene bromides were examined (Fig. 5(a)). **12O-Az-Br** is known to form a soft crystal E phase (SmE).[30] In the DSC curve, **12S-Az-Br** also showed two endothermal peaks during heating at 66 °C and 101 °C, indicating either a second crystalline phase or a mesophase (Fig. S6a, ESI†). Under the POM, platelet textures were observed that are characteristic for SmE phases (Fig. S2a, ESI†).[34] Wide and small angle X-ray scattering experiments (WAXS and SAXS) confirmed the presence of a SmE phase, showing the typical halo of the molten alkyl chains overlapped by three reflexes cause by the herringbone ordering in the layers of the SmE phase (Fig. 7(a)).[35] The phase transition temperatures of **12S-Az-Br** bear a strong similarity to those of **12O-Az-Br** (Table S1, ESI† and Fig. 5(a)). The change of the oxygen atom to its higher homologue sulfur seems to barely affect the packing and electronic structure. The calculated lattice constants also show only little discrepancies between each other (Table S2, ESI†). In contrast the alkyne derivative **12Yne-Az-Br** did not show a mesophase and melted at 43 °C under the POM. The electron donating character of the chalcogen atom enhances the inherent dipole moment of the azulene
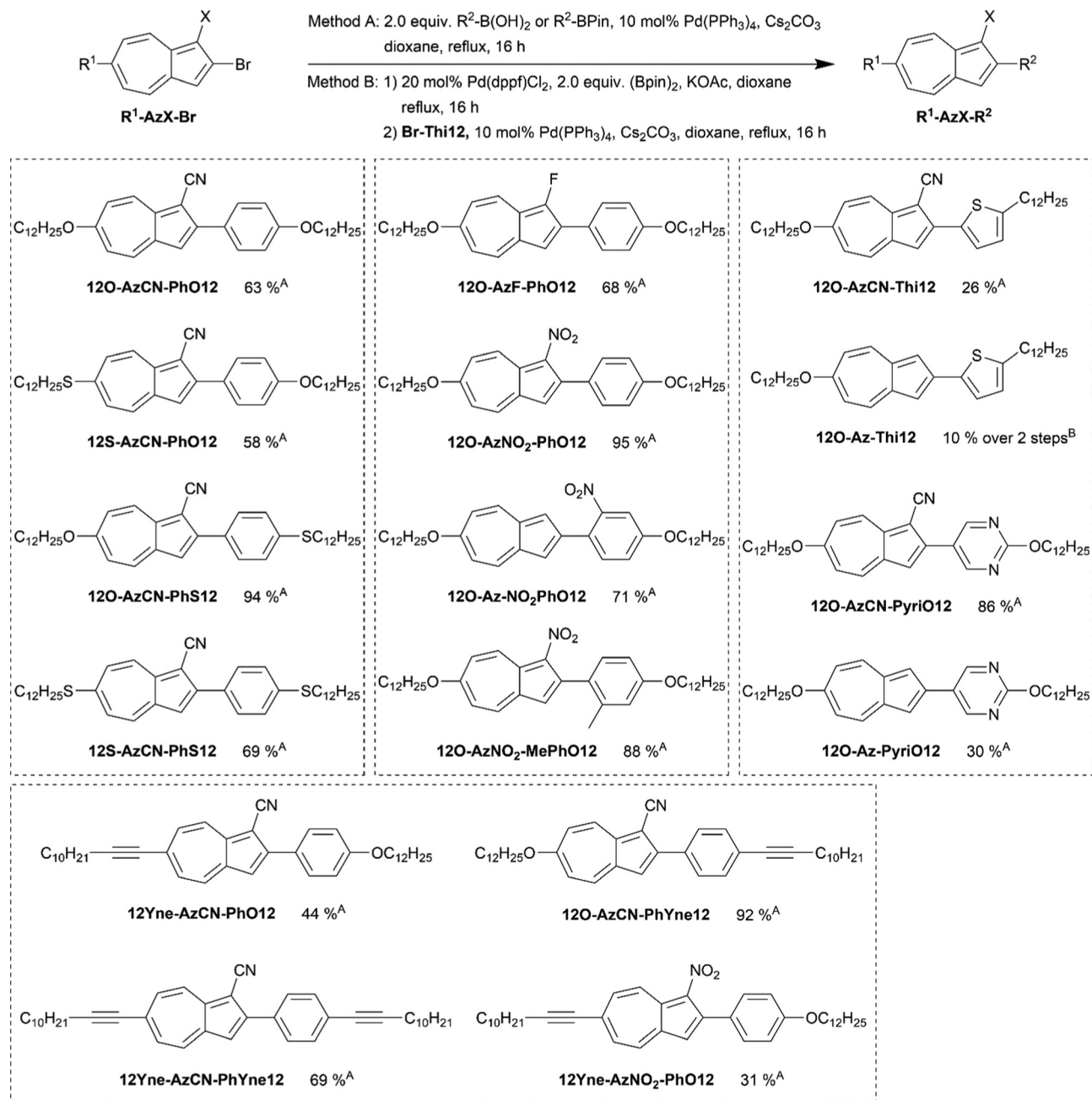
Fig. 4 Synthesis of the target compounds. [A]synthesis *via* method A, [B]synthesis *via* method B. BPin: 4,4,5,5-tetramethyl-1,3,2-dioxaborolane, dppf: 1,1'-bis(diphenylphosphino)ferrocene.

which seems to be crucial for the presence of a mesophase in this case.[30]

In the first series of target compounds, the ether groups were changed to thioether groups successively (Fig. 5(b)). Literature known **12O-AzCN-PhO12** shows a SmA–SmC phase sequence.[24] During cooling, the SmA phase forms from the isotropic liquid at 150 °C. At 133 °C a transition to the SmC phase is observed under the POM. However, the transition is too weak to be detected by DSC. The 65 K broad tilted phase transformed into a crystal at 60 °C. For **12S-AzCN-PhO12** a similar pattern was observed. During the cooling cycle of the

DSC measurement at 144 °C, an exothermic phase transition indicated the formation of a mesophase (Fig. 6(b) and Table S1, ESI†). This mesophase was assigned to a SmA phase due to fan textures and focal conic defects observed by POM (Fig. S2b, ESI†).[36] At 129 °C fan textures changed to broken fans, indicating the transition to a SmC phase (Fig. S2c, ESI†). Again, this transition was not visible in the DSC trace. The compound crystallized at 100 °C with a hysteresis of 16 K compared to the heating cycle. In contrast, the compound with a thioether chain at the phenyl ring **12O-AzCN-PhS12** did not develop a SmC phase. The SmA phase between 138 °C and 72 °C during cooling
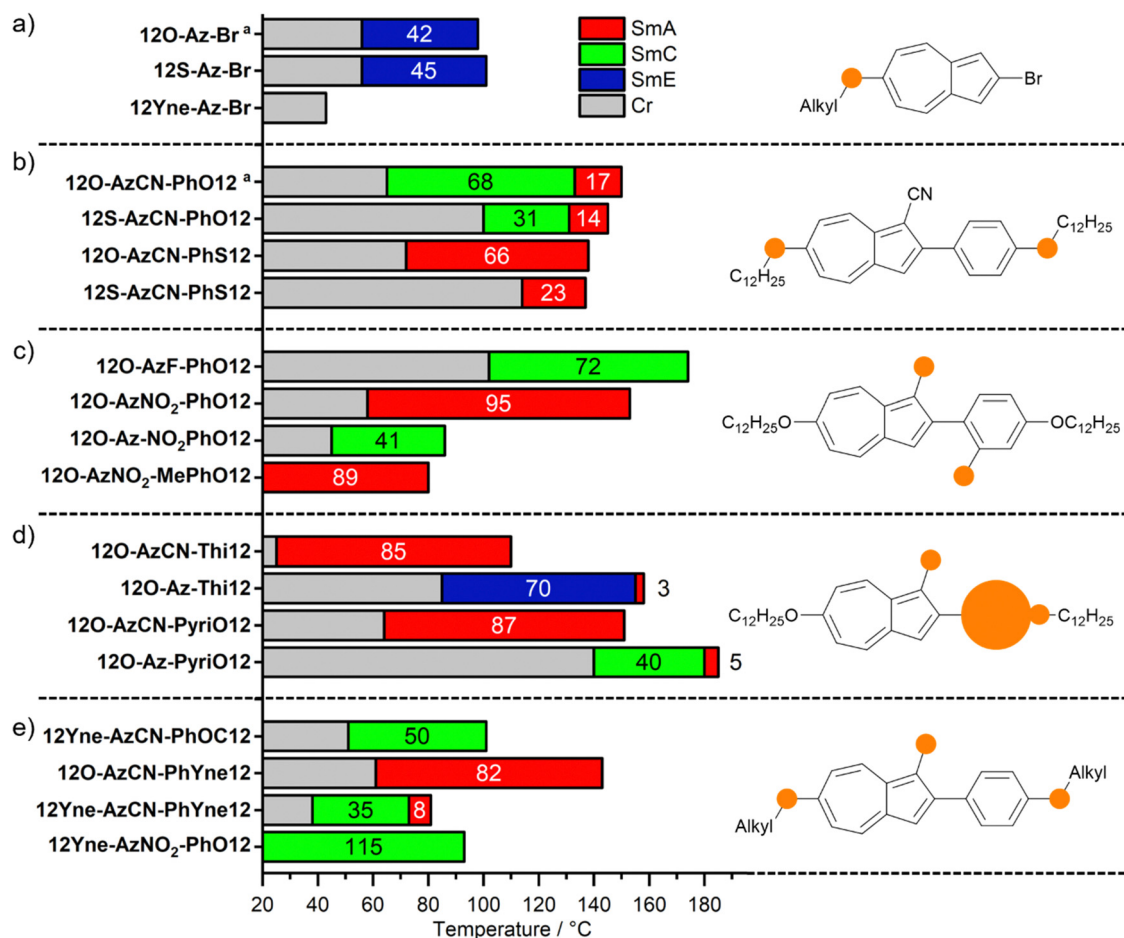
Fig. 5 Phase widths of the investigated mesomorphic compounds determined during cooling by DSC and POM. The position that is varied is marked with an orange circle. [a]Literature known compounds were included for comparison.[24,30]

was identified by fan textures under the POM (Fig. S2d, ESI†). In this case a hysteresis of 25 K was observed. When substituting both oxygen atoms with sulfur atoms in **12S-AzCN-PhS12**, the SmA phase shrinks to only 23 K phase width with similar textures (Fig. S2e, ESI†). The clearing transition did not change compared to **12O-AzCN-PhS12**, but the disulfur derivative crystallized faster at 114 °C. All phase geometries were confirmed by XRD (Fig. S9–S11 and Table S2, ESI†). Due to the lack of well oriented samples, the SmA and SmC phases could not be distinguished from each other by XRD. The observed textures by POM still allow differentiation between those two phases.

In another series we investigated the influence of the lateral substituent on the mesomorphic properties (Fig. 5(c)). When reducing the size of the lateral substituent from nitril to fluoro in **12O-AzF-PhO12**, the clearing point increased to 174 °C (Fig. S6e, ESI†). Moreover, a SmC phase formed directly from the isotropic phase without passing through a SmA phase indicated by Schlieren textures (Fig. S2f, ESI†). **12O-AzF-PhO12** crystallized at 105 °C with only a small hysteresis of 3 K compared to the heating curve of the DSC measurement. In contrast, **12O-AzNO2-PhO12** had similar clearing temperatures with 153 °C compared to **12O-AzCN-PhO12** and showed an orthogonal SmA

phase (Fig. S3a and S6f, ESI†). The thermogram showed a strong hysteresis. While the crystalline to SmA transition was detected at 94 °C during heating, crystallization during cooling was delayed to 58 °C. With the lateral nitro substituent, the SmC phase was suppressed, and **12O-AzNO2-PhO12** only showed a 95 K broad SmA phase. The situation changed dramatically, when moving the nitro group from the azulene to the phenyl substituent like in **12O-Az-NO2PhO12**. In this case the clearing into the isotropic phase was already observed at 86 °C. While the mesophase during heating was rather small with 10 K, the phase width during cooling was expanded to 41 K (Fig. S7a, ESI†). Also, the phase geometry changed back to a SmC phases, indicated by Schlieren textures (Fig. S3c, ESI†). For **12O-AzNO2-MePhO12**, carrying an additional 2-methyl group at the phenyl ring, the heating cycle of the DSC thermogram showed a small mesophase between 70 °C and 79 °C (Fig. S7a, ESI†). However, crystallization seems to be strongly hindered by the second substituent. In the cooling cycle, no crystallization peak was observed. Instead, a weak glass transition at −9 °C indicated freezing of the mesophase. Upon reheating, cold crystallization at 25 °C was followed by melting into the mesophase. Due to fan textures with focal conic defects observed under the POM the mesophase was assigned a SmA phase (Fig. S3b, ESI†). As already
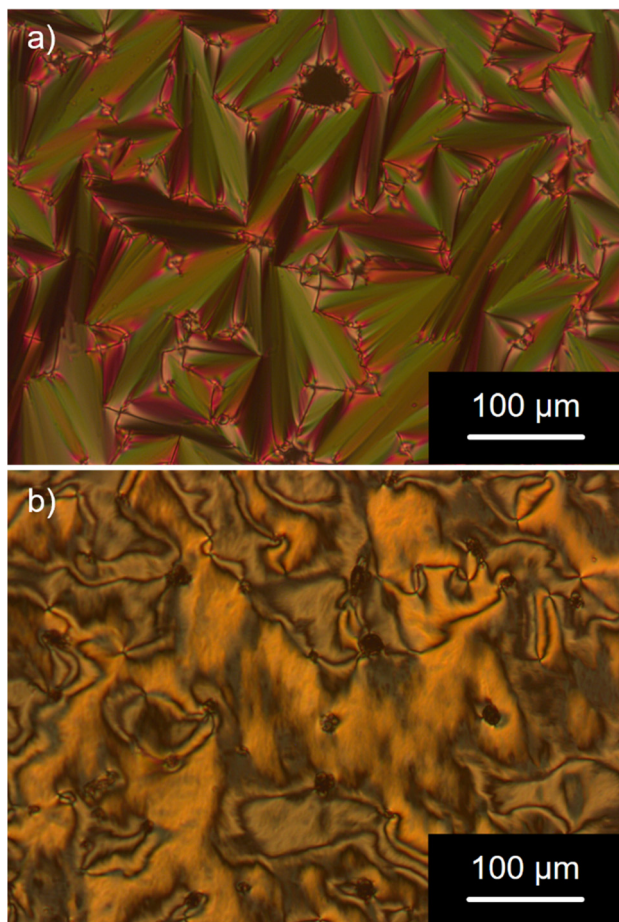
Fig. 6 Optical micrographs between crossed polarizers upon cooling from the isotropic yield in 5 K min⁻¹. (a) Fan textures of the SmA phase of **12O-AzCN-Thi12** at 93 °C and (b) Schlieren textures of the SmC phase of **12Yne-AzNO2-PhO12** at 76 °C.

seen in the sulfur series, XRD measurements indicated the existence of a fluid smectic phase but could not distinguish between an orthogonal or tilted phase (Table S2 and Fig. S12, S13, ESI†).

For further derivatization of **12O-AzCN-PhO12**, the phenyl ring was substituted with heteroaromatic moieties (Fig. 5(d)). We focused on pyrimidine and thiophene heterocycles. The 5-membered thiophene leads to a small kink in the calamitic molecule, while the pyrimidine might drastically change the electronic nature compared to the phenyl. **12O-AzCN-Thi12** cleared at 110 °C, which is about 40 K lower than **12O-AzCN-PhO12** (Fig. S7d, ESI†). In the DSC trace only a weak crystallization at 25 °C with an enthalpy of −5.1 kJ mol⁻¹ was observed. However, in the consecutive heating cycle the melting point at 59 °C had an enthalpy of 26.9 kJ mol⁻¹. Fan textures under the POM identified the mesophase as a SmA phase (Fig. 6(a)). When removing the lateral substituent (**12O-Az-Thi12**) the clearing transition moved to 159 °C. 3 K under the clearing point a second transition with similar enthalpies was detected (Fig. S7c, ESI†). Observation of the phenomena under the POM showed the growth of elongated germs when cooling from the isotropic liquid, so called

bâtonnet textures (Fig. S3d, ESI†). Before the bâtonnets could fully develop into fan textures, rings formed within the textures indicating the second phase transition (Fig. S3e, ESI†). This behavior is known for SmA to SmE phase sequences.[36] Indeed, XRD measurements of the low temperature phase confirmed the presence of a SmE phase (Table S2 and Fig. S14a, b, ESI†). The pyrimidine derivative **12O-AzCN-PyriO12** has the same molecular geometry as **12O-AzCN-PhO12**. The phase transition temperatures determined by DSC were also similar (Fig. S7f, ESI†). The isotropic to mesophase transition was detected at 151 °C, and the compound crystallized at 64 °C. However, under the POM only a SmA phase was observed (Fig. S4c, ESI†). For the pyrimidine derivatives, removal of the lateral substituents also led to increased phase transition temperatures. **12O-Az-PyriO12** clears at 185 °C and crystallizes at 144 °C with only 3 K hysteresis (Fig. S7e, ESI†). Broadening of the clearing transition in iterative cycles indicated slow decomposition of the compound at elevated temperatures. Therefore, the first cycle of the thermogram was used for determination of the transition temperatures. Observations *via* POM showed fan textures that changed to broken fan textures at 179 °C clearly hinting a SmA–SmC phase sequence (Fig. S4a and b, ESI†). Surprisingly, this time the SmA to SmC transition was also visible by DSC as a first order transition with an enthalpy of 0.4 kJ mol⁻¹ (Fig. S7e, ESI†).

The last series of target compounds differed by carrying either alkoxy chains or alkyne side chains. (Fig. 5(e)). This could influence not only the electronic properties of the aromatic system, but also affect the molecular packing due to increased rigidity of the molecule. **12Yne-AzCN-PhO12** with an alkyne at the azulene moiety had a low lying isotropic to mesophase transition at 102 °C (Fig. S8a, ESI†). A broad crystallization peak was observed at 25 °C. Schlieren textures under POM indicated the presence of a tilted SmC phase (Fig. S5a, ESI†). The azulene with **12O-AzCN-PhYne12** inverted substitution pattern melted at 80 °C and cleared at 143 °C (Fig. S8b, ESI†). During cooling, 19 K hysteresis were observed. Moving the alkyne chain to the phenyl ring favored the SmA, indicated by the known combination of fan textures and focal conic defects (Fig. S5b, ESI†). When changing both chains to alkyne groups even lower clearing temperatures were observed. **12Yne-AzCN-PhYne12** formed the mesophase at 81 °C from cooling from the isotropic liquid and crystallized at 38 °C (Fig. S8c, ESI†). POM studies revealed a SmA–SmC phase sequence with a phase transition at 73 °C that was not visible in the DSC measurement (Fig. S5c and d, ESI†). We then combined the SmA promoting nitro group with the SmC promoting alkyne chain at the azulene. **12Yne-AzNO2-PhO12** formed a broad SmC phase indicated by Schlieren textures upon cooling from the isotropic liquid (Fig. 6(b)). Those textures could still be sheared at room temperature. The thermogram confirmed this observation, indicating a mesophase during cooling between 96 °C and −22 °C. Instead of crystallization a glass transition was observed. Cold crystallization was detected during reheating prior to the melting into the mesophase. XRD studies confirmed the presence of fluid smectic phases in all cases (Fig. 7(b) and Fig. S16–S18, ESI†).
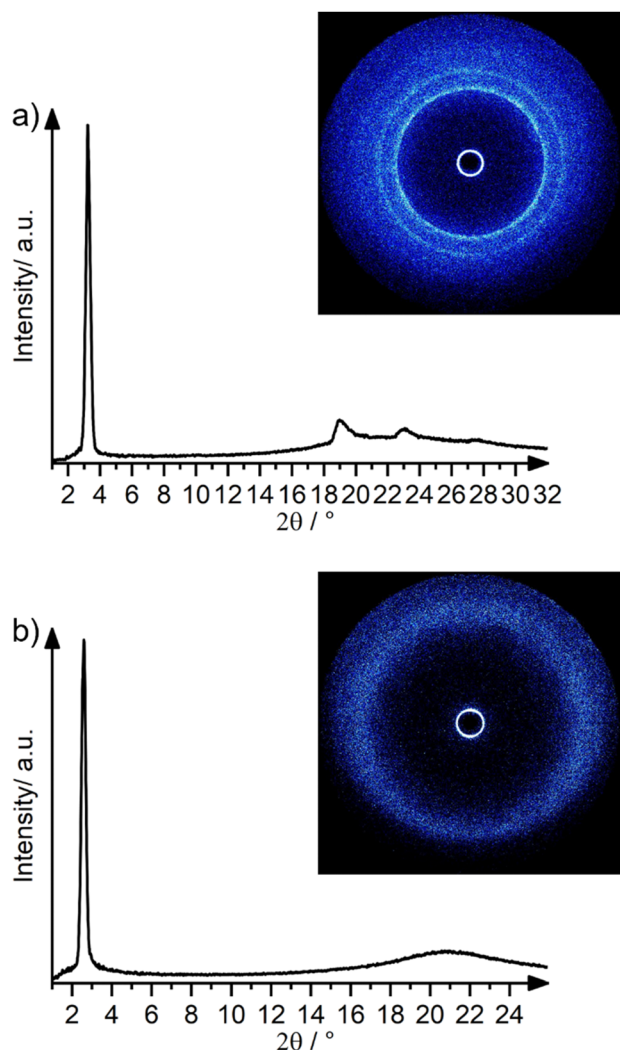
Fig. 7   WAXS diffractogram and diffraction pattern of (a) the SmE phase of **12S-Az-Br** at 75 °C and (b) the SmC phase of **12Yne-AzNO2-PhO12** at room temperature.

Discussion

The calamitic 2-aryl-azulene core with two side chains described in this publication promotes mainly SmA and SmC phases. However, the lateral substituent and the type of side chain and linkage strongly influence which phase is present for each derivative. Larger, more polar lateral groups promote SmA phases, while small groups lead to SmC phases. The nitrile group in **12O-AzCN-PhO12** has the right size and polarity for the compound to form both phases. It might be argued that smaller substituents allow a closer stacking of the aromatic system, thus promoting the SmC phase *e.g.*, in **12O-AzF-PhO12**. In contrast, the bulky nitro group in **12O-AzNO2-PhO12** prevents those interactions, leading to an unordered SmA phase. While the dipole moment is nearly parallel to the aromatic core in the case of nonpolar substituents, a polar substituent leads to an additional transverse dipole moment that could disrupt the SmC phase. It is noteworthy that in general all compounds

show relatively high clearing enthalpies of around 10 kJ mol^{-1} (Table S1, ESI†). **12O-AzF-PhO12** has a remarkably high clearing enthalpy of 14.5 kJ mol^{-1} which might be due to the strong dispersion interactions of the aromatic system. **12O-Az-NO2PhO12** also shows a SmC phase despite possessing the bulky nitro group. In this case the group seems to still allow the aromatic interactions because of being positioned at the phenyl ring.

While larger, polar substituents tend to prefer SmA phases over SmC phases, they also contribute to supercooling. Compounds with small side groups like **12O-AzF-PhO12**, **12O-Az-Thi12** or **12O-Az-PyriO12** show a hysteresis of only a few Kelvins. In contrast, the nitro group super cools with at least 30 K. In the case of **12O-AzNO2-MePhO12** and **12Yne-AzNO2-PhO12**, the mesophase is present even at temperatures below 0 °C.

The change from ether to thioether chains seems to be rather subtle. Therefore, it appears logical that **12S-AzCN-PhO12** behaves similar to the original dioxo derivative **12O-AzCN-PhO12**. The loss of the SmC phase in **12O-AzCN-PhS12** cannot be explained by a different stacking of the side groups. It is known that polar groups situated at the end of the core promote tilted phases.[37] The less polar thioether moieties thus prefer the orthogonal SmA phase. For the compounds **12S-AzCN-PhO12**, **12O-AzCN-PhS12** and **12O-AzNO2-PhO12** single crystal X-ray structures were obtained (Fig. S18–S20, ESI†). All three compounds show nanosegregation in der crystalline form. The compounds form dimers by a non-classical hydrogen bond between the H at the 7-membered ring and the polar lateral substituent. However, this interaction is not expected to be present for the rotating molecules of the mesophase. While **12S-AzCN-PhO12** is present in the all-*trans* configuration, both chains of **12O-AzCN-PhS12** bear one *cis* configuration. **12S-AzCN-PhO12** with 1.134 g cm^{-3} is slightly denser packed than **12O-AzCN-PhS12** (1.124 g cm^{-3}, Table S3, ESI†). This might show that the packing of **12O-AzCN-PhS12** is not that compact in the mesophase and in the crystal and therefore does not form a SmC phase.

The implementation of the alkyne group has multiple effects on the molecule. On the one hand, alkynes reduce the polarity compared to ether derivatives, on the other hand free volume is increased (Fig. 8(a)). Both effects lead to lower phase transition temperatures, as seen in all derivatives with alkyne chains. However, alkynes also enlarge the π-system. They might therefore participate in the stacking of the aromatic core, even though a phenyl to alkyne coordination should be considerably weak due to the different geometry. Assuming an anti-parallel packing of the azulenes, the packing options differ depending on the position of the alkyne. In the case of **12Yne-AzCN-PhO12** the azulene core is between the alkyne moiety and the phenyl ring. Therefore, the dipole moments of the azulene might interact with each other and the bulky substituents move away from each other (Fig. 8(b)). Both effects allow a closer stacking of the azulene, therefore promoting a SmC phase. The alkyne at the phenyl ring in **12O-AzCN-PhYne12** does not benefit from the above-described effects (Fig. 8(c)). The phase transition temperatures are comparable to the **12O-AzCN-PhS12**
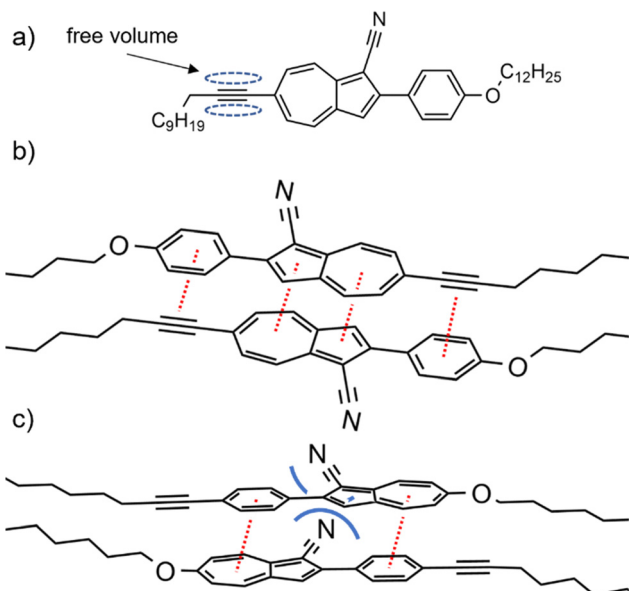
Fig. 8 (a) Free volume caused by alkyne groups at the example of **12Yne-AzCN-PhO12**. (b) Proposed arrangement for **12Yne-AzCN-PhO12** and (c) for **12O-AzCN-PhYne12**.

derivative. Both compounds only show SmA phases, indicating that the linkage at the phenyl ring strongly affects the phase behavior.

When substituting both ether groups with alkyne chains, the extension of the π-system is balanced, thus the SmA–SmC phase sequence is kept. However, due to the loss in polarity and the increase of free volume, phase widths shrink, and phase transition temperatures are reduced. When combining the alkyne with a nitro group as in **12Yne-AzNO2-PhO12**, the SmC phase is preserved. This can be explained with the packing described for **12Yne-AzCN-PhO12** (Fig. 8(b)). In this case neighboring lateral substituents are far enough from each other to not affect the close packing of the core. The situation seems like in **12O-Az-NO2PhO12** which also only shows a SmC phase.

In azulenes with the thiophene unit *e.g.*, **12O-AzCN-Thi12** the SmC phase disappears. This is probably due to the kink caused by the presence of a 5-membered ring. Even without the lateral substituent in **12O-Az-Thi12** the SmC does not reappear. Instead, the close packing of the aromatic core causes a soft-crystalline SmE phase. This phase is mostly observed with a side chain at only one part of the molecule.[30,34] In this case the strong core interactions seem sufficient to form the herring-bone packing that is characteristic for this phase.[35] The loss of the herringbone-packing is shown in the DSC by a strong SmE to SmA transition with 14.7 kJ mol^{-1}. The clearing enthalpy is even higher with 16.4 kJ mol^{-1}. In the case of **12O-AzCN-PyriO12** the pyrimidine moiety is known to prefer the SmA phase.[37] It should be stressed that melting and clearing points of **12O-AzCN-PhO12** and **12O-AzCN-PyriO12** are barely different. Once again subtle changes of the electronic structure at the side ring have a strong impact on the geometry of the mesophase.

De Vries-like properties

After assignment of the mesophases, we picked the three compounds **12S-AzCN-PhO12**, **12Yne-AzCN-PhYne12** and **12O-Az-PyriO12** showing a SmA–SmC phase sequence and investigated their de Vries-like properties. Temperature dependent layer spacing was determined by SAXS (Fig. 9(a)). All compounds showed non classical behavior in the SmC phase and their layer spacing increased upon cooling after going through a minimum. **12S-AzCN-PhO12** and **12Yne-AzCN-PhYne12** showed relatively low maximum layer shrinkages lc$_{max}$ of 0.5% and 0.9%, respectively (Table 1). In contrast, the pyrimidine derivative without lateral substituent **12O-Az-PyriO12** had a high lc$_{max}$ of 3.6%. The higher layer shrinkage can be partially explained when having a look at the tilt angle θ determined by POM (Fig. 9(b)). **12O-Az-PyriO12** shows comparably high angles of up to 27°. **12S-AzCN-PhO12** saturates at 19°, while **12Yne-AzCN-PhYne12** only reaches 16°. Due to geometry a higher tilt angle in the SmC phase also causes a higher layer shrinkage. Knowing lc$_{max}$ and θ, the reduction value R can be calculated (Table 1). The best values were achieved for **12S-AzCN-PhO12** with $R = 0.35$. This outperforms the de Vries-like properties of **12O-AzCN-PhO12** which reached 0.43.[24] For **12Yne-AzCN-PhYne12** $R = 0.58$ was calculated and **12O-Az-PyriO12** had a high value of 0.74.

The de Vries-like properties of **12S-AzCN-PhO12** and **12Yne-AzCN-PhYne12** are similar to those of the known **12O-AzCN-PhO12**. However, **12O-Az-PyriO12** behaves completely different. Previously we argued that the de Vries-like behavior is caused by a combination of multiple effects.[24] One main effect is the strongly increasing nematic order parameter S_2 upon entering the SmC phase. Another reason for de Vries-like behavior was traced down to a shift of mass centers in those molecules. This shift reduced the repulsive interactions of the nitriles in **12O-AzCN-PhO12** and simultaneously increased the layer spacing d. Since **12O-Az-PyriO12** does not bear a lateral substituent, there is no reason for this shift of mass centers. Lacking the identified structural feature for de Vries-like behavior, the R-value of **12O-Az-PyriO12** drops to 0.74. While bulkier lateral substituents seem beneficial for de Vries-like properties, they also destabilize the required SmC phase. Careful balancing of those two effects while considering different chain lengths could lead to materials with even lower lc$_{max}$ and thus improved de Vries-like properties.

Conclusion

In the current study we examined the relationship between the molecular structure of 2-(hetero)aryl-azulene mesogens and the mesophase geometry by synthesizing derivatives with different lateral groups and different functional groups connecting the side chains. It could be demonstrated that the size and position of the lateral substituents determine which phase is present. Heteroaryl substituents like pyrimidyl (**12O-AzCN-PyriO12**, **12O-AzCN-Thi12**) or a phenyl thioether (**12O-AzCN-PhS12**) seem to prevent the formation of a SmC phase. The implementation
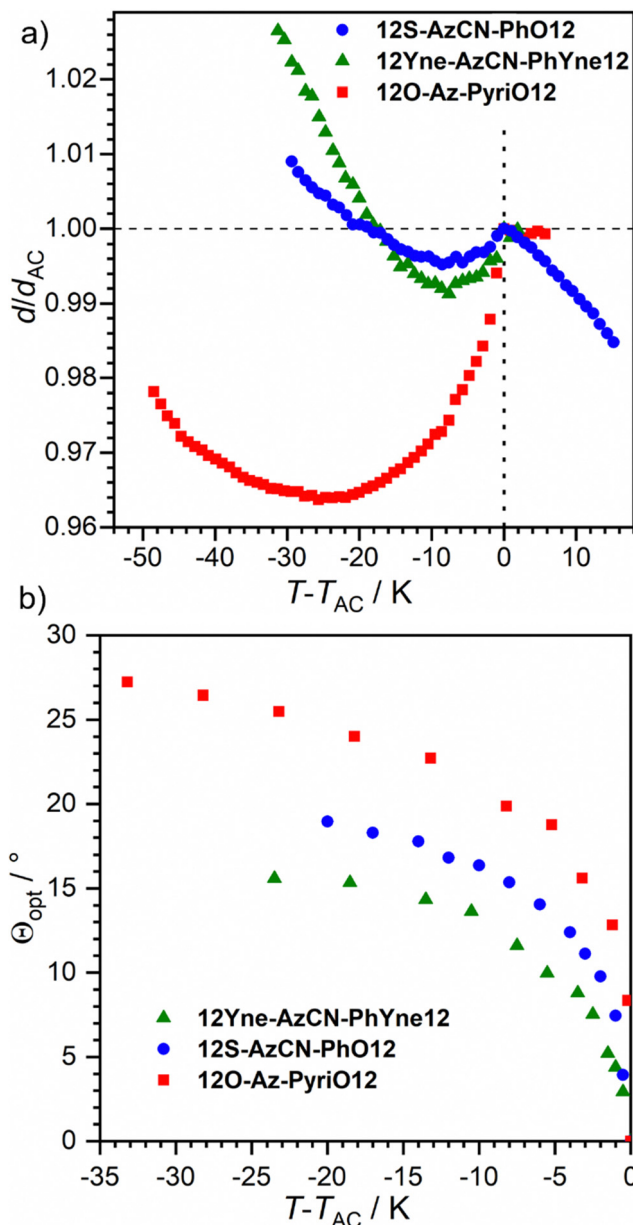
Fig. 9 Temperature dependent de Vries properties of **12Yne-AzCN-PhYne12**, **12S-AzCN-PhO12** and **12O-Az-PyriO12**: (a) relative layer spacing d/d_{AC} as a function of $T - T_{AC}$ and (b) optical tilt angle θ during the SmC phase.

Table 1 Maximum layer contraction lc_{max} measured with SAXS, tilt angles determined by POM and R-values of de-Vries like liquid crystals at $T - T_{AC} = -10$ K of the characterized compounds

Compound	lc_{max}/%	θ_{opt}/°	R
12S-AzCN-PhO12	0.5	16	0.35
12Yne-AzCN-PhYne12	0.9	13	0.58
12O-Az-PyriO12	3.6	21	0.74

of alkyne side chains instead of ether chains promotes the SmC phases and reduces phase transition temperatures. Therefore,

12Yne-AzNO2-PhO12 shows a SmC phase already at room temperature. Furthermore, new compounds with de Vries-like behavior were identified with R-values of down to 0.35 for the best candidate **12S-AzCN-PhO12**. In our previous report,[24] we reasoned that the good de Vries-like properties are due to a shift of mass centers induced by the lateral substituent. Consequently, compounds devoid of a lateral substituent should have weak de Vries-like properties, which was observed for **12O-Az-PyriO12**. The molecular design discovered for calamitic azulenes should help to control the molecular orientation and thus the performance of organic electronic devices.

Author contributions

FS and SL conceived and designed this research. FS, BL, DR, and DB synthesized the compounds and did the liquid crystalline characterization. FS performed and evaluated the X-ray and tilt angle measurements. WF performed and evaluated the single crystal measurements. FS wrote the first draft of the manuscript, SL and BL co-wrote the manuscript. All authors approved the final version of the manuscript.

Conflicts of interest

There are no conflicts to declare.

Acknowledgements

References

1 A. G. Anderson and B. M. Steckler, *J. Am. Chem. Soc.*, 1959, **81**, 4941–4946.
2 R. S. H. Liu, *J. Chem. Educ.*, 2002, **79**, 183.
3 H. Xin, B. Hou and X. Gao, *Acc. Chem. Res.*, 2021, **54**, 1737–1753.
4 J. Huang, S. Huang, Y. Zhao, B. Feng, K. Jiang, S. Sun, C. Ke, E. Kymakis and X. Zhuang, *Small Methods*, 2020, **4**, 2000628.
5 L. C. Murfin and S. E. Lewis, *Molecules*, 2021, **26**, 353.
6 J. Zhang and S. Petoud, *Chem. – Eur. J.*, 2008, **14**, 1264–1272.
7 Y. Zhou, Y. Zhuang, X. Li, H. Ågren, L. Yu, J. Ding and L. Zhu, *Chem. – Eur. J.*, 2017, **23**, 7642–7647.
8 E. Puodziukynaite, H.-W. Wang, J. Lawrence, A. J. Wise, T. P. Russell, M. D. Barnes and T. Emrick, *J. Am. Chem. Soc.*, 2014, **136**, 11043–11049.
9 H. Xin, C. Ge, X. Jiao, X. Yang, K. Rundel, C. R. McNeill and X. Gao, *Angew. Chem., Int. Ed.*, 2018, **57**, 1322–1326.

10 F. Schwarz, M. Koch, G. Kastlunger, H. Berke, R. Stadler, K. Venkatesan and E. Lörtscher, *Angew. Chem., Int. Ed.*, 2016, **55**, 11781–11786.

11 Q. Fan, D. Martin-Jimenez, D. Ebeling, C. K. Krug, L. Brechmann, C. Kohlmeyer, G. Hilt, W. Hieringer, A. Schirmeisen and J. M. Gottfried, *J. Am. Chem. Soc.*, 2019, **141**, 17713–17720.

12 Z. Chen, J. Droste, G. Zhai, J. Zhu, J. Yang, M. R. Hansen and X. Zhuang, *Chem. Commun.*, 2019, **55**, 9047–9050.

13 A. E. Asato, A. Peng, M. Z. Hossain, T. Mirzadegan and J. S. Bertram, *J. Med. Chem.*, 1993, **36**, 3137–3147.

14 T. Tomiyama, M. Yokota, S. Wakabayashi, K. Kosakai and T. Yanagisawa, *J. Med. Chem.*, 1993, **36**, 791–800.

15 H. Nakamura, M. Sekido and Y. Yamamoto, *J. Med. Chem.*, 1997, **40**, 2825–2830.

16 L. C. Murfin, C. M. López-Alled, A. C. Sedgwick, J. Wenk, T. D. James and S. E. Lewis, *Front. Chem. Sci. Eng.*, 2020, **14**, 90–96.

17 F. Ayaz, A. Yuzer, T. Ince and M. Ince, *Inflammation*, 2020, **43**, 1009–1018.

18 S. Ito, H. Inabe, N. Morita, K. Ohta, T. Kitamura and K. Imafuku, *J. Am. Chem. Soc.*, 2003, **125**, 1669–1680.

19 S. Ito, M. Ando, A. Nomura, N. Morita, C. Kabuto, H. Mukai, K. Ohta, J. Kawakami, A. Yoshizawa and A. Tajiri, *J. Org. Chem.*, 2005, **70**, 3939–3949.

20 K. Nakagawa, T. Yokoyama, K. Toyota, N. Morita, S. Ito, S. Tahata, M. Ueda, J. Kawakami, M. Yokoyama, Y. Kanai and K. Ohta, *Tetrahedron*, 2010, **66**, 8304–8312.

21 S. Ito, M. Ueda, R. Sekiguchi and J. Kawakami, *Tetrahedron*, 2013, **69**, 4259–4269.

22 E. de Domingo, M. Barcenilla, J. M. Martín-Alvarez, J. A. Miguel and S. Coco, *Dyes Pigm.*, 2020, **176**, 108195.

23 F. Schulz, S. Takamaru, T. Bens, J. Hanna, B. Sarkar, S. Laschat and H. Iino, *Phys. Chem. Chem. Phys.*, 2022, **24**, 23481–23489.

24 F. Schulz, B. Wank, P. Nacke, W. Frey and S. Laschat, *Mater. Adv.*, 2023, **4**, 1306–1313.

25 J. P. F. Lagerwall and F. Giesselmann, *ChemPhysChem*, 2006, **7**, 20–45.

26 A. de Vries, *J. Chem. Phys.*, 1979, **71**, 25–31.

27 Q. Song, D. Nonnenmacher, F. Giesselmann and R. P. Lemieux, *J. Mater. Chem. C*, 2013, **1**, 343–350.

28 M. D. Radcliffe, M. L. Brostrom, K. A. Epstein, A. G. Rappaport, B. N. Thomas, R. Shao and N. A. Clark, *Liq. Cryst.*, 1999, **26**, 789–794.

29 E. V. Dehmlow and D. Balschukat, *Chem. Ber.*, 1985, **118**, 3805–3816.

30 F. Schulz, P. Ehni, B. Wank, A. Bauer, W. Frey and S. Laschat, *Liq. Cryst.*, 2021, **48**, 832–843.

31 R. S. Muthyala and R. S. H. Liu, *J. Fluorine Chem.*, 1998, **89**, 173–175.

32 H. Xin, J. Li, R.-Q. Lu, X. Gao and T. M. Swager, *J. Am. Chem. Soc.*, 2020, **142**, 13598–13605.

33 C. Schilling, A. Bauer, J. A. Knöller, F. Schulz, A. Zens and S. Laschat, *J. Mol. Liq.*, 2022, **367**, 120519.

34 S. M. Schultz, G. Kehr, R. Fröhlich, G. Erker, N. Kapernaum, C. Hägele, F. Giesselmann, S. Laschat, R. Judele and A. Baro, *Liq. Cryst.*, 2007, **34**, 919–926.

35 S. Diele, S. Tosch, S. Mahnke and D. Demus, *Cryst. Res. Technol.*, 1991, **26**, 809–817.

36 I. Dierking, *Textures of Liquid Crystals*, John Wiley & Sons, 2006.

37 J. W. Goodby, in *Handbook of Liquid Crystals*, John Wiley & Sons, Ltd, 2014, pp.1–39.